Metrology and statistics : from clocks to millisecond pulsars

Antoine Baudiquez

To cite this version:

Antoine Baudiquez. Metrology and statistics : from clocks to millisecond pulsars. Physics [physics]. Université Bourgogne Franche-Comté, 2022. English. NNT : 2022UBFCD061 . tel-04083649

HAL Id: tel-04083649
https://theses.hal.science/tel-04083649

Submitted on 27 Apr 2023

THÈSE DE DOCTORAT

DE L'ÉTABLISSEMENT
UNIVERSITÉ BOURGOGNE FRANCHE-COMTÉ
PRÉPARÉE À L'UNIVERSITÉ DE FRANCHE-COMTÉ

Metrology and statistics: From clocks to millisecond pulsars

Métrologie et statistiques : de l'horlogerie aux pulsars millisecondes

Spécialité : Sciences pour l'ingénieur

soutenue par

ANTOINE BAUDIQUEZ

à Besançon, le 13 Décembre 2022

Thèse supervisée par : **FRANÇOIS VERNOTTE**, **ÉRIC LANTZ**, **GIANNA PANFILO** et **ENRICO RUBIOLA**

Composition du jury :

Yann, LE COQ	Ingénieur de recherche - Observatoire de Paris (LNE-SYRTE)	**Rapporteur**
Pierre, PUDLO	Professeur des universités - Université Aix-Marseille	**Rapporteur**
Claudio, E. CALOSSO	Chargé de recherche - Istituto Nazionale di Ricerca Metrologica	Examinateur
Elizabeth, A. DONLEY	Directrice de recherche - National Institute of Standards and Technology	Examinatrice
Pierre, PUDLO	Professeur des universités - Université Aix-Marseille	**Président**
François, VERNOTTE	Professeur des universités - Université de Franche-Comté	Directeur de thèse
Gianna, PANFILO	Physicienne Principale - Bureau International des Poids et Mesures	Co-directrice de thèse
Éric, LANTZ	Professeur des universités - Université de Franche-Comté	Invité
Enrico, RUBIOLA	Professeur des universités - Université de Franche-Comté	Invité

École doctorale : SPIM, ED 37
Laboratoire : Institut FEMTO-ST
UMR CNRS 6174, Besançon, France

Remerciements formels

Cette thèse a été financée par la Communauté d'Agglomération du Grand Besançon (CAGB). Ce travail a également profité du financement par les projets du Programme d'Investissement d'Avenir (PIA) de l'ANR : Oscillator IMP (Project 11-EQPX-0033) et FIRST-TF (Project 10-LABX-0048). Le laboratoire FEMTO-ST, l'ENSMM, l'université de Bourgogne Franche-Comté à Besançon et le BIPM à Sèvres ont été les lieux d'accueil quotidien pour nos travaux, et nous tenons à remercier les différentes instances qui nous ont soutenu financièrement et administrativement à de nombreuses reprises.

Remerciements informels

Tout d'abord je tiens profondément à remercier et exprimer toute ma gratitude envers François Vernotte. Pendant ces huit dernières années passées à l'université, François a été l'un des Professeurs qui m'a donné envie de continuer dans la recherche pour arriver où j'en suis aujourd'hui. C'est avant tout pour sa personne que j'ai choisi de poursuivre sur ce sujet de thèse qui était un domaine totalement inconnu pour moi. Merci pour sa disponibilité et sa bienveillance ainsi que sa motivation débordante qui a été un moteur dans la réalisation de ces travaux. Merci pour tout ce qu'il m'a appris, tant sur le plan pédagogique et scientifique qu'humain. Merci de m'avoir aider à donner le meilleur de moi-même et orienté le travail vers ce qui me correspondait le plus n'étant pas un “graisse boulon”. Merci de m'avoir poussé à élargir mes connaissances ainsi que le partage de sa passion pour l'astronomie et l'histoire des sciences, le tout agrémenté de sa légèreté et son humour. Ce serait avec un immense plaisir pour moi de pouvoir continuer à travailler ensemble ne serait-ce que pour les quelques années de carrières qu'il lui reste.

Merci également à Gianna Panfilo pour son encadrement lors de mon séjour au BIPM. Gianna a su me faire profiter de sa grande expérience et a toujours été disponible malgré ses responsabilités. Merci notamment d'avoir permis d'élargir mon champ d'expertise et de m'avoir laissé une grande autonomie. Merci pour sa bienveillance ainsi que pour les discussions intéressantes que l'on a pu avoir. Ce serait un grand plaisir de continuer à travailler ensemble.

Merci à Éric Lantz qui a été présent aux moments clés de cette thèse avec ses remarques toujours pertinentes et son intuition sans faille. Éric a été un Professeur d'une grande pédagogie, présent pendant ces huit dernières années. N'étant pas un passionné d'optique il a tout de même su attirer mon attention avec notamment son expertise en statistique. Il a joué un rôle majeur dans mon choix d'enseigner avec en particulier son humour fin reliant actualité et pédagogie. Je lui souhaite une retraite bien méritée.

Je tiens à remercier également Enrico Rubiola, puits de sciences incontesté, c'est toujours un plaisir de l'écouter pour un temps indéterminé par définition. Enrico m'a permis de découvrir le côté applicatif et expérimental en lien avec cette thèse. Toujours prêt à partager ses connaissances, grand passionné de sciences, technologie et photographie, c'est sans modération que l'on s'ennivre de ses récits. C'est un vrai archéologue de la technologie toujours plein de surprise. Il m'a beaucoup apporté sur le plan scientifique ainsi qu'humain et je l'en remercie pour cela.

Je remercie également Patrizia Tavella qui a permis cette collaboration avec le BIPM. Sa bienveillance et sa positivité ont été un plaisir au quotidien. Je tiens à remercier tout les membres du département du Temps au BIPM pour leur accueil chaleureux. Merci particulièrement à Aurélie Harmegnies pour le partage de son expertise et sa disponibilité afin de résoudre mes petits problèmes Windows/Linux.

Merci à tout les membres du département Temps-Fréquence et en particulier l'équipe OHMS. Je pense spécialement à tous mes collègues avec qui j'ai partagé réunions, séminaires, mais aussi de nombreux moments de convivialité. Merci à tout ceux qui ont partagé le même bureau que moi, je pense notamment à Thomas Lauprêtre expert Tetris et musicien dans l'âme, Bachir Achi le calme olympien par excellence et Martina Matusko pour sa joie de vivre. J'adresse tous mes voeux de réussite à mes collègues doctorants et jeunes docteurs qui ont été une incroyable source de soutien et d'échange.

Je remercie également les nouveaux docteurs qui viennent d'autres laboratoires, je pense notamment à Joharimanitra Randrianandraina dont je pourrai désormais épeller le nom sans la moindre erreur et Norhan Omar m'ayant fait découvrir les délices du Liban. Merci à eux pour leur générosité sans pareille et d'avoir été présent tout au long de ma thèse. Je leur souhaite le meilleur pour la suite.

Je tiens aussi à remercier mes amis qui m'ont toujours soutenu et pour tous les bons moments passés ensembles.

Je souhaite remercier tout spécialement Zhanyu pour sa présence à mes côtés accompagnée de son humour dont elle seule a le secret, son soutien indéfectible ainsi que du courage dont elle a fait preuve pour s'intéresser et essayer de comprendre mon travail.

Mes derniers mots de remerciements sont pour ma famille : mes parents, mes soeurs et mon frère qui ont toujours été présents et ont été de grands soutiens tout au long de cette thèse. Je tiens à remercier également tous les autres membres de ma famille dont je ne pourrais citer tous les noms.

Special thanks:

I would like to warmly thank all the members of the jury for their clear interest in my work and for all their comments and suggestions to the improvement of the quality of this Thesis. I also want to express a great thank you to Elizabeth Donley for her help to improve the manuscript language quality.

Abstract

Time is the physical quantity that is measured with the greatest precision, far ahead of all the others. Recent advances in atomic clocks have made it possible to achieve relative stabilities of the order of a few 10^{-18}, thus corresponding to an uncertainty of about one second in the age of the Universe. However, it is not because these uncertainties become ridiculously small that they should be neglected, quite the contrary. The aim of this work is to contribute to improving the determination of these uncertainties. It is divided in two parts and concerns the fine characterization and improvement of a set of estimation methods.

In the present work we first describe a procedure to determine the jumps which can affect the time links used in the Coordinated Universal Time (UTC), calculated by the BIPM. This tool, based on a Kalman filter, should correctly determine the date of the steps and their magnitude, mainly for time steps, and give a warning to the BIPM Time Department about this unexpected problem. This warning will help to understand the nature of the steps which, in some cases, can affect the behavior of UTC. A critical example is the receiver calibration causing a step in time links and potentially impacting UTC behavior. To ensure the long-term stability of UTC, it is crucial to verify the data and identify problems.

The second part of the work mainly concerns a detailed analysis of frequency instabilities in terms of Bayesian statistics. In particular we want to obtain reliable confidence intervals around the measurements of the power spectrum of red noise processes at the lowest frequencies, e.g. the observation of millisecond pulsars in radio astronomy. Thus it is only possible to average on simultaneous observation of multiple instruments. We compare 95% upper limit of the red noise parameter using the spectrum average and cross-spectrum. Checked by massive Monte Carlo simulations, the cross-spectrum estimator leads to the variance-Gamma distribution with two instruments and a generalization to n instruments based on the Fourier transform of characteristic functions is provided.

Résumé en Français

Le temps est la grandeur physique qui se mesure avec la plus grande précision, loin devant toutes les autres. Les progrès récents des horloges atomiques ont permis d'atteindre des stabilités relatives de l'ordre de quelques 10^{-18}, correspondant ainsi à une incertitude d'environ une seconde sur l'âge de l'Univers. Cependant, ce n'est pas parce que ces incertitudes deviennent dérisoires qu'il faut les négliger, bien au contraire. Le but de ce travail est de contribuer à améliorer la détermination de ces incertitudes. Il est divisé en deux parties et porte sur la caractérisation fine et l'amélioration d'un ensemble de méthodes d'estimation.

Dans ce travail, nous décrivons d'abord une procédure pour déterminer les sauts qui peuvent affecter les liens de transfert de temps utilisés dans le calcul de l'échelle du Temps Universel Coordonnée (UTC), calculé par le BIPM. Cet outil, basé sur un filtre de Kalman, devrait déterminer correctement la date des sauts et leur grandeur, principalement pour les sauts de temps, et avertir le service du temps du BIPM de ce problème inattendu. Cet avertissement aidera à comprendre la nature des étapes qui, dans certains cas, peuvent affecter le comportement d'UTC. Un exemple critique est l'étalonnage du récepteur qui provoque un saut dans les transfert de temps et qui a potentiellement un impact sur le comportement d'UTC. Pour assurer la stabilité à long terme d'UTC, il est crucial de vérifier les données et d'identifier les problèmes.

La deuxième partie du travail concerne principalement une analyse détaillée en termes de statistiques bayésiennes des instabilités de fréquence. En particulier, nous voulons obtenir des intervalles de confiance fiables autour des mesures du spectre de puissance des processus de bruit rouge aux fréquences les plus basses, par ex. l'observation des pulsars millisecondes en radioastronomie. Ainsi, il n'est possible de faire la moyenne que sur l'observation simultanée de plusieurs instruments. Nous comparons la limite supérieure à 95% sur le paramètre de bruit rouge en utilisant la moyenne du spectre et le spectre croisé. Vérifié par des simulations massives de Monte Carlo, l'estimateur à spectre croisé conduit à la distribution variance-Gamma avec deux instruments et une généralisation à n instruments basée sur la transformée de Fourier des fonctions caractéristiques est fournie.

Contents

Part I

Context

Part I: Context

CHAPTER 1

From clocks . . .

1.1 Time and Frequency Standards

The most recurring question of all eras is undoubtedly what time is it? It is thus necessary to measure time by defining standards of time and frequency based on a periodic event which is repeated at a constant rate. This device is called a resonator, e.g. the pendulum for a pendulum clock but also the rotation of the earth! This resonator requires a source of energy to operate, the whole then forms an oscillator. This operates at a rate called the resonant frequency. In the case of the pendulum, the clock may be set to swing back and forth at the rate of one second. Counting the number of swings then creates a time scale that can be set for much longer durations, e.g. minutes, hours or even days. The device counting and displaying the result is called a clock. The relationship between the frequency uncertainty of a clock's resonator and the corresponding timing uncertainty of the clock is given in Table 1.1.

1.2 Before the atomic era

Throughout history [1–3], clock designers have sought more stable resonators. The first time scales were based on the repeatability of celestial events. Ancient Egyptian obelisks, built around 3500 B.C., are also among the earliest sundials. Sundials were the first devices used to measure the parts of a day. *Apparent solar time* was defined as the hour angle of the Sun. The inconstancy of these natural celestial frequencies with

This chapter does not constitute original work and the author does not lay any claim to anything discussed here.

Frequency Uncertainty	Measurement Period	Time Uncertainty
$\pm 1.00 \times 10^{-3}$	1 s	±1 ms
$\pm 1.00 \times 10^{-6}$	1 s	±1 μs
$\pm 1.00 \times 10^{-9}$	1 s	±1 ns
$\pm 2.78 \times 10^{-7}$	1 h	±1 ms
$\pm 2.78 \times 10^{-10}$	1 h	±1 μs
$\pm 2.78 \times 10^{-13}$	1 h	±1 ns
$\pm 1.16 \times 10^{-8}$	1 day	±1 ms
$\pm 1.16 \times 10^{-11}$	1 day	±1 μs
$\pm 1.16 \times 10^{-14}$	1 day	±1 ns

Table 1.1: Relationship of frequency uncertainty to time uncertainty. *From* [1].

the highlighting of irregularities was well understood at the time of Ptolemy. The laws of planetary motions showed that the orbit of the earth around the sun is elliptical and inclined with respect to the plane defined by the rotation of the Earth. The improvement of clocks as shown in Table 1.2, e.g. the pendulum invented by Christian Huygens in 1656, contributed to the demonstration of the irregularities of the apparent solar time. The correction effects of the ellipticity of the orbit associated to the concept of local meridian, led to a uniform time called *mean solar time*. In October 1884, the Washington International Conference adopted the Greenwich meridian as the prime meridian for measuring longitude. It is from this meridian that the time zones were also defined giving the *Greenwich Mean Time* (GMT). A day lasts 24 hours, thus the terrestrial globe was divided into 24 time zones. GMT time is the mean solar time calculated at noon in Greenwich. This in in 1948 that the International Astronomical Union (IAU) formally recommended the use of *universal time* (UT). The determination of universal time required astronomical observations to measure the sidereal time. The sidereal time is not time in the usual sense, it is the measure of the angle between the vernal point and the meridian plane but this angle varies proportionnaly to time (to a very small approximation). The instants of stars' meridian transits were detected and corrections to the reference clock were derived with the help of transit instruments.

In order to determine very accurately the sidereal time, many observatories were equipped with meridian telescopes from the 18th century. In 1885, Gautier's meridian telescope with a diameter of 18 cm shown in Figure 1.1 was installed in Besançon and had a central role in chronometric activities. More details on time measurement in Besançon can be found in [4]. The time-scale of the observatory was controled very precisely by noting the moment of passage through the meridian of each fundamental star whose position is known with great accuracy. This time was measured using a second reference instrument: the astronomical pendulum with electric switches built by Auguste Fénon

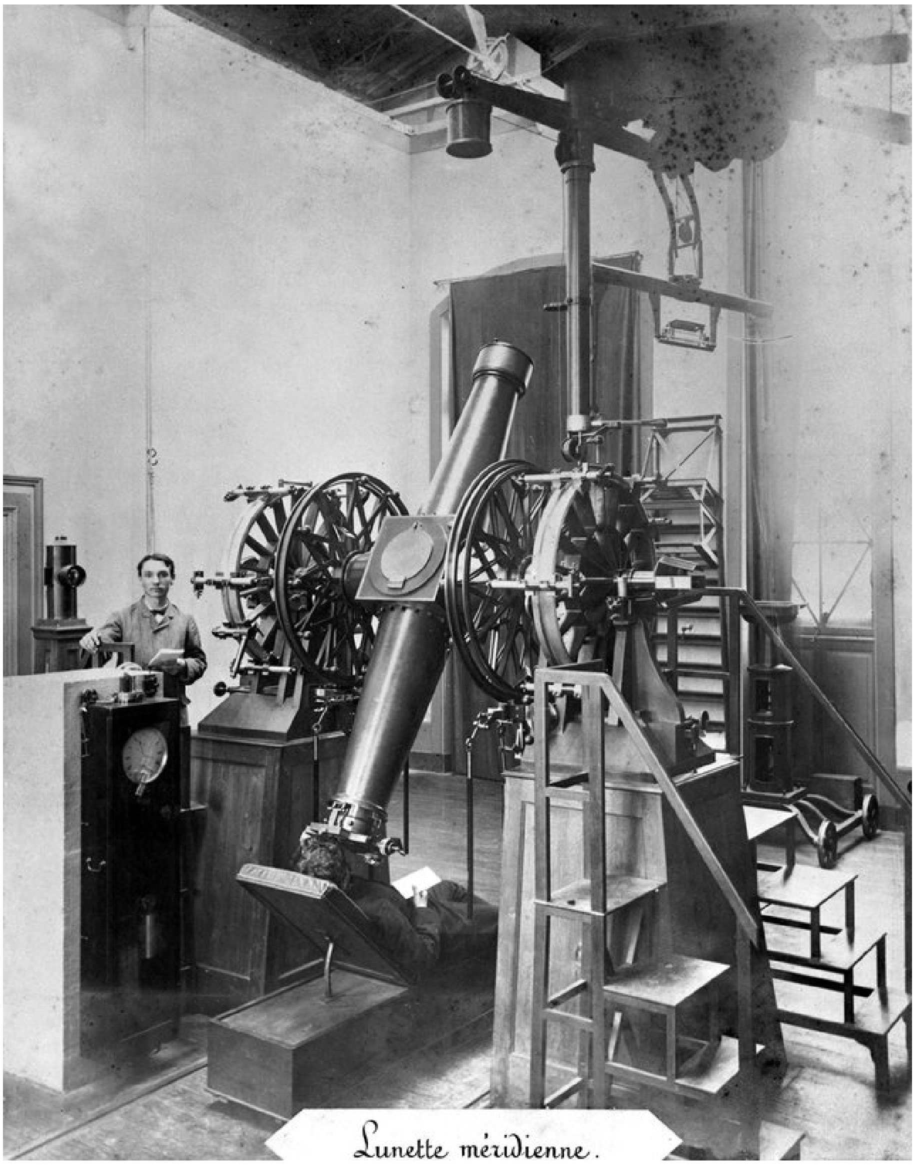

Figure 1.1: The meridian telescope of the Observatory of Besançon in 1892. *From* [4].

which was one of the best clocks at the time. Thus the comparison between the theoretical time of crossing the meridian of the observed star and the time noted on Fénon's clock directly gave the rate of this clock. The unit of rotational time was defined as a fraction of the mean solar day. The second of mean solar time was 1/86 400 (24h x 60min x 60s) of its duration. The clocks had the role of timekeepers and through extrapolation provided real time UT. The clocks produced time signals broadcast by telegraph to the city of Besançon, which had installed a network of electrically synchronized public clocks in 1880.

Like all the other observatories involved in the measurement of time, Besançon observatory successively installed constant pressure clocks (early 20th century), then quartz clocks (1950s). The widespread use of this type of clock highlighted the irregularities of the rotation of the Earth. In the 30's, it was noticed that the rotation of the Earth slows down as the Moon moves away from the Earth (about 4 cm per year): there is transfer of angular momentum via dissipation tides. In 1948 Gerald Maurice Clemence [5] proposed *Ephemeris Time* (ET), adopted as standard in 1952. It was originally designed as an approach to a uniform time scale, to be freed from the effects of irregularity in the rotation of the Earth. It is defined as the argument in the dynamical equations of the bodies of the Solar System and specifically as the geometrical mean longitude of the Sun in Newcomb's theory. It was convenient for astronomers and other scientists, for example for use in ephemerides of the Sun, the Moon, and the planets. In order to define the unit of time more precisely, the 11th Conference Generale des Poids et Mesures (CGPM) adopted ephemeris time in 1960.

The creation of the Bureau International de l'Heure (BIH) was decided upon during the 1912 Conférence internationale de l'heure radiotélégraphique. The following year, an attempt was made to regulate the international status of the bureau through the creation of an international convention. The mission of the BIH was to construct a time reference based on astronomical observations and time signals provided by the astronomers. This time reference was a form of universal time. There are several versions of universal time: UT1 proportional to the rotation angle of the Earth in space and UT2 which overcomes the seasonal variations of UT1.

1.3 The atomic time era

ET was built retrospectively, set as a fraction of the tropical year 1900, and could not be replicated which is a major drawback. A redefinition of the second was then necessary. In 1955, Essen and Parry [6] developed the first operational cesium frequency standard at the National Physical Laboratory (NPL, UK), characterized by an accuracy of the order of 10^{-10}, the highest at that time. Subsequently in 1958, the United States Naval Observatory (USNO) determined the frequency of cesium in terms of ephemeris seconds. Considering that a very precise definition of the unit of time is essential for science and technology, the 13th CGPM (1967-1968) chose cesium to provide the new definition of the second [7, 8]. It is now called the SI second, referenced to the frequency of the ground state hyperfine transition in the cesium-133 atom as a function of the ephemeris second determined by Markowitz et al. [9]. Cesium standards were then built or bought [1] in a number of laboratories, e.g. Besançon observatory (1969) [4], to give independent atomic times. This has led to new challenges: comparing them to the performance level

---

[1] The first commercial Cesium clocks became available at the end of the 50's.

Standard	Resonator	Date of origin	Timing Uncertainty (24h)	Frequency Uncertainty (24h)
Sundial	Apparent motion of the sun	3500 B.C.	NA	NA
Verge escapement	Verge and foliet mechanism	14th century	15 min	1×10^{-2}
Pendulum	Pendulum	1656	10s	1×10^{-4}
Harrison chronometer (H4)	Spring and balance wheel	1759	350ms	4×10^{-6}
Shortt pendulum	Two pendulums, slave and master	1921	10ms	1×10^{-7}
Quartz crystal	Quartz crystal	1927	10μs	1×10^{-10}
Rubidium gas cell	^{87}Rb resonnance $(6,834,682,608$ Hz)	1958	100ns	1×10^{-12}
Cesium beam	^{133}Cs resonance $(9,192,631,770$ Hz)	1952	1ns	1×10^{-14}
Hydrogen maser	Hydrogen resonance $(1,420,405,752$ Hz)	1960	1ns	1×10^{-14}
Cesium fountain	^{133}Cs resonance $(9,192,631,770$ Hz)	1991	100ps	1×10^{-15}

Table 1.2: The Evolution of Time and Frequency Standards. The uncertainties listed for modern standards represent year 2001 devices, and not the original prototypes. *From* [1].

of standards and averaging them to produce a mean atomic scale that is more uniform and reliable than the individual ones.

In 1961, the BIH began coordinating the Coordinated Universal Time (UTC) process internationally, but the name UTC was not formally adopted by the IAU until 1967. Initially, before the establishment of the International Atomic Time (TAI), the atomic time delivered by the atomic clocks was modified in frequency to follow the Earth's rotation and to ensure the difference $|UT1 - UTC| < 0.9$s. This system quickly became cumbersome and too complicated to implement. To remedy all these problems the IAU (1967), the International Union of Radiosciences (URSI 1969) and the International Radio Consultative Committee of the International Telecommunication Union (CCIR 1970) recommended the adoption of the BIH atomic time scale. It was during the 14th CGPM that TAI was officially adopted in 1971. The BIH time scale relied on a non-negligible number of atomic clocks in time laboratories; these time laboratories provided access to the scale and the time community enlarged and started a period of fruitful cooperation that continues today. During the 1980s, the BIH was split into two units:

- in 1985, part of the BIH was integrated into the Bureau International des Poids et

Mesures[2] (BIPM), working on the development of the international atomic time scale;

- in 1988, the rest of the BIH was integrated as the central office of the International Earth Rotation and Reference Systems Service (IERS), while maintaining its activity of determining the Earth's rotation.

1.4 Towards a new redefinition of the second

A revised more precise wording of the same definition of the second was adopted in Resolution 1 of the 26th CGPM (2018). It is now in terms of a fixed numerical value of the unperturbed ground-state hyperfine transition frequency of the caesium-133 atom, $\Delta\nu_{Cs}$.

TAI achieves its stability over 420 atomic clocks worldwide. Aiming at realizing the SI second with the smallest uncertainty, a small number of Primary and Secondary Frequency Standards (PSFS) [10] steers TAI to increase its accuracy. The BIPM publishes every month in Section 3 of Circular T [11], an estimation of the TAI frequency accuracy as measured by those individual frequency standards. The BIPM also provides the result of the computation of an ensemble average. In November 2021, sixteen different frequency standards operated in eleven laboratories contributed to this estimation, including ten Cs fountains, one Rb fountain, one Sr optical lattice and two Yb optical lattice clocks, in addition to the two legacy Cs beams operated by the Physikalisch-Technische Bundesanstalt (PTB). The number of different laboratories as well as the number of different standards constitutes a record of participation.

The present Cs fountains have been surpassed by two orders of magnitude by optical clocks, which are now reaching an accuracy of order 10^{-18} in term of relative frequency. That is why the Consultative Committee for Time and Frequency (CCTF) initiated in 2020 work towards a redefinition of the second. Before changing the definition, a number of mandatory criteria have to be achieved. Thus a task force on the roadmap for the redefinition of the second has been set-up by the CCTF. One of the mandatory criteria states that optical standards should regularly contribute to TAI, with a goal of at least three contributions per month, with a total uncertainty not larger than 2×10^{-16}. Based

---

[2] The BIPM was created by the Meter Convention signed in Paris on 20 May 1875 by seventeen States, during the last session of the Diplomatic Conference of the Meter. Originally limited to measurements of length and mass and metrological studies related to these quantities, the activities of the BIPM were extended to electrical (1927), photometric and radiometric measurement standards. (1937), ionizing radiation (1960), time scales (1988) and chemistry (2000).

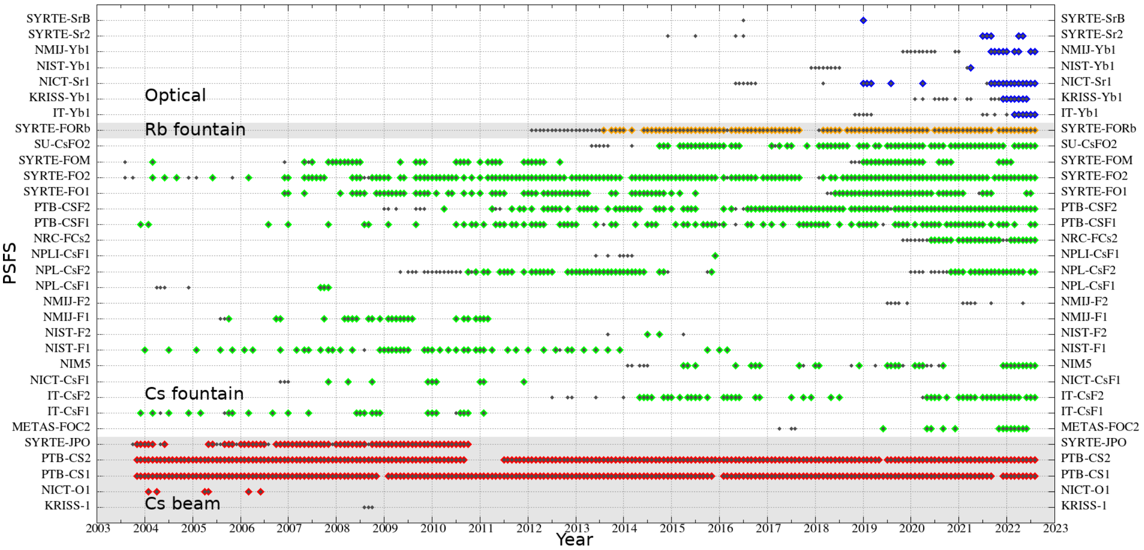

Figure 1.2: Graphical representation of all evaluation of Primary and Secondary Frequency Standards reported since Circular T 190. Enhance color dots indicate evaluation carried out within the month of TAI computation. *From* [12].

on a robust set of optical frequency standards, the criterion ensures that the accuracy of TAI is maintained and hopefully improved, so that the redefinition benefits TAI. After the redefinition, the uncertainty of optical standards will be reduced while the Cs fountains will become secondary standards with enlarged uncertainty.

Figure 1.2 shows significant progress in the operational capabilities, with optical clock uptime exceeding 90% in some cases. This allows longer operating periods and reduced frequency transfer uncertainty, key factors to achieve contributions of optical standards to TAI. The CCTF's current goal is to redefine the second in 2030.

The clock comparisons for the TAI calculation are based on different time transfer techniques. Among these, one uses the comparison between the time scale of the Global Navigation Satellite System (GNSS) with the local clock of a laboratory. However, it is possible that anomalies occur, e.g. time or frequency steps. In order to ensure the reliability of TAI, we have carried out a study on this specific problem and propose an algorithm for an automatic detection which is presented in Part II of this Thesis.

CHAPTER 2

. . . to millisecond pulsars

2.1 Pulsar time scale

A pulsar is a dead dense spinning remnant of a formerly massive star. It is the result of the explosion of a supernova leaving behind dense material consisting mainly of neutrons, thus called a neutron star. Its internal structure is complex, but its composition with the relationship between the density and pressure is well adressed by Oppenheimer and Volkov [13] before the discovery of pulsar. The typical mass of a neutron star is about 1.4 $M_\odot$ (solar mass) and up to a maximum of about two $M_\odot$ [14]. The reader can refer to [15] for a more detailed description of pulsars. Constant radio waves are emitted out of the magnetic poles which are misaligned with the spin axis. If the beam sweeps by the line of sight of the Earth, the pulses are detected. There is still not a consensus on the mechanism behind the emission of the pulses [16, 17]. Millisecond pulsars (MSPs) [18], whose rotation periods are of order of milliseconds, are the most stable natural astronomical clocks. The possibility of using the exceptional rotational stability of millisecond pulsars to generate a time scale had long been of interest. MSPs have been [19–33] considered to be the best clocks in the universe in the past. This assertion is definitively not true nowadays, artificial clocks have substantially better performance than natural astrophysical clocks, at least out to timescales of a few years as shown in Figure 2.1. However a ensemble of clocks can be considered to define a time scale [27, 34] which might prove to be very useful if it were to provide a universally accessible and highly stable time scale over the longest times.

This chapter does not constitute original work and the author does not lay any claim to anything discussed here.

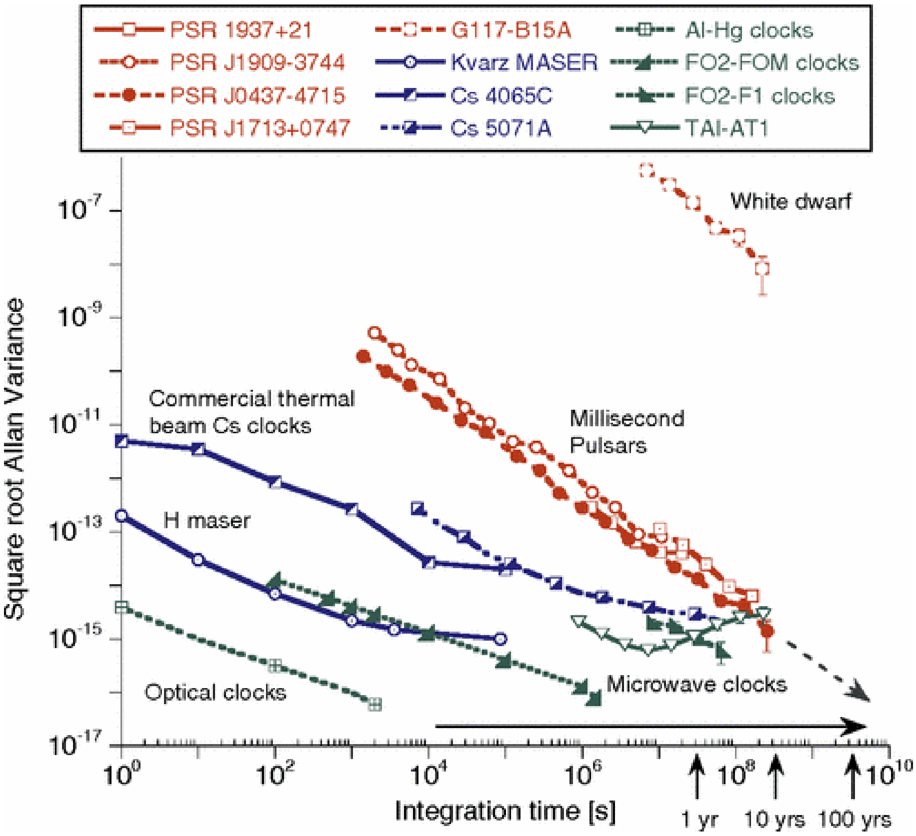

Figure 2.1: Fractional frequency stability of millisecond pulsars compared to atomic clocks. *From* [35].

Figure 2.1 presents the fractional frequency stability of a selection of the best artificial clocks and frequency standards in 2010 [35]. Since then, at least one more order of magnitude has been reached by the best optical clocks, i.e. in the order of 10^{-18} [36]. The trend in Figure 2.1 shows that to achieve stability of the same order of magnitude would require measurements of the best milisecond pulsars over hundreds of years. However, even by averaging an ensemble of pulsars over such long times, the clocks will have undergone improvements also in terms of stability. In fact, since the development of Cesium atomic clocks, the stability of clocks has improved by more than an order of magnitude per decade. While the stability of the best millisecond pulsars has only seen an improvement of less than an order of magnitude in 20 years [37].

The stability of these natural clocks also makes it possible to test Einstein's theory of general relativity [38]. As a consequence of Einstein's theory and according to certain cosmological theories [39], the universe would contain a substantial energy density in the form of a stochastic background of gravitational waves (GWs), analogous to the known cosmic microwave background [40]. Therefore a GW passing the pulsar during time of pulse emission, or passing the earth during reception, would cause changes in

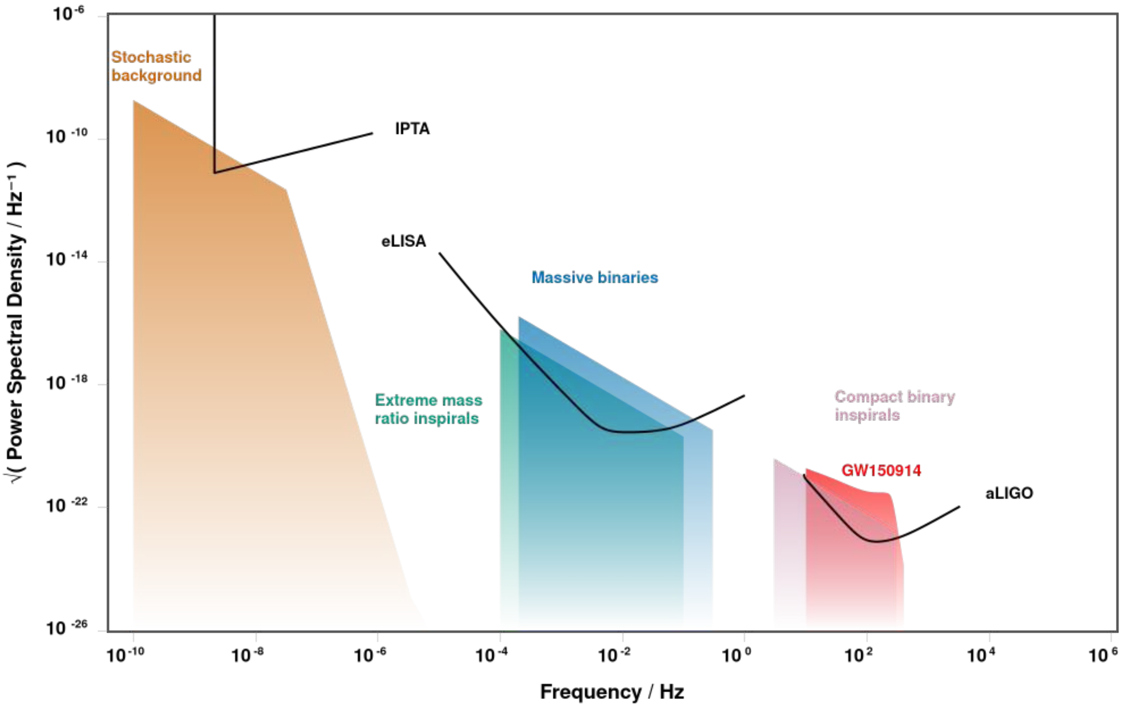

Figure 2.2: Comparison of the sensitivity curves and sources of GWs for the three major running astronomy experiments: PTA, LISA and LIGO using the the amplitude spectral density, produced using the Gravitational Wave Sensitivity Curve Plotter [42].

the rates of local clocks relative to distant clocks [41], decreasing the expected long term stability of the pulsars. Thus by means of pulsar timing observations, the gravitational background could be detected. The interest of such a research program is then twofold: on the one hand, it has a metrological dimension and, on the other hand, it has important astrophysical consequences.

2.2 Gravitational Waves and Pulsars

GW detection using pulsars combines two fields with a rich history dating back to the 1960s. At that time Antony Hewish built his experiment called “Interplanetary Scintillation Array” which led to the unexpected detection of the first pulsar by Jocelyn Bell in 1967 [43]. At about the same time, a pioneer called Joseph Weber announced the evidence of GWs measured with his experiment the “Weber bar” [44]. These two discoveries led to discord in the scientific community. Antony Hewish was awarded the Nobel Prize in Physics in 1974 for his pioneering research in radio astronomy and his decisive role in the discovery of pulsars. However his student Jocelyn Bell who made the observation was not awarded and Weber’s detection could not be replicated. GWs also have a spectrum, in particular due to the different categories of sources.

Subsequently, several experiments have emerged with the ground-based detectors like LIGO [45] measuring the higher frequency, Pulsar Timing Arrays (PTA) [46–49] measuring the lower frequency with approximately 100 millisecond pulsars using the largest telescopes in the world and space-borne detectors like eLISA [50] measuring stuff in the middle. Figure 2.2 shows the square root of the Power Spectral Density (PSD), i.e. the amplitude spectral density, which gives an indication of the sensitivity of the detectors. Ground-based detectors have detected GWs with frequencies of $10 - 100$ Hz from the mergers of stellar mass black holes [51], while the IPTA will probe GW frequencies roughly 10 orders of magnitude smaller. Their primary source of gravitational waves is supermassive black-hole binaries (billions of solar masses) [52, 53], presumed to exist in abundance number in the universe at the centers of galaxies, resulting from previous mergers of those galaxies. The phenomenon should be detected through the interaction with the millisecond pulsar signals by introducing a correlated red noise in the time of arrival series. The PTAs enable the simultaneous measurement of the same pulsar with several radio-telescopes (RTs), especially the Large European Array for Pulsars (LEAP) project [54].

Extracting a weak signal from noise with simultaneous measurements is a well-known method in the case of measurements of oscillators and atomic clocks. For more than 50 years, statistical tools have been developped using the PSD and wavelet variance for this purpose [55–58]. Among them, the cross-spectrum method [59] particularly interests us with its ability to reject the uncorrelated background noise and converge to the common part of the signal even if it is significantly lower than the background. This tool has already been partially characterized in terms of signal processing, but a detailed analysis in terms of Bayesian statistics remains to be done, in particular to obtain reliable confidence intervals around the measurements made by this estimator. We present this study in Part III of this Thesis, starting with the common case, i.e. the cross-spectrum with two measurement instruments and generalizing it to any number taking as an example the LEAP experiment comprising five RTs.

Part II

Time

Part II: Time

CHAPTER 3

Time scales

3.1 Time scales at the BIPM

After the adoption of the atomic definition of the second by the 13th General Conference on Weights and Measures (CGPM) [7, 8], the Consultative Committee for the Definition of the Second (CCDS) created International Atomic Time (TAI) [60]. It is the basis of the disseminated reference time scale Coordinated Universal Time (UTC) and both are equally stable and accurate. However while TAI is continuous, UTC is affected by one second discontinuites (leap seconds) as a result of its definition in [61]. The algorithms for the calculations of TAI and UTC are optimized for a time scale that is both accurate and stable over the long term. It relies on clock readings and it is highly dependent on the quality of the clock comparisons. The BIPM, in a coordinated effort with the world timing community, works to develop and improve these methods. UTC [62] is calculated as a weighted average of about 420 atomic clocks located in 85 laboratories spread wordwide. The BIPM disseminates UTC by publishing monthly the Circular T [11], whereas the rapid solution of UTC called UTCr [63] is published weekly. Another time scale maintained at the BIPM and published yearly is the Terrestrial Time (TT(BIPM)). A scheme of the different time scales and their relation is represented in Figure 3.1. All the presented

This chapter is the result of close collaboration with Gianna Panfilo.

Time scales are a service provided by the BIPM to the National Metrological Institutes (NMIs), observatories and international organizations that contribute to its computation.

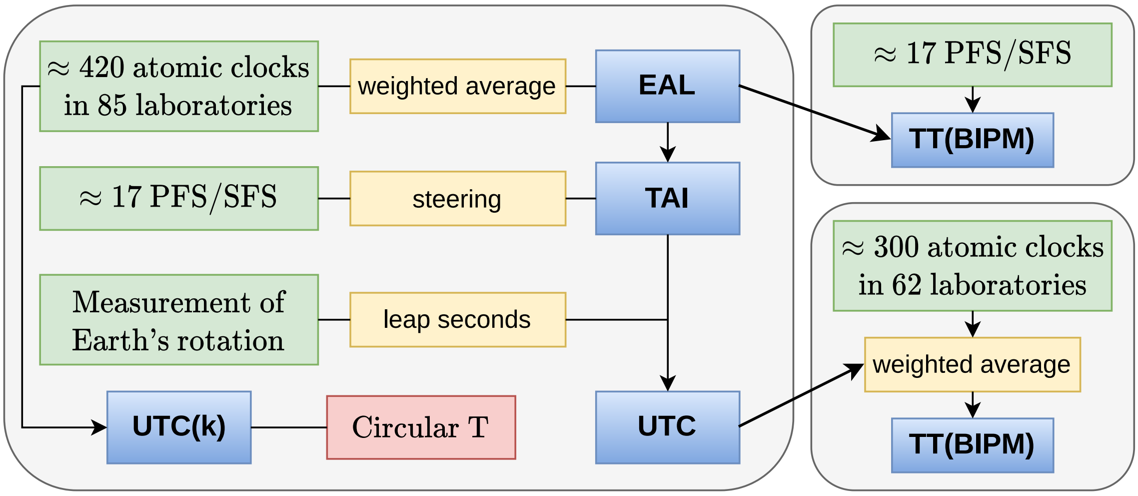

Figure 3.1: Representation of EAL, TAI, UTC, UTC(k), TT(BIPM) and their relations.

3.2 Properties of time scales

Ideally for the basis of a time scale the frequency must be constant and the construction of this one reproducible. However, this is never the case and it is necessary to be able to identify the causes of frequency variations in order to minimize or even eliminate them. The definition of the second, International System (SI) base unit of time, is as follows [64]:

Definition 3.2.1. The **second**, symbol s, is the SI unit of time. It is defined by taking the fixed numerical value of the caesium frequency $\Delta\nu_{Cs}$, the unperturbed ground-state hyperfine transition frequency of the caesium 133 atom, to be $9\,192\,631\,770$ when expressed in the unit Hz, which is equal to s^{-1}.

However the realization of the second differs from its definition. Subsequently these differences should be reproducible during the construction of the time scale, thus the reliability of the time scale is directly linked to the reliability of the clocks and at the same time the redundancy is required as in the case of national time scale (UTC(k)) as for UTC. Considering the characteristics of a time scale as UTC, a large number of clocks is required which is the case today with around 420, most of them being high-performance commercial caesium atomic standards and active hydrogen masers. Important properties of a time scale are referenced in [65] as

Definition 3.2.2. The **frequency stability** of a time scale represents its capacity to maintain a fixed ratio between its unitary scale interval and its theoretical counterpart. The

frequency accuracy represents the aptitude of its unitary scale interval to reproduce its theoretical counterpart.

Definition 3.2.3. The **accessibility** of a time scale represents its capability to provide a way of dating events for everyone.

The primary frequency standards (PFS) are stable oscillators which generate a fundamental frequency at a high degree of accuracy and precision and is generally used as a reference for frequency calibration [66]. The PFSs are used in the national metrological institues as frequency references to steer the H-Maser used for the generation of the time scale. In the case of UTC, the PFSs are used in the steering algorithm used to maintain its frequency close to SI second frequency.

3.3 Coordinated Universal Time

UTC requires high reliability and long-term frequency stability by relying on a wide clock network spread all over the world as shown in Figure 3.2. Each month the differences between the international time scale UTC and its local representation UTC(k), with k referring to a laboratory, are reported in the Circular T [11] as shown in Table 3.1. As UTC(k), these laboratories realize a stable local time scale based on individual atomic clocks or a clock ensemble.

Date 2021/22 0h UTC		DEC 31	JAN 5	JAN 10	JAN 15	JAN 20	JAN 25	JAN 30	Uncertainty/ns			Notes
MJD		59579	59584	59589	59594	59599	59604	59609	uA	uB	u	
Laboratory k						[UTC-UTC(k)]/ns						
GGO	(La Plata)	370.8	370.5	378.0	390.6	402.5	412.8	423.9	1.0	20.0	20.0	
AOS	(Borowiec)	-0.9	-1.3	-2.3	-3.2	-4.2	-5.2	-6.4	0.3	3.0	3.0	
APL	(Laurel)	3.6	5.0	3.8	2.2	2.6	2.9	3.3	0.3	19.7	19.7	
AUS	(Sydney)	-560.0	-560.5	-562.0	-550.4	-557.0	-557.9	-543.2	0.3	11.2	11.2	
BEV	(Wien)	-29.6	-15.3	5.1	14.4	40.1	61.3	67.5	0.3	3.5	3.5	
BFKH	(Budapest)	3994.6	4017.2	4051.1	-	4113.4	4149.4	4181.1	1.5	20.0	20.1	
BIM	(Sofiya)	15646.8	15687.2	15704.7	15719.0	15725.7	15754.4	15770.4	0.3	7.1	7.1	
BIRM	(Beijing)	4.8	13.7	16.2	16.9	15.4	13.9	11.3	0.3	2.9	2.9	(1)
BOM	(Skopje)	-	-28.9	-194.9	-340.3	-501.1	-657.6	-813.2	0.3	3.5	3.5	
BY	(Minsk)	-1.2	0.5	3.7	3.9	2.2	0.7	0.6	1.5	2.8	3.2	

- Notes on section 1:
(1) BIRM : Time step of UTC(BIRM) of about -8 ns on MJD 59579.37.

Table 3.1: Difference between UTC and its local realizations UTC(k) and corresponding uncertainties.

The BIPM receives the clock readings reported by each laboratory k and combines them into an algorithm designed to optimize frequency stability and accuracy as well as time scale reliability beyond the level of performance that can be achieved by any individual clock in the ensemble. Thus each month at the BIPM time department an appropriate algorithm called ALGOS [62, 65, 67–72] is used to generate the international reference UTC. The calculation of UTC using ALGOS is then carried out in three successive steps:

- The free atomic time scale EAL is computed as a weighted average of free-running atomic clocks distributed world-wide. A clock weighting procedure has been designed to optimize the long-term frequency stability of the scale. The number of participating clocks today is about 420.

- The frequency of EAL is steered to maintain agreement with the definition of the SI second. The steering correction is determined by comparing the EAL frequency with that of the PFS/SFS. The number of PFS/SFS maintained in contributing laboratories and contributing to the accuracy of TAI amounts currently to 17 and the ensuing time scale is TAI.

- To maintain agreement with the non-uniform time derived from the rotation of the Earth, leap seconds are inserted and the resulting time scale is UTC.

To guarantee the continuity of EAL the clocks participating should not be affected by time and frequency steps as well as change in the frequency drift.

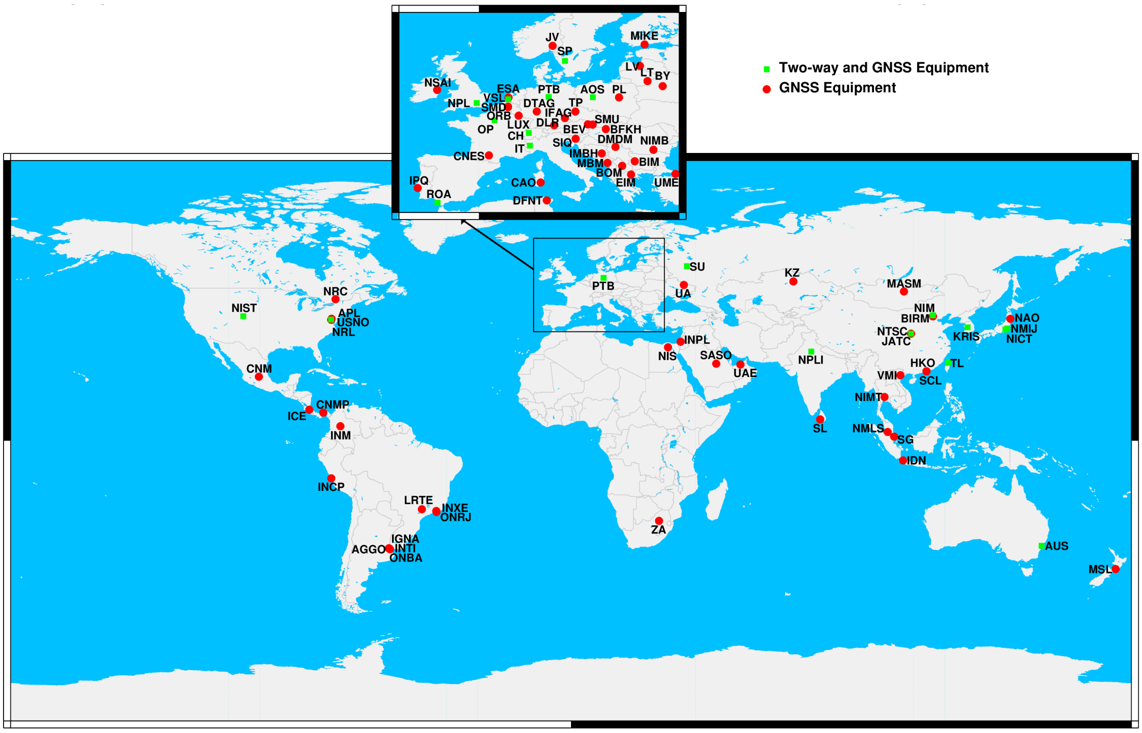

Figure 3.2: Geographical distribution of the laboratories that contribute to UTC and time transfer equipment in 2021. *From* [73].

3.4 Time transfer applied for clock comparisons

As a time scale is built using clocks disseminated world-wide, it is essential to have a way of comparing distant clocks. The most important requisite is that the time transfer method does not affect the frequency stability of the signal, which was in the past the strongest limitation to establish a time scale. The construction of UTC is based on the contribution of 85 laboratories spread world-wide, so the design of the algorithm needs a well defined strategy. The current time link network is treated in UTC as non redundant and consists of star-like scheme linked by a selected pivot. Therefore all time laboratories are compared to this pivot. As different comparison methods are maintained in different laboratories, the pivot has to be selected amongst the laboratories that have at their disposal all the different methods, running on a continuous basis, as represented in Figure 3.2. This condition is fulfilled by several laboratories and currently the pivot is the Physikalisch-Technische Bundesanstalt (PTB) in Germany. The pivot laboratory can be changed in case of need but due to calibration procedures can seriously affect UTC. All the contributing laboratories provide their time transfer data as a comparison of their UTC(k) with another time scale, e.g. the internal time scale of Global Navigation Satellite System (GNSS) or to another UTC(k) in the case of Two-Way Satellite Time and Frequency Transfer (TWSTFT). We will now present these major techniques.

3.4.1 Use of GNSS

The signal broadcast by the GNSS containing the timing and positioning information allow time transfert methods. It relies on a one way method by emitting a signal from the GNSS which is received by a laboratory with specific equipment. The first generation evolved from single-frequency and signel-channel to single-frequency and multi-channel. At the begining of the 2000's, the development of geodetic-type receivers enhanced the time comparison with the laboratory by performing dual-frequency measurement correcting the ionospheric delays. The progress of these developments is described in [74].

3.4.1.1 Common View

The Common-View (CV) method, proposed in 1980 by Allan and Weiss [75] relies on reception of the same emitted signal by several receivers. The signal is composed by time and position information and thus the time transfer is affected by the position error of the satellite and the instability of the satellite clock. The satellite, i.e. the emitter, has to be observable from all the station receivers. The advantage of this method relies on the elimination of the error sources common to the two observing stations, i.e. originated from the satellite clocks and orbits. However the drawback of this method is the needs of the satellite to be observable from all the receivers at the same time. This is a disadvantage especially when the distance between the different laboratories increases and the number of satellites simultaneously observable decreases. This method was used by the BIPM for the calculation of UTC until 2006 with the common-view satellites of the US Global Positioning System (GPS).

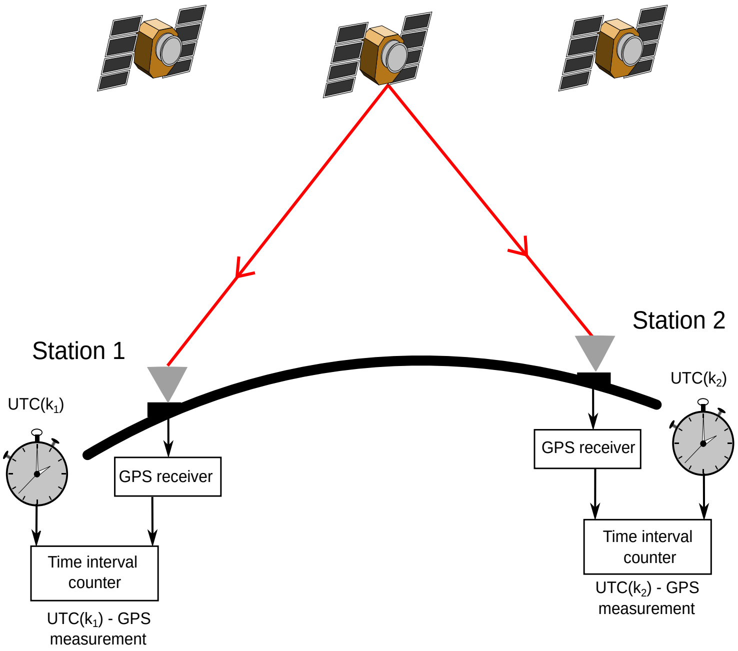

Figure 3.3: GNSS Common View time transfer method. The only satellites that can be used are the ones observable by both laboratories and each laboratory is equipped with a single channel receiver.

3.4.1.2 All in View

To overcome the problem of simultaneous observation, the All in View (AV) [76] method eliminates this constraint. Resulting in an independency of the length of the baseline for having suitable observed satellites. Thus all satellites in view at a station are used. Then the single-channel, single-frequency receivers have been gradually substituted with multi-channel receivers minimizing the impact of the error coming from satellite orbits and clocks. Resulting in an improvement of time links uncertainty by adding data from satellites at high elevations. Consequently the GPS links obtained using dual-frequency receivers, termed GPS P3 [74–78], supply ionosphere-free data and allow clock comparisons with nanosecond statistical uncertainty or better. However the tropospheric delay is still present in the data by adding short-term noise. The Precise Point Positioning technique (PPP) [79, 80] takes into account from geodetic-type receivers the phase measurements. The dual-frequency phase and code measurements are then used for comparing via GPS the reference clock in a station to a reference time scale.

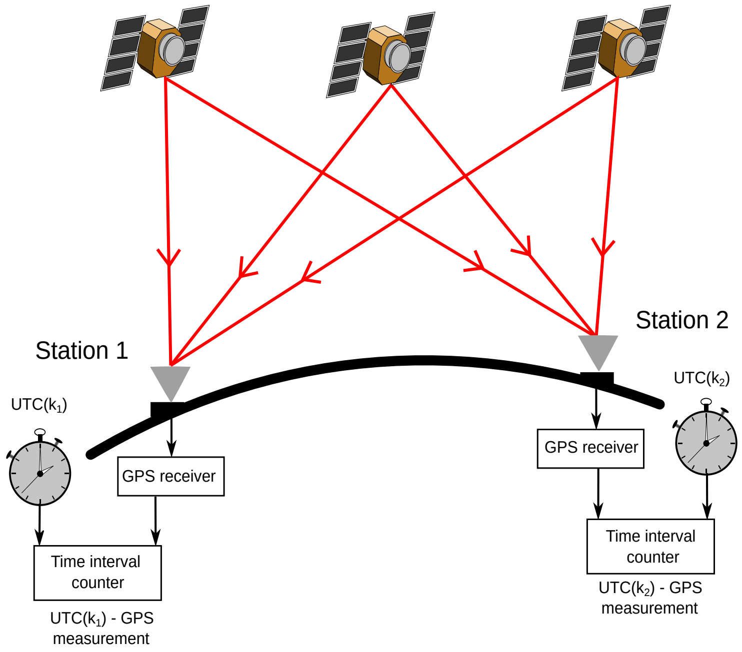

Figure 3.4: GNSS All in View time transfer method. Each laboratory is equipped with multi-channel receivers allowing reception of signals from all the satellites in the laboratory horizon.

3.4.2 Two-Way Satellite Time and Frequency Transfer

From the end of the 1980's, another satellite-based time transfer technique for clock comparison has been studied, called the Two-Way Satellite Time and Frequency Transfer (TWSTFT) [81, 82]. It relies on a telecommunications geostationary satellite comparing clocks located in two receiving-emitting stations. Two laboratories equipped with receiving-emmitting stations schedule measurements at the same time to simultaneously compare their clocks. So the information relative to the clock of each laboratory is sent forward to the other laboratory, both receiving and sending their data simultaneously at both ends of the baseline. Compared to the one-way method, it has the advantage to eliminate or at least reduce some sources of systematic errors, e.g. ionospheric and tropospheric delays, and also the position uncertainty of the satellite and the ground stations. Before the 2000's, the comparisons obtained only once per week were not enough to give a number of observation statistically meaningful. After that the sampling rate was increasing and now gives data every two hours. The accuracy of this time transfer links is excellent due to the long-term stability of the hardware.

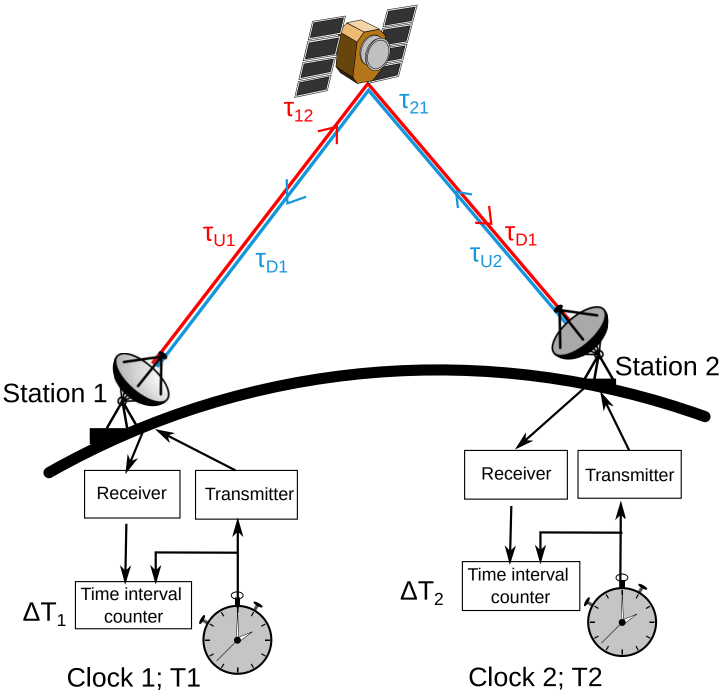

Figure 3.5: Two-Way Satellite Time and Frequency Transfer. Each laboratory is equipped both a receiver and a transmitter. The signal is sent from one laboratory to the satellite, that forwards it to the other laboratory and vice versa.

3.4.3 Link uncertainties

The time links always have an uncertainty component, despite the characteristics described in the time transfer methods. Those uncertainties arise from different sources such as the laboratory equipment, the satellites or even physical processes. Therefore the error types affecting the time links should be estimated and reduced as much as possible. In the last column of Circular T (see Table 3.1), the combined standard uncertainty of [UTC-UTC(k)] is reported for any laboratory k. It is obtained by the combination of two types of uncertainties indicated by u_A and u_B corresponding to two different characteristics of the measurements. These uncertainties are obtained by an appropriate algorithm and depend on the uncertainties of the links (reported in Section 5 of Circular T) and in the global weight of the laboratory contributing in UTC. Section 5 of Circular T provides information on the time links used in the elaboration of each Circular T, including equipment and calibration identifiers, uncertainties and alignment corrections applied by the BIPM, if any. The parameter u_{Stb} is the standard uncertainty representing the link instability and accounting for measurement noise and random effects with typical duration between one and 30 days. Concerning the link uncertainties the u_A component reflects the noise affecting the link and takes into acount the contribution of the clocks at 30 days, the u_B component corresponds to the calibration uncertainties [83,84]. The value u_A and

u_B are the components of the combined standards uncertainty u [85] defined as,

$$u = \sqrt{u_a^2 + u_b^2}. \tag{3.1}$$

Regarding the physical processes, the most significant errors arise from the ionospheric delay, especially in the case of a long baseline. However it can be reduced by means of dual-frequency receivers for the laboraties equipped with the capability.

3.5 Statement of the problem

Regularly, the time transfer links used in UTC calculations are affected by time and frequency steps for various reasons, for example, calibrations or malfunctioning hardware. Considering the number of laboratories participating in UTC, it is normal to experience more than four time links being affected by this kind of event in each monthly calculation. In Figure 3.6 a typical example of time step visible in time link data can be observed. In the red box the time step is highlighted.

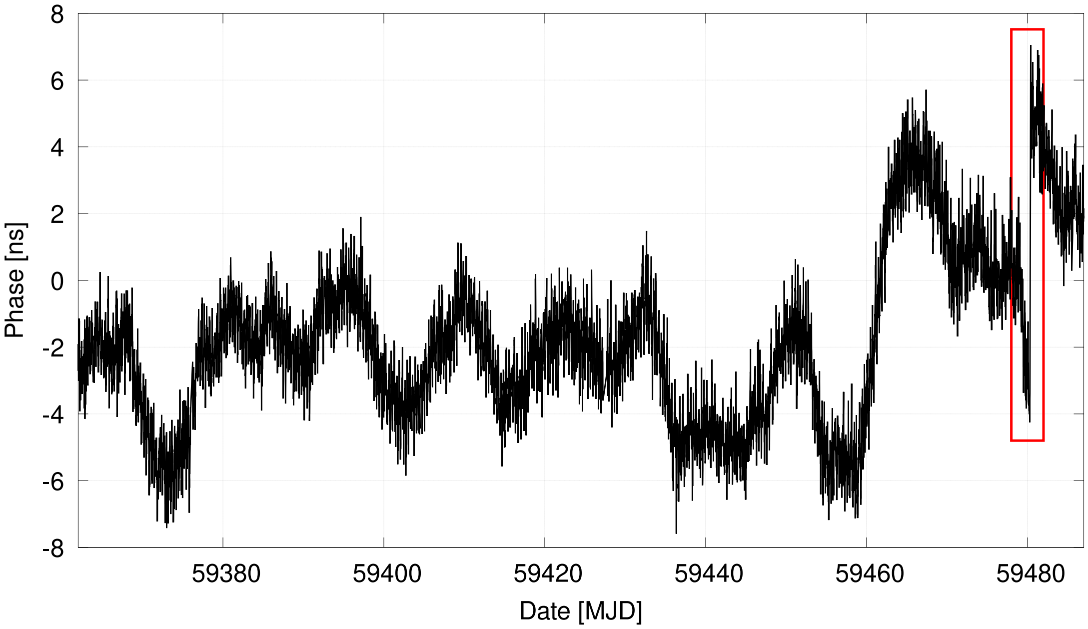

Figure 3.6: Example of a phase jump in a time transfer link. This anomaly is framed by a red box.

To ensure the stability of UTC, it is essential to know when the steps appear and the magnitude of the steps in order to check the corresponding clocks and to contact the concerned laboratories. These time steps are announced to the community by reporting a Note in the last column of Circular T as shown in Table 3.1. An automatic procedure of jump detection should be developed on the one hand to give a warning and on the other hand to provide the necessary information (dates and magnitude). In [86] a tool to detect steps in clock data based on a Kalman Filter has been developed and presented. The tool was optimized for real-time calculation with clocks being affected by frequency steps. As UTC is calculated in post processing, the detector presented in [86] has to be adapted to guarantee a reliable and extremely precise answer. Due to impressive amount of data available at BIPM, it is possible to test the detector in a variety of situations to guarantee a complete optimization of the parameters. The final scope of the work is to develop an automatic procedure allowing the detection of the time steps affecting the time links used to compare clocks in UTC. The tool presented in [86] will be adapted to UTC in terms of the detector definition and in terms of parameter configuration. The analysis will start with a description of the clock model and its relationship with the Allan variance, needed to subsequently define the Kalman filter with the appropriate parameters.

CHAPTER 4

The clock model and its relationship with the Allan variance

In this chapter, the mathematical model of the atomic clock with its errors will be presented. The reader can refer to the literature [87–89] for further details about the clock model. The description will embed some concepts from stochastic process theory. The reader can refer to [90] for a full description of Brownian motion and its properties as well as [91] for white noise and [92] for the Integrated Brownian Motion processes. The clock errors can be modeled by the Stochastic Differential Equation (SDE) [93–95]; an essential approach to using the Kalman filter. By using the SDE approach to describe the clock behaviour we can easily relate the clock noise parameters with the variances of the Wiener processes [96, 97] present in the SDE. In time and frequency metrology these parameters are related to the Allan Variance [98], the most common statistical tool used to characterize clocks. Other tools exist such as the structure functions [99], the Hadamard variance [57] or a combination of some of them [100,101]. Thus it is necessary to give the relation between the diffusion coefficients and such variances as expressed in [87,94,102].

We address in Section 4.1 the basics of the clock model involved in time and frequency metrology and we describe in Section 4.2 the different kinds of noise affecting clocks. Then we present the three-state clock model described by means of the SDE in Section 4.3. Finally we give the relationship between the diffusion coefficients and the Allan variance and its estimation for a pratical application in Section 4.4.

This chapter does not constitute original work and the author does not lay any claim to anything discussed here.

4.1 The metrological clock model

An atomic clock is an oscillator whose ideal signal is defined by [88, 103]

$$u(t) = U_0 \sin(2\pi f_0 t), \tag{4.1}$$

where U_0 is the nominal amplitude and f_0 the nominal frequency. However in real clocks both the amplitude and frequency are affected by random fluctuations. Then a more realistic model is given by

$$u(t) = (U_0 + \varepsilon(t)) \sin(2\pi f_0 t + \varphi(t)) \tag{4.2}$$

where $\varepsilon(t)$ and $\phi(t)$ are respectively the random fluctuations of the amplitude and phase. The amplitude fluctuations can be neglected, thus an approximated model is

$$u(t) = U_0 \sin(2\pi f_0 t + \varphi(t)). \tag{4.3}$$

The oscillation frequency changes with time, due to the phase fluctuation, its instantaneous value is defined by

$$f(t) = f_0 + \frac{1}{2\pi}\frac{d\varphi(t)}{dt}. \tag{4.4}$$

Removing its nominal frequency dependency leads to the normalized frequency deviation,

$$y(t) = \frac{f(t) - f_0}{f_0}. \tag{4.5}$$

The time deviation is then defined as its integral,

$$x(t) = \int_0^t y(\theta) d\theta. \tag{4.6}$$

According to Equations 4.4 to 4.6, we have the deviation of the clock reading from an ideal time reference

$$x(t) = \frac{1}{2\pi f_0}\varphi(t). \tag{4.7}$$

Thus rewriting Equation 4.3 from substituing Equation 4.7 we obtain

$$u(t) = U_0 \sin(2\pi f_0 (t + x(t))). \tag{4.8}$$

The two fundamentals quantities used to characterized an atomic clock are the time deviation $x(t)$ and the frequency deviation $y(t)$. Experimental observation shows that $x(t)$ and $y(t)$ have a noise-like behavior.

4.2 The clock noises

The random perturbations affecting the clocks can be characterized in the frequency domain as a sum of $1/f^{\alpha}$ noise components where α is the noise-type exponent. Typically five types of noise following this power-law are referenced [88, 95]:

- White Phase Modulation (WPM), i.e. white noise on the phase component;
- Flicker Phase Modulation (FPM), i.e. flicker noise on the phase component. It is characterized by a Power Spectral Density (PSD) inversely proportional to its frequency, thus an extremely complicated kind of noise related to a fractionally integrated Brownian motion;
- White Frequency Modulation (WFM), i.e. white noise on the frequency component, inducing a Random Walk or Brownian motion, on the phase (RWPM);
- Flicker Frequency Modulation (FFM), i.e. a flicker noise on the frequency component;
- Random Walk Frequency Modulation (RWFM), i.e. a Random Walk on the frequency.

Table 4.1 reports the presented noises in regards to the phase and frequency. Each type of clock exhibits a different combination of these noises. For example the caesium clocks usually have a WFM and RWFM while a hydrogen maser is characterized by a more complex type of noise, which is the FFM. To identify the kind of noise affecting the clock errors and more generally to estimate its stability, it comes naturally that the classical variance of the frequency deviation $y(t)$ would be the candidate. However the variance of random walk is time-dependent and divergent. Thus the stability would depend on the length of the time series considered.

In 1966, Allan [104] proposed an approach based on the stationary increments according to the random walk properties. It is now commonly used to characterized the stability of a clock and is defined by

$$\sigma_y^2(\tau) = \frac{1}{2}\mathbb{E}\left[(\bar{y}_{k+1} - \bar{y}_k)^2\right], \tag{4.9}$$

where the average frequency is

$$\bar{y}_k = \frac{1}{\tau}\int_{t_k}^{t_{k+1}} y(t)dt, \tag{4.10}$$

Noise	Phase	Frequency
WPM	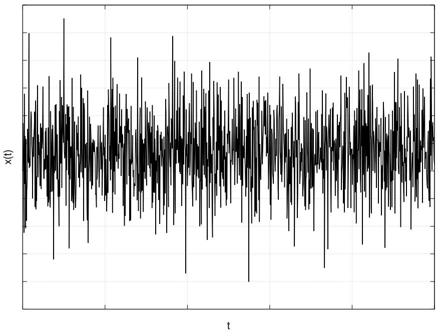	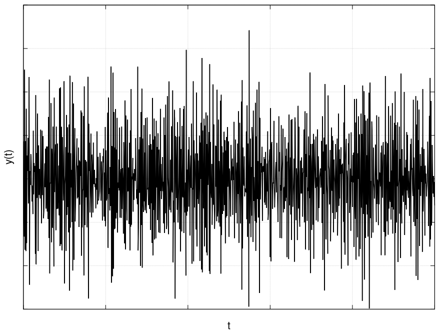
FPM	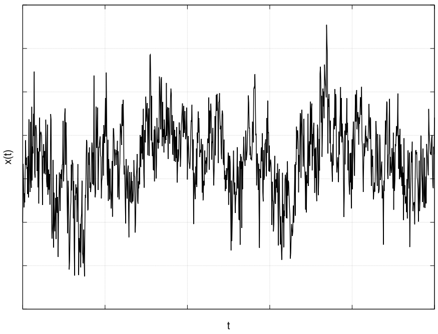	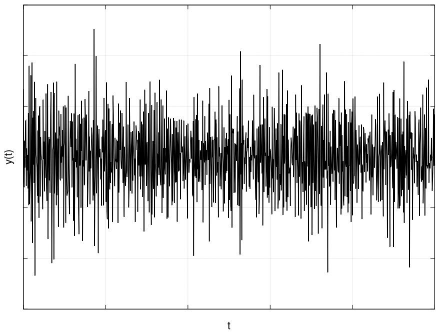
WFM	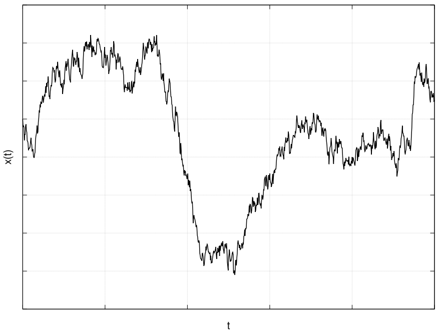	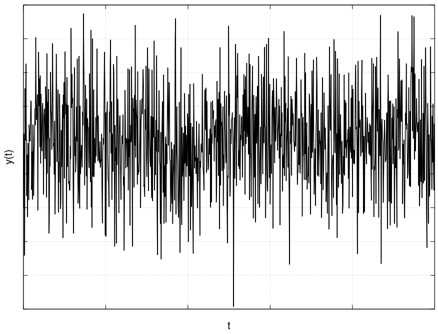
FFM	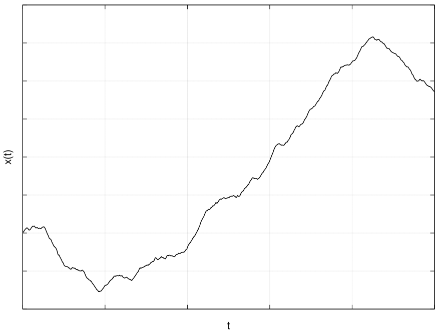	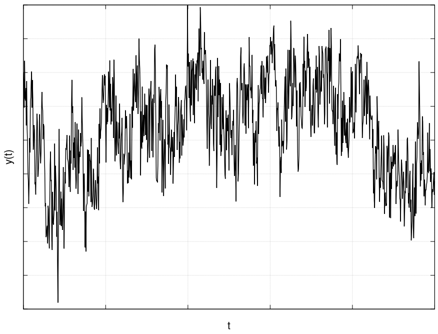
RWFM	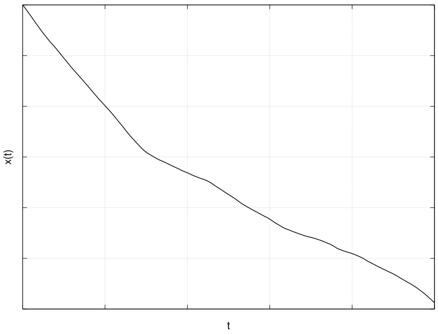	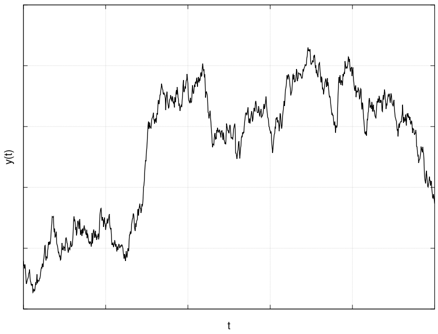

Table 4.1: Different type of noise affecting clocks generated with SigmaTheta Software [105].

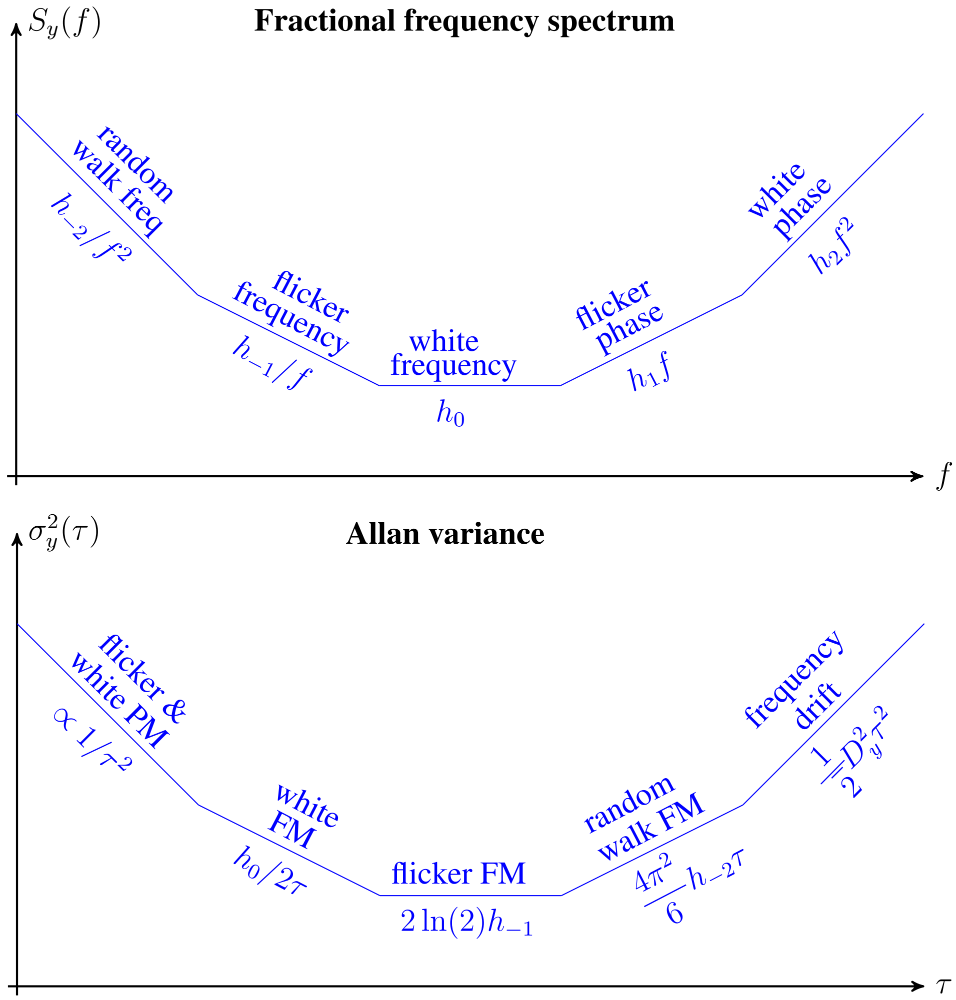

Figure 4.1: Relation between the power law and the noise type for the frequency fluctuation PSD (top) and the Allan variance (bottom).

and $\mathbb{E}[\cdot]$ represents the mathematical expectation of the quantity in the brackets.

It can be proved [104] that the Allan variance is finite and behaves according to a power-law of the type,

$$\sigma_y^2(\tau) = k_\alpha \tau^\alpha, \tag{4.11}$$

where k_α is a constant depending on the α value. By applying logarithm to Equation 4.11 it follows,

$$\log(\sigma_y^2(\tau)) = \log(k_\alpha) + \alpha \log(\tau). \tag{4.12}$$

Thus plotting the Allan variance on a log-log scale, it results as a linear function of slope α whose values are $\{-2, -1, 0, 1, 2\}$. Each of these noises is represented in Figure 4.1

(bottom) and can be estimated for certain region of τ. In addition to the noise referenced in Table 4.1, the presence of a frequency drift D_y can be noticed. However a disadvantage of the Allan variance is that the white and flicker PM noises can not be distinguished and both have a slop of τ^{-2}.

The same analysis can be carried out on the PSD, the reader can refer to [106] for the relationship between the PSD and the Allan variance. In this case a log scale applied on the time interval τ gives symmetrically as the Allan variance but with the distinction between the white and flicker PM noises the power-law frequency attributed to each kind of noise as represented on Figure 4.1 (top). Nevertheless the time-domain analysis is preferred in metrology as the Allan variance provides a quantitative information on the noise intensity related to the clock deviation in time.

4.3 The three-state clock model

Let us consider a three-state clock model described in [87, 93, 94, 102, 107]. It is a generalization of the most common two-state clock [95, 108] where the random walk is referred as a random run in [107] and a linear variation in time of the frequency drift is added. However the drawback of adding the drift is that the clock signal frequency value is not given by integration of the frequency value leading to an Allan variance depending also on time t as well as the observation time τ. Let us notice also that the flicker noise can not be modeled by a finite order state model, thus we are not considering it. The reader can refer to [109, 110] where the problem is addressed from the spectral analysis point of view using transfer function of a white noise to define a colored noise.

The three-state clock is modeled by the SDE as

$$\begin{cases} dX_1(t) = (X_2(t) + \mu_1)dt + \sigma_1 dW_1(t) \\ dX_2(t) = (X_3(t) + \mu_2)dt + \sigma_2 dW_2(t), \qquad t \geq 0 \\ dX_3(t) = \mu_3 dt + \sigma_3 dW_3(t) \end{cases} \tag{4.13}$$

with the initial conditions,

$$\begin{cases} X_1(0) = c_1 \\ X_2(0) = c_2 \\ X_3(0) = c_3 \end{cases} \tag{4.14}$$

where $W_{\{1,2,3\}}$ are the Wiener processes or Brownian motion defined as a Laplace-Gauss distribution with zero mean and variance t, thus $W(t) \sim \mathrm{LG}(0,t)$ referred as the integral of white noise. The variables $X_{\{1,2,3\}}$ respectively represent the phase deviation, a part of the frequency deviation (i.e. random walk componant) and the frequency drift or aging. The white and random walk frequency noises are represented by $W_1(t)$ and $W_2(t)$. Let us notice that the frequency deviation $y(t)$ as described in Section 4.1 corresponds to the derivative of X_1 named $\dot{X}_1$. The constants $\sigma_{\{1,2,3\}}$ are the diffusion coefficients giving the intensity of the three noise components. Whereas the constants $\mu_{\{1,2,3\}}$ correspond to the deterministic phenomena driving the clock or called the drift terms of the Wiener processes. These constants are related to the metrology terminology as $c_2 + \mu_1 = y_0$ the initial frequency offset; $c_3 + \mu_2 = D_y$ the frequency drift and μ_3 corresponds to the linear coefficient of the time variation of D_y. Rewriting Equation 4.13 in term of a matrix form gives,

$$d\boldsymbol{X}(t) = (\boldsymbol{F}\boldsymbol{X}(t) + \boldsymbol{M})dt + \boldsymbol{Q}d\boldsymbol{W}(t), \qquad t \geq 0, \tag{4.15}$$

with the following matrices:

$$\begin{aligned} d\boldsymbol{X}(t) &= \begin{pmatrix} dX_1(t) \\ dX_2(t) \\ dX_3(t) \end{pmatrix}, \quad \boldsymbol{F} = \begin{pmatrix} 0 & 1 & 0 \\ 0 & 0 & 1 \\ 0 & 0 & 0 \end{pmatrix}, \quad \boldsymbol{X} = \begin{pmatrix} X_1(t) \\ X_2(t) \\ X_3(t) \end{pmatrix}, \\ \boldsymbol{M} &= \begin{pmatrix} \mu_1 \\ \mu_2 \\ \mu_3 \end{pmatrix}, \quad \boldsymbol{Q} = \begin{pmatrix} \sigma_1 & 0 & 0 \\ 0 & \sigma_2 & 0 \\ 0 & 0 & \sigma_3 \end{pmatrix}, \quad d\boldsymbol{W}(t) = \begin{pmatrix} dW_1(t) \\ dW_2(t) \\ dW_3(t) \end{pmatrix}. \end{aligned} \tag{4.16}$$

According to [96,97], the solution of Equation 4.15 which is strictly linear, is given by

$$\boldsymbol{X}(t) = \boldsymbol{\Phi}_{t,0}\boldsymbol{X}(t_0) + \boldsymbol{B}_t\boldsymbol{M} + \boldsymbol{G}_t, \tag{4.17}$$

where the transition matrix $\boldsymbol{\Phi}_{t,0}$ and $\boldsymbol{B}_t$ are deterministic and described by,

$$\boldsymbol{\Phi}_{t,0} = e^{\boldsymbol{F}(t-s)} = \begin{pmatrix} 1 & t-s & \dfrac{(t-s)^2}{2} \\ 0 & 1 & t-s \\ 0 & 0 & 1 \end{pmatrix} \quad \text{and} \quad \boldsymbol{B}_t = \begin{pmatrix} t & \dfrac{t^2}{2} & \dfrac{t^3}{6} \\ 0 & t & \dfrac{t^2}{2} \\ 0 & 0 & t \end{pmatrix}, \tag{4.18}$$

where the transition matrix satisfies $\boldsymbol{\Phi}_{t,s} = \boldsymbol{\Phi}_{t-s,0}$. The vector $\boldsymbol{G}_t$ is the innovation of the stochastic process $\boldsymbol{X}(t)$ given by,

$$\boldsymbol{G}_t = \begin{pmatrix} \sigma_1 W_1(t) + \sigma_2 \int_0^t (t-s)dW_2(s) + \sigma_3 \int_0^s \dfrac{(t-s)^2}{2} dW_3(s) \\ \sigma_2 W_2(t) + \sigma_3 \int_0^t (t-s)dW_3(s) \\ \sigma_3 W_3(t) \end{pmatrix} \sim \mathrm{LG}(\boldsymbol{0}, \boldsymbol{\Sigma_t}). \tag{4.19}$$

$\boldsymbol{G}_t$ is a Laplace-Gauss distribution with zero mean and covariance matrix $\boldsymbol{\Sigma_t}$ given by,

$$\boldsymbol{\Sigma}_t = \mathbb{E}\left[\boldsymbol{G}_t\boldsymbol{G}_t^T\right] = \begin{pmatrix} \sigma_1^2 t + \sigma_2^2\dfrac{t^3}{3} + \sigma_3^2\dfrac{t^5}{20} & \sigma_2^2\dfrac{t^2}{2} + \sigma_3^2\dfrac{t^4}{8} & \sigma_3^2\dfrac{t^3}{6} \\ \sigma_2^2\dfrac{t^2}{2} + \sigma_3^2\dfrac{t^4}{8} & \sigma_2^2 t + \sigma_3^2\dfrac{t^3}{3} & \sigma_3^2\dfrac{t^2}{2} \\ \sigma_3^2\dfrac{t^3}{6} & \sigma_3^2\dfrac{t^2}{2} & \sigma_3^2 t \end{pmatrix} \tag{4.20}$$

where the superscript T denotes the transposed matrix. Thus $\boldsymbol{G}_t$ is the only stochastic term of Equation 4.17 and because $\boldsymbol{X}(t)$ is a linear combination of Laplace-Gauss processes it can be rewritten as a Laplace-Gauss process itself with mean,

$$\mathbb{E}[\boldsymbol{X}(t)] = \begin{pmatrix} c_1 + (c_2+\mu_1)t + (c_3+\mu_2)\dfrac{t^2}{2} + \mu_3\dfrac{t^3}{6} \\ c_2 + (c_3+\mu_2)t + \mu_3\dfrac{t^2}{2} \\ c_3 + \mu_3 t \end{pmatrix} \tag{4.21}$$

and covariance matrix $\boldsymbol{\Gamma}_{\mathbf{x}}(t) = \boldsymbol{\Sigma}_t$. It is important to notice that the covariance matrix is not dependent of the drifts $\mu_{\{1,2,3\}}$, thus we can simplify by setting $\mu_1 = \mu_2 = 0$ without losing of generality leading to

$$\begin{cases} X_1(t) = c_1 + c_2 t + c_3\dfrac{t^2}{2} + \mu_3\dfrac{t^3}{6} + \sigma_1 W_1(t) + \sigma_2\displaystyle\int_0^t (t-s)dW_2(s) + \\ \qquad +\sigma_3 \int_0^t \dfrac{(t-s)^2}{2} dW_3(s) \\ X_2(t) = c_2 + c_3 t + \mu_3\dfrac{t^2}{2} + \sigma_2 W_2(t) + \sigma_3\displaystyle\int_0^t (t-s)dW_3(s) \\ X_3(t) = c_3 + \mu_3 t + \sigma_3 W_3(t). \end{cases} \tag{4.22}$$

Considering later the Kalman filter it is interesting to rewrite Equation 4.17 discretized. Thus we consider a fixed interval $[0,T]$ and subdivised it with M equally spaced points $0 \equiv t_0 < t_1 < \ldots < t_N \equiv T$ and set $\tau = t_{k+1} - t_k$. Equation 4.17 becomes at a time t_k,

$$\boldsymbol{X}(t_{k+1}) = \boldsymbol{\Phi}_{t_{k+1},t_k}\boldsymbol{X}(t_k) + \boldsymbol{B}_\tau\boldsymbol{M} + \boldsymbol{J}_k, \tag{4.23}$$

whose components are,

$$\begin{cases} X_1(t_{k+1}) = X_1(t_k) + X_2(t_k)\tau + X_3(t_k)\dfrac{\tau^2}{2} + \mu_3\dfrac{\tau^3}{6} + J_{k,1} \\ X_2(t_{k+1}) = X_2(t_k) + X_3(t_k)\tau + \mu_3\dfrac{\tau^2}{2} + J_{k,2} \\ X_3(t_{k+1}) = X_3(t_k) + \mu_3\tau + J_{k,3} \end{cases} \tag{4.24}$$

where $J_{k,1}$, $J_{k,2}$ and $J_{k,3}$ are the three components of the vector $\boldsymbol{J}_k$ called the innovation,

$$\boldsymbol{J}_k = \begin{pmatrix} \Big[\sigma_1(W_1(t_{k+1}) - W_1(t_k)) + \sigma_2 \int_{t_k}^{t_{k+1}} (W_2(s) - W_2(t_k))ds + \\ +\sigma_3 \int_{t_k}^{t_{k+1}} (t_{k+1} - s)(W_3(s) - W_3(t_k))ds\Big] \\ \sigma_2(W_2(t_{k+1}) - W_2(t_k)) + \sigma_3 \int_{t_k}^{t_{k+1}} (W_3(s) - W_3(t_k))ds \\ \sigma_3(W_3(t_{k+1}) - W_3(t_k)) \end{pmatrix} \sim \mathrm{LG}(\boldsymbol{0}, \boldsymbol{Q}) \tag{4.25}$$

of covariance matrix $\boldsymbol{Q}$:

$$\boldsymbol{Q} = \begin{pmatrix} \sigma_1^2\tau + \sigma_2^2\frac{\tau^3}{3} + \sigma_3^2\frac{\tau^5}{20} & \sigma_2^2\frac{\tau^2}{2} + \sigma_3^2\frac{\tau^4}{8} & \sigma_3^2\frac{\tau^3}{6} \\ \sigma_2^2\frac{\tau^2}{2} + \sigma_3^2\frac{\tau^4}{8} & \sigma_2^2\tau + \sigma_3^2\frac{\tau^3}{3} & \sigma_3^2\frac{\tau^2}{2} \\ \sigma_3^2\frac{\tau^3}{6} & \sigma_3^2\frac{\tau^2}{2} & \sigma_3^2\tau \end{pmatrix}. \tag{4.26}$$

This iterative writing is particularly useful for simulation purposes or data processing.

4.4 Relation between the clock model and the Allan variance

Now that the clock model is set in terms of different noise components related to the diffusion coefficients, we give the relationship with the Allan variance defined in Equation 4.9. Thus this makes it possible to identify the nature of the noises affecting the clock. Different approaches exist in the literature, the first one [94] allows one to trace step by step the integrated effect of the different noise and the second one [102] simplier which can be extended easily to others kinds of variances will be presented here. Rewriting Equation 4.10, i.e. the average frequency deviation, in terms of phase deviation it follows,

$$\bar{y_k} = \frac{1}{\tau}\int_{t_k}^{t_{k+1}} \dot{X}_1(t)dt = \frac{1}{\tau}(X_1(t_{k+1}) - X_1(t_k)) \tag{4.27}$$

and thus the Allan variance,

$$\sigma_y^2(\tau) = \frac{1}{2\tau^2}\mathbb{E}\Big[\Big((X_1(t_{k+2}) - X_1(t_{k+1})) - (X_1(t_{k+1}) - X_1(t_k))\Big)^2\Big]. \tag{4.28}$$

Applying Equation 4.24 we get,

$$\begin{aligned} \Delta &= (X_1(t_{k+2}) - X_1(t_{k+1})) - (X_1(t_{k+1}) - X_1(t_k)) \\ &= \tau^3\mu_3 + \tau^2 X_3(t_k) + J_{k+1,1} - J_{k,1} + \tau J_{k,2} + \frac{\tau^2}{2}J_{k,3}. \end{aligned} \tag{4.29}$$

The quantity Δ is a Laplace-Gauss distribution of mean and variance,

$$\begin{aligned} \mathbb{E}[\Delta] &= \tau^2[c_3 + \mu_3(t_k + \tau)] \\ \mathbb{V}[\Delta] &= 2\sigma_1^2\tau + 2\sigma_2^2\frac{\tau^3}{3} + \sigma_3^2\left(\frac{23}{30}\tau^2 + \tau^2 t_k\right). \end{aligned} \tag{4.30}$$

This is due to the fact that the quantities involved in Δ are independent with the variances,

$$\begin{aligned} \mathbb{V}[X_3(t_k)] &= \sigma_3^2 t_k, \\ \mathbb{V}[J_{k+1,1}] &= \sigma_1^2\tau + \sigma_2^2\frac{\tau^3}{3} + \sigma_3^2\frac{\tau^5}{20}, \\ \mathbb{V}\left[-J_{k,1} + \tau J_{k,2} + \frac{\tau^2}{2}J_{k,3}\right] &= \begin{pmatrix} -1 & \tau & \frac{\tau^2}{2} \end{pmatrix} \boldsymbol{Q} \begin{pmatrix} -1 \\ \tau \\ \frac{\tau^2}{2} \end{pmatrix} \\ &= \sigma_1^2\tau + \sigma_2^2\frac{\tau^2}{3} + \sigma_3^2\frac{43}{60}\tau^5. \end{aligned} \tag{4.31}$$

Thus Equation 4.28 can be rewritten in term of time-dependent Allan variance,

$$\begin{aligned} \sigma_y^2(t_k, \tau) &= \frac{1}{2\tau^2}\mathbb{E}[\Delta^2] = \frac{1}{2\tau^2}(\mathbb{V}[\Delta] + \mathbb{E}[\Delta]^2) \\ &= \left(\frac{\sigma_1^2}{\tau} + \frac{\sigma_2^2\tau}{3} + \frac{\sigma_3^2\tau^3}{20}\right) + \sigma_3^2\left(\frac{\tau^3}{3} + \frac{\tau^2 t_k}{2}\right) + \\ &\quad + \frac{\tau^2}{2}[c_3 + \mu_3(\tau + t_k)]^2. \end{aligned} \tag{4.32}$$

Setting $\sigma_3 = \mu_3 = 0$, corresponding to a constant frequency drift, leads to

$$\sigma_y^2(\tau) = \frac{\sigma_1}{\tau} + \frac{\sigma_2^2\tau}{3} + \frac{\tau^2}{2}c_3^2. \tag{4.33}$$

In practical application, it is interesting to have the relationship between the diffusion coefficients and the Allan variance as for example to build the Kalman filter with the appropriate parameters which will be presented in the next chapter. By computing the Allan variance and looking at a specific region of τ, according the power-law, the noises affecting the data can be deducted. For example, in a τ region characterized only by WFN, σ_1 can be evaluated and we will get $\sigma_1^2 = \sigma_y^2\tau$.

CHAPTER 5

Kalman filter for the detection of time step

In this chapter a new algorithm is developed to improve the reliability of UTC. The new algorithm is based on the Kalman filter routine. It was presented by Kalman in 1960 in a pioneering article [111] used in many fields, e.g. UTC obtained by using the Kalman filter [112], because of its ability to smooth out the WFN component considered as a measurement noise. In this chapter the Kalman filter is presented as a tool to detect time and frequency steps in the time links (GNSS or TWSTFT) used in UTC calculation. The predicted state obtained with the Kalman Filter is compared to the real measurement, called innovation. If this value is larger than a defined threshold an anomaly is detected. Therefore no additionnal equations are needed as the detector is embedded in the Kalman filter. Moreover the use of the innovation as a criterion is a known technique [113] which is mentioned in [114] for the detection of time steps.

In Section 5.1 is presented the Kalman filter with its application to atomic clocks. Section 5.2 reports the preliminary analysis performed on the data. The results for the detection of time steps obtained are reported in Section 5.3 and the optimization of the detection factor is given in Section 5.4. Finally Section 5.5 concludes the chapter.

This chapter is done by the author under the supervision of Gianna Panfilo.

5.1 Kalman filter

The Kalman filter is based on a linear dynamical system which require the knowledge of different informations:

1. a state vector $\boldsymbol{X}(t)$ defined by

$$\boldsymbol{X}(t) = \boldsymbol{\Phi}_{t,t-\tau}\boldsymbol{X}(t-\tau) + \boldsymbol{W}(t) \tag{5.1}$$

   where $\boldsymbol{\Phi}_{t,t-\tau}$ is the state transition matrix;

2. noises of the system represented by the random vector $\boldsymbol{W}(t)$, defined as a multivariate zero-mean Laplace-Gauss distribution with covariance matrix $\boldsymbol{Q}$;
3. an initial estimate state vector $\widehat{\boldsymbol{X}}(t_0)$ whose covariance matrix is $\boldsymbol{\Gamma}(t_0)$;
4. the true measurements $\boldsymbol{Z}(t)$ of the observable variables affected by noises.

5.1.1 Algorithm

The Kalman filter algorithm is composed of two different parts. The first, based on the knowledge of the system, an *a priori* estimation is performed. In the second this estimation is updated by comparison with the true measurement and called the *a posteriori* estimation. Thus the discretized algorithm is described at every time instant t_k by four steps:

S1: Prediction:
The predicted state estimate, given an initial estimate $\widehat{\boldsymbol{X}}(t_0)$ is,

$$\widehat{\boldsymbol{X}}(t_k|t_{k-1}) = \boldsymbol{\Phi}_{t_k,t_{k-1}}\widehat{\boldsymbol{X}}(t_{k-1}|t_{k-1}), \tag{5.2}$$

whose covariance matrix, initialized by $\boldsymbol{\Gamma}(t_0)$ is given by,

$$\boldsymbol{\Gamma}(t_k|t_{k-1}) = \boldsymbol{\Phi}_{t_k,t_{k-1}}\boldsymbol{\Gamma}(t_{k-1}|t_{k-1})\boldsymbol{\Phi}^T_{t_k,t_{k-1}} + \boldsymbol{Q}. \tag{5.3}$$

S2: Innovation:
The measurement vector can be written as $\boldsymbol{Z}(t_k) = \boldsymbol{H}\boldsymbol{X}(t_k) + v(t_k)$ where $\boldsymbol{H}$ denotes the transformation matrix and $v(t_k)$ the measurement noise described by a zero-mean Laplace-Gauss distribution with covariance $\boldsymbol{R}$. Then the innovation process, i.e. the deviation of the new measurement from the predicted state, is given by

$$\boldsymbol{\nu}(t_k) = \boldsymbol{Z}(t_k) - \boldsymbol{H}\widehat{\boldsymbol{X}}(t_k) \tag{5.4}$$

with covariance matrix,

$$\boldsymbol{\sigma}_{\boldsymbol{\nu}}^2(t_k) = \boldsymbol{H}\Gamma[t_k|t_{k-1}]\boldsymbol{H}^T + \boldsymbol{R}. \tag{5.5}$$

The **Kalman gain** is then defined by

$$\boldsymbol{K}(t_k) = \boldsymbol{\Gamma}(t_k|t_{k-1})\boldsymbol{H}^T \left(\boldsymbol{\sigma}_{\boldsymbol{\nu}}^2(t_k)\right)^{-1}. \tag{5.6}$$

S3: Update:
By using the innovation and the Kalman gain the state estimate is updated such as,

$$\widehat{\boldsymbol{X}}(t_k|t_k) = \widehat{\boldsymbol{X}}(t_k|t_{k-1}) + \boldsymbol{K}(t_k)\nu(t_k) \tag{5.7}$$

whose covariance matrix is

$$\boldsymbol{\Gamma}(t_k|t_k) = (\boldsymbol{I} - \boldsymbol{K}(t_k)\boldsymbol{H})\boldsymbol{\Gamma}(t_k|t_{k-1}) \tag{5.8}$$

where $\boldsymbol{I}$ is the identity matrix.

S4: Time step detection:
Following the described procedure, the jump in the data is defined if

$$|\boldsymbol{\nu}(t_k)| > k\boldsymbol{\sigma}_{\boldsymbol{\nu}}(t_k). \tag{5.9}$$

where k is a parameter, already described in [86], which must be optimized to UTC situation.

5.1.2 Kalman filter for atomic clocks

An atomic clock is characterized by fundamental quantities such as the time deviation $x(t)$ and the normalized frequency deviation $y(t)$. However, only the difference between two clocks can be measured. We thus define the difference between the time deviation of a clock from any laboratory j and a referring laboratory i by:

$$x_{ij}(t) = x_j(t) - x_i(t). \tag{5.10}$$

Considering an ensemble of two clocks, the state vector will contain the phase, frequency and drift offsets for each clock. The observation matrix $\boldsymbol{H}$ which exhibits the difference of the time deviation of two clocks according to Equation 5.10 is written

$$\boldsymbol{H} = \begin{pmatrix} -1 & 1 & 0 \end{pmatrix}. \tag{5.11}$$

The transition matrix $\mathbf{\Phi}$ according to Equations 4.23 and 4.24 leads to

$$\mathbf{\Phi}(\tau) = \begin{pmatrix} 1 & \tau & \frac{\tau^2}{2} \\ 0 & 1 & \tau \\ 0 & 0 & 1 \end{pmatrix}. \tag{5.12}$$

According to Equation 4.26, the noise matrix $\boldsymbol{W}$ is a zero-mean Laplace-Gauss distribution of covariance matrix,

$$\boldsymbol{Q} = \begin{pmatrix} \sigma_1^2\tau + \sigma_2^2\frac{\tau^3}{3} + \sigma_3^2\frac{\tau^5}{20} & \sigma_2^2\frac{\tau^2}{2} + \sigma_3^2\frac{\tau^4}{8} & \sigma_3^2\frac{\tau^3}{6} \\ \sigma_2^2\frac{\tau^2}{2} + \sigma_3^2\frac{\tau^4}{8} & \sigma_2^2\tau + \sigma_3^2\frac{\tau^3}{3} & \sigma_3^2\frac{\tau^2}{2} \\ \sigma_3^2\frac{\tau^3}{6} & \sigma_3^2\frac{\tau^2}{2} & \sigma_3^2\tau \end{pmatrix}. \tag{5.13}$$

5.2 Preliminary data analysis

We start considering GPS Multi-Channel (MC) technique but the analysis will be extended to GPS P3 and GPS PPP. The GPS data (in the GGTTS format) provided by the Time laboratories to the BIPM report the difference between the local time, T_L, of the laboratory and the time of each satellite (identified by PRN in the file). To improve the stability of the data the BIPM processes the data in two steps; at the first step data are processed to refer T_L to GNSTT (Reference Time scale of the GNSS) and in the second step a weighted average based on the elevation of the satellite is done and a unique value is obtained for each epoch of T_L-GPST. These last files are internally named respectively "G1I" and "GPI". When a significant step is present in the time link the algorithm used to process data from G1I to GPI causes a loss of a few hours of data because when the step occurs these data are considered as outliers and automatically eliminated. When the observed step is not greater than the noise affecting the G1I the data are not eliminated. In the following sections we start considering an example of step correctly visible in the GPI data (without missing data) but the analysis will be extended to G1I data in case of missing data.

Figure 5.1 shows phase data extracted from the G1I file for four different satellite used to obtain the final data reported in Figure 3.6 (GPI). The different levels of noise are perfectly visible in the graphics. Figure 5.1 (a) and (d) show a perceptible time step framed by a red box, whereas it is not the case for the other ones. Let us note also that the date of the jump will be different for each satellite, because they are not all visible at the same time.

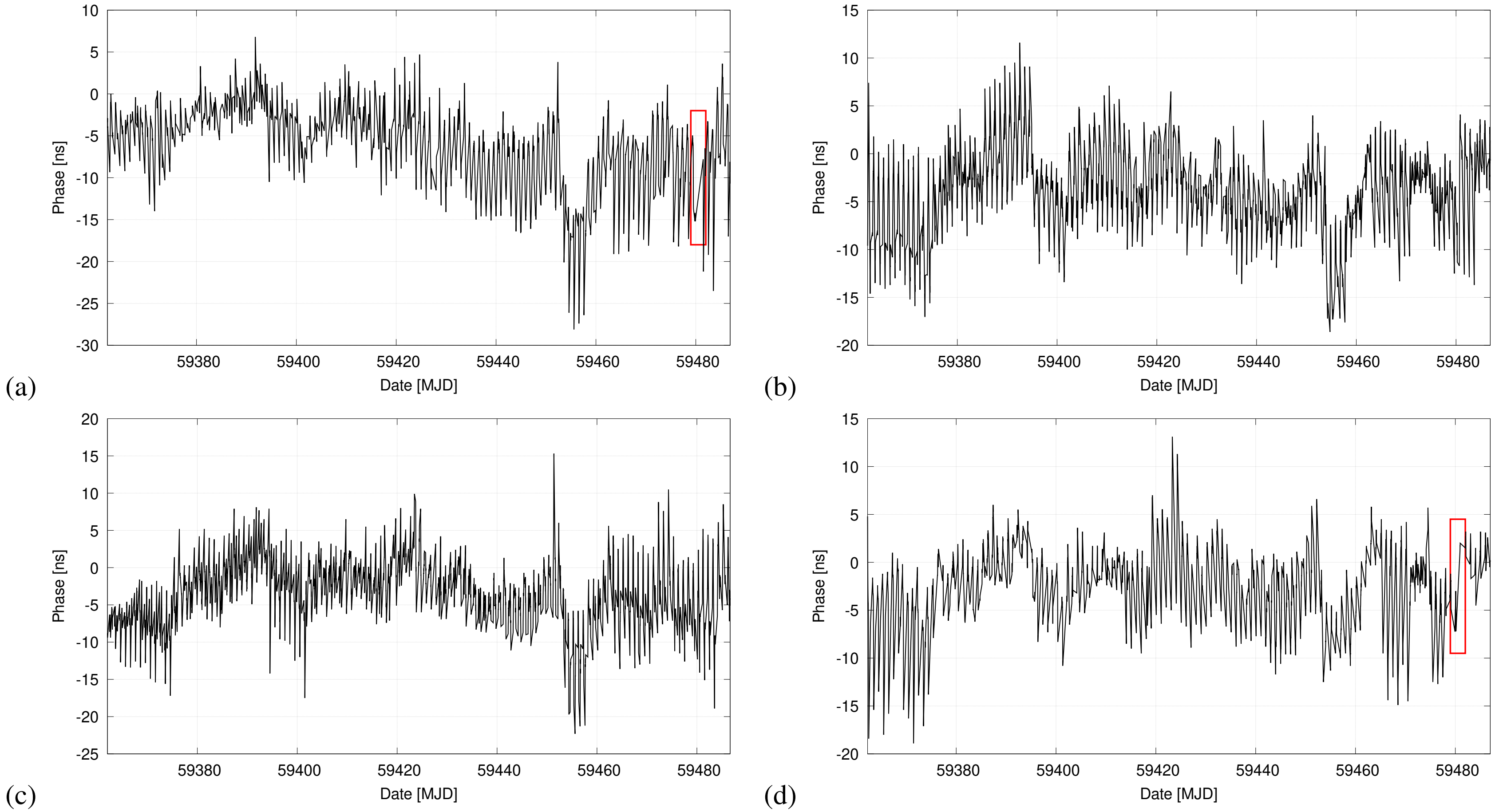

Figure 5.1: Example of time transfer link of the same signal represented in Figure 5.1 with four different satellites. The noticeable time step are framed by a red box.

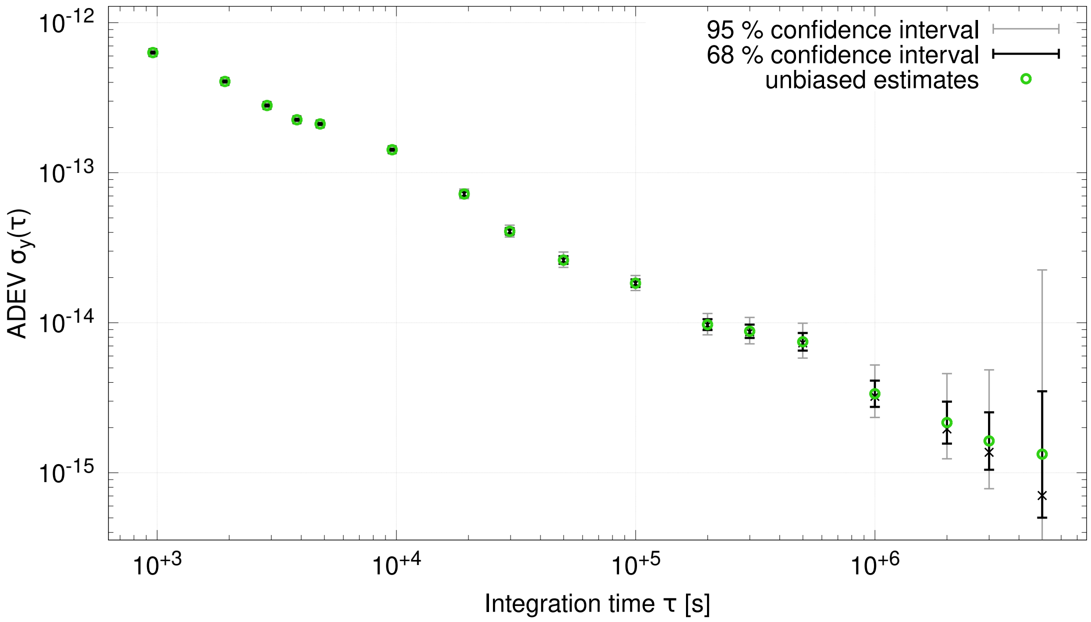

Figure 5.2: Allan deviation of the time transfer link. At short sampling times the time transfer link is dominated by the white frequency noise component.

5.3 Time steps detection

In Figure 3.6 the example of phase jump occurring in a time link used to compute UTC is reported. The detector, presented in Section 5.1, is tested on this set of data to check his ability to give a warning and the related information on the jump. These data, as described in Section 5.2, originated from the "GPI" file are already processed from outliers. The anomaly occurs after MJD 59480 and should not be confused with the drift observed after MJD 59460. In order to apply the Kalman filter to this data, we need to define two parameters: the noise included in the state equation whose covariance matrix $\boldsymbol{Q}$ is given by Equation 5.13 and the measurement noise or phase noise (in covariance matrix $\boldsymbol{R}$) that we want to filter. The clock model described in Section 4.3 is based on three different noises: the white frequency noise (WFN), the random walk frequency noise (RWFN) and the random perturbation of the frequency drift that usually is not taken into account ($\sigma_3^2 = 0$). We neglect also the RWFN because the variation is very low, so $\sigma_2^2 = 0$. In case of WFN the σ_1 parameter is directly related to the Allan variance according to Equation 4.33 by the following relation: $\sigma_1^2 = \sigma_y^2 \tau$. According to Figure 5.2, we can clearly observe that the slope of the Allan deviation decrease as $\tau^{-1/2}$ thus indicating the presence of WFN. At τ equal to one day, we have approximately:

$$\sigma_y^2 = (1.8 \times 10^{-14})^2. \tag{5.14}$$

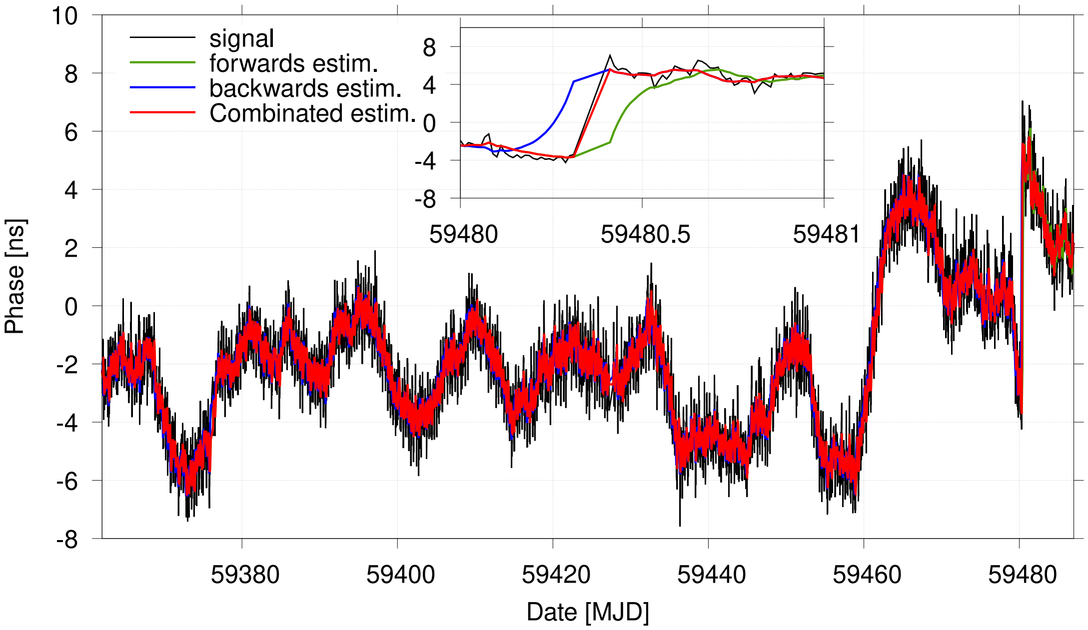

Figure 5.3: Detection of a time step in the phase data. The time deviation of the time link signal (in black) is filtered by the Kalman procedure(in red).

To limit the propagation of numerical errors, the simulations are carried out with parameters in ns per day which gives $\sigma_1 \approx 1.56$ ns/day. Finally, to determine the parameter $\boldsymbol{R}$ we consider the u_{Stb} value reported in Section 5 of Circular T [11] for the considered time link. This uncertainty takes in to account the level of phase noise in the raw data. It gives

$$\boldsymbol{R} = 1.5^2 \; ns^2 = 2.25 \; ns^2. \tag{5.15}$$

The Kalman algorithm is processed for few time steps initialized with the first value in the data set, then the first estimate is taken as the initial value for the true run. Another method could be to propagate the Kalman filter backwards in time, thus having the last estimate corresponding to the initial value. Considering that UTC is not computed in real time we adapt and optimize the detection algorithm by applying the filter forwards and backwards in time; these filtered data are then combined after stopping both series at the date of the step. Applying these Kalman filters to the “GPI” data we obtain the results reported in Figure 5.3 where the black line shows the original data, the green and the blue lines the filter forwards and backwards respectively. Finally the red line shows the combination of both. It is clear from the zoomed figure that the combined solution gives a more correct information concerning the value of the step. According to [86] we start choosing a value of the parameter k equal to 5. To detect the time step in the data the Equation 5.9 must be verified. The value of the parameter k is strictly depending on the amplitude of the jump. An automatic procedure to fix its value needs to be implemented. With the described method we detect a phase jump at MJD 59480.3115. This data corresponds perfectly to the information needed by the BIPM. The clear advantage to use both filters is for the evaluation of the value of the step because even if by using only one filter the phase noise is smoothed out very well, the value of the jump is not perfectly catched. If we stop the filters forwards and backwards at the date of the step and we combine them, the final solution allows a better evaluation of the step. This method represents a novelty with respect to the detector presented in previous publication and is tested to other cases in order to be generalized.

We are now taking another example of jump in the time transfer link using multichannel technique. Figure 5.4 (top) and (bottom) respectively show to the “G1I” having a phase noise level lower than the jump and the “GPI” having a much lower sampling. The Kalman filter is applied forwards (green curve) and backwards (blue curve) in time with the combined estimate to give a better value of the jump magnitude. There are just over 20 satellites implied in this process to obtain the “GPI” data, but some of them have very few data thus are not exploitable. The “G1I” data represented here correspond to the one that give the date of the jump which occurs first, i.e. MJD 59 547.6292 whereas it is detected at MJD 59 548 for the “GPI”. The magnitude of the jump is approximately the same for both data set close to 202 ns. The detector works with both data sets, but we then focus only on the “GPI” to have a better probability of detecting phase jumps.

Finally we extend the analysis to other time transfer technique such as GPS P3 and GPS PPP. Figure 5.5 (top) and (bottom) correspond respectively to GPS P3 and GPS PPP data sets. Both data sets exhibit a lower phase noise than with the multichannel technique which greatly increases the probability of detecting jumps when there are any. The Kalman process is exactly the same as with the multichannel technique with a lower R value. The magnitude of the jump is not inherent to the time transfer technique but generally to the laboratory itself. We detect respectively for the GPS P3 and GPS PPP technique a phase jump at MJD 59 696.2198 and MJD 59 283.99632. It sometimes happens that the jumps all occur approximately on the same date for different laboratories while their clocks are totally independent. These anomalies therefore come directly from the satellites involved in the time transfer. However, this has no effect on the links that are made with the pivot if it exhibits the same kind of problem.

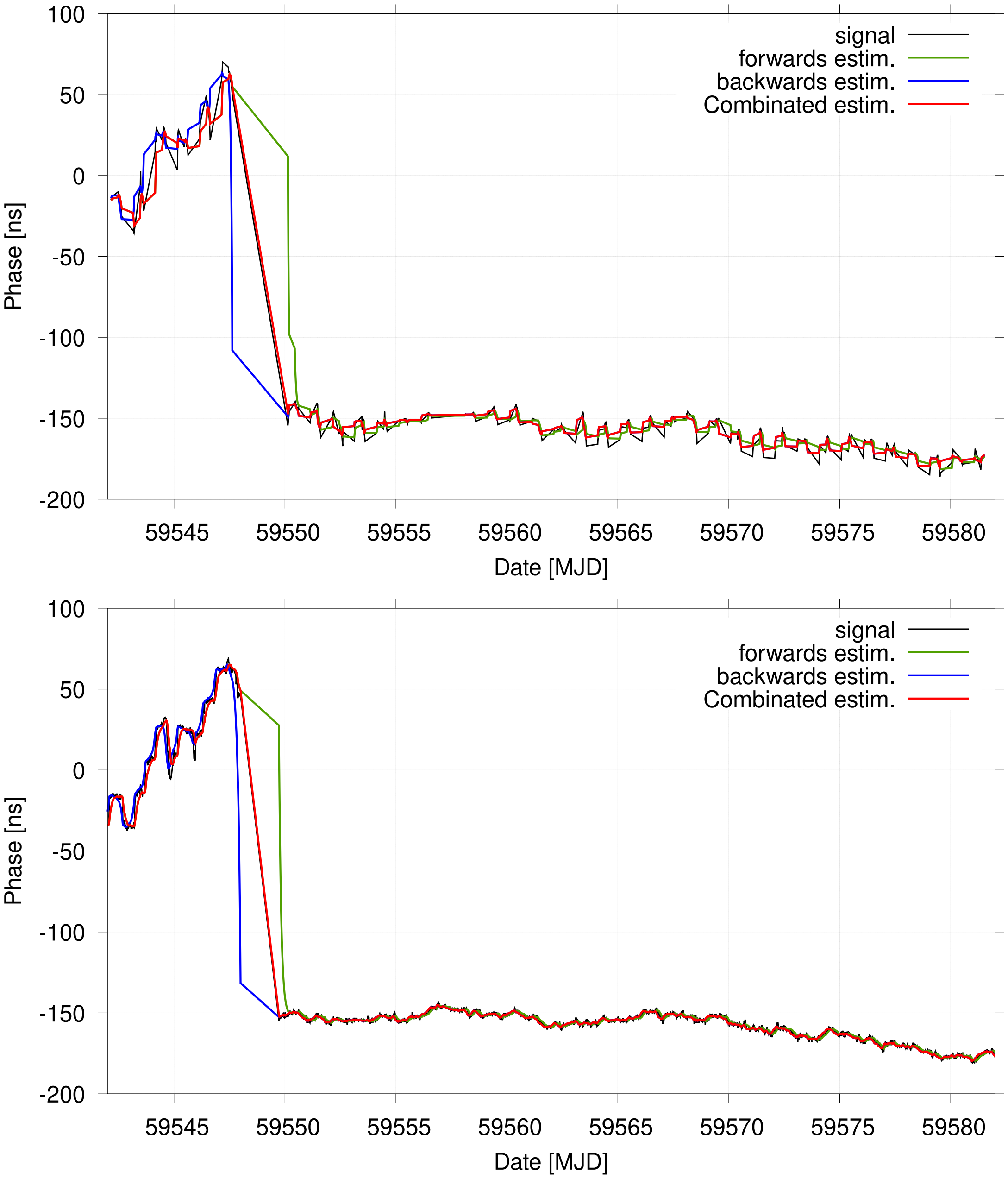

Figure 5.4: Detection of a time step between “G1I” (top) and “GPI” (bottom) data sets. The time deviation of the time link signal (in black) is filtered by the Kalman procedure (in red).

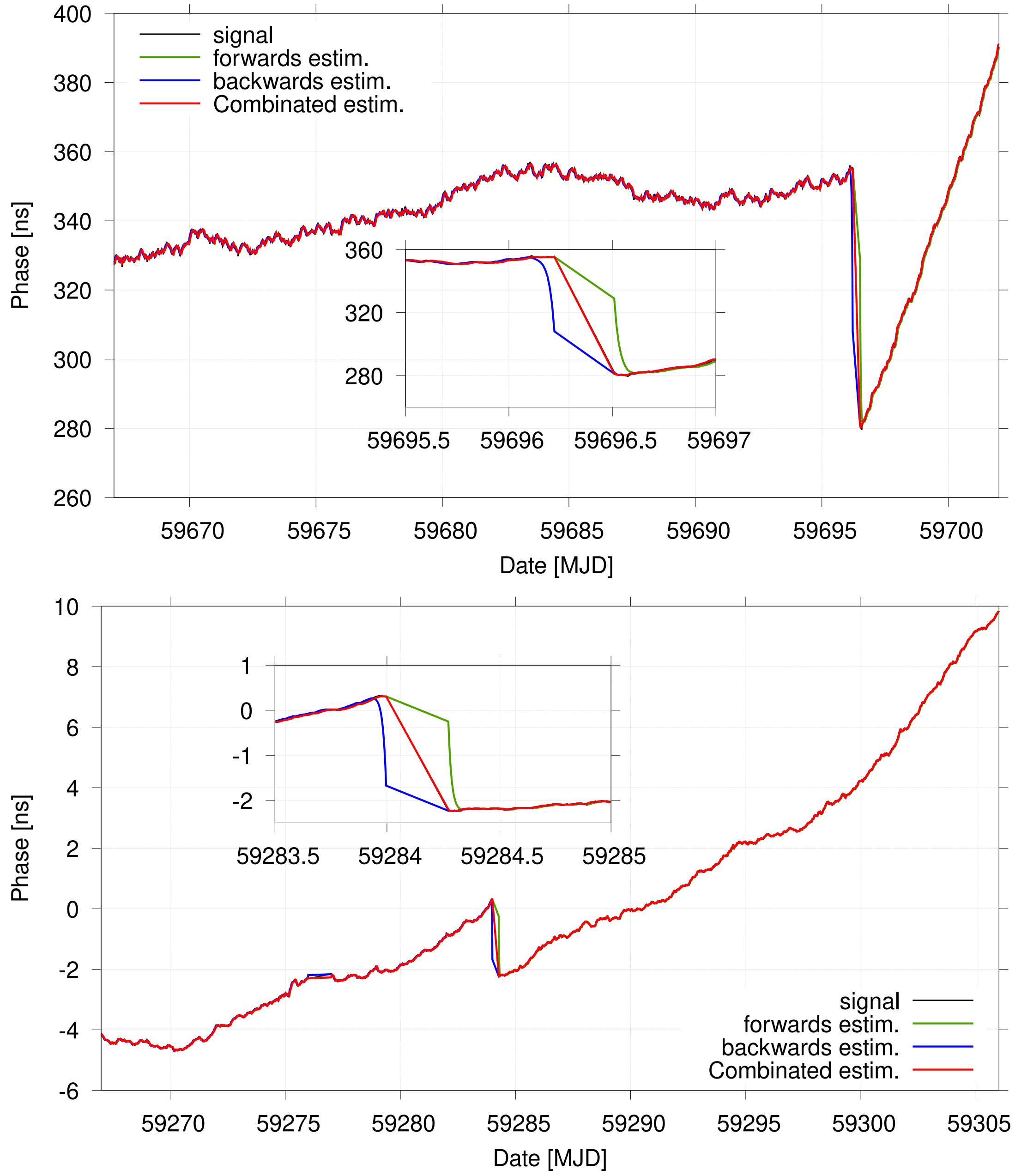

Figure 5.5: Detection of a time step for GPS P3 and GPS PPP time transfer link. The time deviation of the time link signal (in black) is filtered by the Kalman procedure (in red). A zoom on the jump is show enlightening the difference between the Kalman filter processed forwards and backwards in time.

5.4 Detection factor optimization

An automatic detection procedure for the parameter k needs to be developped. In order to determine a procedure for this parameter we simulate the time transfer link accordingly to Equations 4.23 and 4.24. Thus the simulated data set does not contain anomalies such as phase jumps, outliers or missing data. According to the data set studied, we apply the same process as in Section 5.3 to determine the phase noise parameter R and the WFN parameter σ. The result is presented is Figure 5.6 by the blue curve whereas the Kalman filter corresponds to the green curve. Therefore we use the same detector as described by Equation 5.9 and we define the factor k by

$$max[k] < \frac{|\boldsymbol{\nu}(t_k)|}{\boldsymbol{\sigma_{\nu}}(t_k)}, \tag{5.16}$$

for each simulation. Finally we performed hundred of simulations and Table 5.1 reports the mean, standard deviation, minimum and maximum value obtained. We notice that the value chosen in Section 5.3, i.e. $k = 5$ corresponds well to the values of the table for the parameters $\sqrt{\boldsymbol{R}} = 1.5$ ns and $\sigma_1 = 1.56$ ns/day. Figure 5.7 shows the variation of the minimum in red, maximum in black and the average in blue of the parameter k according to the phase noise and the WFN. The threshold of detection determined by k is very sensitive to the small value of the phase noise. The parameter sigma has also a non negligible influence on the parameter k. To evaluate correctly this parameter, we calculate the Allan deviation on a selected sample of data large enough but without anomalies.

5.5 Discussion

In this chapter the use of the Kalman filter to detect jumps in time transfer links used in UTC computation is presented. The algorithm succeeds in correctly identifying the step and the magnitude. This information is essential to guarantee the reliability and the stability of UTC. The algorithm is extended to different sets of data (GPI and G1I) depending on the magnitude of the steps and takes into account the already existing algorithms used to process UTC data at BIPM Time Department. An automatic estimation of the noises and of the deterministic parameters is essential to build an automatic procedure without external intervention. A robust algorithm for the estimation of parameters is the key issue for this kind of tool. The algorithm described in this part is implemented and operational at the BIPM. To go further, the detector should differentiate the phase jumps from the outliers. One way to do this is to look not just at the next instant as Kalman's algorithm does, but at a window with several data points. In order to increase the precision one can also add a linear drift needed to have a better description of certain clocks.

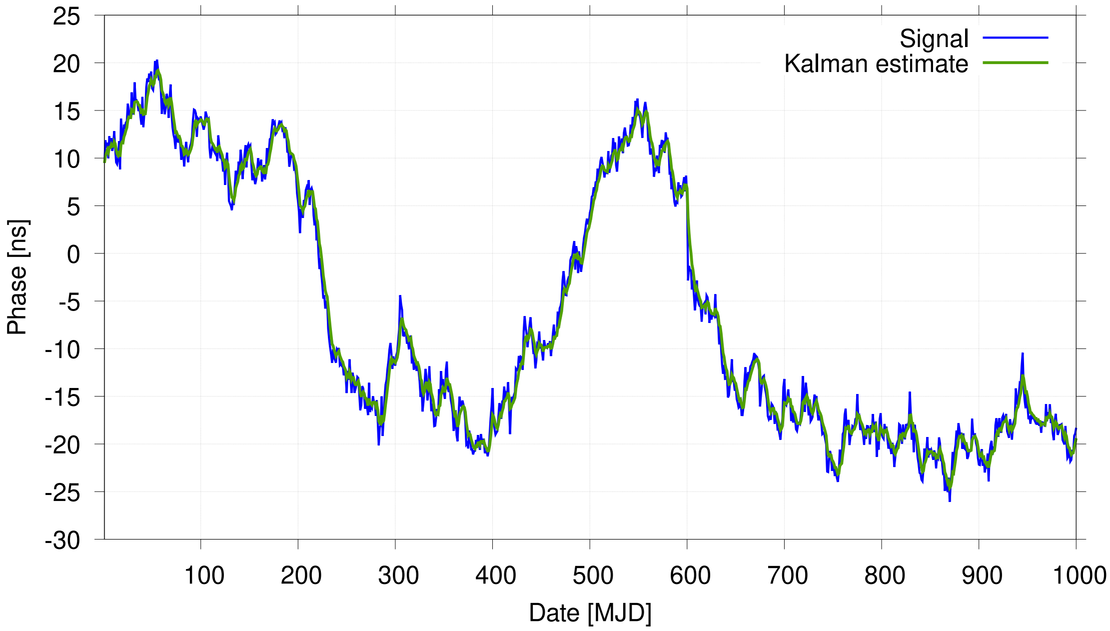

Figure 5.6: Simulation of time transfer link (in blue) without anomalies and the estimated signal obtained by the Kalman filter (in green).

$\sqrt{R}$[ns]	σ[ns/day]	mean(k)	std(k)	min(k)	max(k)
1.4020	1.0000	6.0408	0.2774	4.8861	7.2498
1.5120	1.0000	5.9821	0.2974	4.9498	7.2784
1.5880	1.0000	5.7620	0.1541	4.9244	6.4338
1.7400	1.0000	5.6712	0.4575	4.7259	7.6655
1.8250	1.0000	5.8547	0.3325	4.7844	7.3041
1.8750	1.0000	5.6663	0.3727	4.9205	7.2909
1.9250	1.0000	5.6292	0.4471	4.4949	7.5779
1.4020	2.0000	7.7639	0.5068	6.3950	9.9731
1.5120	2.0000	7.4682	0.2133	6.7187	8.3980
1.5880	2.0000	7.2434	0.2309	5.9216	8.2498
1.7400	2.0000	7.3639	0.3206	6.2339	8.7614
1.8250	2.0000	7.1116	0.4931	5.8146	9.2611
1.8750	2.0000	7.0653	0.5407	5.9708	9.4220
1.9250	2.0000	7.1270	0.3005	5.8697	8.4368

Table 5.1: One hundred simulated time transfer links giving the mean, standard deviation, minimum and maximum value of the parameter k according to the WPM and the WFM parameters.

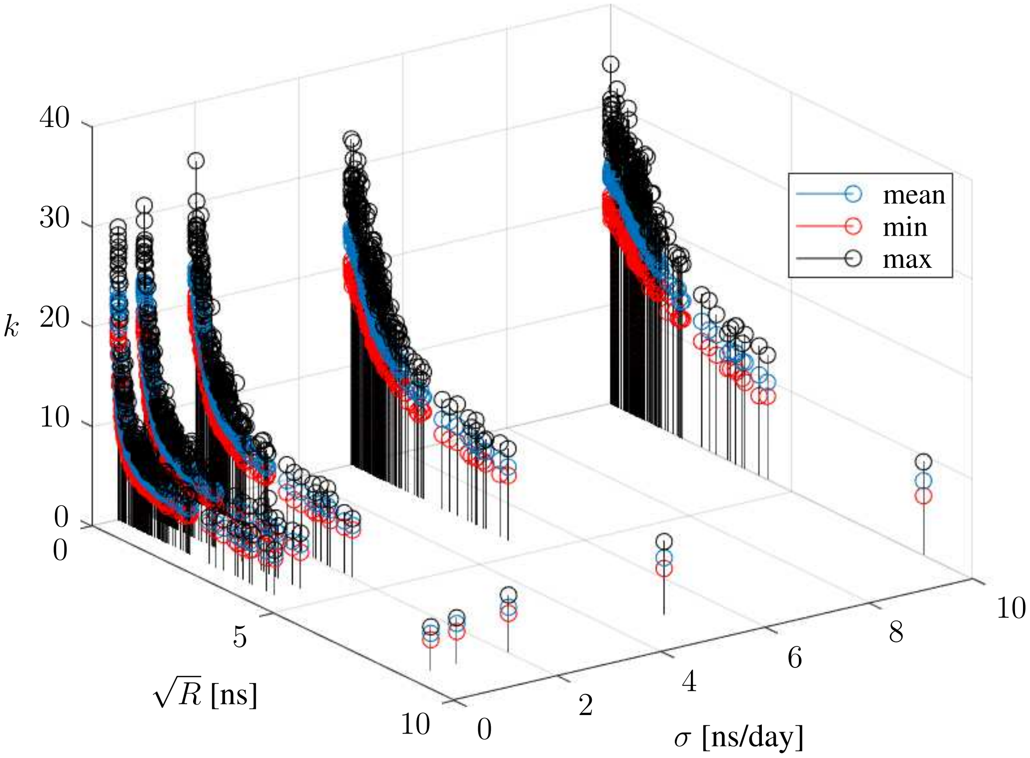

Figure 5.7: The minimum (in red), maximum (in black) and the mean (in blue) value of the parameter k are given according to the WPM and the WFM parameters

Part III

Frequency

Part III: Frequency

CHAPTER 6

Power spectra

6.1 Context

The measurement of power spectra is a classical problem, ubiquitous in numerous branches of physics, as explained below. Power spectra are efficiently measured using Fourier transform methods with digitized data. Relevant bibliography is now found in classic books [115–118].

We are interested in the measurement of weak statistical phenomena, which challenge the instruments and the mathematical tools, using the cross-spectrum method. This method consists of the simultaneous measurement of the signal with two separate and independent instruments [59]. The other approach, consisting on the observation of the spectral contrast in a chopped signal, broadly equivalent to the Dicke radiometer [119], is not considered here. Regarding the duration of the data record used to evaluate the Fast Fourier Transform (FFT), two asymptotic cases arise.

The first case is that of the measurement of fast phenomena, where a large number of records denoted η is possible in a reasonable observation time. At large η, the central limit theorem holds and the background noise can be rejected by a factor approximately equal to $1/\sqrt{p}$, depending on the estimator. Numerous examples are found in the measurement of noise in semiconductors [120], phase noise in oscillators

This chapter is done by the author under the supervision of François Vernotte and Enrico Rubiola.

and components [121–124], frequency fluctuations and relative intensity noise in lasers [125, 126], electromigration in thin films [127], etc. Restricting to one bin of the Fourier transform, the power spectral density integrated over a suitable frequency range is used in radiometry [128,129], Johnson thermometry [130] and other applications.

The second case is that of slow phenomena, where the fluctuations are very long term or non ergodic. On one hand the background noise is still rejected as before but with a very low η which can actually be equal to one. On the other hand, the central limit theorem does not apply and the statistical uncertainties are not trivial. This case is of great interest in radio astronomy, where the observations are limited by the available resources and take a long time. As instance millisecond pulsars (MSP) can be used as very stable clocks at astronomical distances [30]. The radio pulses times of arrival (TOA) of MSP are affected by numerous physical process, one of them are gravitational-wave (GW) perturbations [41, 131]. Like the analysis of the signals provided by the LIGO/VIRGO interferometers which use cross correlation methods [132, 133], the LEAP experiment (i.e. Large European Array for Pulsars) [54] could use such methods in order to access lower frequencies and observe imperceptible phenomena such as early phases well before the coalescence of black holes or GW of cosmological origin (for example cosmic strings, inflation, primordial black holes). Red noise originated from GW perturbations in the signal path common to the radio-telescopes can be detected [52, 53]. The term red noise refers to a variety of processes sharing the property that the Power Spectral Density (PSD) grows at low frequency as $1/f^2$ (Brownian noise) or $1/f^\alpha$, with $\alpha > 2$.

We are interested in the estimation of the PSD of such random signals out of the background noise of the instrument in the specific case of very slow phenomena, which take too long acquisition time for the average on a sequence of data sets to be visible. Therefore, averaging out the background is possible only by exploiting simultaneous measurements of the same signal taken with multiple instruments, under the obvious hypothesis that they are independent. The frequency stability of the millisecond pulsars is the example we have in mind. Such rapidly rotating neutron stars, emitting highly stable periodic pulses out of the magnetic poles, rival the best atomic clocks [25, 28, 35, 134]. Among other fields, slow phenomena are found in climatology [135] and geodesy, the latter nowadays measured with Very Large Baseline Interferometry [136]. The measurement of noise and phase noise with fully digital instruments is another appealing application because increasing the number of channels is reasonably simple. The phase noise of oscillators can be measured with the multi-channel tracking DDS [137]. An improved 16-channel version of the Tracking DDS is now a semi-commercial instrument (we have recently purchased two beta-test samples), albeit there is still no official announcement. In Si, Ge and GaAs semiconductors, low $1/f$ noise is a quality indicator related to the effective number of defects [138].

This part is intended to put an upper limit on the uncertainty of the cross-spectrum estimate. The method proposed here is totally general regardless the power law type of noise. Indeed, even if the pulsar signal would be constituted by white noise, the realisations of this white noise would be the same, for low frequency, at different observatories where realisations of measurement white noise are independent. However this part shows a particular interest to red noise. Gravitational-waves have not been yet discovered in the TOA of millisecond pulars. Thanks to the very long line of sight between the pulsars and us (several thousand light-years), we could access very low frequencies, inaccessible to LIGO/VIRGO, thus revealing much slower astrophysical phenomena. It is therefore important to develop statistical tools to improve measurement sensitivity to pulsar timing observations. With these purposes stated in mind, we compare the efficiency of the spectrum average (s.a) and of the cross-spectrum (c-s) measuring the signal with n instruments simultaneously. The s.a estimator is the average of the n observed spectra S_i, weighted with the background noise $\sigma^2_{W,i}$ of the i-th instrument. The c-s method is the average of the all combinatorial choices of the cross-spectrum $S_{j,i}$, $i \neq j$. The s.a is the classical estimator used in these cases [139], while the c-s is rather uncommon. Data are analyzed with the Bayesian statistics, also known as the inverse problem, which consists of estimating the most probable value of the signal (the slowest spectral components) from the experimental outcomes and their statistical properties. We take the 95% upper limit as the efficiency criterion. Accordingly, the most efficient estimator is the one that provides the most stringent upper limit with the same data set.

We run a simulation with up to five instruments, inspired by the LEAP experiment [54]. Such experiment gathers the five largest European radio telescopes (RTs) in order to increase the sensitivity of high-precision pulsar timing. Interestingly, Pulsar Timing Arrays seem a promising option to explore the low-frequency gravity waves crossing our Galaxy [140, 141]. The c-s estimator commonly used in the frequency metrology has recently been used in [142] to show the detection limit of correlated red noise. Hence defining a confidence interval on this estimator and comparing it with the commonly used s.a will give hints on which estimator has to be privileged to improve the sensitivity.

In this respect, we propose in this Chapter to define the scheme of the experiment, described by a random signal measured by n devices and establish the resulting properties. This signal of interest is considered to be a red noise and thus simulating this kind of noise could introduce an artifact which is presented in Chapter 7. Based on the principle that the experiment is repeated η times, it is important to note that the estimation of the measurement uncertainty is A-Type as defined by the VIM [143]. Moreover, it raises questions about the correlation between these different sequences, so we give a description of it in Chapter 8. Finally Chapters 9 and 10 are intended to compare the s.a and the c-s estimators respectively for $n = 2$ instruments and generalized to multiple instruments measuring a random signal, e.g. a red noise. We will give the probability density function (i.e. “direct problem”) of these estimators used to compute an upper limit by using a bayesian inference approach (i.e. “inverse problem”).

6.2 Statement of the problem

6.2.1 Spectral measurement

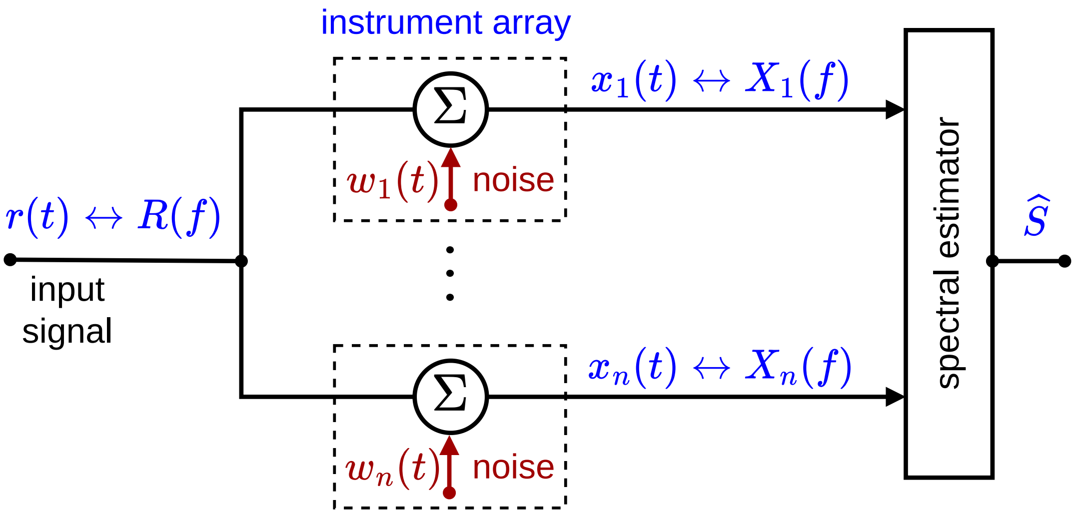

Figure 6.1: Array of n instruments measuring the signal $r(t)$. Each instrument adds a white noise to the output $x_i(t)$ whose Fourier transform is $X_i(f)$. Then the estimate $\widehat{S}$ is computed.

Let us consider a **red** noise $r(t)$ which is measured by an array of n independent instruments as shown in Figure 6.1. We assume that each instrument adds a white noise $w_i(t)$ to the measurement and that all these white noises are uncorrelated. In the following, we call the red noise the “**signal**” and the white noise from the measurement instrument is referred as the “**measurement noise**”. The output of each channel is then

$$x_i = r + w_i \leftrightarrow X_i = R + W_i \tag{6.1}$$

where the subscript i corresponds to the i-th instrument, $\leftrightarrow$ stands for the Fourier transform and inverse Fourier transform pair, lower case is time domain, upper case is frequency domain, and the variables t and f are implicit. The estimates will be noted with a "hat" and $\widehat{S}$ is computed. Figure 6.2 shows the time sequence of the sum of a red and white noise whereas Figure 6.3 represents its spectrum emphasizing the randomness of the real and imaginary part. Let us remind that the Fourier transform of a white noise is a white noise, at least for sampled signals. Indeed, even if continuous pure white noise have an infinite power, the Fourier transform for discrete simulations can be defined. A realistic white noise corresponds to a Markov process of the first order, more details about colored noise are given in [144]. On the other hand, a red noise can be described as a filtered white noise. Its spectrum is then the product of a white spectrum by a deterministic function; so the random part of a red noise is uncorrelated for each frequency bin. Consequently in term of random variable (r.v.), working in the frequency domain gives a precious advantage because the Fourier components (frequency bins) are statistically independent unlike the time data.

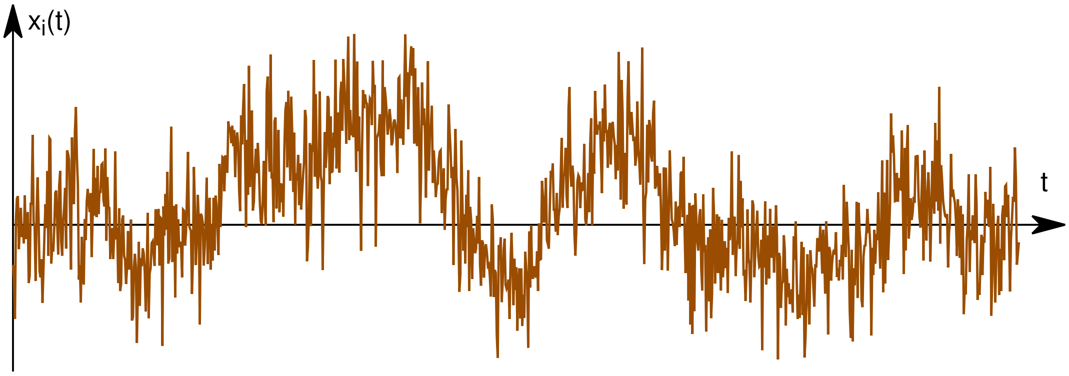

Figure 6.2: Time sequence.

6.2.2 Periodogram and Power Spectral Density

First, let us recall some basics of frequency analysis. Using a data record of duration T sampled at a suitable frequency, the periodogram is

$$P_x(f) = \frac{2}{T}|X(f)|^2, \qquad f > 0 \tag{6.2}$$

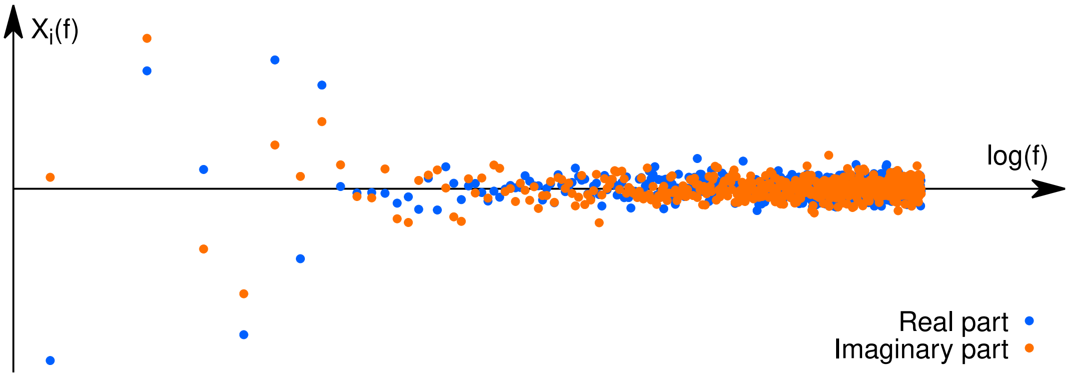

Figure 6.3: Spectrum.

where the factor "2" is needed for energy conservation after deleting the negative frequencies. The expectation of the periodogram is the Power Spectral Density,

$$S_x(f) = \mathbb{E}\left[\frac{2}{T}|X(f)|^2\right], \qquad f > 0. \tag{6.3}$$

In this part, we aim to measure the mathematical expectation of the amplitude for a given frequency bin, e.g. f_1 as represented by a blue box on Figure 6.4. This amplitude depends on the frequency and this is what we are looking for. The periodogram is represented by the orange dots and its expectation the PSD by the green curve. The red and gray curves correspond respectively to the asymptotes arising from the power law of the red and white noise. We estimate the PSD as the average periodogram, with the ultimate goal of expecting the red noise parameters of r out of the measurement noise w. Of course r is the same for all instruments, while the w_i are specific to the i-th instrument and its environnement. So we can only estimate the periodogram of r. The total duration of the experiment is the major problem, as the lowest frequency of interest sets T. In turn, a long T goes with a small number η of averages because the total duration of the experiment is ηT. In the following chapters we focus on the slowest red noise phenomena, up to years, for which we have to set $\eta = 1$. In other words, the phenomena of interest are so slow that we cannot average on multiple acquisitions.

6.2.3 Variance of the spectra

In the following we focus solely on **one frequency bin** and we introduce the notations,

$$\begin{aligned} \Re[W_i] &= W_i' & \Im[W_i] &= W_i'' \\ \Re[R] &= R' & \Im[R] &= R'' \end{aligned} \tag{6.4}$$

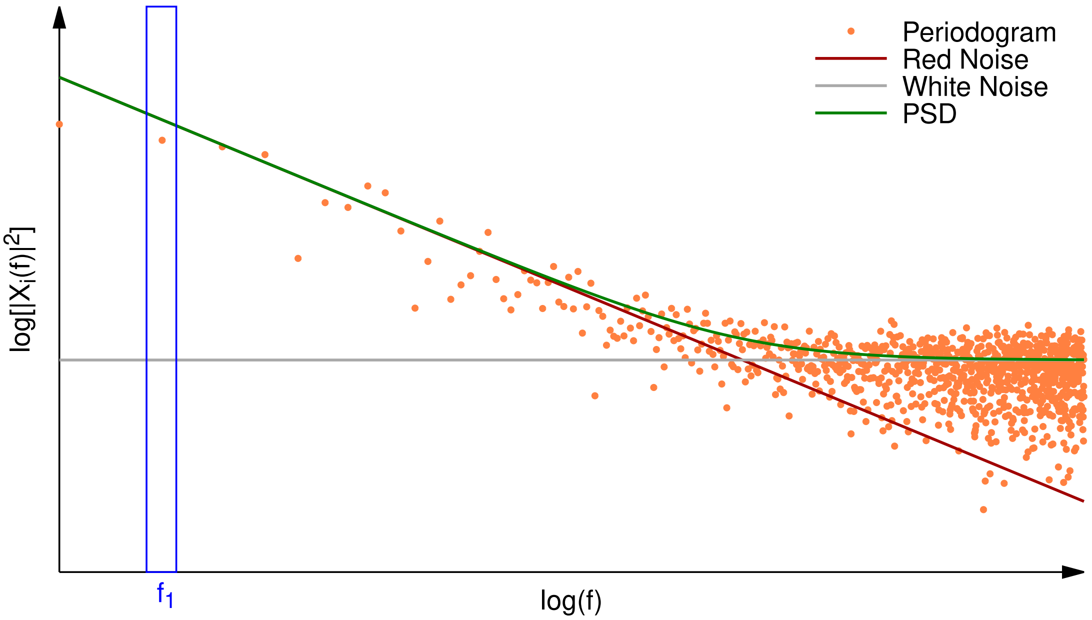

Figure 6.4: Periodogram of x (white noise plus red noise). The PSD is the expectation of the periodogram.

where $\Re[\cdot]$, $\Im[\cdot]$ respectively denote the real and imaginary part of the quantity within the brackets. Furthermore throughout this manuscript the prime and double prime symbols respectively denote the real and imaginary part of the variable placed before. Then thanks to energy equipartition it follows,

$$\begin{aligned} \mathbb{V}[W_i] &= 2\mathbb{V}[W_i'] = 2\mathbb{V}[W_i''] = \sigma_{W,i}^2 \\ \mathbb{V}[R] &= 2\mathbb{V}[R'] \;\; = 2\mathbb{V}[R''] \;\; = \sigma_R^2 \end{aligned} \tag{6.5}$$

where $\mathbb{V}[\cdot]$ denote the variance of the quantity within the brackets.

We simulate two independent white noise sequences $w_1(t)$ and $w_2(t)$ by generating Gaussian processes and a red noise sequence $r(t)$ by integrating a white noise. After computing the Fast Fourier Transform (FFT) on these processes, it turns out that the variances of the real and imaginary part of the red noise are not equal. Figure 6.5 highlights the ratio of the variance of the imaginary part over the real part of the spectrum. The red and orange curves correspond to the two white noise sequences and the blue curve to the red noise sequence. The white noise processes show as expected no important variation whereas regarding the red noise, the ratio is equal to three for the lowest frequency f_{min} and $1/3$ for the highest frequency f_{max} of the sequence. This artefact complicates the problem insofar as the real and imaginary part of the red noise are no longer Independent and Identically Distributed (IID) random variables. Let us give more details about this artifact in the next chapter.

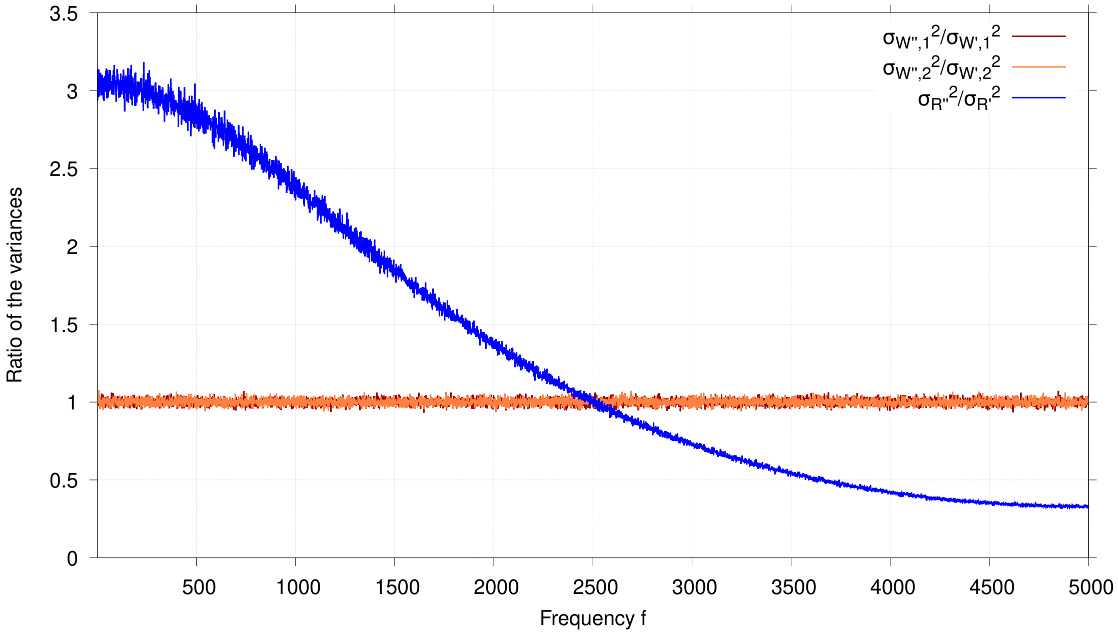

Figure 6.5: Ratio of variance of the imaginary part over the real part of the spectrum.

CHAPTER 7

Red noise simulation artifact

In this chapter we will present how to simulate a process of white noise and red noise by integrating a white temporal sequence. Thus we will explain the dissymmetry introduced between the real and imaginary parts of the variance of such a red noise process.

7.1 Simulation of a realistic white noise

In this section we describe how to simulate a realistic white noise. Let y_k, with $k \in \{1, \dots, N\}$, be a random variable following a $\mathrm{LG}(0, \sigma)$[1], i.e. a Laplace-Gauss distribution with mathematical expectation zero and standard deviation σ. From this time series, we introduce a continuous function $y(t)$ in such a way that

$$y_k = \frac{1}{\tau_0} \int_{t_k - \tau_0}^{t_k} y(\theta) \mathrm{d}\theta \quad \text{with} \quad t_k = k\tau_0 \tag{7.1}$$

where k is an integer and τ_0 the sampling period. Denoting $R_y(t)$ the autocorrelation function of the process $y(t)$, we assume that

$$\begin{cases} R_y(t) = 0 & \text{if} \quad t \geq \tau_0 \\ R_y(t) > 0 & \text{if} \quad t < \varepsilon \quad \text{with} \quad 0 < \varepsilon \ll \tau_0 \end{cases} \tag{7.2}$$

---

[1] In part II, the Laplace-Gauss distribution was defined by $\mathrm{LG}(0, \sigma^2)$

This chapter is the result of close collaboration with François Vernotte.

in such a way that $y(t)$ is continuous for short term ($t < \varepsilon$). Thanks to the assumption given on $R_y(t)$ in Equation 7.2, we will consider that the Fourier transform $Y(f)$ of $y(t)$ exists. The PSD, considered to be "2-sided" according to Equation 6.3 of $y(t)$, $S_y(f)$, verifies the following properties:

$$\begin{cases} S_y(f) = h_0 = \sigma^2 \tau_0 \quad \text{if} \quad 0 \leq f \leq \dfrac{1}{\tau_0} \\ \lim\limits_{f \to \infty} S_y(f) = 0 \end{cases} \tag{7.3}$$

where the constant value h_0 stands for the white noise level. From these properties, we can deduce than, for $0 \leq f \leq 1/\tau_0$:

$$\mathbb{E}\left[\Re[Y(f)]\right] = \mathbb{E}\left[\Im[Y(f)]\right] = 0 \qquad \Rightarrow \quad \mathbb{E}\left[|Y(f)|\right] = 0 \tag{7.4a}$$

$$\mathbb{V}\left[\Re[Y(f)]\right] = \mathbb{V}\left[\Im[Y(f)]\right] = N\tau_0 h_0/2 \quad \Rightarrow \quad \mathbb{V}\left[|Y(f)|\right] = N\tau_0 h_0 \tag{7.4b}$$

where $\mathbb{E}[\cdot]$ stand for the mathematical expectation of the quantity in the brackets and $|z|$ stand for the modulus of a complex number z. Equation 7.4b must be understood as ensemble statistics over an infinite number of realizations of the same LG process. Moreover, this yields an interesting alternative definition of the PSD since

$$S_y(f) = \frac{\mathbb{V}\left[|Y(f)|\right]}{N\tau_0}. \tag{7.5}$$

The denominator $N\tau_0$ is due to the normalization of the PSD by the duration in order to have the dimension of power and not energy. This normalization is essential to ensure the convergence for signal of finite power and infinite energy [145].

7.2 Red noise simulation

7.2.1 Raw red noise

We can easily simulate a red noise, i.e. with a PSD following a f^{-2} power law, from the time series $\{y_k\}$

$$x_k = \tau_0 \sum_{i=1}^{k} y_i \quad \text{with} \quad k \in \{1, \ldots, N\}. \tag{7.6}$$

Here also, we can introduce a continuous function $x(t)$

$$x(t) = \int_0^t y(\theta) \mathrm{d}\theta. \tag{7.7}$$

The time series $\{x_k\}$ may be rewritten as

$$x_k = \int_0^{t_k} y(\theta)\mathrm{d}\theta = \tau_0 \sum_{i=1}^{k} \frac{1}{\tau_0} \int_{t_i-\tau_0}^{t_i} y(\theta)\mathrm{d}\theta = \tau_0 \sum_{i=1}^{k} y_i \tag{7.8}$$

with $t_i = i\tau_0$.

7.2.2 Pure red noise and "fake drift"

Let us define $\bar{y}$ as the mean of the $\{y_k\}$ time series:

$$\bar{y} = \frac{1}{N} \sum_{k=1}^{N} y_k. \tag{7.9}$$

Since each y_k is a r.v. following a $\mathrm{LG}(0,\sigma)$ distribution, $\bar{y}$ is a $\mathrm{LG}(0,\sigma/\sqrt{N})$ r.v. Therefore, $\bar{y} \neq 0$ and acts as a continuous background. In the integration of the time series $\{y_k\}$ to generate the time series $\{x_k\}$, this continuous background will be transformed into a drift of slope $\bar{y}$. We will call it "fake" drift because it is purely random and not the result of deterministic effects (for further details about fake or false drift, see [146]). We will then define the raw red noise as the red noise including this drift, i.e. the time series $\{x_k\}$, and the pure red noise $\{x_{Pk}\}$ as

$$x_{Pk} = x_k - k\tau_0\bar{y} = x_k - \bar{y}t_k. \tag{7.10}$$

Figure 7.1 shows an example of realization of such a time series. Obviously, the raw red noise is a realistic time series although the pure red noise is nothing but a theoretical concept. It will be helpful however to explore the properties of red noises defined by PSD modelized as power laws.

In the same way as $\{x_{Pk}\}$, we can define the time series $\{y_{Pk}\}$ by $y_{Pk} = y_k - \bar{y}$ and its extension as $y_P(t) = y(t) - \bar{y}$. Let $Y_P(f)$ be the Fourier transform of $y_P(t)$. Since the removal of the mean value only affects the null frequency, we know that

$$\begin{cases} Y_P(0) = 0 \\ Y_P(f) = Y(f) \quad \text{if} \quad f \neq 0. \end{cases} \tag{7.11}$$

The continuous extension $\{x_{Pk}\}$ may be written as

$$x_P(t) = \int_0^{t} y_P(\theta)\mathrm{d}\theta = \int_{-\infty}^{t} y_P(\theta)\mathrm{d}\theta - x_P(0). \tag{7.12}$$

Let us assume that $X_P(f)$, its Fourier transform, exists. Thanks to the properties of the

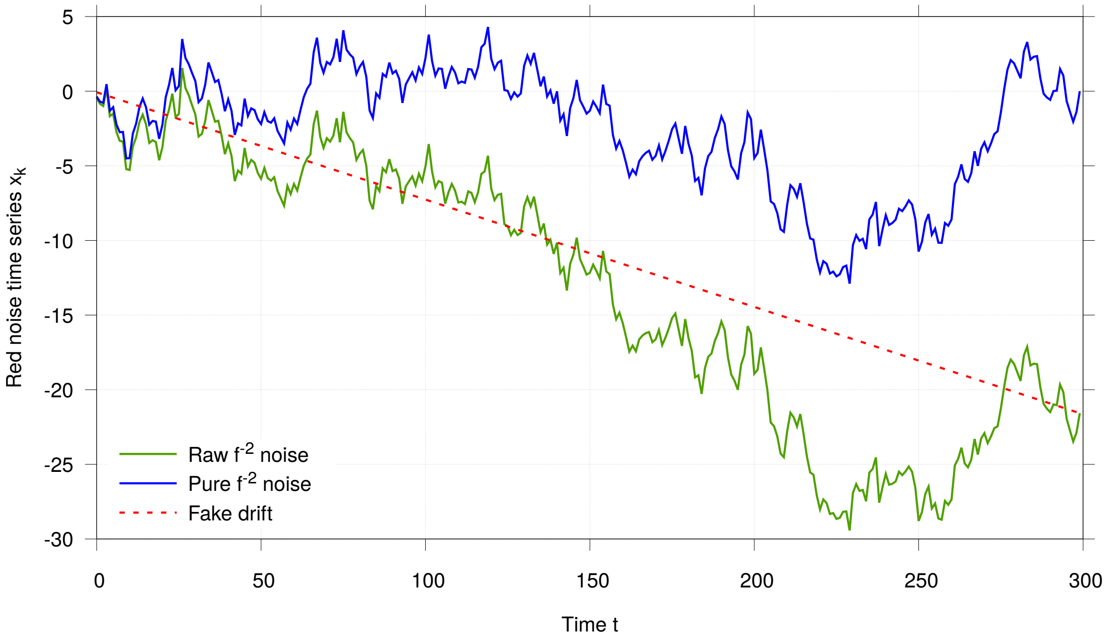

Figure 7.1: Raw red noise (green), pure red noise (blue) and drift induced by the mean value of one realization of a $\{y_k\}$ time series (red dashed line). The X-axis units as well as the Y-axis units are arbitrary.

Fourier transform applied to Equation 7.12, it comes

$$X_P(f) = \frac{1}{j2\pi f} Y_P(f). \tag{7.13}$$

Therefore, its statistical properties are, for $0 \leq f \leq 1/\tau_0$:

$$\begin{cases} \mathbb{E}\left[\Re[X_P(f)]\right] = \mathbb{E}\left[\Im[X_P(f)]\right] = 0 & \Rightarrow \quad \mathbb{E}\left[|X_P(f)|\right] = 0 \\ \mathbb{V}\left[\Re[X_P(f)]\right] = \mathbb{V}\left[\Im[X_P(f)]\right] = \dfrac{N\tau_0 h_0}{8\pi^2 f^2} & \Rightarrow \quad \mathbb{V}\left[|X_P(f)|\right] = \dfrac{N\tau_0 h_0}{4\pi^2 f^2} = N\tau_0 S_{XP}(f) \end{cases} \tag{7.14}$$

where $S_{XP}(f) = \frac{h_0}{4\pi^2 f^2}$ is the PSD of $X_P(f)$. It may be noticed that, if we assume that $y(t)$ is a frequency, $x(t)$ is a phase and the mean removal in $y_P(t)$ is a syntonization process. In the same way, if we would set x_0 to 0, it would be a synchronization process but we will not consider this setting.

7.2.3 Spectral aliasing effect

Let us define $x_{Ps}(t)$ as the sampling of $x_P(t)$:

$$x_{Ps} = x_P(t) \cdot \text{III}\left(\frac{t}{\tau_0}\right) \tag{7.15}$$

where $Ш\left(x\right)$ stands for a Dirac comb defined by

$$Ш\left(x\right) \equiv \sum_{n=-\infty}^{+\infty} \delta(x-n), \tag{7.16}$$

with $\delta(x)$ the Dirac distribution of the variable $x \in \mathbb{R}$; so $Ш\left(x\right) = 0$ for $x \notin \mathbb{Z}$ (i.e., x is not an integer). In this section, we will not study the windowing effect. The Fourier transform of $x_{Ps}(t)$ is:

$$X_{Ps}(f) = X_P(f) * \left[\tau_0 \cdot Ш\left(\tau_0 f\right)\right]. \tag{7.17}$$

Its PSD is then

$$\begin{aligned} S_{XPs}(f) &= \tau_0^2 \left| \int_{-\infty}^{+\infty} X_P(\nu) \cdot \sum_{n=-\infty}^{+\infty} \delta\left[\tau_0\left(f-\nu\right)-n\right] \mathrm{d}\nu \right|^2 \\ &= \tau_0^2 \left| \sum_{n=-\infty}^{+\infty} \int_{-\infty}^{+\infty} X_P(\nu)\delta\left[\tau_0\left(f-\nu\right)-n\right] \mathrm{d}\nu \right|^2 \\ &= \left| \sum_{n=-\infty}^{+\infty} X_P\left(f-\frac{n}{\tau_0}\right)\right|^2 = \sum_{m=-\infty}^{+\infty} \sum_{n=-\infty}^{+\infty} X_P\left(f-\frac{m}{\tau_0}\right) \cdot \overline{X_P\left(f-\frac{n}{\tau_0}\right)} \end{aligned} \tag{7.18}$$

where $\bar{\cdot}$ stands for the complex conjugate of the quantity which is below. Since $x_p(t)$ is a noise, its Fourier Transform is also a noise and the amplitudes separated by at least $1/\tau_0$, i.e $|n-m| \geq 1$, are uncorrelated [2]

$$\mathbb{E}\left[X_P\left(f-\frac{m}{\tau_0}\right) \cdot \overline{X_P\left(f-\frac{n}{\tau_0}\right)}\right] = 0 \quad \text{if} \quad m \neq n. \tag{7.19}$$

Moreover, the products $X_P\left(f-\frac{m}{\tau_0}\right) \cdot \overline{X_P\left(f-\frac{n}{\tau_0}\right)}$ may be positive or negative if $m \neq n$ whereas they are necessarily positive if $m = n$. Therefore, the sum of the products with $m \neq n$ may be neglected and we keep only the products with $m = n$

$$S_{XPs}(f) = \sum_{n=-\infty}^{+\infty} \left|X_P\left(f-\frac{n}{\tau_0}\right)\right|^2 = \sum_{n=-\infty}^{+\infty} S_{XP}\left(f-\frac{n}{\tau_0}\right). \tag{7.20}$$

Finally, we get

---

[2] This property is obvious if $x_P(t)$ has a finite support bounded by $\left[\frac{-1}{2\tau_0}, \frac{+1}{2\tau_0}\right]$, i.e. if it is sampled acoordingly with the Nyquist-Shannon sampling theorem.

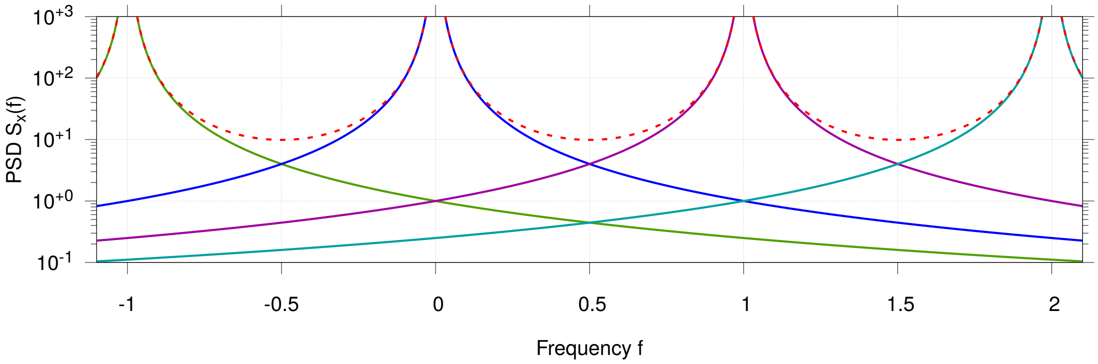

Figure 7.2: Spectral aliasing caused by sampling. The dashed red line is the infinite sum of all hyperbolas in accordance with Equation 7.23. The X-axis units are the frequency divided by the sampling period τ_0 and are then dimensionless. The Y-axis units are arbitrary.

$$S_{XPs}(f) = S_{XP}(f) * \left[\tau_0^2 \cdot \text{Ш}\left(\tau_0 f\right)\right] = \sum_{n=-\infty}^{+\infty} \frac{h_0 \tau_0^2}{4\pi^2(\tau_0 f + n)^2}. \tag{7.21}$$

Therefore, this convolution product with a Dirac comb means that the shape of $X_P(f)$ will be infinitely duplicated on each multiple of $1/\tau_0$ (see Figure 7.2). However, thanks to the following equality [147, Equation 9.47, p. 281]

$$\sum_{n=-\infty}^{+\infty} \frac{1}{(a+n)^2} = \frac{\pi^2}{\sin^2(\pi a)} \tag{7.22}$$

we know that the infinite sum of Equation 7.21 converges and can be rewritten as

$$S_{XPs}(f) = \frac{h_0 \tau_0^2}{4\sin^2(\pi\tau_0 f)}. \tag{7.23}$$

As for $X_P(f)$, the real and imaginary parts of $X_{Ps}(f)$ follow the same statistics and their variances are then equal to

$$\mathbb{V}\left[\Re[X_{Ps}(f)]\right] = \mathbb{V}\left[\Im[X_{Ps}(f)]\right] = \frac{N\tau_0^3 h_0}{8\sin^2(\pi\tau_0 f)}. \tag{7.24}$$

Thus, even in the case of a f^{-2} noise, the sampling process produces a slight but significant spectral aliasing (see Figure 7.3).

7.2.4 Fake drift effect

According to the definition of the pure red noise in Equation 7.10, the fake drift $d(t)$ is nothing but the difference between the raw red noise and the pure red noise:

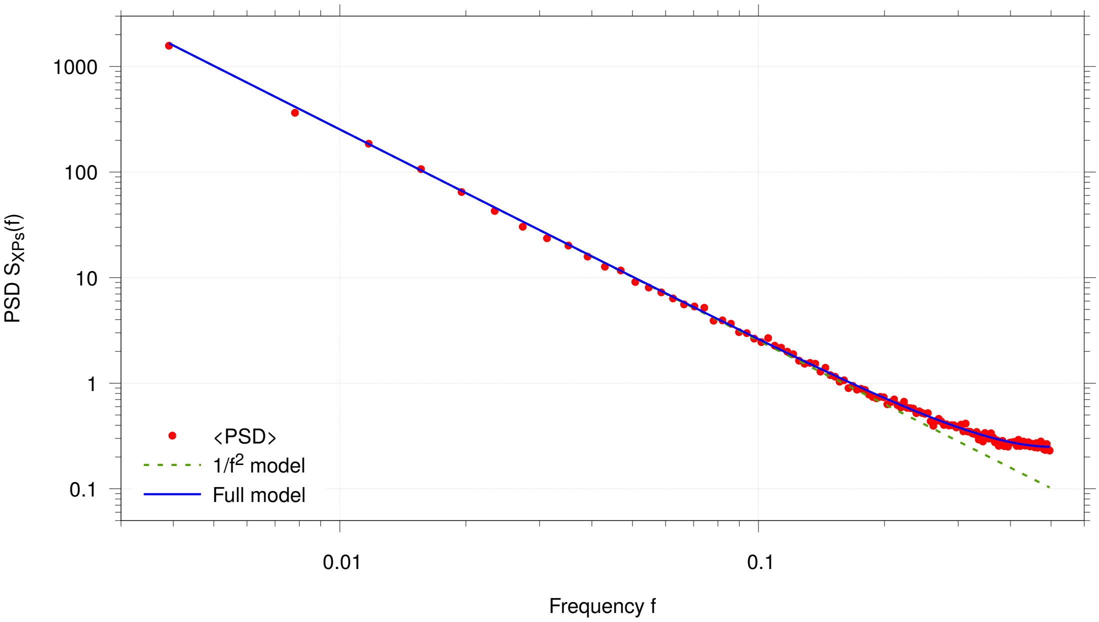

Figure 7.3: PSD of a pure red noise. The simulated PSD (red dots) was obtained from 300 realizations of a pure red noise sequence of 256 samples. The $1/f^2$ asymptote is the dashed green line and the model of Equation 7.23 is the blue line. The spectral aliasing effect induces a discrepancy beween the PSD and the $1/f^2$ asymptote, visible for $f > 0.2$. The X-axis units are the frequency divided by the sampling period τ_0 and the Y-axis units are arbitrary.

$$d(t) = x(t) - x_P(t) = \alpha t \tag{7.25}$$

with α is the slope of the drift. As stated in Section 7.2.2, for a given $\{y_k\}$ realization which generates the corresponding $\{x_k\}$ realization, this slope is $\alpha = \bar{y}$, where $\bar{y}$ is the mean of the $\{y_k\}$ time series. But we must keep in mind that, considering the ensemble of all possible realizations (see Figure 7.4), $\bar{y}$ is a LG$(0, \sigma/\sqrt{N})$ distribution. Then, since $\sigma^2 = h_0/\tau_0$, α is a LG r.v. with the following statistics parameters:

$$\mathbb{E}[\alpha] = 0, \quad \mathbb{V}[\alpha] = \frac{h_0}{N\tau_0}. \tag{7.26}$$

In order to take into account the effect of the fake drift in the spectrum of the raw red noise, let us calculate the Fourier transform of the following time series:

$$d(t_k) = \alpha t_k \quad \text{with} \quad k \in \{1, \dots, N\}\,. \tag{7.27}$$

This can be rewritten as a continuous function

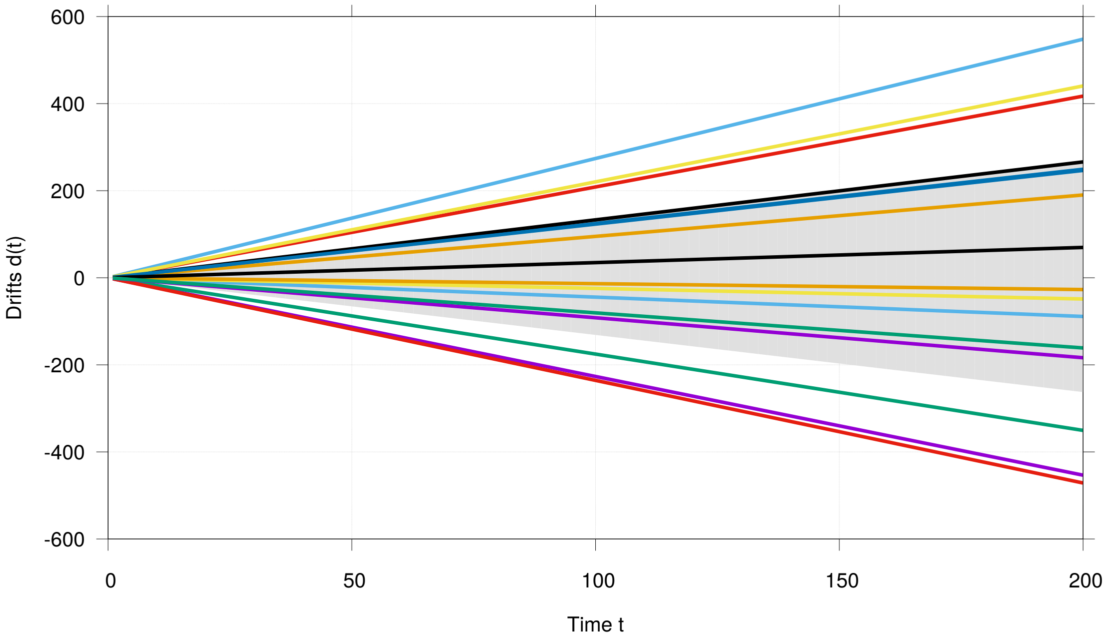

Figure 7.4: Realizations of fake drifts $d(t)$ corresponding to 16 realizations of $\{x_k\}$ times series with the same statistics parameters. In the grey area, the line slopes are within $\pm\sigma_\alpha$ the standard deviation of the r.v. α. The X-axis units as well as the Y-axis units are arbitrary.

$$d(t) = \left\{ \left[(\alpha t)_{(0<t<N\tau_0)} \right] \cdot \text{III}\left(\frac{t}{\tau_0}\right) - \frac{\alpha N \tau_0}{2} \delta\left(\frac{t}{\tau_0}\right) \right\} * \left\{ \frac{1}{N\tau_0} \text{III}\left(\frac{t}{N\tau_0}\right) \right\} \tag{7.28}$$

where the direct product with $\text{III}\left(\frac{t}{\tau_0}\right)$ accounts for the time sampling and the convolution product with $\frac{1}{N\tau_0}\text{III}\left(\frac{t}{N\tau_0}\right)$ accounts for the implicit assumption of the data-run periodicity imposed by the discrete Fourier transform algorithm. This periodicity induces a discontinuity: at the beginning as well as at the end of the ramp, $d(t)$ equals $\alpha N\tau_0$ as well as 0 which leads to the mean value $\frac{\alpha N\tau_0}{2}\delta\left(\frac{t}{\tau_0}\right)$. The correction $-\frac{\alpha N\tau_0}{2}\delta\left(\frac{t}{\tau_0}\right)$, which is applied after sampling, forces $d(0) = 0$.

Let us first calculate $D_c(f)$, the Fourier transform of the continuous ramp $d_c(t) = (\alpha t)_{(0<t<N\tau_0)}$

$$D_c(f) = \alpha \int_0^{N\tau_0} t e^{-j2\pi f t} \mathrm{d}t \tag{7.29}$$

which can be easily solved by using an integration by parts

$$D_c(f) = j\frac{\alpha N\tau_0}{2\pi f} e^{-j2\pi N\tau_0 f} + \frac{\alpha e^{-j2\pi N\tau_0 f}}{4\pi^2 f^2} - \frac{\alpha}{4\pi^2 f^2}. \tag{7.30}$$

Let us now consider the effect of the time sampling. Let $d_s(t)$ be the sampled version of $d_c(t)$:

$$d_s(t) = d_c(t) \cdot \text{Ш}\left(\frac{t}{\tau_0}\right). \tag{7.31}$$

Its Fourier transform is $D_s(f) = D_c(f) * [\tau_0 \cdot \text{Ш}\,(\tau_0 f)]$

$$D_s(f) = \sum_{n=-\infty}^{+\infty} \left[j\frac{\alpha N \tau_0^2}{2\pi(\tau_0 f - n)} e^{-j2\pi N(\tau_0 f - n)} + \frac{\alpha \tau_0^2 e^{-j2\pi N(\tau_0 f - n)}}{4\pi^2(\tau_0 f - n)^2} - \frac{\alpha \tau_0^2}{4\pi^2(\tau_0 f - n)^2} \right]. \tag{7.32}$$

Since $n, N \in \mathbb{Z}$ and $e^{j2\pi Nn} = 1$

$$D_s(f) = j\frac{N\tau_0^2 e^{-j2\pi N\tau_0 f}}{2\pi} \sum_{n=-\infty}^{+\infty} \frac{1}{\tau_0 f - n} + \frac{\tau_0^2 e^{-j2\pi N\tau_0 f}}{4\pi^2} \sum_{n=-\infty}^{+\infty} \frac{1}{(\tau_0 f - n)^2} - \frac{\tau_0^2}{4\pi^2} \sum_{n=-\infty}^{+\infty} \frac{1}{(\tau_0 f - n)^2}. \tag{7.33}$$

The expressions in the sums can be simplified since [148, Equation 1.41, p. 33]

$$\frac{\pi}{\tan(\pi z)} = \sum_{k=-\infty}^{\infty} \frac{1}{z-k}. \tag{7.34}$$

Thus, from this relationship and [147, Equation 9.47, p. 281], it comes

$$D_s(f) = j\frac{\alpha N \tau_0^2 e^{-j2\pi N\tau_0 f}}{2\tan(\pi\tau_0 f)} + \frac{\alpha\tau_0^2}{4\sin^2(\pi\tau_0 f)} \left[e^{-j2\pi N\tau_0 f} - 1\right]. \tag{7.35}$$

The whole sampled function includes also the end-beginning discontinuity

$$d_d(t) = d_s(t) - \frac{\alpha N \tau_0}{2} \delta\left(\frac{t}{\tau_0}\right) \tag{7.36}$$

whose Fourier transform is

$$D_d(f) = D_s(f) - \frac{\alpha N \tau_0^2}{2}. \tag{7.37}$$

Finally, let us take into account the time data-run periodicity assumption. Since $d(t) = d_d(t) * \left\{\frac{1}{N\tau_0}\text{Ш}\left(\frac{t}{N\tau_0}\right)\right\}$, its Fourier transform $D(f) = D_d(f) \cdot \text{Ш}\,(N\tau_0 f)$

$$D(f_k) = j\frac{\alpha N \tau_0^2 e^{-j2\pi k}}{2\tan(\pi k/N)} + \frac{\alpha\tau_0^2}{4\sin^2(\pi k/N)} \left[e^{-j2\pi k} - 1\right] - \frac{\alpha N \tau_0^2}{2} \tag{7.38}$$

with $f_k = k\tau_0$. Taking into account that $k \in \mathbb{Z}$ and then $e^{-j2\pi k} = 1$, we obtain the final expression of $D(f)$:

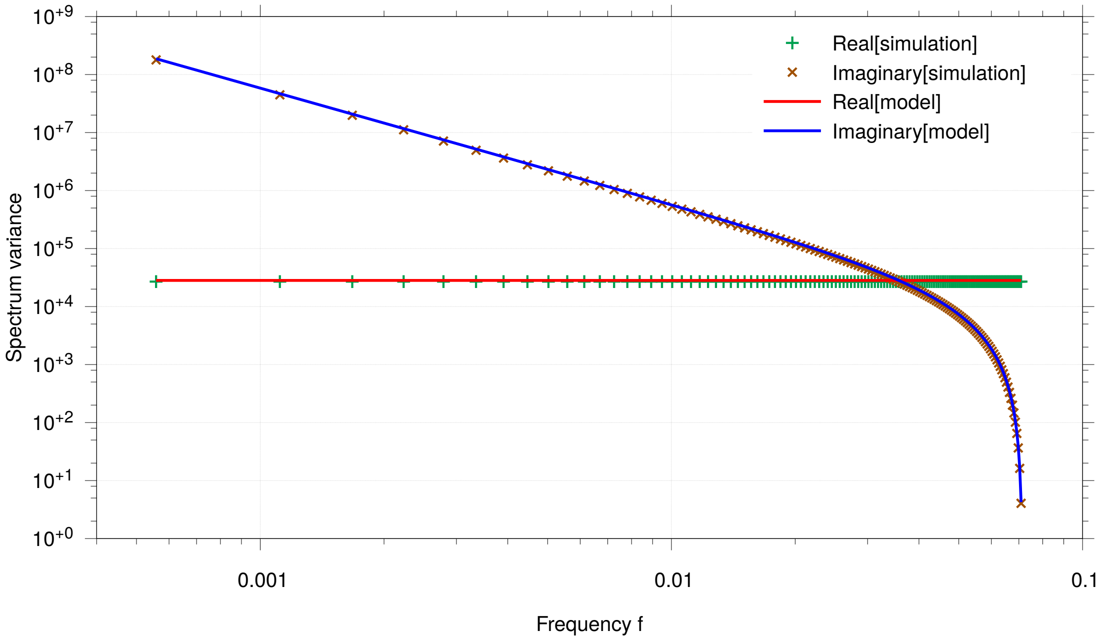

Figure 7.5: Variance of the spectra of 300 drift realizations (crosses) and theoretical model of Equation 7.40 (solid lines). The X-axis units are the frequency divided by the sampling period τ_0 and the Y-axis units are arbitrary.

$$\begin{cases} D(f) = -\frac{\alpha N \tau_0^2}{2} + j\frac{\alpha N \tau_0^2}{2\tan(\pi k/N)} & \text{if} \quad f = f_k = \frac{k}{N\tau_0} \\ D(f) = 0 & \text{if} \quad f \neq f_k. \end{cases} \tag{7.39}$$

Therefore, in the case of a raw red noise, this drift signature will be added to the pure red noise signal inducing a dissymmetry between real and imaginary parts.

7.2.5 Raw red noise spectrum

In the case of a raw red noise, i.e. a time series simulated by using Equation 7.6, we will have to take into account the spectral aliasing effect as well as the adding of the fake drift.

Equation 7.39 gives the Fourier transform of a single drift of slope α. We must now deduce from this the statistical behavior of the fake drifts of an ensemble of raw noises. As already stated in Sections 7.2.2 and 7.2.4, the slope of the fake drift of one realization of a raw red noise is a centered Gaussian r.v of variance $\frac{h_0}{N\tau_0}$. The ensemble statistics of the fake drifts are then:

$$\begin{cases} \mathbb{E}\left[\Re[D(f)]\right] = \mathbb{E}\left[\Im[D(f)]\right] = 0 \\ \mathbb{V}\left[\Re[D(f)]\right] = \dfrac{N\tau_0^3 h_0}{4}, \qquad \mathbb{V}\left[\Im[D(f)]\right] = \dfrac{N\tau_0^3 h_0 \cos^2(\pi\tau_0 f)}{4\sin^2(\pi\tau_0 f)}. \end{cases} \tag{7.40}$$

Figure 7.5 shows the behavior of both real and imaginary part of $D(f)$.

Therefore, since a pure red noise realization is not correlated with the corresponding fake drift[3], the mathematical expectation and variance of the spectrum of a raw red noise are the sum the ones of the spectrum of the corresponding pure red noise plus the ones of the spectrum of the corresponding fake drift. Thus, for $0 \leq f \leq 1/\tau_0$:

$$\begin{cases} \mathbb{E}\left[\Re[X(f)]\right] = \mathbb{E}\left[\Im[X(f)]\right] = 0 \\ \mathbb{V}\left[\Re[X(f)]\right] = \dfrac{N\tau_0^3 h_0}{8\sin^2(\pi\tau_0 f)} + \dfrac{N\tau_0^3 h_0}{4}, \quad \mathbb{V}\left[\Im[X(f)]\right] = \dfrac{N\tau_0^3 h_0}{8\sin^2(\pi\tau_0 f)} + \dfrac{N\tau_0^3 h_0 \cos^2(\pi\tau_0 f)}{4\sin^2(\pi\tau_0 f)}. \end{cases} \tag{7.41}$$

It can be observed that the ratio $\mathbb{V}\left[\Im[X(f)]\right]/\mathbb{V}\left[\Re[X(f)]\right]$ ranges from three at $f = 0$ to $1/3$ at $f = \frac{1}{2\tau_0}$ (see Figure 7.6-B).

7.3 Discussion

The simulation of a red noise by integration of a white time series induces spectral aliasing as well as a fake drift which modifies the shape of the spectrum, especially in rising its slope for high frequencies and in introducing a dissymmetry between its real and imaginary parts (see Figure 7.6-A).

It is very easy to remove the fake drift of the red noise by removing the mean value of the white time series but is it a good practice? In the true life, would not a real red noise be the result of an integration process of a white noise? If yes, a raw red noise would definitely be more realistic than a pure red noise.

---

[3] On the other hand, a raw red noise realization is correlated with its fake drift.

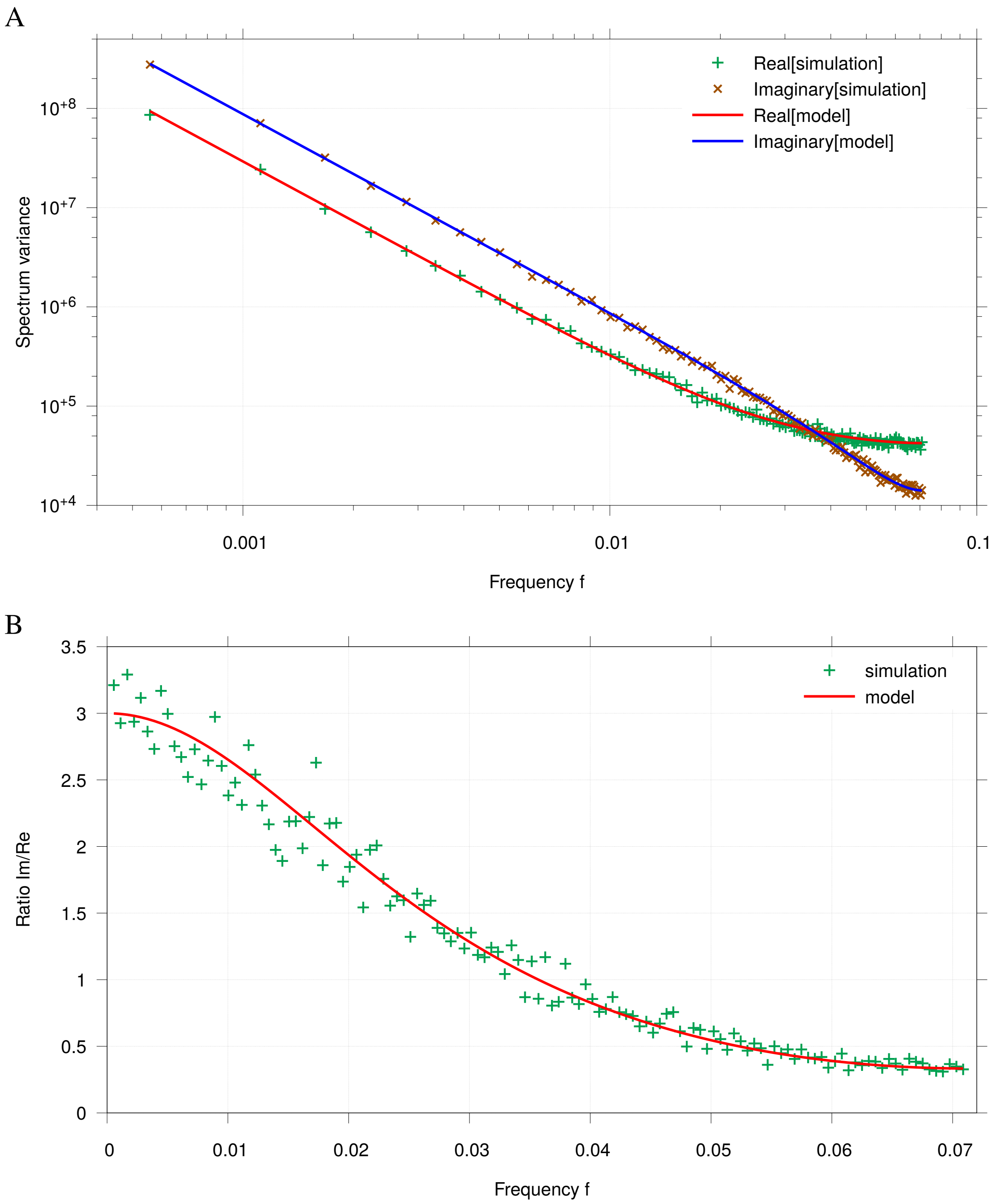

Figure 7.6: A (top) – Variance of the spectra of 300 raw red noise realizations (crosses) and theoretical model of Equation 7.41 (solid lines). The X-axis units are the frequency divided by the sampling period τ_0 and the Y-axis units are arbitrary. B (bottom) – Ratio imaginary part/real part of the variance of the red noise spectrum above. The crosses are the ratio calculated from the variance of the 300 realizations and the solid line is the ratio of the theoretical model. The X-axis units are the frequency divided by the sampling period τ_0.

CHAPTER 8

Spectrum Decorrelation

This chapter presents a very simple method ensuring the independence of consecutive spectra of the phase or frequency noise of an oscillator. This condition is essential for using cross-spectrum averages.

The best improvement provided by the cross-spectrum method [59] arises from the average of consecutive cross-spectra. Such average relies on the decorrelation of the cross-spectra. Are the cross-spectra really uncorrelated? More generally, are not several consecutive spectra of the same process correlated?

8.1 Theoretical approach

8.1.1 The Fourier transform of a white noise is a white noise

First of all, let us remind that the Fourier transform of a white noise is a white noise [149]. To be convinced, we may recall that the Fourier transformation is an orthogonal transformation which preserves the non-correlation of the data. Therefore, the periodogram of a white noise, i.e. the square of the modulus of its Fourier transform divided by the number

This chapter is the result of close collaboration with François Vernotte.

of samples, is a sequence of χ^2 random variables with two degrees of freedom: they are always positive and fluctuate around the white noise level but they remain fundamentally random. Only the PSD of a white noise is supposed to be a constant deterministic function since it is defined as a mathematical expectation. For this very reason, the PSD is an ideal mathematical quantity which can be only estimated (e.g. by an average of periodograms).

8.1.2 Filtering a white noise preserves the non correlation of the Fourier components

A colored noise is generally considered as a filtered white noise. For instance, filtering a white noise with a transfer function $\propto 1/f$ yields a random walk, i.e. a noise characterized by a f^{-2} PSD. Since filtering is nothing but a product by a deterministic function in the Fourier domain, such a process modulates the initial white spectrum but does not introduce any correlation between the data of the random part of the spectrum. For example, the red noise of Figure 6.2 may be obtained by filtering a white noise. Thus, we retrieve in its Fourier transform (see Figure 6.3) the uncorrelated complex r.v. of the white noise Fourier transform modulated by an envelope which is the transfer function of the filter.

Therefore, the amplitudes of the spectrum of a pure colored noise are uncorrelated. Likewise, by extension, the random part of the spectra of two consecutive sequences of a pure colored noise are also uncorrelated.

8.1.3 The residual mean of a sequence induces a drift after integration

Let us consider a finite time series composed of N uncorrelated centered Gaussian r.v. z_k ($k \in \{1, N\}$), i.e. a white noise, with a standard deviation σ. According to the discussion in Section 7.2.2, the mathematical expectation of each r.v. is null whereas the arithmetic mean of the time series is not: it is a centered r.v. with a standard deviation $\sigma_0 = \sigma/\sqrt{N}$

$$z_0 = \frac{1}{N}\sum_{k=1}^{N} z_k = \mathrm{LG}(0, \sigma_0) \qquad \text{with} \qquad \sigma_0 = \frac{\sigma}{\sqrt{N}}. \tag{8.1}$$

If this white noise occurs in an integrator process of an oscillator, this constant z_0 will induce a linear drift of slope z_0. Considering a sampling time τ_0, the following “fake drift” will be added to the integrated time series: $d_k = z_0 k \tau_0$. Admittedly the mathematical expectation of the slope z_0 decreases as $1/\sqrt{N}$, but its influence over the whole sequence increases as N: at the end of the time series, the mathematical expectation of the drift reaches

$$\mathbb{E}[d_N] = \frac{\sigma}{\sqrt{N}} N\tau_0 = \sigma\sqrt{N}\tau_0. \tag{8.2}$$

Therefore, the influence of the fake drift increases as the square root of the number of elements in the time series. For large N, this can even overwhelm the random behavior of the integrated time series.

8.1.4 Only deterministic behaviors induce correlations

Now, let us come back to the main issue of this chapter: are the cross-spectra of consecutive time series uncorrelated? From Section 8.1.2, we can answer that the random part of these cross-spectra are uncorrelated. On the other hand, if the filtering corresponds to an integration (transfer function $\propto 1/f$ or $1/f^n$ for n^{th} order integration), a fake drift will appear as described in Section 8.1.3. This drift will add a deterministic component in the spectrum as described in Chapter 7 which will induce strong correlations between the frequency data as well as between the spectra of consecutive time series. Throughout this chapter, “consecutive time series” means consecutive subdivisions of the whole time series.

Therefore, such an effect completely prohibits the use of consecutive cross-spectra if a drift, fake or real, spans several consecutive time series.

8.1.5 Syntonizing: a simple but effective way to decorrelate spectra

Nevertheless, the remedy for this major failure is quite obvious: we just have to break the correlations between spectra of consecutive time series by removing the linear drift of each consecutive time series or, and this is perfectly equivalent, by forcing the mean of each consecutive time series to zero before integration.

But, since we are only interested in the decorrelation of the spectra of consecutive time series and not in the decorrelation of the frequency data within a spectrum, a simpler way exists: it suffices to force the first data of each time series to zero before integration. In this case, there will still be a residual drift in each time series after integration but all these residual drifts will be uncorrelated from one spectrum to another. If we consider that the final time series corresponds to phase-time data, this means that the initial time series before integration are frequency deviation data. This forcing at zero corresponds therefore to a syntonization process at the beginning of each consecutive time series.

8.2 Monte-Carlo approach

We will first simulate the case of a Random Walk FM noise (f^{-2} frequency noise $\equiv f^{-4}$ phase noise) and then extend to other types of noises.

8.2.1 Red noise simulation

In order to simulate a f^{-4} red noise, we will integrate twice a white noise. Let us define the aging $z(t)$ as a Laplace-Gauss r.v. of mathematical expectation zero and of standard deviation 1: $z(t_k) = \mathrm{LG}(0,1)$ with $k \in \{1,\ldots,N\}$ and $t_{k+1} - t_k = \tau_0$, the sampling time. For the sake of simplification, we set $\tau_0 = 1$ s and we denote $z_k = z(t_k)$. The top graph of Figure 8.1 represents a sequence of 512 consecutive realizations of such a r.v..

Although $z(t)$ is discontinuous at the scale given by τ_0, let us assume that $z(t)$ is smooth and continuous for very short term, i.e. at a scale $\varepsilon \ll \tau_0$ (e.g. $z(t)$ could be a first order Markov process with a time constant ε [144]). Thanks to this assumption, this process has a finite power and its Fourier transform $Z(f)$ exists.

Since aging is defined as the time derivative of the frequency deviation $y(t)$, $z_k = \frac{y(t_k+\tau_0)-y(t_k)}{\tau_0}$, we can compute the mean frequency deviation between t_{k-1} and t_k, that we denote $\bar{y}_k = \frac{1}{\tau_0}\int_{t_{k-1}}^{t_k} y(t)\mathrm{d}t$, as the cumulative sum of the aging samples z_k from the beginning of the sequence:

$$\bar{y}_k = \bar{y}_{k-1} + z_k\tau_0 = \tau_0 \sum_{j=1}^{k} z_j. \tag{8.3}$$

The left hand graph in the middle of Figure 8.1 represents the corresponding 512 frequency deviation samples.

Similarly, we can deduce the phase-time data by integrating the frequency deviation data-run:

$$x(t_k) = \int_0^{t_k} y(t)dt = \tau_0 \sum_{j=1}^{k} \bar{y}_j. \tag{8.4}$$

The result of this process is plotted on the left hand graph at the bottom of Figure 8.1.

As stated in Section 8.1.3, the slight residual mean of the aging sequence induces a linear drift in the frequency deviation sequence which induces a quadratic drift in the phase-time sequence. The 512 data sequence are divided in four subsequences of 128 data (see blue, red, green and purple dots in Figure 8.1). It is clear that this effect, and then the correlations between subsequences, increases drastically with the order of the subsequence.

On the other hand, as expected in Section 8.1.5, the syntonization breaks the correlations between the subsequences. The right hand side of Figure 8.1 shows the syntonized frequency deviation sequence (middle) and the induced phase-time sequence (bottom). The frequency deviation subsequences are the same as the ones without syntonization except that they are shifted in such a way that the first sample is null. The changes in the phase-time subsequences are a little bit more significant since, in addition to the shift of the subsequences, there is also a change of slope due to a change of the mean-value of the frequency deviation subsequences.

8.2.2 Spectrum correlation analysis

In order to analyze the correlation between the subsequences spectra, we applied the method described in Section 8.2.1 to realize a f^{-4} red noise data-run with $2\,095\,152$ samples, i.e. 16384 subsequences $\times 128$ data. Figure 8.2-top represents such a realization with a sampling period of one second and then a whole length of $T \approx 24$ days.

Within this whole continuous data-run, we define three sequences each containing four sub-sequences of 128 data:

- Sequence #1 is close to the beginning (from samples $128\,000$ to $128\,511$)
- Sequence #2 is close to the center (from samples $1\,048\,576$ to $1\,049\,087$)
- Sequence #3 is close to the end (from samples $1\,969, 152$ to $1\,969\,663$).

Figure 8.2-middle-left shows these three sequences in the same plot, i.e. an enlargement of the three areas pointed by the arrows in Figure 8.2-top. The main features are drifts which range over a few tens of ps over each sequence.

On the other hand, if the syntonization process is done at the beginning of each 128-data subsequence, the curve appearance is quite different (see 8.2-middle-right) and is limited to less than one ps peak-to-peak: the linear drift is much lower revealing other features like random behavior as well as quadratic drifts.

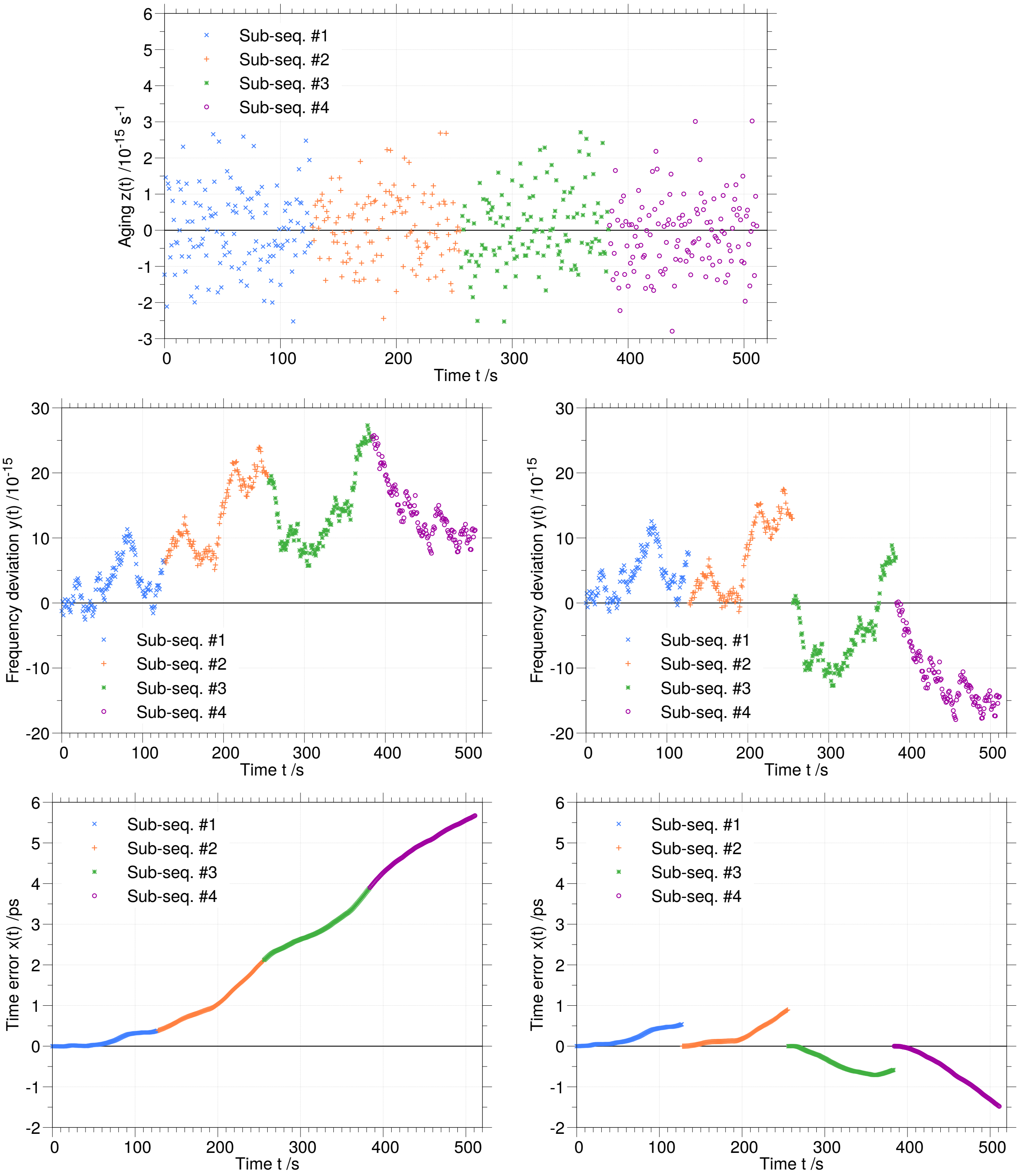

Figure 8.1: From $z(t)$ to $x(t)$ without (left) or with (right) syntonisation.

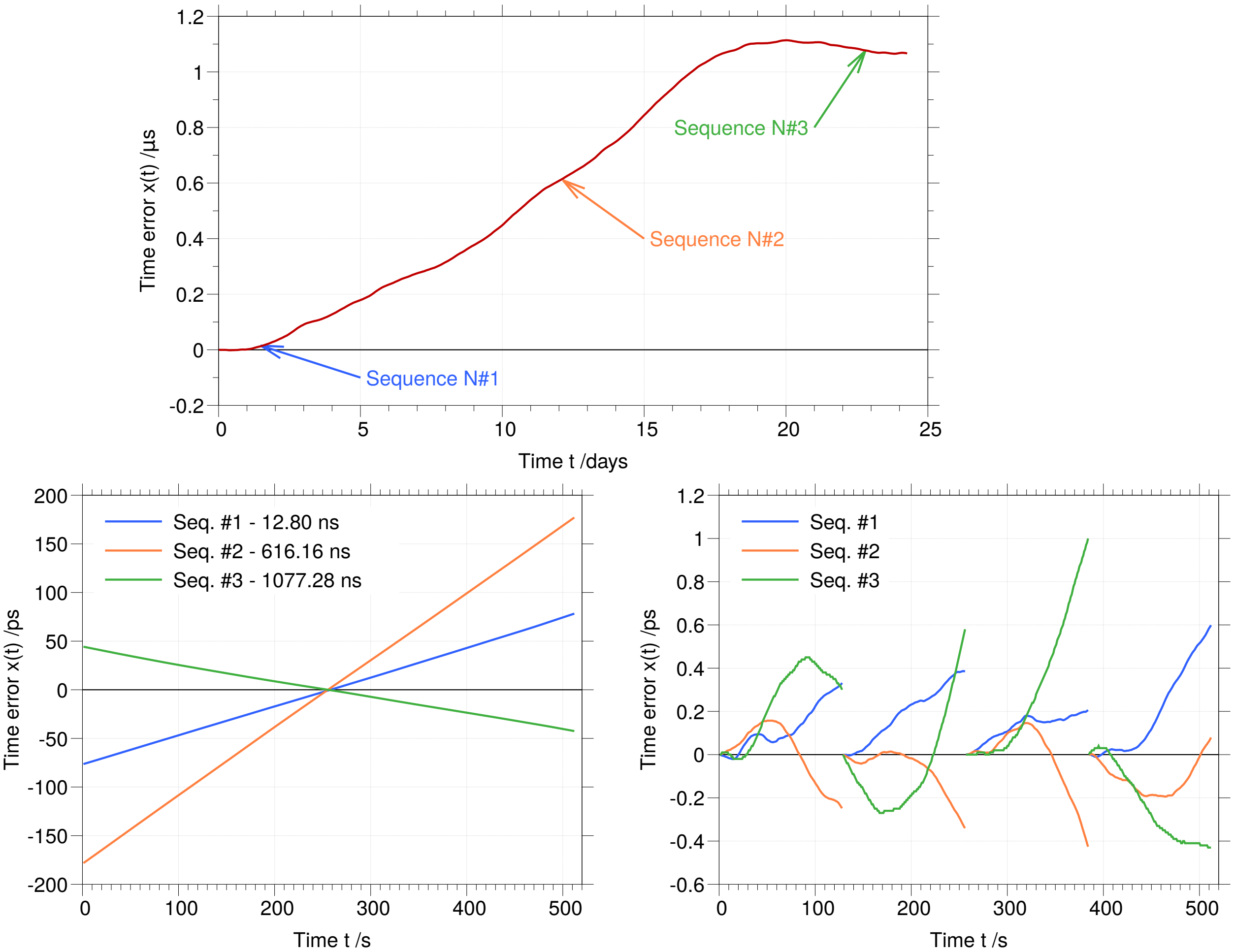

Figure 8.2: Definition of three sequences and four subsequences without (left) or with (right) syntonisation.

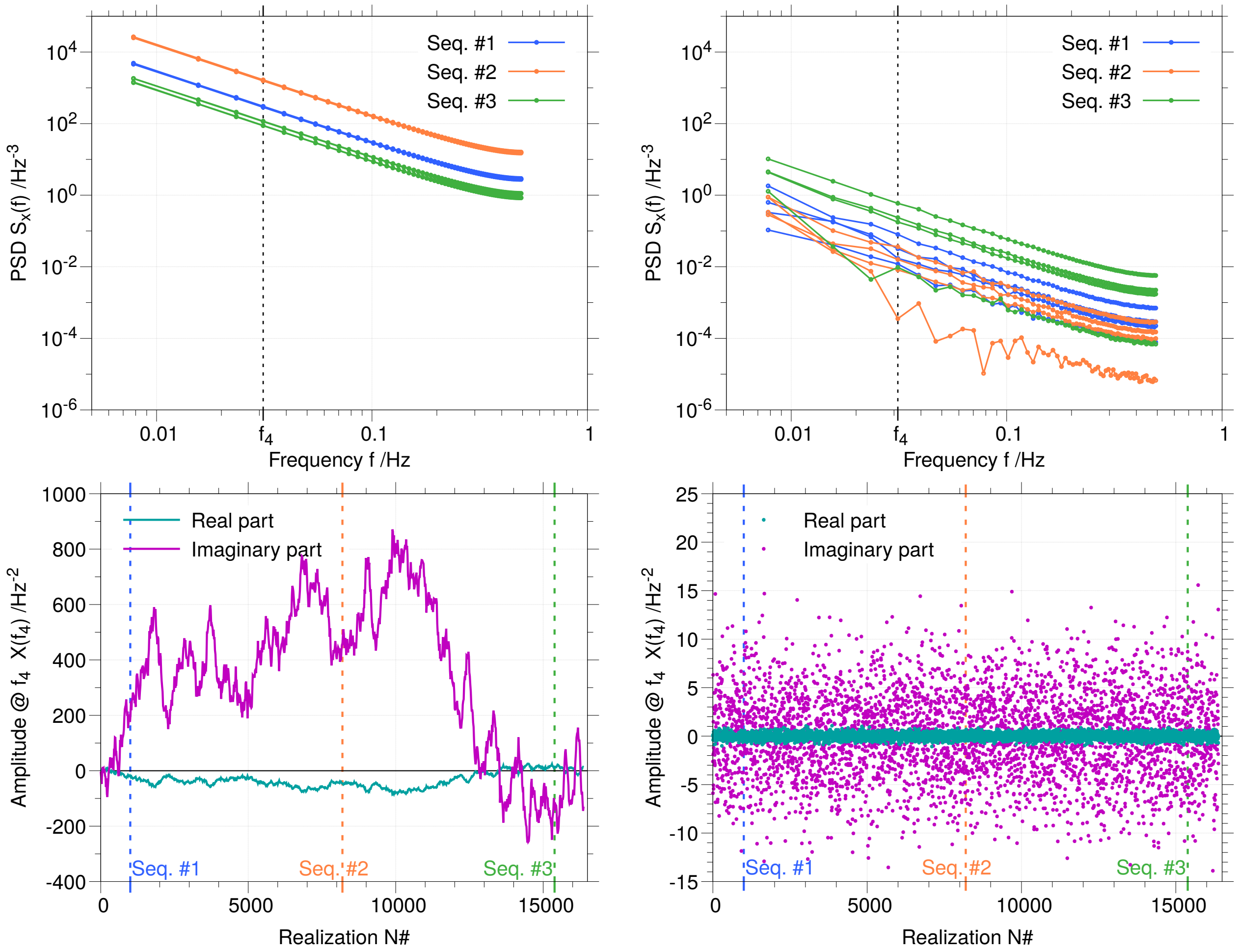

Figure 8.3: PSD (above) and realizations of the fourth amplitude of the spectrum (below) without (left) or with (right) syntonisation.

We computed the periodograms of the $16\,384$ subsequences of the rough and syntonized data-runs. Figure 8.3-top shows the periodograms of 3×4 subsequences defined above. Without syntonization (left), the periodograms are smooth and do not follow the expected f^{-4} slopes. Although their shapes are very similar, their levels are quite different depending of the sequence N#, e.g. the level of Sequence # 2 is about 15 times higher than the one of Sequence # 3. These features have to be related to the time curves of Fig 8.2-middle-left: we observe the periodograms of strong linear drifts which completely mask the random behavior of these subsequences.

With syntonization (see Figure 8.3-top-right), the periodograms are much lower and the random behavior becomes visible. It is particularly clear on the lowest orange curve which exhibits a f^{-4} trend from 0.01 to 0.1 Hz.

The lower part of Figure 8.3 focuses on the behavior of one of the amplitudes of the Fourier transform of all $16\,384$ subsequences. We arbitrarily chose the amplitude at $f_4 = \frac{4}{128\tau_0} = 31.25$ mHz. In other words, the sum of the square of the real part plus the square of the imaginary part divided by 128 at the blue dotted line gives the amplitude of the blue periodogram at f_4. Figure 8.3-bottom-left shows clearly that the real parts are strongly correlated from one subsequence to another as well as the imaginary parts. On the other hand, Figure 8.3-bottom-right shows that with syntonization these correlations seems to disappear. But before to conclude this theoretical study, let's analyze more thoroughly the correlations of these data.

In order to characterize these correlations, let us remind that, for each subsequence, its Fourier transform at f_4 is a complex r.v. The issue consists then to observe how these r.v. are correlated versus the time shift of the corresponding subsequences. E. g., with syntonization, 8.3-bottom-left shows a strong correlation between neighboring sequences. Therefore, we ought to estimate the autocorrelation of all these complex r.v. versus the N# of the realization (i.e. the N# of the sequence). The easiest way to perform such an estimation consists in computing the periodogram of these complex r.v. (the periodogram of periodogram amplitudes at f_4!) and then compute its inverse Fourier transform. This is what is presented on Figure 8.4: above the periodograms of the amplitudes at f_4 without (purple) or with syntonization (cyan), below the corresponding autocorrelation functions. These results confirm what we guessed at the previous paragraph: with syntonization, the autocorrelation function tends toward a Dirac peak and then the complex r.v. are uncorrelated. On the other hand, it is interesting to notice that, without syntonization, this complex r.v. follows a random walk noise.

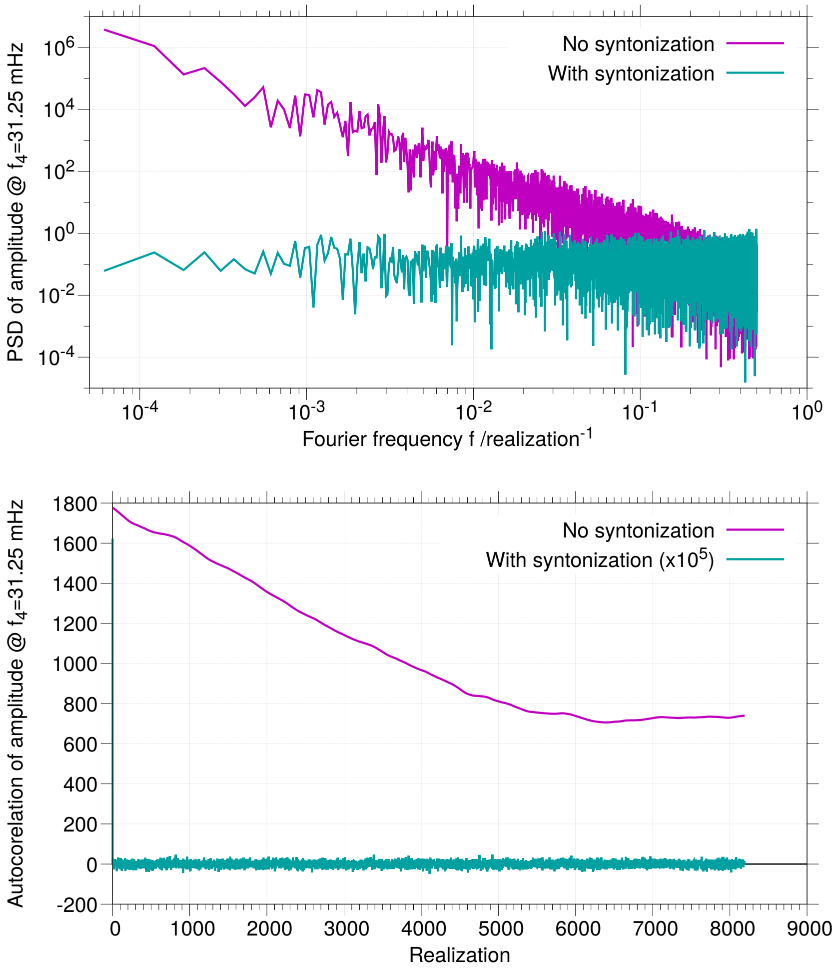

Figure 8.4: PSD (above) and autocorrelation (below) of the fourth amplitude of the spectrum without (purple) or with (cyan) syntonisation.

By using a similar study on f^{-3} red noise, we remarked that the amplitude at f_4 without syntonization is also a complex r.v. but follows a flicker noise. For the other three types of noise generally encountered in time and frequency metrology (white FM, flicker PM and white PM), syntonization is innocuous though useless.

8.3 Discussion

This study proves that a simple syntonization of an oscillator breaks the memory of the non stationary processes which are in its phase or frequency noise and then, gives uncorrelated spectra. Using this property allows us to average all the cross-spectra obtained after syntonization in order to converge to the phase or frequency PSD of the oscillator.

CHAPTER 9

Uncertainties and detection limit with two devices

The main purpose of this chapter concerns the comparison of the efficiencies of the

This chapter is done by the author under the supervision of François Vernotte, Éric Lantz and Enrico Rubiola. It is based on an article published as [150].

cross-spectrum estimator, i.e. the covariance of two spectra, with a simple average of these spectra. We assume that each spectrum is composed of a common red noise, that we call signal, and an uncorrelated white noise with the same noise level σ_W^2. Such a comparison imposes the perfect knowledge of this parameter σ_W^2 in order to be able to evaluate the signal variance σ_R^2 with the spectrum average method. However, this latter estimator exhibits a lower estimate variance than the other one, suggesting that it could be more efficient even if it is biased in essence. In order to get a more objective evaluation of the performances of these methods, we will compare the confidence intervals given by each of them by using a Bayesian estimation of the signal parameter σ_R^2: the narrower the confidence interval, the better the estimator.

9.1 Estimators

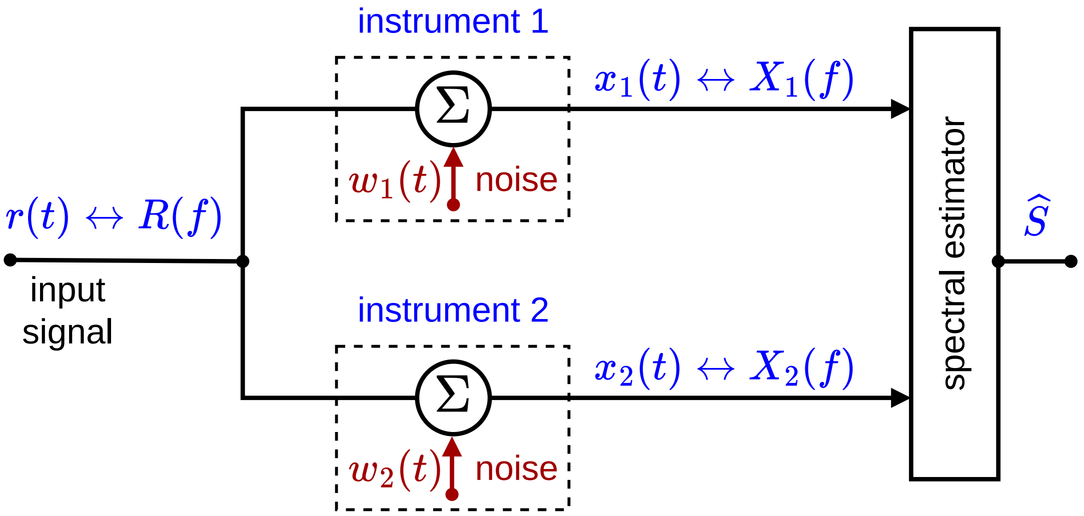

Figure 9.1: Dual channel instruments measuring the signal $r(t)$. Each instrument adds a white noise to the output $x_1(t)$ and $x_2(t)$ whose Fourier transform is respectively $X_1(f)$ and $X_2(f)$. Then the estimate $\widehat{S}$ is computed..

Let us consider three statistically independent signals: $w_1(t)$, $w_2(t)$ and $r(t)$ as shown in Figure 9.1. On one side the two first $w_1(t)$ and $w_2(t)$ are respectively the noise of instruments 1 and 2. On the other side $r(t)$ is an input signal which we want to characterize. This signal is stochastic and not necessarily stationary. In the case of pulsar measurement, this input signal is generally a red noise. The output of each channel is

$$\begin{aligned} x_1(t) &= w_1(t) + r(t) \\ x_2(t) &= w_2(t) + r(t). \end{aligned} \tag{9.1}$$

Processing experimental signals, we can assume that white noise is a continuous function of time, and that the Fourier transform always exists if we look at a very short interval regarding the sampling period. Applying the Fourier transform on each channel and focus solely on one frequency bin as stated in Section 6.2.3, it gives

$$\begin{aligned} X_1 &= W_1 + R \\ X_2 &= W_2 + R. \end{aligned} \tag{9.2}$$

where W_1, W_2 are uncorrelated normal complex r.v. of variance σ_W^2, i.e. the white noise level, and R a normal complex r.v. of variance σ_R^2/f^α, with σ_R^2 the signal level and α the red noise exponent.

Our interest is carried out on the PSD rather than the spectrum. Experimentaly we average over η spectra realizations. When the number of observations is large enough, the mathematics is made simple by the central limit theorem, by which all the PDF become Gaussian. More interesting for us is the case of a small number of realizations, each of which taking long observation time-up to several years in the case of the millisecond pulsars as stated in Section 6.2.2 and set $\eta = 1$. Let us emphasize on the term periodogram which designates a unique realization of the red noise since all instruments observe this red noise realization at the same time. Nevertheless, taking into account the uncorrelated white noises coming from the instruments, we have to deal with the PSD S for the instrument noise. One bin of S represents the power in a given bandwidth, i.e. the second central moment, or variance. Hereinafter, we work on a generic bin, thus $S(f)$ at that frequency is replaced with σ^2. Then the spectrum average and cross-spectrum estimators are respectively defined as (see Appendix A for the definition of these estimators)

$$\begin{cases} \widehat{S}_{cs} &= \Re\left[X_1 \cdot \overline{X}_2\right] \\ \widehat{S}_{sa} &= \Re\left[\dfrac{X_1 + X_2}{2}\right]^2 + \Im\left[\dfrac{X_1 + X_2}{2}\right]^2 - \dfrac{\sigma_W^2}{2}. \end{cases} \tag{9.3}$$

We do not take into account the imaginary part for the c-s estimate because it has a zero expectation (see Appendix A). The s.a estimator is “biased in essence” because, in order to get an unbiased estimator of the signal level, we must subtract half the noise level from it, i.e. its bias.

9.2 Expectation and variance of the estimates

One can easily verify that these estimators are unbiased.

$$\left\{ \begin{array}{lcl} \mathbb{E}\left[\widehat{S}_{cs}\right] & = & \mathbb{E}\left\{[\Re(W_1+R)+i\Im(W_1+R)]\,[\Re(W_2+R)-i\Im(W_2+R)]\right\} \\ & = & \mathbb{E}\left[\Re\left(R^2\right)\right]+\mathbb{E}\left[\Im\left(R^2\right)\right]=\mathbb{E}\left[|R|^2\right]=\sigma_R^2 \\ \mathbb{E}\left[\widehat{S}_{sa}\right] & = & \frac{1}{4}\mathbb{E}\left\{\Re\left[(W_1+W_2+2C)^2\right]\right\}+\frac{1}{4}\mathbb{E}\left\{\Im\left[(W_1+W_2+2C)^2\right]\right\}-\frac{1}{2}\sigma_W^2 \\ & = & \frac{1}{4}\left\{\mathbb{E}\left[\Re\left(W_1^2\right)\right]+\mathbb{E}\left[\Im\left(W_1^2\right)\right]+\mathbb{E}\left[\Re\left(W_2^2\right)\right]+\mathbb{E}\left[\Im\left(W_2^2\right)\right]\right\}+ \\ & & \quad +\mathbb{E}\left[\Re\left(R^2\right)\right]+\mathbb{E}\left[\Im\left(R^2\right)\right]-\frac{1}{2}\sigma_W^2 \\ & = & \frac{1}{4}\left\{\mathbb{E}\left[|W_1|^2\right]+\mathbb{E}\left[|W_2|^2\right]\right\}+\mathbb{E}\left[|R|^2\right]-\frac{1}{2}\sigma_W^2=\sigma_R^2 \end{array} \right. \tag{9.4}$$

since the mathematical expectation of all cross-terms vanish and $\mathbb{E}\left[|W_1|^2\right]=\mathbb{E}\left[|W_2|^2\right]=\sigma_W^2$ and $\mathbb{E}\left[|R|^2\right]=\sigma_R^2$. Furthermore i denotes the imaginary number such as $i^2=-1$

On the other hand, denoting $\mathbb{V}[\cdot]$ the variance of the quantity within the brackets, we can demonstrate (see Appendix B) that

$$\left\{ \begin{array}{ll} \mathbb{V}\left[\widehat{S}_{cs}\right]\approx\mathbb{V}\left[\widehat{S}_{sa}\right] & \text{if} \quad \sigma_R^2\gg\sigma_W^2 \\ \mathbb{V}\left[\widehat{S}_{cs}\right]\approx 2\mathbb{V}\left[\widehat{S}_{sa}\right] & \text{if} \quad \sigma_R^2\ll\sigma_W^2. \end{array} \right. \tag{9.5}$$

This is confirmed by Figure 9.2 (top) which exhibits the variance of the estimates of both estimators applied to a signal composed of a mixture of uncorrelated white noise of level one arbitrary unit (a.u) and a common f^{-8} noise which crosses the white noise level at $f=8$ a.u. At $f=4$ a.u, the signal level is 256 times higher than the white level and the variances of both estimators coincide. On the other hand, for frequencies higher than 16 a.u, the signal level is less than 256 times lower than the white level and the variance of the c-s estimates is two times higher than the variance of the s.a estimates. This seems to indicate a better efficiency of the s.a estimator.

Frequency (arbitrary units)	Cross-spectrum (%)	Spectrum average (%)
4	2.9	3.0
8	25.0	28.4
16	47.1	58.9
32	49.8	62.9

Table 9.1: Proportion of negative estimates vs frequency.

However, the histograms of the estimates of both estimators exhibit a very different

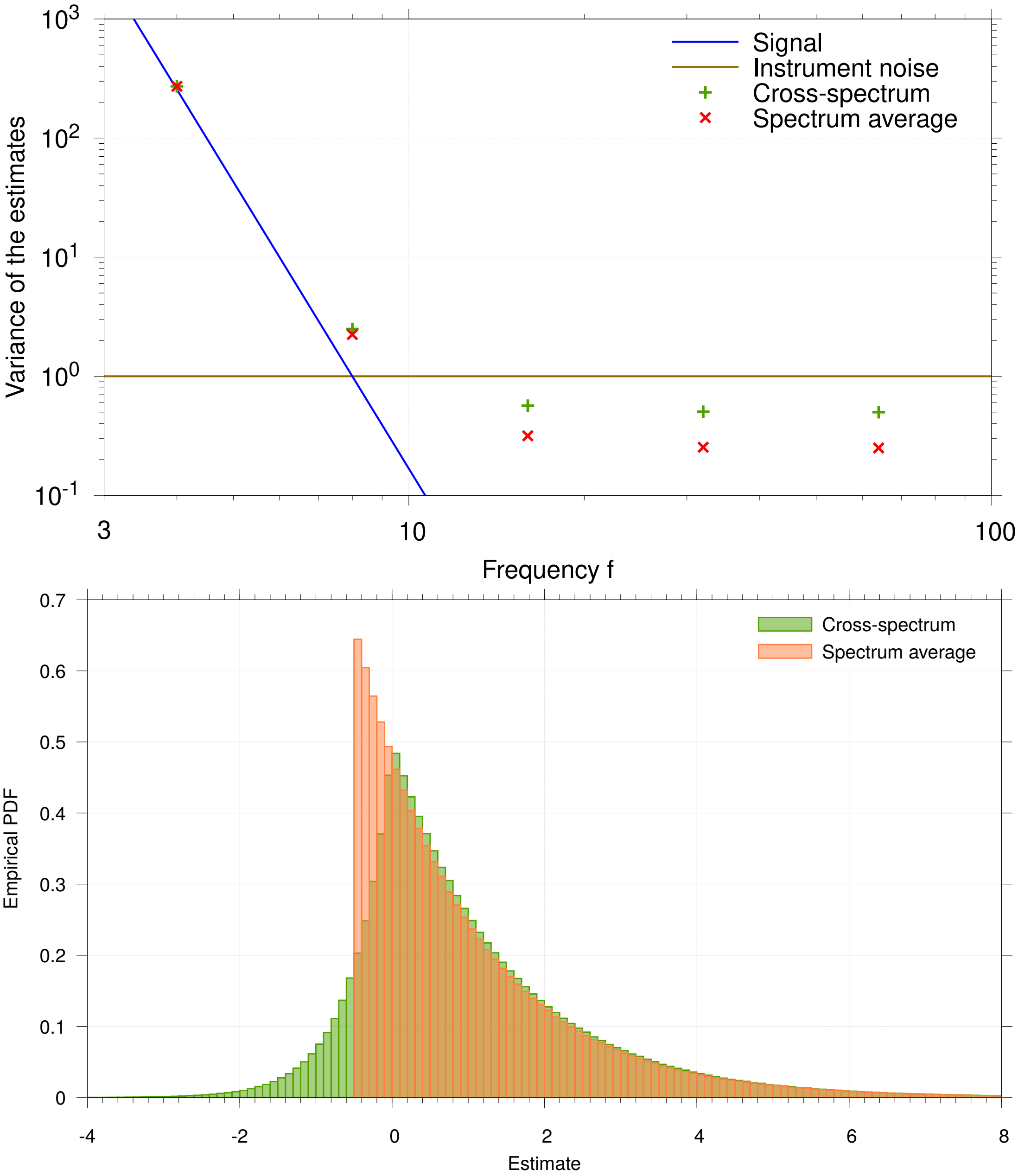

Figure 9.2: Variance (above) and histogram (below) of the estimates. These data were obtained from a set of one million simulated spectra. Below is the histogram of the estimates at $f = 8$ a.u where $\sigma_R^2 = \sigma_W^2 = 1$ a.u.

shape (see Figure 9.2 bottom): a double exponential increasing until 0 then decreasing being not symmetric for the c-s estimates and a function decreasing exponential for the s.a estimates. Then, although the negative part are very different, the positive part of the histograms are quite similar. However, for low positive estimates, the c-s histogram is a little bit higher. Therefore, this shows the probability to get a positive estimate, i.e. an informative estimate, is very slightly higher with the c-s estimator than with the s.a estimator. This property, which seems to point out a benefit in favor of the c-s method, is clearly visible in Table 9.1. Moreover, this table shows that the lower the signal level, the higher the discrepancy between the methods. This reinforces then the interest of the c-s method since we are interested in detecting a low signal in a high measurement noise.

The question is then: which of these methods is the most efficient? The only way to get an objective answer is to search for the Bayesian upper limit, e.g. at 95 % confidence, of the σ_R^2 estimation knowing one estimate: the most efficient method is the one which provides the most stringent upper limit.

In order to assess the uncertainty over the estimator σ_R^2, called the *signal* level, we will have to distinguish to main issues:

- The **direct problem** consists in calculating the statistics of the cross-spectrum $\widehat{S}_{cs}$ and the spectrum average $\widehat{S}_{sa}$, knowing the model parameters $\sigma_{W,1}^2$, $\sigma_{W,2}^2$, σ_R^2.
- The **inverse problem**, conversely consists in calculating a confidence interval over the unknown model parameter σ_R^2, from the known parameters $\sigma_{W,1}^2$, $\sigma_{W,2}^2$ and respectively the cross-spectrum and spectrum average measurement $\widehat{S}_{cs}$ and $\widehat{S}_{sa}$.

9.3 Empirical determination of the Probability Density Function of cross-spectrum data

In this section we focus on the direct problem, i.e. the determination of the Probability Density Function (PDF) of the cross-spectrum only. Here we carry out an empirical study to determine the PDF of the cross-spectrum and thus estimate its parameters.

9.3.1 A first approach

It is known that each cross-spectrum datum, i.e. the value obtained for each frequency, is a sum of three r.v. following a Variance-Gamma (VΓ) statistics [151,152]. Expanding $\widehat{S}_{cs}$

from Equation 9.3 and according to Equation 9.2, i.e. the output of each channel, these three r.v. are the terms within brackets in the following equation:

$$\begin{aligned} \widehat{S}_{cs} &= [W_1'W_2' + W_1''W_2''] + \\ &\quad + [W_1'R' + W_2'R' + W_1'' + W_2''R''] + \\ &\quad + [R'^2 + R''^2] \end{aligned} \tag{9.6}$$

where $\widehat{S}_{cs}$ is a cross-spectrum datum, all W_1, W_2 and R with $'$ or $''$ are independent normal random variables: W_1', W_1'', W_2', W_2'' are the real parts ($'$) and imaginary parts ($''$) of the measurement noises introduced by the measuring devices 1 and 2, and R', R'' are the real and imaginary parts of the intrinsic noise of the oscillator, e.g. pulsar, R (it may be noticed that the χ^2 distributions are special cases of the general VΓ distributions). Moreover, the second term may be rewritten as $R'(W_1'+W_2')+R''(W_1''+W_2'')$. Therefore, these three terms have two Degrees of Freedom (DoF) because they all are complex and their real parts are independent of their imaginary parts.

It is easy to determine the PDF of each of these three terms but very difficult to calculate the global PDF of the r.v. $\widehat{S}_{cs}$ since the three terms may be not independent. However, it turns out that with two DoF, the PDF of the VΓ distributions are simple exponential functions: from [153, p. 182] and [154, p. 326], we know that

$$p_{V\Gamma}(x) = \frac{\alpha^2 - \beta^2}{2\alpha} e^{-\alpha|x|+\beta x} = \kappa e^{-\alpha|x|+\beta x} \tag{9.7}$$

with $\alpha, \beta \in \mathbb{R}^+$ and $\beta < \alpha$.

We formulate the assumption that the statistics of the sum of the three terms of Equation 9.6 is also a VΓ with two DoF and, therefore, that the PDF of the r.v. $\widehat{S}_{cs}$ may be described by Equation 9.7.

- The **first step** is then to check this VΓ PDF assumption.
- If the first step is successful, the **second step** is to express the parameters κ, α, β versus σ_W and σ_R, respectively the noise standard deviation, i.e. the standard deviation of the W_1', W_1'', W_2', W_2'' r.v., and the "signal" standard deviation, i.e. the standard deviation of the R', R'' r.v.;
- Finally, the **third** and last **step** is to check if $\kappa = \dfrac{\alpha^2 - \beta^2}{2\alpha}$.

We decided to perform these tasks by fitting the histogram of Monte-Carlo simulations of $\widehat{S}_{cs}$.

9.3.2 Fitting the empirical PDF

The logarithm of Equation 9.7 gives a linear combination of the parameters:

$$\ln\left(p_{V\Gamma}(x)\right) = \ln(\kappa) - \alpha|x| + \beta x = K - \alpha|x| + \beta x \tag{9.8}$$

where $K = \ln(\kappa)$. We have then discomposed the problem in two parts:

$$\begin{cases} \text{if } x < 0 & f_n(x) = K + (\alpha+\beta)x = K_n + D_n x \\ \text{if } x \geq 0 & f_p(x) = K + (-\alpha+\beta)x = K_p + D_p x \end{cases} \tag{9.9}$$

with $K_n \approx K_p \approx K$, $D_n = \alpha + \beta$ and $D_p = \beta - \alpha$. We can thus estimate K, D_n, D_p by a least square fit.

In order to perform this estimation, we used the following algorithm:

S1: draw $6 \cdot 10^8$ normal pseudo-random data to simulate $N = 10^8$ realizations of each of the data $W_1', W_1'', W_2', W_2'', R', R''$ of Equation 9.6

S2: compute 10^8 simulated cross-spectrum data $\widehat{S}_{cs}$ according to Equation 9.6

S3: perform the histogram of the $\widehat{S}_{cs}$ data

S4: normalize this histogram by dividing by Nw where w stands for the width of the histogram bins

S5: calculate the linear regression of the logarithm of the negative part of the histogram and estimate the coefficient K_n and D_n

S6: calculate the linear regression of the logarithm of the positive part of the histogram and estimate the coefficient K_p and D_p

S7: estimate K by an average of K_n and K_p weighted by the number of bins of each part of the histogram, and deduce $\kappa = e^K$

S8: estimate α and β thanks to the following relatisonships

$$\begin{cases} \alpha = \dfrac{D_n - D_p}{2} \\ \beta = \dfrac{D_n + D_p}{2}. \end{cases} \tag{9.10}$$

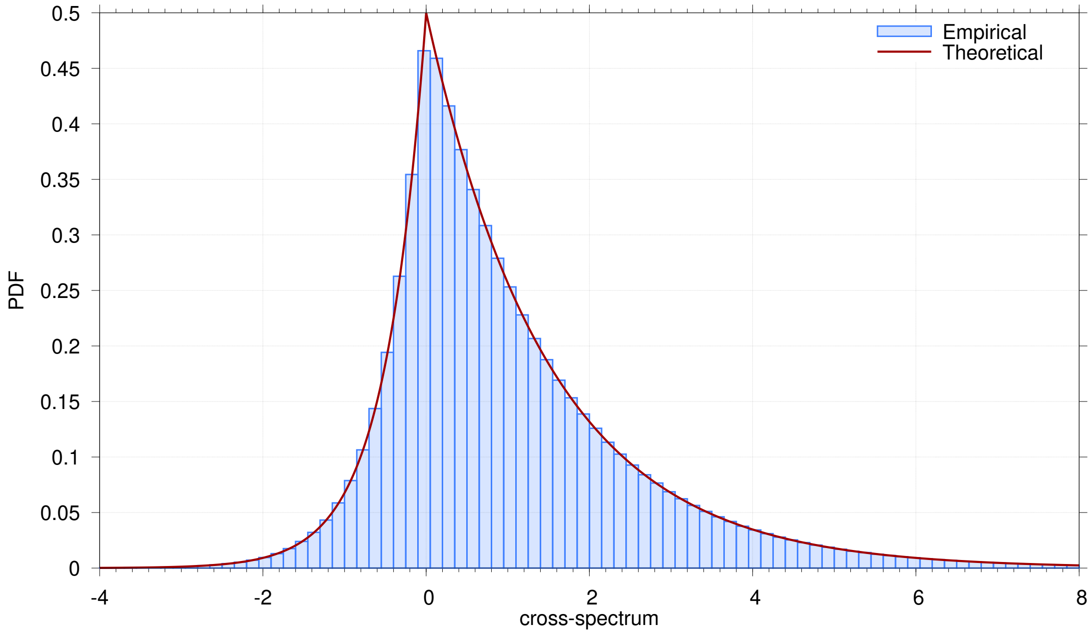

Figure 9.3: Comparison between the empirical and theoretical PDF of the cross-spectrum with $\sigma_R = 1$ and $\sigma_W = 1$.

9.3.3 Validation of the VΓ hypothesis

At first, this algorithm was used to simulate $\widehat{S}_{cs}$ data with $\sigma_R = \sigma_W = 1$ and the fit of the histogram was excellent as shown in Figure 9.3. We check with several other ratios of σ_R/σ_W and we observed a perfect agreement between the fit and the histogram at each time. Therefore, the VΓ hypothesis (first step of Section 9.3.1) was validated.

9.3.4 Estimation of the κ, α, β parameters

Secondly, we set $\sigma_W = 1$ and we varied σ_R from 0.1 to 10 by using a logarithmic increment of $1/10^{th}$ of a decade. Then, we set $\sigma_R = 1$ and we varied σ_W from 0.1 to 10 by using the same logarithmic increment. Figure 9.4 shows the evolution of the κ, α, β parameters versus σ_R and versus σ_W.

From theses graph, it is easy to deduce the dependence of the parameters on the standard deviations. For instance, the coefficient α on the top graph of Figure 9.4 reaches an horizontal asymptote at one when σ_R tends toward zero. On the other hand, it reaches an other horizontal asymptote at $1/2$ when σ_R tends toward infinity. Between, it is equal to $2/3$ when $\sigma_R = 1$. This suggests that α is a ratio of the form $(\sigma_R + p)/(q\sigma_R + r)$:

- if $\sigma_R \to 0$, this ratio becomes $p/r = 1$ so $p = r$
- if $\sigma_R \to \infty$, this ratio becomes $1/q = 1/2$ so $q = 2$

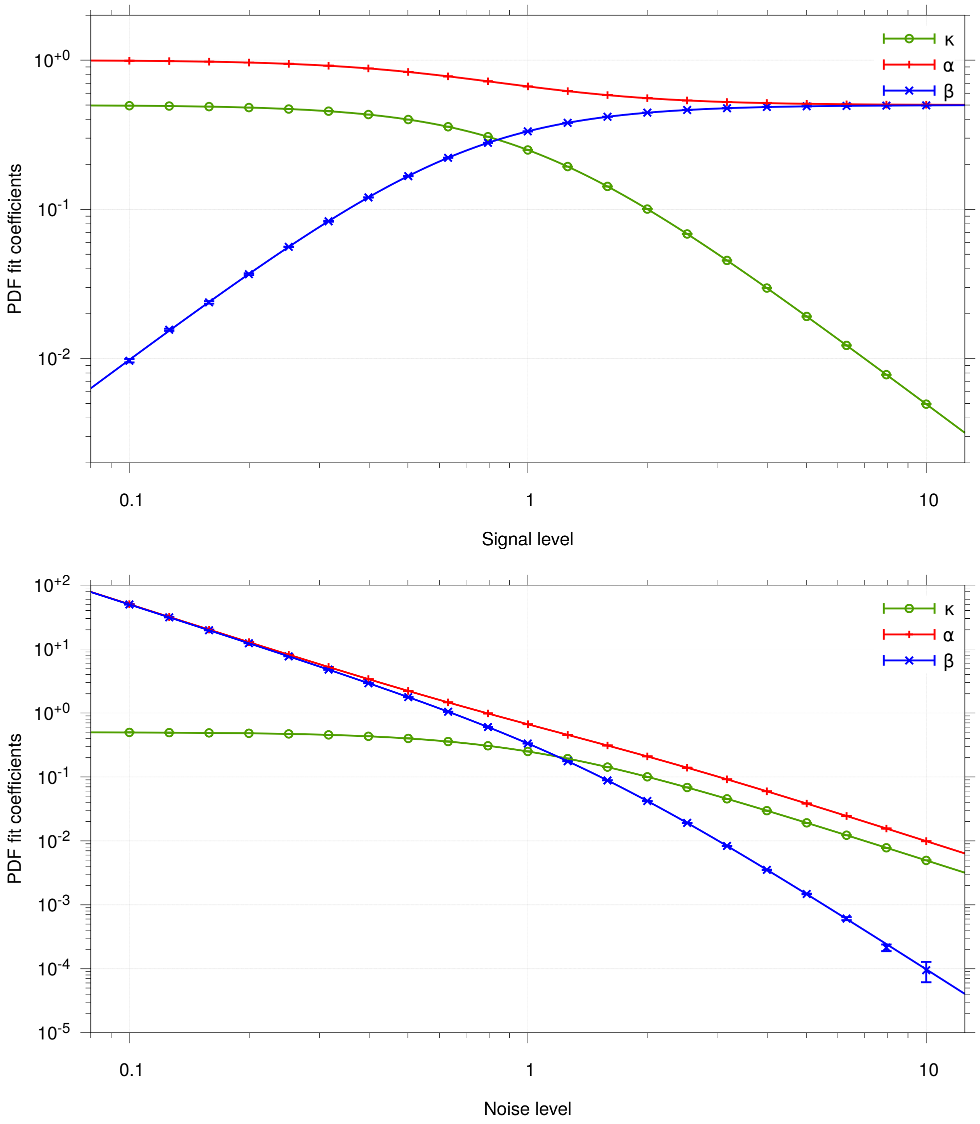

Figure 9.4: Dependence of the parameters κ, α, β on the standard deviations σ_R (above) and σ_W (below).

Parameter	vs σ_R ($\sigma_W = 1$)	vs σ_W ($\sigma_R = 1$)	vs σ_R and σ_W
κ	$\dfrac{1}{2(1+\sigma_R)}$	$\dfrac{1}{2(\sigma_W+1)}$	$\dfrac{1}{2(\sigma_W+\sigma_R)}$
α	$\dfrac{1+\sigma_R}{1+2\sigma_R}$	$\dfrac{\sigma_W+1}{\sigma_W(\sigma_W+2)}$	$\dfrac{\sigma_W+\sigma_R}{\sigma_W(\sigma_W+2\sigma_R)}$
β	$\dfrac{\sigma_R}{1+2\sigma_R}$	$\dfrac{1}{\sigma_W(\sigma_W+2)}$	$\dfrac{\sigma_R}{\sigma_W(\sigma_W+2\sigma_R)}$

Table 9.2: Dependence of the parameters κ, α, β on the standard deviations σ_R, σ_W.

- if $\sigma_R = 1$, this ratio becomes $(1+p)/(1+2) = 2/3$ so $p = 1$.

Such an analysis has been performed for all parameters, versus σ_R and σ_W, and we obtained the two central columns of Table 9.2. From these results, we inferred the right-hand side column showing the dependence of κ, α, β on σ_R as well as on σ_W (second step of Section 9.3.1).

9.3.5 Theoretical PDF, CDF and confidence interval

From the expression of the parameters κ, α, β given in Table 9.2 we can derivate the analytical expression of the cross-spectrum data PDF. First, let us calculate the argument of the exponential:

$$\begin{cases} \alpha+\beta = \dfrac{\sigma_W+\sigma_R}{\sigma_W(\sigma_W+2\sigma_R)} + \dfrac{\sigma_R}{\sigma_W(\sigma_W+2\sigma_R)} = \dfrac{1}{\sigma_W} \\ -\alpha+\beta = -\dfrac{\sigma_W+\sigma_R}{\sigma_W(\sigma_W+2\sigma_R)} + \dfrac{\sigma_R}{\sigma_W(\sigma_W+2\sigma_R)} = \dfrac{-1}{\sigma_W+2\sigma_R}. \end{cases} \tag{9.11}$$

We have found that $\kappa = \dfrac{1}{2(\sigma_W+\sigma_R)}$. On the other hand, we have written in Equation 9.7 that $\kappa = \dfrac{\alpha^2-\beta^2}{2\alpha}$. The subtitution of α and β by their expression given in Table 9.2 proves these two expressions of κ are fully compatible (third step of Section 9.3.1). Therefore, the analytical expression of the PDF is:

$$\begin{cases} p_{V\Gamma}(x) = \dfrac{1}{2(\sigma_W+\sigma_R)} e^{\frac{x}{\sigma_W}} & \text{if } x < 0 \\ p_{V\Gamma}(x) = \dfrac{1}{2(\sigma_W+\sigma_R)} e^{\frac{-x}{\sigma_W+2\sigma_R}} & \text{if } x \geq 0. \end{cases} \tag{9.12}$$

Integrating this PDF leads to the CDF:

$$\begin{cases} P_{V\Gamma}(x) = \dfrac{\sigma_W}{2(\sigma_W+\sigma_R)} e^{\frac{x}{\sigma_W}} & \text{if } x < 0 \\ P_{V\Gamma}(x) = 1 - \dfrac{\sigma_W + 2\sigma_R}{2(\sigma_W+\sigma_R)} e^{\frac{-x}{\sigma_W+2\sigma_R}} & \text{if } x \geq 0 \end{cases} \tag{9.13}$$

and, especially, we see that $P_{V\Gamma}(0) = \dfrac{\sigma_W}{2(\sigma_W+\sigma_R)}$.

The upper graph of Figure 9.5 shows the comparison of the PDF computed from Equation 9.12 with the histogram of 10^8 simulations of $\widehat{S}_{cs}$. Similarly, the middle graph shows the comparison of the CDF computed from Equation 9.13 with the cumulated histogram of these 10^8 simulations of $\widehat{S}_{cs}$. In both cases, the agreement is excellent. This is confirmed by the lower graph which shows that the deviation between the CDF and the cumulated histogram are of the order of a few 10^{-5}.

Finally, we calculated the inverse of the CDF in order to compute confidence intervals. Taking the logarithm of the CDF yields:

$$\begin{cases} P_{V\Gamma}^{-1}(p) = \sigma_W \ln\left[\dfrac{2(\sigma_W+\sigma_R)p}{\sigma_W}\right] & \text{if } p < P_{V\Gamma}(0) \\ P_{V\Gamma}^{-1}(p) = (\sigma_W + 2\sigma_R)\ln\left[\dfrac{\sigma_W+2\sigma_R}{2(1-p)(\sigma_W+\sigma_R)}\right] & \text{if } p \geq P_{V\Gamma}(0) \end{cases} \tag{9.14}$$

These relationships are useful to find the bounds which ensure a given probability. Table 9.3 shows an example of such a calculation: the probabilities 0.5%, 2.5%, $\ldots 97.5\%$ are achieved at the theoretical bounds. The empirical bounds are the probability to be below these bounds given by the empirical cumulative histogram. The right-hand side table gives the corresponding confidence intervals by subtracting the probabilities: for instance, the 95% confidence interval is between the bound at 2.5%, i.e. -2.590 and the bound at 97.5%, i.e. 6.567; the empirical probability is the probability to get a data within this interval given by the cumulative histogram (97.51% in Table 9.3). Here also, the agreement is almost perfect.

9.3.6 Discussion

Although the determination of the PDF and of the CDF have been empirically obtained, the agreement between the Monte-Carlo simulations and the analytical expression is so perfect that we are sure to have more than a simple approximation but the exact expressions of the PDF and CDF.

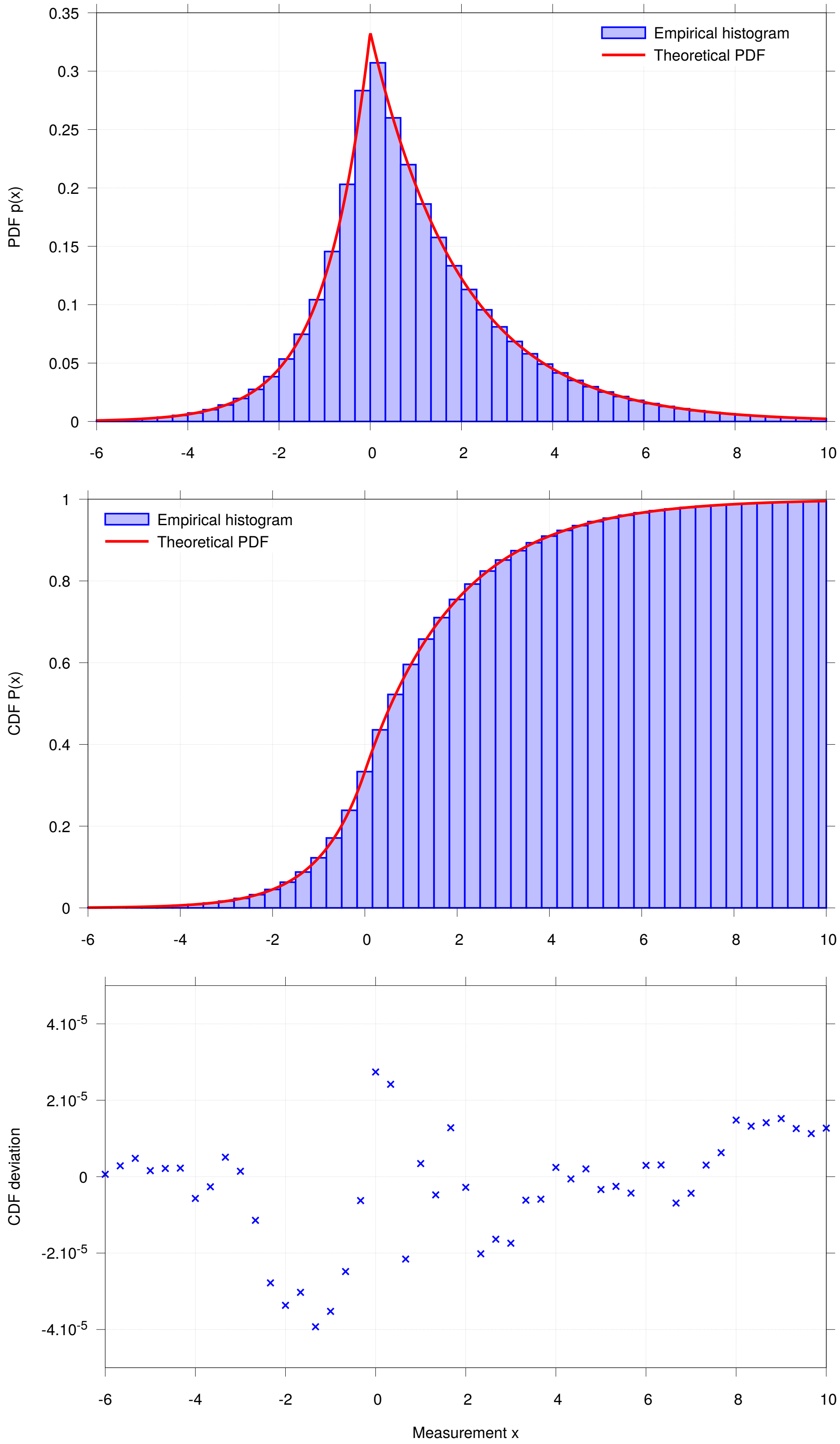

Figure 9.5: Comparison of the empirical and theoretical PDF (above) and CDF (below). The deviations between the empirical and the theoretical CDV are given in the bottom plot. The standard deviations are: $\sigma_R = 1/2$ and $\sigma_W = 1$.

Probability (%)	Theoretical bounds	Empirical prob. (%)
0.5	-4.200	0.51
2.5	-2.590	2.55
5.0	-1.897	5.09
16.0	-0.734	16.26
50.0	0.575	50.37
84.0	2.854	84.11
95.0	5.181	95.03
97.5	6.567	97.51
99.5	9.786	99.50

Theoretical intervals (%)	Empirical intervals (%)
68.0	67.85
90.0	89.94
95.0	94.97
99.0	98.99

Table 9.3: Comparison of the theoretical bounds (left table) and intervals (right table) given by Equation 9.14 with empirical probabilities/intervals. The standard deviations are: $\sigma_R = 1/2$ and $\sigma_W = 1$.

9.4 Direct Problem: the cross-spectrum theoretical PDF

In this section we will give a formalization of the direct problem which leads to the theoretical PDF only for the cross-spectrum estimate, the PDF of the spectrum average being already analytically well-defined.

9.4.1 Measurement and estimates

In Sections 9.4.2 to 9.4.6 we will omit the "*hat*" for estimates since we deal with the mathematical models. In the following, the real and imaginary parts of the spectrum induce two DoFs. According to Equation 9.3 we refer the cross-spectrum measurement at a given frequency to

$$\widehat{S}_{cs} = \langle (W_1 + R)(W_2 + R) \rangle_\nu \tag{9.15}$$

where all W_1, W_2, R are r.v. which are independent, centered and normal and $\langle \cdot \rangle$ is the average over ν DoFs. In the following, we will assume that W_1, W_2, R have only one DoF, their real or their imaginary part, and that $\widehat{S}_{cs}$ does not come from the average of different spectra. A generalization of this problem to two DoF (real and imaginary parts) and then 2η DoF (average of η spectra) will be given. To simplify the notation, we will omit the average over the DoFs as we set $\nu = 1$.

9.4.2 Vector Formalization of the Problem

We will reuse here the formalism we developed in [152], i.e. a vector space of normal laws. Since we have three normal r.v., we are in a vector space of three dimensions that we will denote $\mathbb{LG}^3$ and which has the basis $(\vec{E}_{W,1}, \vec{E}_{W,2}, \vec{E}_R)$ defined as

$$\begin{cases} \vec{E}_{W,1} &= \text{LG}_{W,1}(0,1) \\ \vec{E}_{W,2} &= \text{LG}_{W,2}(0,1) \\ \vec{E}_R &= \text{LG}_R(0,1) \end{cases} \tag{9.16}$$

where $\text{LG}(0,1)$ stands for a Laplace-Gauss (or normal) r.v. with zero-mean (centered) and unity standard deviation ($\sigma = 1$). We assume that $\text{LG}_{W,1}(0,1)$, $\text{LG}_{W,2}(0,1)$, $\text{LG}_R(0,1)$ are independent. We can define the scalar product between the basis vectors of $\mathbb{LG}^3$ in such a way:

$$\begin{cases} ||\vec{E}_{W,1}||^2 &= \vec{E}_{W,1} \cdot \vec{E}_{W,1} &= \text{LG}_{W,1} \cdot \text{LG}_{W,1} &= \chi^2_{W,1} \\ ||\vec{E}_{W,2}||^2 &= \vec{E}_{W,2} \cdot \vec{E}_{W,2} &= \text{LG}_{W,2} \cdot \text{LG}_{W,2} &= \chi^2_{W,2} \\ ||\vec{E}_R||^2 &= \vec{E}_R \cdot \vec{E}_R &= \text{LG}_R \cdot \text{LG}_R &= \chi^2_R \end{cases} \tag{9.17}$$

$$\begin{cases} \vec{E}_{W,1} \cdot \vec{E}_{W,2} &= \text{LG}_{W,1} \cdot \text{LG}_{W,2} &= \text{V}\Gamma_{W_1 W_2} \\ \vec{E}_{W,2} \cdot \vec{E}_R &= \text{LG}_{W,2} \cdot \text{LG}_R &= \text{V}\Gamma_{W_2 R} \\ \vec{E}_R \cdot \vec{E}_{W,1} &= \text{LG}_R \cdot \text{LG}_{W,1} &= \text{V}\Gamma_{R W_1} \end{cases} \tag{9.18}$$

where $\chi^2_{W_1,W_2,R}$ are three independent χ^2 rv with one DoF and $\text{V}\Gamma_{W_1 W_2, W_2 R, R W_1}$ are three variance-Gamma ($\text{V}\Gamma$) r.v. [152, 155]. Any vector $\vec{U}$ may be written as

$$\vec{U} = \begin{pmatrix} u_{W,1} \\ u_{W,2} \\ u_R \end{pmatrix} = u_{W,1}\vec{E}_{W,1} + u_{W,2}\vec{E}_{W,2} + u_R\vec{E}_R \tag{9.19}$$

where $u_{W,1}, u_{W,2}, u_R$ are three constant scalars since all the random part is carried by the basis vectors. The scalar product between two vectors $\vec{U}$ and $\vec{V}$ is then:

$$\begin{aligned} \vec{U} \cdot \vec{V} &= \left(u_{W,1}\vec{E}_{W,1} + u_{W,2}\vec{E}_{W,2} + u_R\vec{E}_R\right) \cdot \left(v_{W,1}\vec{E}_{W,1} + v_{W,2}\vec{E}_{W,2} + v_R\vec{E}_R\right) \\ &= u_{W,1}v_{W,1}\vec{E}_{W,1} \cdot \vec{E}_{W,1} + u_{W,2}v_{W,2}\vec{E}_{W,2} \cdot \vec{E}_{W,2} + u_R v_R \vec{E}_R \cdot \vec{E}_R + \\ &\quad +(u_{W,1}v_{W,2} + u_{W,2}v_{W,1})\vec{E}_{W,1} \cdot \vec{E}_{W,2} + \\ &\quad\quad +(u_{W,2}v_c + u_R v_{W,2})\vec{E}_{W,2} \cdot \vec{E}_R + \\ &\quad\quad\quad +(u_R v_{W,1} + u_{W,1}v_R)\vec{E}_R \cdot \vec{E}_{W,1}. \end{aligned} \tag{9.20}$$

On the other hand, if we consider the mathematical expectation of these expressions, we obtain

$$\mathbb{E}\left[\vec{E}_P \cdot \vec{E}_Q\right] = \delta_{P,Q} \quad \text{with} \quad P, Q \in \{W_1, W_2, R\} \tag{9.21}$$

where $\delta_{P,Q}$ is the Kronecker delta. We see that we obtain the classical scalar product by using the mathematical expectation:

$$\mathbb{E}\left[\vec{U}\cdot\vec{V}\right] = u_{W,1}v_{W,1} + u_{W,2}v_{W,2} + u_R v_R. \tag{9.22}$$

Therefore, we will define that 2 vectors $\vec{U}$ and $\vec{V}$ are orthogonal if $\mathbb{E}\left[\vec{U}\cdot\vec{V}\right] = 0$.

9.4.3 From a normal Random Variable Product to a Chi-squared RV Difference

Following this formalism, Equation 9.15 may be rewritten as

$$\begin{aligned} S_{cs} = \left(\vec{W}_1 + \vec{R}\right)\cdot\left(\vec{W}_2 + \vec{R}\right) = \begin{pmatrix} \sigma_{W,1} \\ 0 \\ \sigma_R \end{pmatrix} \cdot \begin{pmatrix} 0 \\ \sigma_{W,2} \\ \sigma_R \end{pmatrix} \\ = \sigma_{W,1}\sigma_{W,2}\mathrm{V}\Gamma_{W_1W_2} + \sigma_{W,1}\sigma_R\mathrm{V}\Gamma_{W_1R} + \sigma_{W,2}\sigma_R\mathrm{V}\Gamma_{W_2R} + \sigma_R^2\chi_R^2 \end{aligned} \tag{9.23}$$

where $\sigma_{W,1}, \sigma_{W,2}, \sigma_R$ are respectively the standard deviations of the r.v. W_1, W_2, R. As a consequence, $\mathbb{E}[S_{cs}] = \sigma_R^2$.

As demonstrated in [151], a product of independent normal r.v. may be expressed as a difference of χ^2 r.v. For this purpose, although we know that $(W_1 + R)$ and $(W_2 + R)$ are not independent, we introduce the r.v. $V_1 = (W_1 + W_2)/2 + R$ and $V_2 = (W_1 - W_2)/2$ in such a way that $W_1 + R = V_1 + V_2$, $W_2 + R = V_1 - V_2$ and therefore $(W_1 + R)(W_2 + R) = V_1^2 - V_2^2$. In this vectorial formalism:

$$\vec{V}_1 = \begin{pmatrix} \sigma_{W,1}/2 \\ \sigma_{W,2}/2 \\ \sigma_R \end{pmatrix}, \quad \text{and} \quad \vec{V}_2 = \begin{pmatrix} \sigma_{W,1}/2 \\ -\sigma_{W,2}/2 \\ 0 \end{pmatrix}. \tag{9.24}$$

Therefore, $(\vec{V}_1, \vec{V}_2)$ is the basis of the 2-dimensional subspace of $\mathbb{LG}^3$ in which lies our whole problem. Since the squared modulus of $\vec{V}_1, \vec{V}_2$ are:

$$\left\{ \begin{array}{rcl} ||\vec{V}_1||^2 & = & \frac{\sigma_{W,1}^2}{4}\chi_{W_1}^2 + \frac{\sigma_{W,2}^2}{4}\chi_{W_2}^2 + \sigma_R^2\chi_R^2 \\ & & +\frac{\sigma_{W,1}\sigma_{W,2}}{2}\mathrm{V}\Gamma_{W_1W_2} + \sigma_{W,1}\sigma_R\mathrm{V}\Gamma_{W_1R} + \sigma_{W,2}\sigma_R\mathrm{V}\Gamma_{W_2R} \\ ||\vec{V}_2||^2 & = & \frac{\sigma_{W,1}^2}{4}\chi_{W_1}^2 + \frac{\sigma_{W,2}^2}{4}\chi_{W_2}^2 - \frac{\sigma_{W,1}\sigma_{W_2}}{2}\mathrm{V}\Gamma_{W_1W_2}, \end{array} \right. \tag{9.25}$$

their difference is consistent with Equation 9.23 and then $S_{cs} = (\vec{W}_1 + \vec{R})\cdot(\vec{W}_2 + \vec{R}) =$

$||\vec{V}_1||^2 - ||\vec{V}_2||^2$. Moreover, we can calculate the mathematical expectations of these squared modulus:

$$\begin{aligned} v_1^2 &= \mathbb{E}\left[||\vec{V}_1||^2\right] = \frac{\sigma_{W,1}^2 + \sigma_{W,2}^2}{4} + \sigma_R^2 \\ v_2^2 &= \mathbb{E}\left[||\vec{V}_2||^2\right] = \frac{\sigma_{W,1}^2 + \sigma_{W,2}^2}{4}. \end{aligned} \tag{9.26}$$

On the other hand, since

$$\mathbb{E}\left[\vec{V}_1 \cdot \vec{V}_2\right] = \frac{\sigma_{W,1}^2 - \sigma_{W,2}^2}{4} \tag{9.27}$$

the vector $\vec{V}_1$ and $\vec{V}_2$ are not orthogonal unless $\sigma_{W,1} = \sigma_{W,1}$, i.e. measurement instruments 1 and 2 have the same variance.

9.4.4 A Particular Case: W_1 and W_2 have the Same Variance

Let us define $\sigma_W^2 = \sigma_{W,1}^2 = \sigma_{W,2}^2$. In this case

$$\mathbb{E}\left[\vec{V}_1 \cdot \vec{V}_2\right] = \frac{\sigma_W^2}{4} - \frac{\sigma_W^2}{4} = 0, \tag{9.28}$$

$\vec{V}_1, \vec{V}_2$ are orthogonal which means that their squared modulus are two independent χ^2 rv:

$$||\vec{V}_1||^2 = v_1^2\chi_{v1}^2 \quad \text{and} \quad ||\vec{V}_2||^2 = v_2^2\chi_{v2}^2 \tag{9.29}$$

Thanks to [152, Appendix A], we know that this χ^2 r.v. difference is a VΓ r.v. with a PDF, introduced by [156]:

$$p(x) = \frac{\gamma^{2\lambda}|x-\mu|^{\lambda-1/2}K_{\lambda-1/2}\left(\alpha|x-\mu|\right)}{\sqrt{\pi}\Gamma(\lambda)(2\alpha)^{\lambda-1/2}}e^{\beta(x-\mu)} \tag{9.30}$$

where $\gamma = \sqrt{\alpha^2 - \beta^2}$, $\Gamma(\lambda)$ is the gamma function, $K_w(z)$ is a hyperbolic Bessel function of the second kind ($w \in \mathbb{R}$ and $z \in \mathbb{C}$) and with the following parameters:

$$\mu = 0, \quad \alpha = \frac{v_1^2 + v_2^2}{4v_1^2v_2^2}, \quad \beta = \frac{v_1^2 - v_2^2}{4v_1^2v_2^2}, \quad \lambda = \frac{1}{2} \tag{9.31}$$

where λ is the number of DoF divided by 2. In this particular case, since $\sigma_{W,1}^2 = \sigma_{W,2}^2 = \sigma_W^2$, v_1^2 and v_2^2 becomes

$$v_1^2 = \mathbb{E}\left[||\vec{V}_1||^2\right] = \frac{\sigma_W^2}{2} + \sigma_R^2 \quad \text{and} \quad v_2^2 = \mathbb{E}\left[||\vec{V}_2||^2\right] = \frac{\sigma_W^2}{2}, \tag{9.32}$$

and we obtain

$$\alpha = \frac{\sigma_W^2 + \sigma_R^2}{\sigma_W^2(2\sigma_W^2 + \sigma_R^2)} \quad \text{and} \quad \beta = \frac{\sigma_R^2}{\sigma_W^2(2\sigma_W^2 + \sigma_R^2)} \tag{9.33}$$

9.4.5 General Case

If $\sigma_{W,1}^2 \neq \sigma_{W,2}^2$, $\vec{V}_1$ and $\vec{V}_2$ are no longer orthogonal and therefore they are two correlated r.v. We have then to search another set of basis vectors which are orthogonal. For this purpose, let us use the Gram-Schmidt process.

9.4.5.1 Gram-Schmidt Orthogonalization

Let us keep $\vec{V}_1$ unchanged. Let $\vec{V}_{2P}$ be the projection of $\vec{V}_2$ onto $\vec{V}_1$. In the same way as the orthogonality between two vectors is defined by the null mathematical expectation of their scalar product, the angles as well as the other relationships between vectors must be taken into account as mathematical expectation since they are valid on average but not for only one particular realization of these vectors. Denoting θ the angle between $\vec{V}_1$ and $\vec{V}_2$, it comes

$$\vec{V}_{2P} = v_2 \cos(\theta) \frac{\vec{V}_1}{v_1}. \tag{9.34}$$

with

$$\cos(\theta) = \frac{\mathbb{E}\left[\vec{V}_1 \cdot \vec{V}_2\right]}{v_1 v_2} \tag{9.35}$$

and then

$$\vec{V}_{2P} = \frac{\mathbb{E}\left[\vec{V}_1 \cdot \vec{V}_2\right]}{v_1^2} \vec{V}_1. \tag{9.36}$$

Therefore, we can build the vector $\vec{V}_{2N}$ which is the component of $\vec{V}_2$ orthogonal to $\vec{V}_1$:

$$\vec{V}_{2N} = \vec{V}_2 - \vec{V}_{2P} = \vec{V}_2 - \frac{\mathbb{E}\left[\vec{V}_1 \cdot \vec{V}_2\right]}{v_1^2} \vec{V}_1. \tag{9.37}$$

Using Equations 9.26 and 9.27 yields

$$\begin{aligned}\vec{V}_{2N} &= \begin{pmatrix} \sigma_{W,1}/2 \\ -\sigma_{W,2}/2 \\ 0 \end{pmatrix} - \frac{\sigma_{W,1}^2-\sigma_{W,2}^2}{\sigma_{W,1}^2+\sigma_{W,2}^2+4\sigma_R^2}\begin{pmatrix} \sigma_{W,1}/2 \\ \sigma_{W,2}/2 \\ \sigma_R \end{pmatrix} \\ &= \begin{pmatrix} \dfrac{\sigma_{W,1}(\sigma_{W,2}^2+2\sigma_R^2)}{\sigma_{W,1}^2+\sigma_{W,2}^2+4\sigma_R^2} \\ -\dfrac{\sigma_{W,2}(\sigma_{W,1}^2+2\sigma_R^2)}{\sigma_{W,1}^2+\sigma_{W,2}^2+4\sigma_R^2} \\ -\dfrac{\sigma_R(\sigma_{W,1}^2-\sigma_{W,2}^2)}{\sigma_{W,1}^2+\sigma_{W,2}^2+4\sigma_R^2} \end{pmatrix} = \begin{pmatrix} v_{2nW_1} \\ v_{2nW_2} \\ v_{2nR} \end{pmatrix}.\end{aligned} \tag{9.38}$$

We have now to express the measurement vectors $\vec{W}_1+\vec{R}$ and $\vec{W}_2+\vec{R}$ as linear combinations of the new basis of orthogonal vectors $\vec{V}_1$ and $\vec{V}_{2N}$. In order to do this, we must project these two measurement vectors onto the two basis vectors in the same way that we have projected $\vec{V}_2$ onto $\vec{V}_1$ in Equation 9.36:

$$\begin{cases} \vec{W}_1+\vec{R} = k_{W_1R1}\vec{V}_1 + k_{W_1R2n}\vec{V}_{2N} \\ \vec{W}_2+\vec{R} = k_{W_2R1}\vec{V}_1 + k_{W_2R2n}\vec{V}_{2N} \end{cases} \tag{9.39}$$

with

$$\begin{aligned} k_{W_1R1} &= \frac{\mathbb{E}\left[\left(\vec{W}_1+\vec{R}\right)\cdot\vec{V}_1\right]}{\mathbb{E}\left[||\vec{V}_1||^2\right]} & k_{W_1R2n} &= \frac{\mathbb{E}\left[\left(\vec{W}_1+\vec{R}\right)\cdot\vec{V}_{2N}\right]}{\mathbb{E}\left[||\vec{V}_{2N}||^2\right]} \\ k_{W_2R1} &= \frac{\mathbb{E}\left[\left(\vec{W}_2+\vec{R}\right)\cdot\vec{V}_1\right]}{\mathbb{E}\left[||\vec{V}_1||^2\right]} & k_{W_2R2n} &= \frac{\mathbb{E}\left[\left(\vec{W}_2+\vec{R}\right)\cdot\vec{V}_{2N}\right]}{\mathbb{E}\left[||\vec{V}_{2N}||^2\right]}. \end{aligned} \tag{9.40}$$

Therefore, $S_{cs} = (\vec{W}_1+\vec{R})\cdot(\vec{W}_2+\vec{R})$ may be written as

$$\begin{aligned} S_{cs} &= k_{W_1R1}k_{W_2R1}||\vec{V}_1||^2 + k_{W_1R2n}k_{W_2R2n}||\vec{V}_{2N}||^2 \\ &\quad + \left(k_{W_1R1}k_{W_2R2n} + k_{W_1R2n}k_{W_2R1}\right)\vec{V}_1\cdot\vec{V}_{2N} \\ &= k_{W_1R1}k_{W_2R1}\dot{\chi}^2 + k_{W_1R2n}k_{W_2R2n}\ddot{\chi}^2 \\ &\quad + \left(k_{W_1R1}k_{W_2R2n} + k_{W_1R2n}k_{W_2R1}\right)\mathrm{V}\Gamma \end{aligned} \tag{9.41}$$

where $\dot{\chi}^2$ and $\ddot{\chi}^2$ are independent χ^2 rv corresponding respectively to the squared norm of $\vec{V}_1$ and $\vec{V}_{2N}$. Thus, this relationship involves the difference of two χ^2 r.v. (it can be proved that $k_{W_1R2n}k_{W_2R2n} < 0$), which is well known [151, 152], plus a VΓ r.v, which makes the problem more complex. In order to simplify this problem, we should find a representation of Equation 9.41 in which the cross term is identically null.

9.4.5.2 Normalization and Rotation of the Basis Vectors

Let $(\vec{V}_1', \vec{V}_2')$ be the normalized equivalent of the basis $(\vec{V}_1, \vec{V}_{2N})$:

$$\vec{V}_1' = \frac{\vec{V}_1}{\mathbb{E}\left[||\vec{V}_1||\right]} \quad \text{and} \quad \vec{V}_2' = \frac{\vec{V}_{2N}}{\mathbb{E}\left[||\vec{V}_{2N}||\right]}. \tag{9.42}$$

With this new basis, Equation 9.41 may be rewritten as

$$\begin{aligned} S_{cs} &= k_{W_1R1}k_{W_2R1}\mathbb{E}\left[||\vec{V}_1||\right]^2 ||\vec{V}_1'||^2 \\ &\quad + k_{W_1R2n}k_{W_2R2n}\mathbb{E}\left[||\vec{V}_{2N}||\right]^2 ||\vec{V}_2'||^2 \\ &\quad + k_{W_1R1}k_{W_2R2n}\mathbb{E}\left[||\vec{V}_1||\right]\mathbb{E}\left[||\vec{V}_{2N}||\right]\vec{V}_1'\cdot\vec{V}_2' \\ &\quad + k_{W_1R2n}k_{W_2R1}\mathbb{E}\left[||\vec{V}_1||\right]\mathbb{E}\left[||\vec{V}_{2N}||\right]\vec{V}_1'\cdot\vec{V}_2' \\ &= k_{11}'||\vec{V}_1'||^2 - k_{22}'||\vec{V}_2'||^2 + k_{12}'\vec{V}_1'\cdot\vec{V}_2' \end{aligned} \tag{9.43}$$

with

$$\begin{cases} k_{11}' &= k_{W_1R1}k_{W_2R1}\mathbb{E}\left[||\vec{V}_1||\right]^2 \\ k_{22}' &= -k_{W_1R2n}k_{W_2R2n}\mathbb{E}\left[||\vec{V}_{2N}||\right]^2 \\ k_{12}' &= k_{W_1R1}k_{W_2R2n}\mathbb{E}\left[||\vec{V}_1||\right]\mathbb{E}\left[||\vec{V}_{2N}||\right] \\ &\quad + k_{W_1R2n}k_{W_2R1}\mathbb{E}\left[||\vec{V}_1||\right]\mathbb{E}\left[||\vec{V}_{2N}||\right]. \end{cases} \tag{9.44}$$

We can then consider Equation 9.43 as the expression of a quadratic form Q which associate a scalar z_0 to any vector $\vec{Z} = z_1\vec{V}_1' + z_{2n}\vec{V}_2'$. Such a quadratic form may be described as

$$z_0 = \vec{Z}^T[Q]\vec{Z} \quad \text{with} \quad [Q] = \begin{pmatrix} k_{11}' & k_{12}'/2 \\ k_{12}'/2 & -k_{22}' \end{pmatrix}. \tag{9.45}$$

The simplification of our problem relies then in a rotation of the basis vectors in such a way that the quadratic form matrix $[Q]$ is diagonal. The eigenvalues of $[Q]$ are given by

$$\ell_1 = \frac{k_{11}' - k_{22}' - \sqrt{\Delta}}{2} \quad \text{and} \quad \ell_2 = \frac{k_{11}' - k_{22}' + \sqrt{\Delta}}{2}. \tag{9.46}$$

with $\Delta = (k_{11}' + k_{22}')^2 + k_{12}'^2$. Thanks to this rotation of the basis vectors, Equations 9.41 and 9.43 become

$$S_{cs} = \ell_1\dot{\chi}^2 + \ell_2\ddot{\chi}^2. \tag{9.47}$$

As already stated in Section 9.4.4, S_{cs} is a VΓ rv with the following PDF parameters:

$$\mu = 0, \quad \alpha = \frac{\ell_1^2 + \ell_2^2}{4\ell_1^2\ell_2^2}, \quad \beta = \frac{\ell_1^2 - \ell_2^2}{4\ell_1^2\ell_2^2}, \quad \lambda = \frac{1}{2}. \tag{9.48}$$

9.4.6 Generalization to Larger Degrees of Freedom

In the case of 2η DoF, i.e. real part + imaginary part multiplied by η averaged uncorrelated spectra, the only change to apply concerns the parameter λ in Equations 9.31 and 9.48 which becomes $\lambda = \eta$. According to [157, Equation 12 p.80] we have the following relation:

$$K_{n+\frac{1}{2}}(z) = \left(\frac{\pi}{2z}\right)^{\frac{1}{2}} e^{-z} \sum_{r=0}^{n} \frac{(n+r)!}{r!(n-r)!(2z)^r} \tag{9.49}$$

with $n \in \mathbb{N}$ and $z \in \mathbb{C}$. Moreover $\eta \in \mathbb{N}^*$ which leads to the relation $n = \eta - 1$. Therefore let us expand Equation 9.30 using Equation 9.49:

$$p(x) = \frac{\kappa(\alpha,\beta)^{\eta}\varepsilon(x,\mu,\alpha,\eta)}{\Gamma(\eta)} e^{-\alpha|x-\mu|+\beta(x-\mu)} \tag{9.50}$$

with the following parameters:

$$\begin{aligned} \kappa(\alpha,\beta) &= \frac{\alpha^2-\beta^2}{2\alpha} \qquad \Gamma(\eta) = (\eta-1)! \\ \varepsilon(x,\mu,\alpha,\eta) &= \sum_{r=0}^{\eta-1} \frac{(\eta+r-1)!|x-\mu|^{\eta-r-1}}{r!(\eta-r-1)!(2\alpha)^r} \end{aligned} \tag{9.51}$$

9.4.7 Validation of the Theoretical Probability Laws by Monte Carlo Simulations

9.4.7.1 Algorithm Description

According to Section 9.4.5.2 the probability density of $\widehat{S}_{cs}$, equal to the difference of two independent χ^2 r.v, can now be calculated using the function $p(x)$ of the Equation 9.50 by assigning the values to the parameters in Equations 9.31 and 9.48. In order to perform this comparison we use two algorithms, one for Monte Carlo (MC) simulation and the other one for computing Equation 9.50.

– *MC simulation algorithm*

The simulation algorithm follows these six steps

S1: Assignement of the two noise levels $\sigma^2_{W,1}$, $\sigma^2_{W,2}$, signal level σ^2_R and the number of averaging spectra η.

S2: Drawing of W_1, W_2, R, following a normal centered distribution with respectively $\sigma_{W,1}$, $\sigma_{W,2}$, σ_R as standard deviation.

S3: Computation of $\widehat{S}_{cs} = (W_1 + R)(W_2 + R)$.

S4: Repetition 2η times of the steps S2 to S3 and sum all $\widehat{S}_{cs}$ values.

S5: Repetition $N = 10^7$ times of the steps S2 to S4 of this sequence.

S6: Drawing the histogram of $\widehat{S}_{cs}$.

In all simulations, we chose a number of DoF $\nu = 2\eta$ in order to have a real and imaginary part in agreement with the experiment shown in Figure 6.1.

– Modeling algorithm
The modeling algorithm follows also 6 steps:

S1: Assignement of the two noise levels $\sigma^2_{W,1}$, $\sigma^2_{W,2}$, signal level σ^2_R and the number of averaging spectra η.

S2: **Independent basis**

- Computation of coefficients v_1^2, v_2^2 according to Equation 9.26
- if $\sigma^2_{W,1} = \sigma^2_{W,2}$ go to step S5 else perform steps S3 and S4

S3: **Orthogonalization of the basis**

- Computation of coefficients k_{W_1R1}, k_{W_1R2n}, k_{W_2R1}, k_{W_2R2n} to determine the new basis according to Equation 9.41
- Normalization of the basis by determing coefficients k'_{11}, k'_{22}, k'_{12} according to Equation 9.43

S4: **Vector rotation**

- Diagonalization of the matrix Q according to Equation 9.45
- Computation of its roots l_1 and l_2

S5: Compute the coefficients α, β, and $\lambda = \eta$ according to Equations 9.31 and 9.48.

S6: Plotting the probability density with Equation 9.50.

9.4.7.2 When can the Instrument Noises be Assumed to be "About the Same"?

Although the problem is quite simple when the instrument noises $\sigma^2_{W,1}$ and $\sigma^2_{W,2}$ are the same (see Section 9.4.4), it becomes more complex when $\sigma^2_{W,1} \neq \sigma^2_{W,2}$. The question is then how far can we assume that $\sigma^2_{W,1} \approx \sigma^2_{W,2}$ and then use the particular case formalism of Section 9.4.4? In order to answer this question, we use Monte-Carlo simulations which were performed according to Section 9.4.7.1.

Afterwards we perform a histogram of these realizations and compare it first with the PDF obtained from the model without rotation, i.e. by using the VΓ parameters of Equation 9.31, and next with the PDF obtained from the model with rotation, i.e. by using the VΓ parameters of Equation 9.48. Figure 9.6 shows an example of such a comparison. In this case ($\sigma_{W,1}^2 = 2, \sigma_{W,2}^2 = 1/2, \sigma_R^2 = 0$), the PDF of the model with rotation is in perfect agreement with the histogram whereas there are large discrepancies with the PDF of the model without rotation. We have thus a first result: the model without rotation should not be used when the ratio $\sigma_{W,1}^2/\sigma_{W,2}^2 \geq 4$.

To improve the efficiency of the test, we compute the theoretical quantiles by using the model without rotation and then deduce from them the theoretical confidence intervals which are often used (68 %, 90 %, 95 % and 99 %). These quantiles and intervals are compared to the ones obtained from the simulation histogram. In one example of Table 9.4, which corresponds to the case plotted in Figure 9.6, the confidence intervals are strongly overestimated. For instance, the expected 68 % confidence interval is significantly too large since it encompasses an interval of 76 %. Similarly, the expected 90 % interval is actually a 94 % interval. This reinforces our decision of using the model with rotation for a noise variance ratio ≥ 4.

We use these two approaches, i.e. PDF curve as well as confidence intervals, for many different parameter sets (see Table 9.4). In any case, the agreement between the model with rotation and the Monte-Carlo simulation histograms were perfect, since the residual deviations can be largely assumed to be due to the finite sample number of the simulation (less than 0.05 % of the CDF). However, this test is very interesting for the model without rotation since it allows us to answer to the question which is the title of this section: when can the instrument noises be assumed to be "about the same"? Table 9.4 is very useful in this connection. In a first step, let us study the case where the number of DoF is two and there is no signal since it is the case which is the most sensitive to the difference between the noise levels. We can see on this table that the model without rotation is perfect when the two noise levels are equal ($\sigma_{W,2}^2 = 2$), fair when the ratio of the noise levels is equal to 2 ($\sigma_{W,2}^2 = 1$), at the limit of acceptance when the ratio is three but not suitable for a ratio ≥ 4. The other columns of Table 9.4, obtained with eight DoF and with $\sigma_R^2 = \sigma_{W,1}^2/4$, confirm that the model without rotation is acceptable when the ratio of the noise variances is equal to 2.

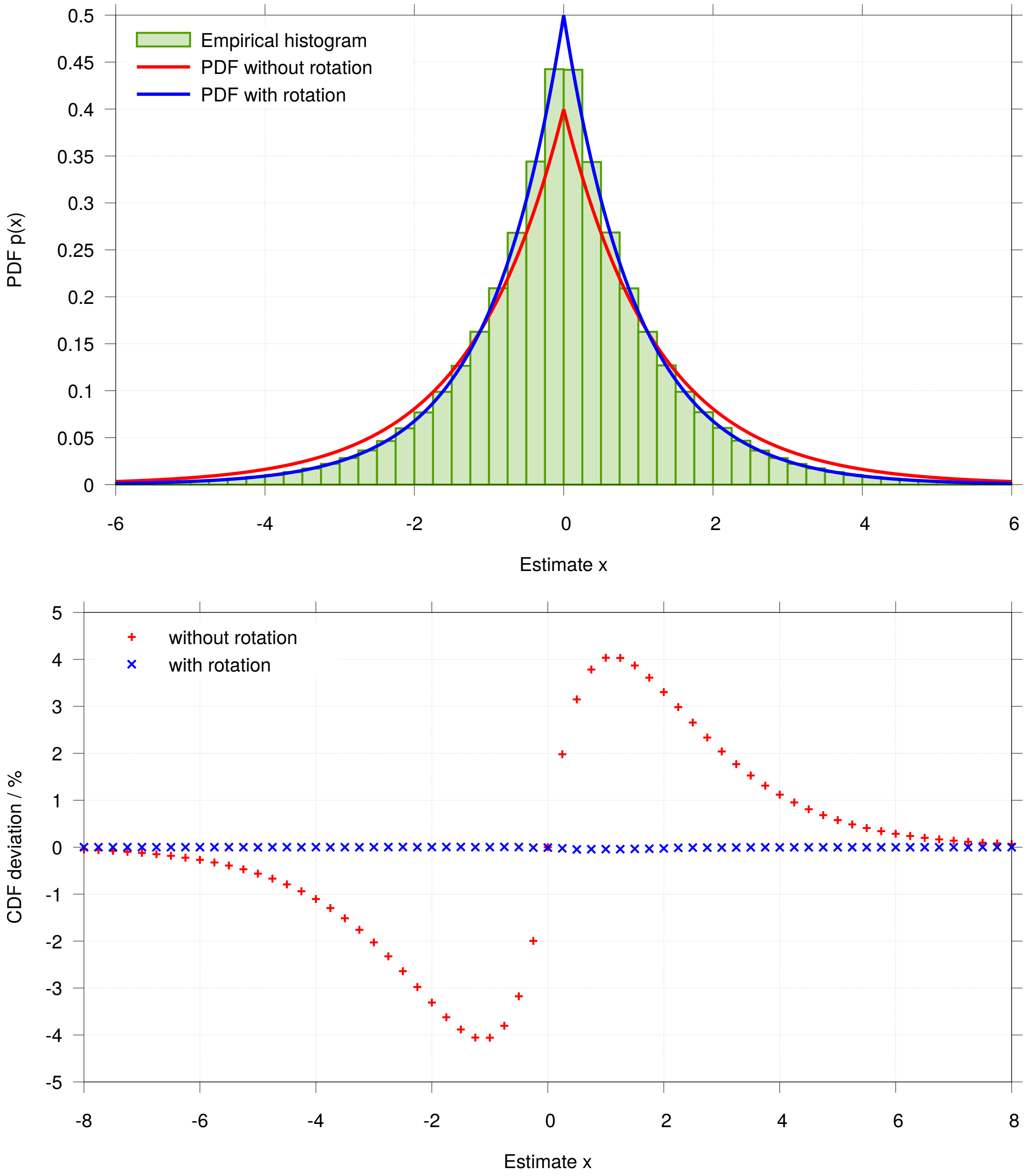

Figure 9.6: Comparison of the empirical and theoretical PDF (above) with and without rotation of the basis vectors. The deviations between the empirical and the theoretical CDF are given in the bottom plot. The variances are: $\sigma_R^2 = 0, \sigma_{W,1}^2 = 2, \sigma_{W,2}^2 = 1/2$ and there are two DoF.

Table 9.4: Comparison of the expected quantiles and intervals. The expected quantiles (above) and intervals (below) are computed by using the parameters from Equation 9.31 with empirical probabilities. For all realizations $\sigma_{W,1}^2 = 2$.

Expected probabilities (%)	**True probabilities (%)**					
	Degrees of freedom: 2				DoF: 8	
	σ_R^2 =0				0	0.5
	$\sigma_{W,2}^2$ =2	1	2/3	1/2	1	1
Quantiles						
0.5	0.50	0.39	0.25	0.16	0.35	0.39
2.5	2.50	2.10	1.58	1.19	1.98	2.13
5.0	5.00	4.36	3.51	2.82	4.18	4.44
16.0	16.00	14.95	13.43	12.05	14.68	15.18
50.0	50.00	50.01	50.00	50.00	50.00	49.99
84.0	84.00	85.07	86.59	87.96	85.32	84.58
95.0	95.00	95.65	96.50	97.19	95.82	95.37
97.5	97.50	97.91	98.43	98.82	98.02	97.73
99.5	99.50	99.62	99.75	99.84	99.65	99.57
Intervals						
68.0	68.00	70.12	73.16	75.91	70.64	69.41
90.0	90.00	91.29	92.98	94.37	91.64	90.93
95.0	95.00	95.82	96.84	97.63	96.04	95.60
99.0	99.00	99.23	99.50	99.68	99.30	99.18

Then we recommend to use the vector rotation process if the ratio of the noise variance greater than 2.

9.5 Inverse Problem

We have already studied the direct problem, i.e. the statistics of the cross-spectrum estimates knowing the signal level (the noise level is assumed to be known). Now, we have to deduce the inverse problem from the direct problem, i.e. the statistics of the signal level from a cross-spectrum (or spectrum average) estimate.

9.5.1 Principle of the Method

The bayesian statistician has to solve the inverse problem in order to define a confidence interval for the true variance σ_R^2, given a set of measurements and a priori information. Thereby the cross-spectrum measurement $\widehat{S}_{cs}$ is now fixed as well as the instrument noise levels $\sigma_{W,1}^2$ and $\sigma_{W,2}^2$, whereas the signal true variance σ_R^2 appears as a random variable. Now, we have to deduce the inverse problem from the direct problem, i.e. the statistics of the signal level from a c-s (or s.a) estimate. In a classical Bayesian formalism, this is achieved by using the Bayes formula [158–161] which states

$$\begin{cases} p(\theta|\widehat{S}_{cs}) \propto p(\widehat{S}_{cs}|\theta) \cdot \pi(\theta) \\ \int_0^{\infty} p(\theta|\widehat{S}_{cs}) d\theta = 1 \end{cases} \tag{9.52}$$

where $\pi(\theta)$ stands for the "*prior*" of the argument, i.e. the "*a priori*" PDF of the argument before any measurement. Moreover $p(\widehat{S}_{cs}|\theta)$ is the PDF which corresponds to Equation 9.30 determined in the direct problem. It remains to determine the prior $\pi(\theta)$ (i.e. the PDF before any measurement) to compute the a posteriori density.

One of the main issue of Bayesian analysis concerns the choice of this prior. This prior has to be a PDF and according to the litterature on the study of pulsars [162–164] log-uniform distributed as we have no a priori knowledge about the behavior of the parameter θ. We use an improper prior [165] as an uniformative prior [166], so the prior is the reciprocal function of the parameter θ. This ensures that all order of magnitudes have the same probability as shown on Figure 9.7 (right).

The choice of θ is subject to discussion and the reader should refer to [161, Appendix B]. The quantity that can be actually measured is the sum of the signal and the measurement noise. Hence the prior should be accordingly given as a function of this sum. In other words, it is not possible to have any information on a signal with a level much smaller than the measurement noise. Hence choosing a prior function of $\sigma_W^2 + \sigma_R^2$ ensures that the corresponding magnitude order of σ_R^2 do not dominate the a posteriori probability distribution according to Figure 9.7 (right). The measurement noise level decreases as η^{-1}, according to [59, Equation 11], when averaging over different spectra realizations η. So it should depend on the number of DoF $\nu = 2\eta$ (i.e. taking in account the real and imaginary part). From these considerations, we choose the following prior according to Figure 9.7 (left):

$$\pi(\theta) = \frac{1}{\theta} = \frac{1}{\sigma_W^2/\nu + \sigma_R^2}, \tag{9.53}$$

where $\sigma_W^2 = (\sigma_{W,1}^2 + \sigma_{W,2}^2)/2$ is the known, "not random" averaged noise level. It also turns out that θ is the expectation of the s.a estimate according to Equation 9.4 when the bias is not removed.

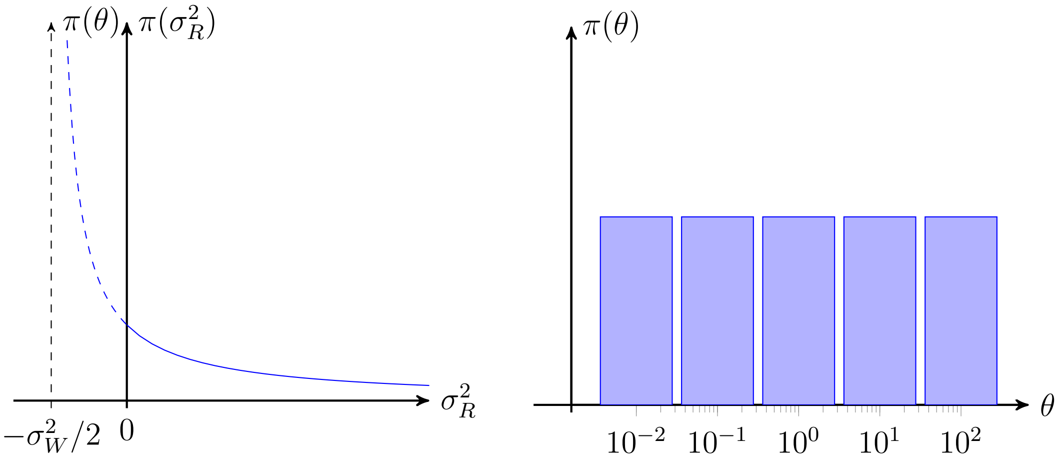

Figure 9.7: Prior of the sum of the noise σ_W^2 and signal σ_R^2 levels (left) and its log-histogram (right) in the case when there is no averaging spectra (i.e. $\nu = 2$).

9.5.2 Check of the Posterior Probability Density Function

According to Equation 9.50, for two DoF or $\eta = 1$ spectrum average and the particular case $\sigma_{W,1}^2 = \sigma_{W,2}^2 = \sigma_W^2$, we know that

$$p\left(\widehat{S}_{cs}|\sigma_R^2\right) = \frac{e^{\widehat{S}_{cs}/\sigma_W^2}}{2(\sigma_W^2 + \sigma_R^2)}. \tag{9.54}$$

Therefore, the posterior PDF of the cross-spectrum estimator is

$$\begin{cases} p\left(\sigma_R^2|\widehat{S}_{cs}\right) \propto \dfrac{e^{\widehat{S}_{cs}/\sigma_W^2}}{2(\sigma_W^2+\sigma_R^2)(\sigma_W^2+2\sigma_R^2)} & \text{if} \quad \widehat{S}_{cs} \leq 0 \\ \\ p\left(\sigma_R^2|\widehat{S}_{cs}\right) \propto \dfrac{e^{-\widehat{S}_{cs}/(\sigma_W^2+2\sigma_R^2)}}{2(\sigma_W^2+\sigma_R^2)(\sigma_W^2+2\sigma_R^2)} & \text{if} \quad \widehat{S}_{cs} \geq 0. \end{cases} \tag{9.55}$$

It can be noticed that these posterior PDF depend on σ_R^2 whereas the other parameters are known. We have checked this posterior PDF by using the inverse problem Monte-Carlo algorithm we already used in [152, Section IV.B.1)] and [167, Section IV.A.]. The principle is the following:

S1: Select a target estimate $\widehat{S}_{cs} = S_0$.

S2: Draw at random the signal level σ_R^2 according to

$$\sigma_R^2 = 10^{\left[\eta + u_{[0,1]}(e_{max} - \eta)\right]} - \frac{\sigma_W^2}{2} \tag{9.56}$$

where $\eta = \log_{10}(\sigma_W^2/2)$ and $u_{[0,1]}$ is a pseudo-random function which is uniform within $[0, 1]$. This draw ensures the parameter follows the prior of Equation 9.53 up to $10^{e_{max}}$. We have chosen $e_{max} = 4$ which is in accordance with Figure 9.7

S3: Draw at random (Gaussian) the noise and signal estimates W_1, W_2, R and compute the measurements X_1, X_2 according to Equation 9.2.

S4: Compute the estimate $\widehat{S}_{cs}$.

S5: Compare the estimate $\widehat{S}_{cs}$ with the target S_0: if $\widehat{S}_{cs} = S_0 \pm q$, store the current σ_R^2 value as it is able to generate an estimate equal to the target; otherwise throw this σ_R^2 value. We have chosen $q = (S_0 + \sigma_W^2/2)/50$ when $S_0 > 0$ and $q = \sigma_W^2/100$ when $S_0 \leq 0$.

S6: Go to step 2.

S7: Stop when a set of 10 000 σ_R^2 values is reached.

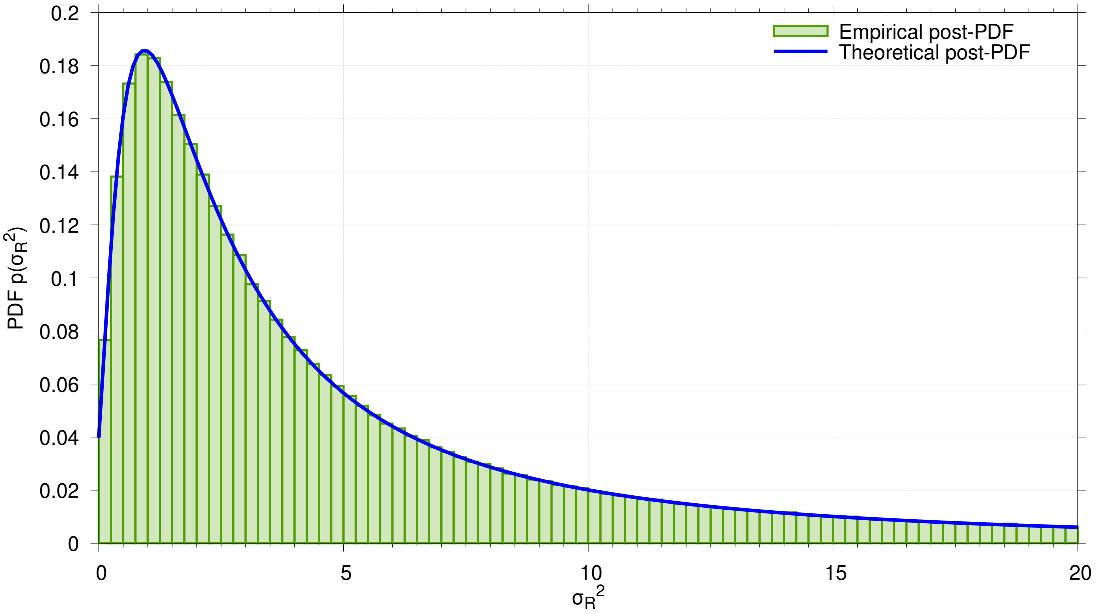

Figure 9.8: Comparison of the empirical and theoretical posterior PDF for a noise level $\sigma_W^2 = 1$ a.u and a target estimate $S_0 = 1$ a.u.

It must be noticed that such an algorithm is obviously not able to justify the choice of the prior since this prior is included in the algorithm. It will only ensure that no mistake has been done in the expression of the posterior PDF.

Figure 9.8 shows the comparison of the posterior PDF computed according to Equation 9.55 (blue curve) and the histogram obtained thanks to the inverse problem

Target	5 % bound		95 % bound		True prob. (%)	
S_0 (a.u)	Emp	Theo	Emp	Theo	L. b.	H. b.
-1.00	0.035	0.036	14.04	13.65	5.270	94.90
0.00	0.034	0.036	15.11	13.65	5.220	94.53
0.10	0.035	0.038	14.52	14.27	5.410	94.91
0.20	0.040	0.040	14.98	14.90	4.970	94.96
0.32	0.043	0.043	15.87	15.66	5.060	94.94
0.50	0.050	0.048	17.37	16.90	4.850	94.87
1.00	0.062	0.065	20.40	20.14	5.120	94.93
2.00	0.116	0.118	27.61	28.65	5.060	95.18
3.16	0.225	0.224	38.19	39.08	4.910	95.08
5.00	0.476	0.475	57.15	56.55	4.900	94.91
10.00	1.295	1.306	109.66	104.82	5.090	94.78

Table 9.5: Comparison of the quantiles (5 % and 95 %) obtained by Monte-Carlo simulation (empirical) and by the posterior CDF with a noise level $\sigma_W^2 = 1$ a.u. The 5% bounds are given here even if they are not relevant (they are generally less than 100 times lower than the 95% bounds).

Monte-Carlo algorithm (green boxes) with a noise level $\sigma_W^2 = 1$ a.u and a target estimate $S_0 = 1$ a.u. We can verify that the agreement is excellent.

Table 9.5 compares the quantiles at 5% and 95% obtained by the inverse problem Monte-Carlo algorithm (denoted “Emp” for empirical) and by the integration of the posterior PDF (denoted “Theo” for theoretical), i.e. the posterior CDF, for different values of target and for a noise level $\sigma_W^2 = 1$. Here also the agreement is very good whether for the 5% and 95% bounds or for the true probabilities of the theoretical bounds. Moreover, the fluctuations of the empirical bounds proves that the slight differences between empirical and theoretical values are due to the fluctuations of the empirical bounds because of the limited number of realizations ($10\,000$) of the inverse problem Monte-Carlo algorithm.

9.5.3 KLT Method

The KLT method stands for “Karhunen-Loève Tranform” and was developed in [167]. In that paper, KLT has proved to be as efficient as well as a rigorous method, making the most of the property of “*sufficient statistics*". However the cross-spectrum estimate does not have this property (see [168]). The KLT method requires knowledge of spectral densities in addition to covariances. Therefore, we can have multiple combinations of KLT estimate in order to get the same cross spectrum estimate. First let us remind the theory. Then in a second time, we will explain what can bring the KLT method in addition to the cross-specrum one.

9.5.3.1 A Posteriori Distribution

The KLT method relies on the use of X_1, and X_2 measurements according to Equation 6.1, which are Gaussian r.v. instead of the product of W_1W_2, W_1R, W_2R and R^2, which are linear combination of Bessel of the second kind functions and χ^2 random variables. The main advantage of this approach lays in the property of the Gaussian r.v. which remain Gaussian when they are linearly combined. However, these measurements are not independent. That is why we aim to determine two linear combinations of these r.v. that are independent one of each other. Hence we define the covariance matrix between X_1 and X_2 given by

$$M = \begin{pmatrix} \sigma_{W,1}^2 + \sigma_R^2 & \sigma_R^2 \\ \sigma_R^2 & \sigma_{W,2}^2 + \sigma_R^2 \end{pmatrix}. \tag{9.57}$$

The KLT consists in using the r.v. corresponding to the diagonalization of this matrix. In order to simplify the equations we study solely the case where $\sigma_{W,1}^2 = \sigma_{W,2}^2 = \sigma_W^2$. The eigenvalues of M are

$$\begin{aligned} \lambda_1 &= \sigma_W^2 + 2\sigma_R^2 \\ \lambda_2 &= \sigma_W^2 \end{aligned} \tag{9.58}$$

with the following normalized eigenvectors,

$$V_1 = \tfrac{1}{\sqrt{2}} \begin{pmatrix} 1 \\ 1 \end{pmatrix} \qquad V_2 = \tfrac{1}{\sqrt{2}} \begin{pmatrix} 1 \\ -1 \end{pmatrix} \tag{9.59}$$

The likelihood function is then given by

$$p(\widehat{S}_{KLT}|\sigma_R^2) = \prod_{i=1}^{2} \frac{1}{\lambda_i^{\nu/2}} \exp\left(- \frac{\sum_{j=1}^{\nu} \widehat{z}_{i,j}^2}{2\lambda_i} \right) \tag{9.60}$$

The numerator of the exponential argument is then the only term that depends on the actual measurements:

$$\widehat{z}_{i,j}^2 = V_{i,1}^2 X_{1,j}^2 + V_{i,2}^2 X_{2,j}^2 + 2V_{i,1}V_{i,2}\widehat{S}_{KLT,j} \tag{9.61}$$

where $||V_i||^2 = \sum_j V_{i,j}^2$. So the KLT method involve the spectral density X_1^2, X_2^2 in addition to the cross-spectrum. Keeping the same prior defined in Equation 9.53 we have the following a posteriori density,

$$\begin{cases} p(\sigma_R^2|\widehat{S}_{KLT}) \propto \dfrac{1}{\sigma_W^2/2+\sigma_R^2} \cdot p(\widehat{S}_{KLT}|\sigma_R^2) \\ \displaystyle\int_{\mathbb{R}} p(\sigma_R^2|\widehat{S}_{KLT}) d\sigma_R^2 = 1. \end{cases} \tag{9.62}$$

9.5.3.2 Validation of the Method by Monte Carlo Simulation

In order to validate the KLT method, we have compared its results to Monte Carlo simulations. In comparison to the c-s method the spectral densities have to be chosen. The algorithm is as follows:

S1: Select a noise level $\sigma_W^2 = \sigma_{W,1}^2 = \sigma_{W,2}^2$, a target $\widehat{S}_{KLT} = S_0$ and a combination $X_1 = X_{1,0}$, $X_2 = X_{2,0} = S_0/X_{1,0}$ for all the DoF.

S2: Draw at random the signal level σ_R^2 according to Equation 9.56. This draw ensures that the parameter follows the prior of Equation 9.53 up to $10^{e_{max}}$. We have chosen $e_{max} = 4$.

S3: Draw at random (Gaussian) the noise and signal estimates W_1, W_2, R and compute the measurements X_1, X_2 according to Equation 9.2.

S4: Compare the estimates X_1, X_2 with the targets $X_{1,0}$, $X_{2,0}$ for all the DoF: if $X_1 = X_{1,0} \pm q$, $X_2 = X_{2,0} \pm r$, store the current σ_R^2 value as it is able to generate an estimate equal to the target; otherwise throw this σ_R^2 value. We have chosen a precision q, r of tenths of respectively $X_{0,1}$ and $X_{2,0}$.

S5: Go to step 2.

S6: Stop when a set of N σ_R^2 values is reached. The number of values N depending on the computation time.

9.5.3.3 Results and Discussion

Figure 9.9 shows the comparison between the PDF of VΓ method developed in Section 9.4 and the PDF of KLT method for two different realizations. The theoretical post-PDF fits very well the empirical histogram for each method. Different combinations of the spectral density X_1 and X_2 were tested and are given in Table 9.6. Indeed KLT$_{r1}$ and KLT$_{r2}$ realizations do not give the same PDF unlike the VΓ method for a given c-s estimate. KLT$_{r1}$ has then a peak which is higher than the VΓ method whereas KLT$_{r2}$ has a smaller one. This is explained by a more stringent confidence interval for KLT$_{r1}$ than

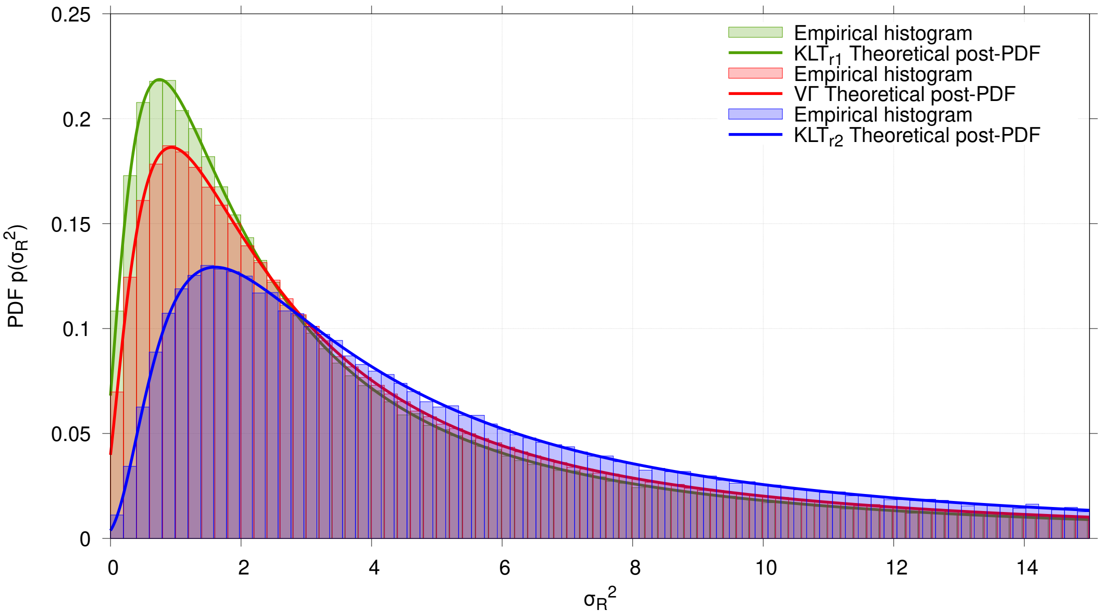

Figure 9.9: Comparison of the empirical and theoretical posterior PDF for VΓ and KLT methods with a noise level $\sigma_W^2 = 1$ a.u and a target estimate $S_0 = 5$ a.u. KLT$_{r1}$ and KLT$_{r2}$ are the same method but differ by their combination of spectral density X_1^2 and X_2^2 which are fixed, see Table 9.6, whereas they are r.v. for the VΓ method.

VΓ, and a less stringent for KLT$_{r2}$ as refered in Table 9.6. The 95 % quantiles obtained with MC simulations are in a good agreement with the theoretical ones, especially for KLT$_{r1}$ and VΓ methods. It is explained by the number of data which is not the same for all of these simulations. VΓ, KLT$_{r1}$ and KLT$_{r2}$ have respectively $1\,000\,000$; $500\,000$ and $245\,000$ data. VΓ MC simulations takes only two minutes whereas it needs respectively 54 hours and 35 days using 17 cores, for KLT$_{r1}$ and KLT$_{r2}$. KLT$_{r1}$ is chosen to have the spectral density combination which leads to the most stringent confidence interval. Whereas KLT$_{r2}$ is chosen to be more defavourable than the general case VΓ using only the knowledge of the cross-spectrum measurement.

The KLT method can then have a slightly more stringent confidence interval than the cross-spectrum method using VΓ for certain case. However it requires to have the knowledge of both spectral density of each channel. So the KLT method is preferred when the spectral densities are known.

Table 9.6: Comparison of the 95 % quantiles obtained by Monte-Carlo simulation (empirical) and by the posterior CDF. The 95 % quantiles are computed for a noise level $\sigma_W^2 = 1$ and a target estimate $S_0 = 5$ a.u.

Method	Measurement				95 % bound	
	X_1'	X_1''	X_2'	X_2''	Emp	Theo
VΓ	rv	rv	rv	rv	56.4	56.6
KLT$_{r1}$	1.6	1.6	1.6	1.6	48.4	48.3
KLT$_{r2}$	4.0	0.6	2.5	1.0	82.3	80.8

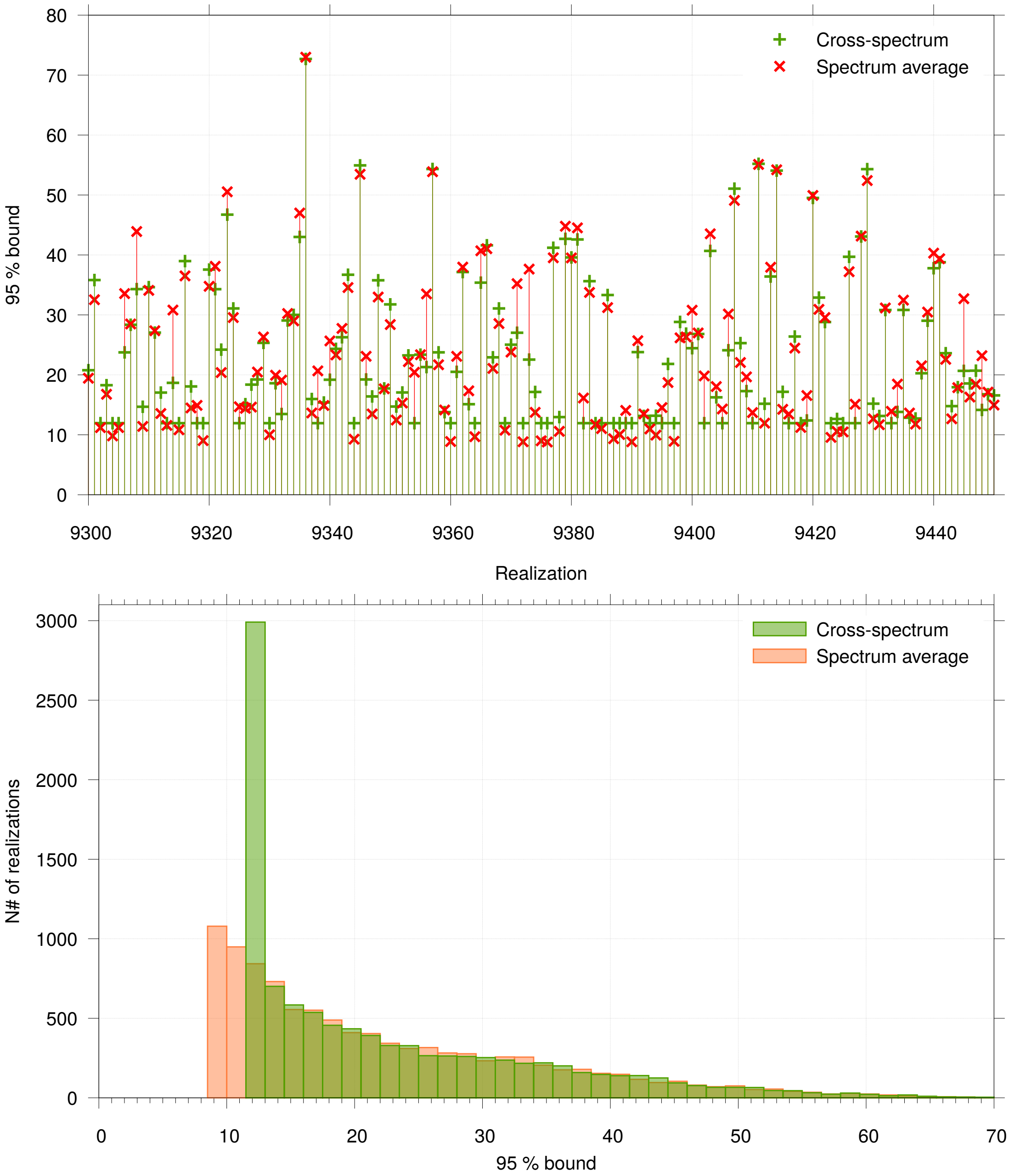

Figure 9.10: Set of 150 realizations of 95 % bounds for cross-spectrum (green +) and spectrum average (red ×) and their histograms (below).

9.5.4 Comparison of the 95 % confidence limits: cross-spectrum vs spectrum average

The PDF of a s.a estimate knowing the signal level is a classical χ^2-PDF with two degrees of freedom (real and imaginary parts) shifted by $-\sigma_W^2/2$:

$$p\left(\widehat{S}_{sa}|\sigma_R^2\right) = \frac{\exp\left[-\dfrac{\widehat{S}_{sa}+\sigma_W^2/2}{\sigma_W^2+2\sigma_R^2}\right]}{\sigma_W^2+2\sigma_R^2}. \tag{9.63}$$

Choosing the prior of Equation 9.53 yields the following posterior PDF

$$p\left(\sigma_R^2|\widehat{S}_{sa}\right) \propto \frac{\exp\left[-\dfrac{\widehat{S}_{sa}+\sigma_W^2/2}{\sigma_W^2+2\sigma_R^2}\right]}{(\sigma_W^2+2\sigma_R^2)^2}. \tag{9.64}$$

Thanks to the posterior PDFs of both estimators, we can compute the 95% bounds for both estimators by integrating these PDF. In order to compare the efficiency of the estimators $\widehat{S}_{cs}$ and $\widehat{S}_{sa}$, we used the following process:

S1: Choose the noise and the signal levels.

S2: Draw at random (Gaussian) the noise and signal estimates W_1, W_2, R and compute the measurements X_1, X_2 according to Equation 9.2.

S3: Compute the estimates $\widehat{S}_{cs}$ and $\widehat{S}_{sa}$.

S4: Compute the 95% bounds for both estimators by integrating the posterior PDF according to Equations 9.55 and 9.64.

S5: Compute the difference between these 95% bounds.

S6: Go to step 2.

S7: Stop the process after $10\,000$ iterations.

An example of result of such a process is given in Figure 9.10 for $\sigma_W^2 = 1$ a.u and $\sigma_R^2 = 1$. The upper graph shows that the 95% bounds obtained by both estimators have a relatively high dispersion (between 10 and 100 a.u) and are generally very close together. Moreover, in some cases the c-s bound is the most stringent and in other cases, which seems a little be more frequent, the s.a bound is the most stringent. The lower graph of Figure 9.10 plots the histograms of the bounds of both estimators. The only differences between them are concentrated in the three first bins, the following bins being quite the

σ_R^2	Best %	Min %	Mean %	Max %
0.00	19.90	-85.52	16.56	27.72
0.10	23.80	-93.56	16.10	27.73
0.20	27.30	-139.87	16.10	27.75
0.32	28.00	-149.70	16.24	27.75
0.50	30.60	-145.66	16.14	27.74
0.71	32.40	-168.26	16.81	27.71
1.00	33.51	-209.98	14.35	27.74
1.41	36.00	-210.22	13.26	27.66
2.00	37.60	-169.03	12.52	27.59
3.16	35.40	-203.49	10.91	27.70
5.00	37.30	-187.15	8.60	27.67
10.00	40.00	-132.69	5.31	26.70

Table 9.7: Comparison of the 95% bounds given by the c-s and s.a estimators for a noise level $\sigma_W^2 = 1$ a.u. The second column ("Best") exhibits the percentage of cases where the 95% bound from the c-s estimator is more stringent (lower) than the 95% bound obtained by the s.a estimator. The following columns show respectively the minimum, the mean and the maximum values of the relative differences between the 95% bounds of both estimators: $(B95_{cs} - B95_{sa})/B95_{cs}$.

same. The first bin of the c-s estimator is particularly high: this is due to the negative estimates which yields all the same minimal bound. Indeed, Equation 9.55 shows that for a negative estimate, the argument of the exponential of the PDF does not depend on the signal level σ_R^2 which means that its scale factor, i.e. its horizontal dimension, is constant and only the amplitude, i.e. its vertical dimension, is affected. But, since the PDF is normalized in such a way that its integral from 0 to $+\infty$ is equal to one, it remains the same for all negative $\widehat{S}_{cs}$ estimate. From these considerations, we can deduce that the main differences between the bounds of both estimators will appear for the negative estimates, the other ones being of the same order of magnitude.

A more quantitative analysis can be found in Table 9.7: for different signal level values (the noise level is set to one a.u), this table gives the proportion of most stringent bound given by the c-s estimator. This percentage increases from 20% when there is no signal to 40% when the signal level is 10 times the noise level, i.e. when the number of negative estimates decreases, which is consistent with the considerations we formulated from the histogram of Figure 9.10. It is highly probable that the percentage tends toward 50% when $\sigma_R^2 \gg \sigma_W^2$, i.e. when the probability to get a negative $\widehat{S}_{cs}$ estimate tends toward 0. On the other hand, Table 9.7 shows that the mean deviation between the bounds obtained by both estimator is as low as $10 \sim 15\%$ and that the maximum deviation, i.e. when the c-s bound is higher the s.a bound, does not exceed 28%. However, the minimum deviation can be of the order of -200% meaning that in some rare cases the s.a 95% bound can be two times higher than the c-s bound. Such an occurrence is visible on the top graph of Fig. 9.10, at realizations 9373 and 9445.

Nevertheless, these results definitely show that the difference between the spectrum average estimator and the cross-spectrum estimator is really small.

9.6 Conclusion

The method developed, VΓ, provides the Probability Density Function of the signal level studied when using the cross-spectrum method. It allows the determination of confidence intervals through numerical integration, where only the high bound has a physical meaning. It is especially relevant for one or several measurements of the cross-spectrum as the PDF will tend to a Gaussian distribution for many DoF.

VΓ is a rigorous method since it is the exact density solution of the cross-spectrum real part statistics, with no approximation. We shall notice that the noise level of each measurement instruments has to be known. If these noise levels are the same except at a factor of four and smaller, we can assume that all the theoretical part of orthogonalizing and the rotation of the basis is not necessary. This method works whatever the number of measurement spectra and noise level.

However using KLT method to compute the confidence interval is a more rigorous method because it uses the knowledge of the spectral density in addition to the cross-spectrum. That is why we recommend to use the KLT method which turns out to be a slightly better estimator than VΓ.

In order to compare the efficiency of the cross-spectrum estimator and the spectrum average estimator to assess the signal level, we first calculated the variances of these estimators and observed that the variance of the latter estimator is lower than the variance of the former one, suggesting that the spectrum average estimator is the best. We decided then to compare the Bayesian limit at 95% of confidence of the signal level given by both estimators. Here also we found a slight advantage for the spectrum average estimator. This estimator is then the winner of this trial, at least for two degrees of freedom. An extension of this study will be presented for higher degrees of freedom in the next chapter.

Nevertheless, considering on one hand the very small differences between the efficiencies of these estimator and on the second hand the significant discrepancies between the 95% bounds that may occasionally appear, the wiser solution could be to systematically compute the bounds given by both estimators and choose the lower one.

Finally, we must also remind that the second estimator implies a perfect knowledge of the noise level since half of it has to be subtracted from the spectrum average. The least uncertainty about this noise level knowledge could drastically decrease the efficiency of the spectrum average method. The estimator of the c-s does not require the knowledge of the noise variances however the c-s posterior PDF does.

CHAPTER 10

Generalization to multiple instruments

In this chapter we are focusing on one bin of the periodogram of a single simultaneous measurement with n instruments as represented on Figure 6.1. We will compare the Bayesian confidence interval of the red noise parameter using two estimators, the spectrum average and the cross-spectrum. We have shown in chapter 9 in the case of two instruments that the cross-spectrum estimator leads to the Variance-Gamma distribution. A generalization to n devices based on the Fourier transform of characteristic functions is provided here, with the example of the observation of millisecond pulsars with five radio telescopes.

10.1 Two estimators of the PSD

According to Figure 6.1 the noises of each instrument W_i are all different. Then it is appropriate to use a weighted average, where the weights α_i are to be found for the optimum detection of R. Thus it comes

This chapter is done by the author under the supervision of François Vernotte, Éric Lantz and Enrico Rubiola. It is based on an article published as [169].

$$\widehat{M} = \frac{\sum_i^n \alpha_i X_i}{\sum_i^n \alpha_i}, \tag{10.1}$$

where n is the number of instruments and $X_i = R + W_i$. Given that we have only one realization of the red noise collected on n instruments, σ_R^2 can not be estimated from the fluctuations between instruments: R appears here as a deterministic signal to be estimated, which does not influence the fluctuations of the estimator **from one telescope to another**. The variance of the estimate $\widehat{M}$ is

$$\mathbb{V}\left[\widehat{M}\right] = \sigma_R^2 + \frac{\sum_i^n \alpha_i^2 \sigma_{W,i}^2}{\left[\sum_i^n \alpha_i\right]^2}. \tag{10.2}$$

An optimal choice is obtained by solving,

$$\frac{\partial \mathbb{V}\left[\widehat{M}\right]}{\partial \alpha_i} = 0 \tag{10.3}$$

which leads to the solution,

$$\alpha_i = \frac{1}{\sigma_{W,i}^2}. \tag{10.4}$$

Therefore the inverse-variance weighted average, described in [170] with applications examples, has the least variance among all weighted averages. Then Equation 10.2 becomes

$$\mathbb{V}\left[\widehat{M}\right] = \sigma_R^2 + \left(\sum_i^n \frac{1}{\sigma_{W,i}^2}\right)^{-1} = \sigma_R^2 + \sigma_\mu^2. \tag{10.5}$$

Let us define now the two estimators of interest: the spectrum average weighted by the noise variance $\sigma_{W,i}^2$ and the cross-spectrum,

$$\begin{aligned} \widehat{S_{\text{sa}}} &= \left\{\Re\left[\sigma_\mu^2 \sum_i^n \frac{X_i}{\sigma_{W,i}^2}\right]\right\}^2 + \left\{\Im\left[\sigma_\mu^2 \sum_i^n \frac{X_i}{\sigma_{W,i}^2}\right]\right\}^2 \\ \widehat{S_{\text{cs}}} &= \langle \Re\left[X_i \cdot \overline{X}_j\right]\rangle_m \qquad \text{with} \quad i \neq j. \end{aligned} \tag{10.6}$$

Moreover σ_μ^2 corresponds to the noise weight normalization factor defined in Equation 10.5. Finally $\langle\cdot\rangle$ stands for the m average over the different combinations of instruments with $m = \binom{n}{2}$. For better readability, we have omitted in Equation 10.6 a factor $2/T$, where T is the measurement time (acquisition of the data record for one FFT), necessary for $S(f)$ to have the dimension of a PSD, and the factor fix the total power after deleting the negative frequencies. In addition, only the random part has a direct influence on the probability density function. Denoting $\mathbb{E}[\cdot]$ the mathematical expectation of the quantity within the brackets,

$$\left\{\begin{array}{lcl}\mathbb{E}\left[\widehat{S_{\text{sa}}}\right] & = & \sigma_R^2+\sigma_\mu^2\\ \mathbb{E}\left[\widehat{S_{\text{cs}}}\right] & = & \sigma_R^2\end{array}\right. \tag{10.7}$$

which means that the spectrum average estimator is **biased**. Usually one removes the bias to have the s.a estimate average over realizations which tends towards the sought signal level σ_R^2. This gives a clear advantage to the c-s estimator. However, we will see that the computation of the confidence interval over the signal level σ_R^2 requires an estimation of this bias σ_μ^2 whatever the chosen estimator, s.a or c-s. Therefore we want to estimate the PSD and we assume it follows a $1/f^\alpha$ power law, then we only have to estimate a level and exponent of the first frequency bins.

We now compare the estimator defined in Equation (10.6) by determining their variance. We can demonstrate provided that $\forall i,\ \sigma_{W,i}^2=\sigma_W^2$ (see Appendix B),

$$\mathbb{V}\left[\widehat{S_{\text{cs}}}\right]\approx\left\{\begin{array}{ll}\mathbb{V}\left[\widehat{S_{\text{sa}}}\right] & \text{if}\quad \sigma_R^2\gg\sigma_W^2\\ \dfrac{n}{n-1}\mathbb{V}\left[\widehat{S_{\text{sa}}}\right] & \text{if}\quad \sigma_R^2\ll\sigma_W^2.\end{array}\right. \tag{10.8}$$

This seems to indicate a better efficiency of the s.a estimator. Indeed the spectrum average estimator is a sufficient estimator which means of minimal variance. However what about the PDF of the estimates knowing the parameter σ_R^2 for a given frequency?

10.2 Probability Density Function

10.2.1 Spectrum Average Method

The spectrum average estimator leads to the following χ^2 distribution with two degrees of freedom resulting from the real and imaginary part of the spectrum,

$$p(\widehat{S_{\text{sa}}}|\sigma_R^2)=\frac{e^{-\frac{\widehat{S_{\text{sa}}}}{2\sigma^2}}}{2\sigma^2} \tag{10.9}$$

where,

$$\sigma^2 \;=\; \tfrac{1}{2}\left(\sigma_\mu^2+\sigma_R^2\right). \tag{10.10}$$

where σ_μ^2 is the weighted noise level according to Equation 10.5 and σ_R^2 the signal level of interest.

10.2.2 Karhunen-Loève Transform

The KLT method, denoting to the Karhunen-Loève transform, has been developed in [167]. It uses the statistics of the data themselves instead of the statistics of the estimates. This method has the advantage to combine linearly independent Gaussian estimates. Furthermore it also forms a sufficient statistics like the s.a method. It is based on determining the covariance matrix M associated to the real or imaginary part of the measurement X_i obtained by the n instruments,

$$\begin{cases} M_{ii} = \frac{1}{2}\left(\sigma^2_{W,i} + \sigma^2_R\right) \\ M_{ij} = \frac{1}{2}\sigma^2_R \qquad \text{with} \quad i \neq j \end{cases} \tag{10.11}$$

where the extra factors $1/2$ come from Equation 6.5. This covariance matrix has to be diagonalized and we denote the eigenvalues λ_i. Their associated normalized eigenvectors are V_i and the PDF is then given by

$$p(\widehat{S_{\text{KLT}}}|\sigma^2_R) = \prod_{i=1}^{n} \frac{1}{(2\pi\lambda_i)^{\nu/2}}\,\mathrm{e}^{\left(-\frac{\sum_{j=1}^{\nu} z^2_{ij}}{2\lambda_i}\right)} \tag{10.12}$$

where j highlights the real and imaginary part obtained through the Fourier transform therefore $\nu = 2$. Let us remind that X corresponds to the matrix containing the set of Fourier transform of the measurements at the output of each instrument. The numerator of the exponential argument is then

$$z = X \cdot V \tag{10.13}$$

where V are the eigenvectors obtained from the diagonalized covariance matrix.

10.2.3 Cross-spectrum

The cross-spectrum estimator leads to the variance-gamma (VΓ) distribution for two instruments as described in chapter in 9 but for more than two instruments it is no longer the case. Having no exact solution known nowadays, we propose a solution based on the characteristic functions. Expanding the model from the case of 2 instruments, we define a basis such as in [150],

$$\mathcal{B} = \begin{pmatrix} \sigma_{W,1}/2 & \sigma_{W,1}/2 & \dots & \dots & \sigma_{W,1}/2 \\ \sigma_{W,2}/2 & -\sigma_{W,2}/2 & 0 & \dots & 0 \\ 0 & 0 & -\sigma_{W,3}/2 & \dots & 0 \\ \vdots & \vdots & \vdots & \ddots & -\sigma_{W,n}/2 \\ \sigma_R & 0 & 0 & \dots & 0 \end{pmatrix}. \tag{10.14}$$

We apply an orthogonalization algorithm, the DGEQRF LAPACK subroutine, on $\mathcal{B}$. The outputs enable the computation of the product of elementary reflectors which is a matrix $\mathcal{Q}(n+1, n+1)$. Then we define $\mathcal{W}$ the matrix where each column contains the standard deviation of the spectrum according to Equation 6.1 as

$$\mathcal{W} = \frac{1}{\sqrt{2}} \begin{pmatrix} \sigma_{W,1} & 0 & \dots & \dots & 0 \\ 0 & \sigma_{W,2} & 0 & \dots & 0 \\ 0 & 0 & \sigma_{W,3} & \dots & 0 \\ \vdots & \vdots & \vdots & \ddots & \sigma_{W,n} \\ \sigma_R & \sigma_R & \sigma_R & \dots & \sigma_R \end{pmatrix}. \tag{10.15}$$

All the measurement noises are independent, as assumed, whereas the signal is common. Then the columns of $\mathcal{W}$ are projected onto the orthogonal basis $\mathcal{Q}$ and each pair of cross-spectra according to Equation 10.6 is determined. Finally we compute the eigenvalues λ_j of the resulting components by using the DSYEV LAPACK subroutine. This leads to a linear combination of χ^2 distribution as follows,

$$\widehat{S_{\text{cs}}} = \sum_{j}^{n} \lambda_j \chi_k^2 \tag{10.16}$$

where k is the number of degrees of freedom corresponding to each eigenvalue, e.g. equal to two for the real and imaginary part without degeneration. In the special case of two instruments we obtain the subtraction of two χ^2 random variables with the same number of degrees of freedom. The characteristic function of the $\lambda_j \chi_k^2$ distribution is defined by

$$\phi_j(t) = (1 - 2i\lambda_j t)^{-k/2} \tag{10.17}$$

where i is the imaginary unit and we apply a variable change of $-t$ for the negative eigenvalues. Let us notice that The parameter t is the dual random variable of the measurement random variable in the same way that the Fourier frequency is the dual variable of time in a Fourier transform. The χ^2 distributions according to Equation 10.16 being independent, the characteristic function of the c-s becomes

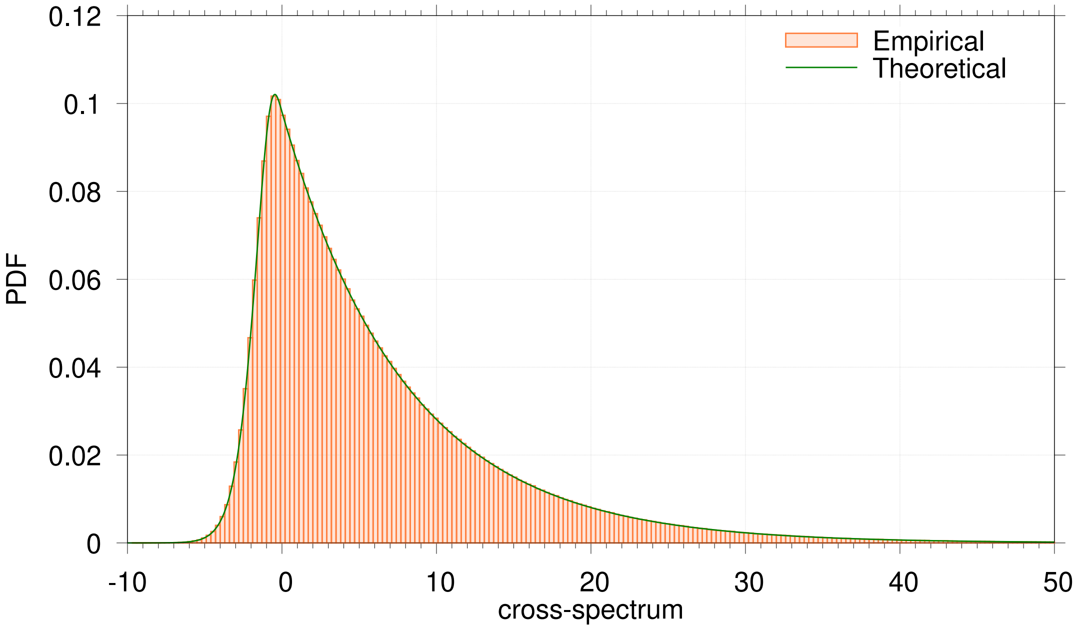

Figure 10.1: Comparison of the empirical (red boxes) and theoretical (green line) PDF of the c-s for five instruments where the variances are $\sigma_R^2 = 6$ a.u. and $\sigma_W^2 = 10$ a.u.

$$\phi(t) = \prod_j^n \phi_j(t). \tag{10.18}$$

It leads to the moment generating function of the VΓ distribution for two instruments but it is no longer the case for more instruments. When all the instruments have the same level of intrinsic noise σ_n^2, the diagonalization of the matrix $\mathcal{W}$ defined by Equation 10.15 leads to two eigenvalues. One is unique and the second one has a degeneration of $n-1$ with n the number of instruments. Consequently, it leads to the difference of two χ^2 random variables with different degrees of freedom. However even if it looks like the case with two instruments, the difference in the degrees of freedom of the χ^2 distributions has no analytical solution. Therefore the probability density function of the c-s for any noise level is defined as

$$p(\widehat{S_\mathrm{cs}}|\sigma_R^2) = \frac{1}{2\pi}\int_{\mathbb{R}} \mathrm{e}^{-it\widehat{S_\mathrm{cs}}}\,\phi(t)dt. \tag{10.19}$$

We perform the integration of the real part of the function by using the Simpson method only on the positive reals because the real part of this function is even whereas the imaginary part is odd. Figure 10.1 shows that the theoretical probability density function fits very well the histogram obtained by 10^7 Monte Carlo simulations for five instruments. The variance of each white noise is the same $\sigma_W^2 = 10$ a.u. whereas the signal level is $\sigma_R^2 = 6$ a.u.

10.2.4 Bayesian inference

10.2.4.1 A posteriori distribution

We seek to determine a confidence interval on σ_R^2, but Equations 10.9, 10.12 and 10.19 define the PDF of a set of measurement X given the sought parameter σ_R^2. So we have to solve the inverse problem which means to determine the PDF of σ_R^2 given a set of measurement X called the *posterior* distribution. The Bayes theorem leads to the following relation,

$$\begin{cases} p(\sigma_R^2|X) \propto p(X|\sigma_R^2) \cdot \pi(\sigma_R^2) \\ \int_0^\infty p(\sigma_R^2|X) d\sigma_R^2 = 1 \end{cases} \tag{10.20}$$

where $\pi(\sigma_R^2)$ is the prior, i.e. the PDF before any measurement. One of the main issue of Bayesian analysis concerns the choice of this prior.

10.2.4.2 Choice of the prior

In order to be as general as possible, we will assume a total ignorance of the signal level. In such a case, it is generally considered that any order of magnitude has the same probability which suggests a constant prior in a logarithmic scale, i.e $\pi\left(\sigma_R^2\right) = 1/\sigma_R^2$. However, our perfect knowledge of the measurement noise level induces an implicit scale factor. In other words, since we did not remove the "bias" σ_μ^2 in Equation 10.7, the s.a estimator is shifted by σ_μ^2. In a very similar case [161], we decided that the true parameter should be the sum of both levels $\theta = \sigma_\mu^2 + \sigma_R^2$. Moreover according to Equation 10.5 higher noise will have lower weight and in our case, since the mathematical expectation of the s.a estimator is $\sigma_\mu^2 + \sigma_R^2$, it comes naturally that the true parameter should be:

$$\theta = \sigma_\mu^2 + \sigma_R^2. \tag{10.21}$$

From these considerations, we will choose $\pi(\theta) = 1/\theta = \dfrac{1}{\sigma_\mu^2 + \sigma_R^2}$ and then, our prior for the s.a estimator will be

$$\pi(\sigma_R^2) \propto \frac{1}{\sigma_\mu^2 + \sigma_R^2}. \tag{10.22}$$

In order to be fair in the trial of c-s against s.a, the same prior will be used for both estimators.

In the following we will compare the different methods, starting with the spectrum average and KLT in Sec. 10.3.

10.3 Spectrum average and KLT comparison

10.3.1 A particular case: all the instruments have the same variance

Let us define $\forall i, \sigma_{W,i}^2 = \sigma_W^2$, i.e. all the n instruments have the same noise level. At a first step we determine the s.a PDF, in this case according to Equations 10.5 and 6.5, the variance defined by Equation 10.10 leads to the following expression,

$$\sigma^2 = \frac{1}{2}\left(\frac{\sigma_W^2}{n} + \sigma_R^2\right). \tag{10.23}$$

From Equation 10.6, the estimate $\widehat{S_{\text{sa}}}$ now becomes

$$\begin{aligned} \widehat{S_{\text{sa}}} &= \left\{\Re\left[\sigma_\mu^2 \sum_i^n \frac{X_i}{\sigma_{W,i}^2}\right]\right\}^2 + \left\{\Im\left[\sigma_\mu^2 \sum_i^n \frac{X_i}{\sigma_{W,i}^2}\right]\right\}^2 \\ &= \frac{1}{n^2}\left(\left\{\Re\left[\sum_i^n X_i\right]\right\}^2 + \left\{\Im\left[\sum_i^n X_i\right]\right\}^2\right) \end{aligned} \tag{10.24}$$

According to Equation 10.9, the s.a PDF is given by

$$p(\widehat{S_{\text{sa}}}|\sigma_R^2) = \frac{e^{-\frac{\frac{1}{n^2}\left\{\Re[\sum_i^n X_i]^2 + \Im[\sum_i^n X_i]^2\right\}}{\frac{\sigma_W^2}{n}+\sigma_R^2}}}{\frac{\sigma_W^2}{n} + \sigma_R^2}. \tag{10.25}$$

In a second step let us define the KLT PDF. The eigenvalues of the covariance matrix resulting from Equation 10.11 are given by

$$\begin{aligned} \lambda_1 &= \frac{1}{2}\left(\sigma_W^2 + n\sigma_R^2\right) \\ \lambda_i &= \frac{1}{2}\sigma_W^2 \qquad \text{with} \quad i \in \{2, ..., n\} \end{aligned} \tag{10.26}$$

The first and highest eigenvalue being the only one to depend of σ_R^2, we solely define its associated eigenvector

$$V_1 = \frac{J_{n,1}}{\sqrt{n}} \tag{10.27}$$

where $J_{n,1}$ is the all-ones column vector. Then the numerator in the exponential in Equation 10.12 is

$$\begin{aligned}\sum_j^\nu \widehat{z}^2_{1,j} &= \sum_j^\nu \left[X_j \cdot V_1\right]^2 \\ &= \frac{1}{n}\sum_j^\nu \left[X_j \cdot J_{n,1}\right]^2 \\ &= \frac{1}{n}\sum_j^\nu \left[\sum_i^n X_{ij}\right]^2 \\ &= \frac{1}{n}\left\{\Re\left[\sum_i^n X_i\right]^2 + \Im\left[\sum_i^n X_i\right]^2\right\}.\end{aligned} \tag{10.28}$$

The KLT PDF defined by Equation 10.12 is given by

$$p(\widehat{S_{\text{KLT}}}|\sigma_R^2) = C\frac{e^{-\frac{\frac{1}{n}\left\{\Re\left[\sum_i^n X_i\right]^2 + \Im\left[\sum_i^n X_i\right]^2\right\}}{\sigma_W^2 + n\sigma_R^2}}}{\pi\left(\sigma_W^2 + n\sigma_R^2\right)} \tag{10.29}$$

where C is the Gaussian remaining product with a variance depending only on the measurement noise level. However what we want to characterize is not the estimates but the parameter σ_R^2. According to Equation 10.20, the PDF of the true parameter σ_R^2 is proportional to the prior $\pi(\sigma_R^2)$ multiplied respectively by Equations 10.25 and 10.29 for the s.a and KLT estimates. The Bayes theorem leads then to

$$p(\sigma_R^2|\widehat{S_{\text{sa}}}) \quad \propto \quad \pi(\sigma_R^2)\frac{e^{-\frac{\frac{1}{n}\left\{\Re\left[\sum_i^n X_i\right]^2 + \Im\left[\sum_i^n X_i\right]^2\right\}}{\sigma_W^2 + n\sigma_R^2}}}{\sigma_W^2 + n\sigma_R^2} \tag{10.30}$$

and

$$p(\sigma_R^2|\widehat{S_{\text{KLT}}}) \quad \propto \quad \pi(\sigma_R^2)\frac{e^{-\frac{\frac{1}{n}\left\{\Re\left[\sum_i^n X_i\right]^2 + \Im\left[\sum_i^n X_i\right]^2\right\}}{\sigma_W^2 + n\sigma_R^2}}}{\sigma_W^2 + n\sigma_R^2}. \tag{10.31}$$

Multiplying respectively Equations 10.30 and 10.31 by a factor $1/n$ and π does not change the PDF since it is normalized. It is exactly the same for Equation 10.31 where C does not depend on σ_R^2 and vanish through the normalization. Therefore both expressions are exactly the same. It should also be noted that the noise level σ_W^2 is necessary in both cases and the bias does not influence the sought parameter density whereas it does regarding the estimates. This implies a very interesting consequence: both PDF for the s.a and KLT leads to the exact **same** confidence interval for the same noise level.

10.3.2 General case

In this part any number of instruments and different noise level for each of them can be considered. In Section 10.3.1, we showed analytically that both methods lead to the same PDF of the signal level knowing the estimates in the event that all noise levels are the same. However when each noise level is different Equation 10.26 giving the relation between the eigenvalues and the signal becomes much more complicated without degeneration. In this case, let us consider a number of instruments solely up to five, refering as instance to the number of radio telescopes (RTs) part of the LEAP project. Then we make several empirical comparisons by computing the upper limit at 95% for the spectrum average and KLT methods. It should be noticed that the 5% lower bound has no interest since we are more particularly interested in the case where the signal is weaker than the noise level. This bound then greatly depends on the prior and is very close to zero.

Table 10.1 gives the average over $1\,000$ realizations of the 95% upper bound for two to five RTs. The signal and noise levels are respectively $\sigma_R^2 = 1$ a.u. and $\sigma_{W,i}^2 = i$ a.u. where i is the i-th RT. Then the second and third RT are respectively two and three times more noisy than the first one and so forth.

First, these comparisons show as expected that the 95% bounds obtained by both estimators as in Section 10.3.1 for the same noise variance, are exactly the same. Second, the mean and median of the 95% upper limit of the s.a and KLT estimates obtained over $1\,000$ realizations are decreasing as the number of RTs increases. Therefore adding a new instrument to the array, as long as we have a perfect knowledge of its noise level, necessarily contributes to lowering the upper limit and then improve the parameter estimation. The maximum value is not really significant since the tail of the distribution is very long and thin. Finally, it should be noticed that both methods require the knowledge of the noise level, for the expression of the probability density function. The spectrum average method being the fastest way to compute the confidence interval is then to be privileged. Therefore we will only compare the spectrum average method with the cross-spectrum in the next section.

Table 10.1: Upper limit average of the parameter σ_R^2 taking into account two to five RTs. These data were obtained from a set of 1 000 simulated spectra. The signal and noise level used for the computation are $\sigma_R^2 = 1$ and $\sigma_{W,i}^2 = i$ where i is the index of the RT.

	Spectrum average / KLT			95% upper limit	
RTs number	Mean	Median	Std	Min	Max
2	17.44	12.88	3.10	6.30	115.32
3	16.32	11.78	2.39	5.16	91.78
4	15.66	11.10	2.95	4.54	108.82
5	14.84	10.67	2.28	4.14	86.99

10.4 95% upper limit: spectrum average vs cross-spectrum

We have set the direct problem, i.e. the statistics of the s.a or c-s knowing the signal level and noise level (which is assumed to be known), respectively in Sections 10.2.1 and 10.2.3. Now we tackle the inverse problem from the direct problem, i.e. the statistics of the signal level knowing the s.a or c-s estimate. The Bayes theorem enables us to establish this link as described in Section 10.2.4. The posterior distribution of the s.a and c-s are given by

$$p(\sigma_R^2|\widehat{S_{\mathrm{sa}}}) \quad \propto \quad \frac{1}{(\sigma_\mu^2+\sigma_R^2)^2}\, \mathrm{e}^{\frac{-\widehat{S_{\mathrm{sa}}}}{\sigma_\mu^2+\sigma_R^2}} \tag{10.32}$$

and

$$p(\sigma_R^2|\widehat{S_{\mathrm{cs}}}) \quad \propto \quad \frac{1}{2\pi(\sigma_\mu^2+\sigma_R^2)} \int_{\mathbb{R}} \mathrm{e}^{-it\widehat{S_{\mathrm{cs}}}}\, \phi(t)dt \tag{10.33}$$

where σ_μ^2 is the noise variance weighting according to Equation 10.5. Let us describe our simulation algorithm in order to assess the 95% upper limit.

First simulation (S_1 to S_3): simulate a set of real data from q instruments, assuming the red noise level is known (as well as, of course, the measurement noise levels).

S_1: Assign the number of RTs, the noise variance of each one and the sought **true** signal level.

S_2: Generate a set of spectral measurement according to Equation (6.1)

S_3: Compute the s.a and c-s estimates, as stated in Equation (10.6), which are now fixed as parameters.

Second simulation: we no longer modify the data (these are acquired measurement results) and we look for a confidence interval on the red noise, assuming the level of the measurement noise is known.

S_4: Define any basis and perform an orthogonalization and normalization of it by using the DGEQRF subroutine from LAPACK

S_5: Establish, from Equation 10.15, one $\mathcal{W}$ matrix for each signal level **varying** from 0 to an upper limit for which Equations 10.32 and 10.33 are close enough to zero according to the required precision.

S_6: Peform S_7 to S_{11} for each σ_R^2 value.

S_7: Project the $\mathcal{W}$ matrix onto the orthogonal basis.

S_8: Compute the c-s denoted $\mathcal{Z}$ from the result of S_6.

S_9: Determine the eigenvalues of $\mathcal{Z}$ by using the DSYEV subroutine from LAPACK which has now the form of Equation 10.16.

S_{10}: Define the product of each characteristic function defined by Equation 10.17.

S_{11}: Compute the posterior distribution respectively of the s.a and c-s estimates according to Equations 10.32 and 10.33. For the c-s, we perform a numerical integration of one signal value by using the Simpson method.

S_{12}: Normalize the s.a and c-s posterior PDF.

S_{13}: Determine the cumulative distribution function (cdf) by integrating the s.a and c-s posterior PDF and find the 95% upper limit corresponding onto the cdf value associated to the signal level.

The loops for the different values of the signal are computed in parallel in order to save computing time. Let us give an example of such a process. We set the number of RTs to five and the variances of the signal and noise are respectively $\sigma_R^2 = 6$ a.u, $\sigma_W^2 = 10$ a.u. Then we produce two sets of random measurement with these parameters, shown in Table 10.2. The first measurement set gives respectively $\widehat{S_{\text{sa},1}} = 14.886$ a.u. and $\widehat{S_{\text{cs},1}} = 13.226$ a.u. for the s.a and c-s estimates whereas the second one gives $\widehat{S_{\text{sa},2}} = 20.730$ a.u. and $\widehat{S_{\text{cs},2}} = 18.564$ a.u. It leads for the first set to the 95% upper limit on the signal σ_R^2 following value, 125.8 for the s.a and 127.3 for the c-s. Furthermore the second set gives us 167.1 for the s.a and 164.8 for the c-s. These results show that either the c-s or the s.a can be the most efficient even with the same parameters, then it only depends on the measurement set. However, the difference between the 95% upper limit for both methods is relatively low.

Table 10.2: Measurement set for the outputs of each RT (five in total) where $\sigma_R^2 = 6$ a.u. and $\sigma_W^2 = 10$ a.u.

	measurement set 1		measurement set 2	
	Real part	Imaginary part	Real part	Imaginary part
X_1	-3.8947	-1.7994	-0.1494	8.9456
X_2	-5.0950	-3.9125	-0.5275	4.4659
X_3	-2.5133	-5.5431	0.2176	5.7742
X_4	0.6433	-1.9566	1.6044	3.2146
X_5	-0.2294	-2.5738	-0.5284	0.3563

Let us now compare the s.a and c-s 95% upper limit over 100 simulations as shown in Table 10.3 for the sought signal level set to 6 a.u. and a noise level equal to 10 a.u. for each RT. The 95% upper limit is given respectively for, from the top of the Table to the bottom, the spectrum average, the cross-spectrum and the ratio of the 95% bound of s.a over c-s. The mean and median are decreasing when the number of RTs is increasing. However for four RTs the results are much lower but it is just an artefact of “luck". Indeed the maximum value is 1.4 times lower than for five RTs and the standard deviation (std) is also very much lower. The sample size can have a significant effect on the values obtained but is necessary to have a good precision with a reasonable computation time. However, the minimum value of the 95% bound obtained for both methods permits to override this randomness. Indeed when the cross-spectrum estimate is negative or the spectrum average estimate tends towards zero it leads to the smallest 95% bound. Whereas the maximum 95% bound obtainable for a reasonable amount of simulations can “wriggle" a lot as the tail of the posterior PDF is very long especially with higher noise level than signal level which is of interest. The minimum value of the upper bound decreases as the number of RTs increases. The differences between the s.a and c-s methods are not significant.

Figure 10.2 shows the histogram of the 95% limit with five RTs for $10\,000$ realizations, $\sigma_R^2 = 6$ a.u. and $\sigma_W^2 = 10$ a.u. Both histograms exhibit a similar distribution which extend up to high values. However the first bin corresponding to the lowest 95% bound shows a high number of realizations for the c-s method. This can be explained by a negative estimate for the cross-spectrum which may corresponds to a spectrum average estimate having a not so small value and so a higher 95% bound. Figure 10.3 shows the comparison of the 95% upper limit for the s.a and c-s methods for a window of hundred data among the same set of realizations. The $6\,620$-th realization framed by a blue rectangle highlights the fact that the c-s can sometimes be much more stringent than the s.a method. However in most of the other realizations we notice that the 95% limit is almost the same.

Figure 10.4 depict the 95% upper bound median among 1 000 simulations with five RTs, for the s.a over c-s ratio depending on the signal-to-noise level ratio (with $\sigma_W^2 = 1$ a.u). When $\sigma_R^2 \ll \sigma_W^2$ then the s.a seems to be the most stringent most of the time. However when the signal level becomes higher than the noise level, both the s.a and the c-s methods give in median the same 95% limit.

Considering all these observations it is wiser to compute both estimators and use the most restrictive one. Even if most of the time both estimators give a very close upper bound, sometimes the gap is clearly significant.

Table 10.3: 95% upper limit statistics for the s.a (top), c-s (middle) and the ratio of the s.a by the c-s over 100 simulations where $\sigma_R^2 = 6$ a.u. and $\sigma_W^2 = 10$ a.u. Each rows respectively from the left to the right corresponds to the number of RTs, the mean, median, standard deviation, minimun and maximum value of the 95% upper bound.

	Spectrum average 95% upper limit				
RTs number	Mean	Median	Std	Min	Max
2	112.99	79.45	32.93	48.50	440.60
3	98.41	72.60	35.66	31.70	453.20
4	78.00	51.50	18.30	23.80	260.10
5	90.11	67.95	28.47	19.00	373.40

	Cross-spectrum 95% upper limit				
RTs number	Mean	Median	Std	Min	Max
2	116.49	83.00	27.38	67.90	388.90
3	99.74	79.65	34.54	41.00	443.40
4	76.37	54.10	18.03	28.50	255.80
5	91.87	65.35	28.98	22.20	380.20

	s.a/c-s 95% upper limit				
RTs number	Mean	Median	Std	Min	Max
2	0.97	0.90	0.12	0.71	2.21
3	0.98	0.94	8.13×10^{-2}	0.74	1.79
4	1.02	0.98	4.86×10^{-2}	0.74	1.50
5	0.97	0.96	3.73×10^{-2}	0.78	1.34

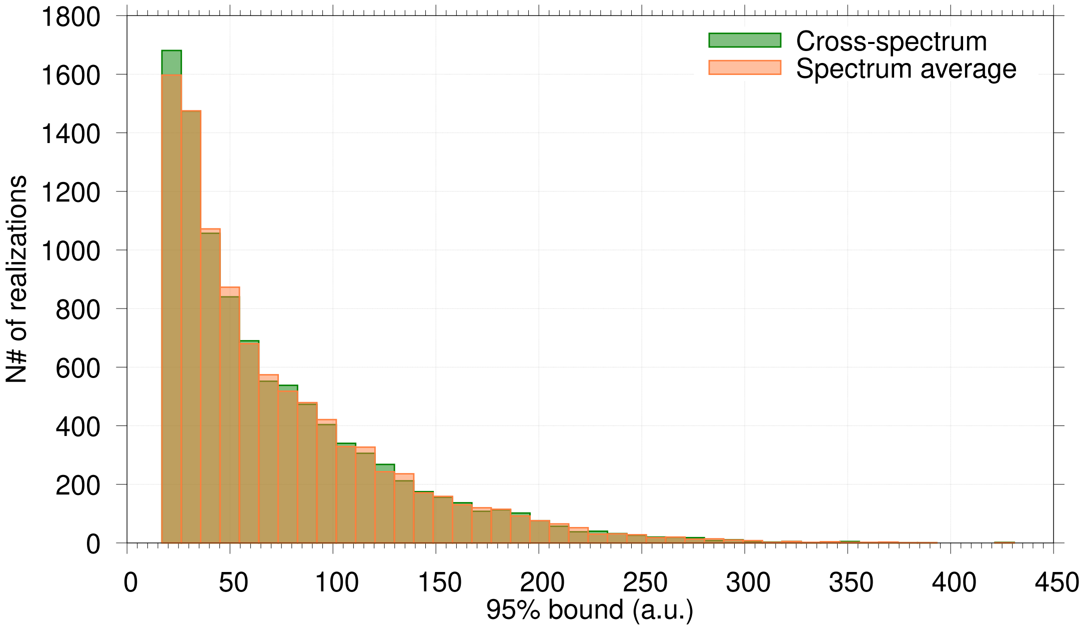

Figure 10.2: Histogram comparison of 95% upper bound between the c-s and s.a for $10\,000$ realizations. The parameters are set for five RTs, $\sigma_R^2 = 6$ a.u. and $\sigma_W^2 = 10$ a.u.

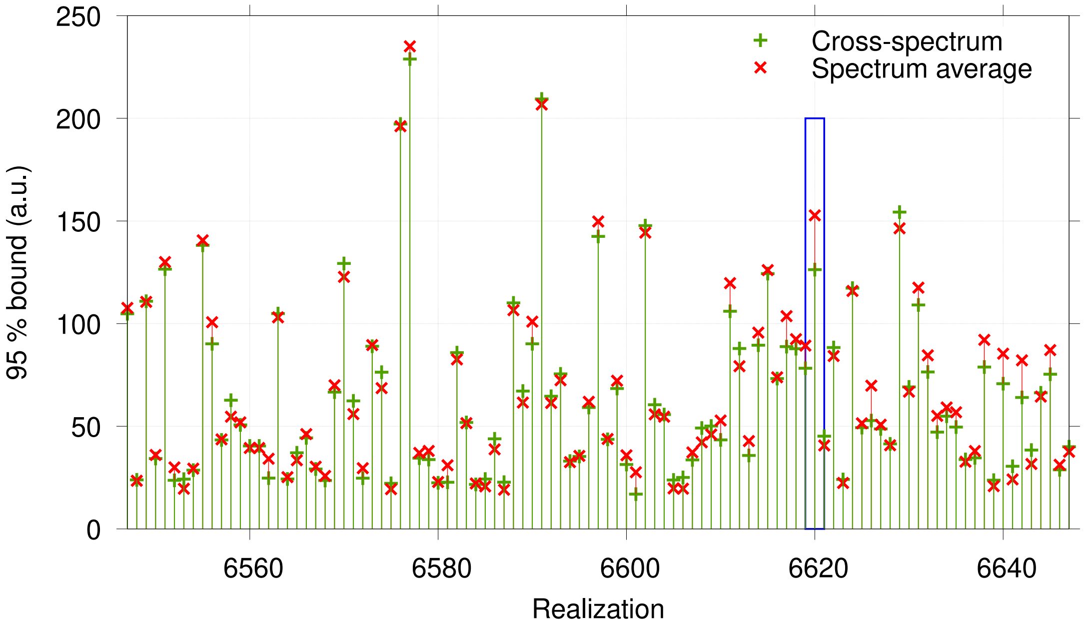

Figure 10.3: Set of 100 realizations for five RTs of 95% bounds for cross-spectrum (green $+$) and spectrum average (red $\times$) where $\sigma_R^2 = 6$ a.u. and $\sigma_W^2 = 10$ a.u.

10.5 Conclusion

First, we demonstrated that the spectrum average variance is $n/(n-1)$ lower than the cross-spectrum variance for $n \geq 2$.

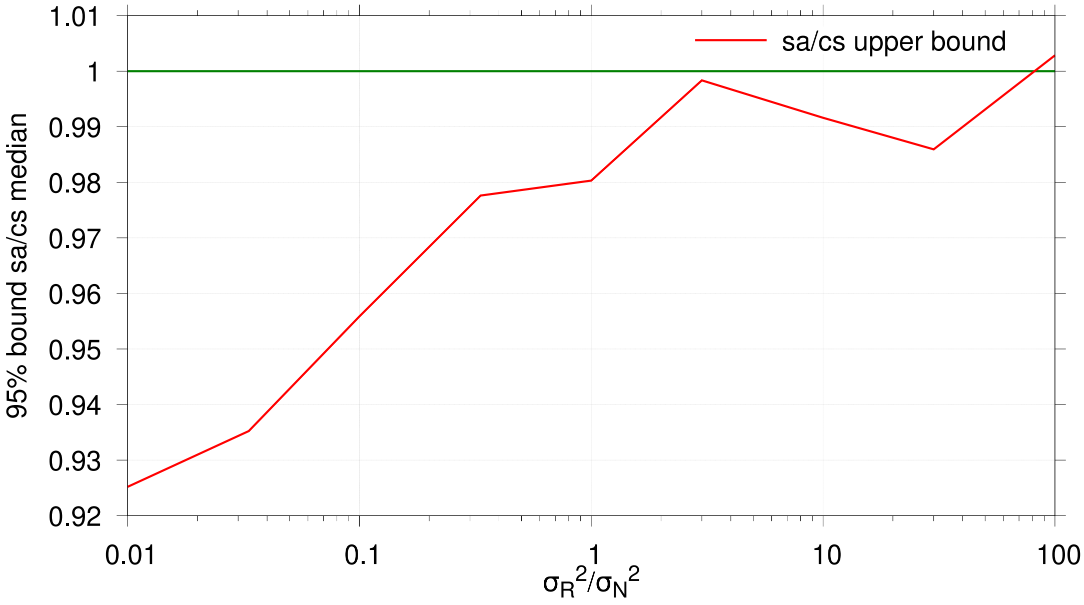

Figure 10.4: Evolution of the 95% upper bound median of the s.a over c-s ratio obtained for $1\,000$ realizations depending on the signal-to-noise level ratio. The parameters are set for five RTs and $\sigma_W^2 = 1$ a.u. The red curve corresponds to the sa/cs upper bound and the green curve indicates when both s.a and c-s have the same upper bound in median.

Second, in order to assess the confidence interval of the signal level we defined its probability density function knowing the s.a and c-s estimates but also the noise of each instruments (radio telescopes). In addition a method directly using the statistics of the measurement (KLT) has also been compared. It turns out that the KLT and the s.a methods lead to the exact same PDF of the signal level σ_R^2 knowing the estimates, so the precision is the same. Furthermore whereas the cross-spectrum has a well-defined analytic probability density function for two instruments called $\mathrm{V}\Gamma$, there is no equivalent for more than two instruments. We proposed then a generalized method based on a numerical integration of the characteristic function product. This method works very well according to the Monte Carlo simulations.

Finally the efficiency of both estimators, the spectrum average versus the cross-spectrum, is highlighted through the comparison of the 95% Bayesian upper limit. We found a slight advantage for the spectrum average estimator when the noise level is higher than the signal level. However we showed that sometimes the c-s gives the most stringent confidence interval but above all a little more often than the s.a for the lowest upper limit. Nevertheless it is the s.a method which gives us the minimum 95% limit reachable. To conclude it is wiser to compute both estimates and use the most stringent.

Part IV

General conclusion

General conclusion

In this part, we remind the reader some of the global questioning and partly describe the timeline of the presented work. We present our approach to solve the problems encountered and the main results already discussed in depth individually. Furthermore we provide general insights and discuss what could be the role of the tools we have developed for time and frequency metrology but also in astronomy.

In this study, we have presented the work carried out at both the BIPM in Sèvres and at FEMTO-ST in Besançon. The objective of the work at the BIPM was to develop a procedure to determine the jumps which can affect the time links used in UTC calculation. This tool, based on the Kalman filter, had to correctly determine the date of the steps and their magnitude (mainly for time steps) and give a warning to the BIPM Time Department about this unexpected problem. This warning should help us to understand the nature of the steps which, in some cases, can affect the behavior of UTC. A critical example is the receiver calibration causing a step in time links and potentially impacting UTC behavior. To ensure the long-term stability of UTC, it is crucial to verify the data and identify problems. The second part of the work, carried out at FEMTO-ST, concerns a Bayesian statistics development on the cross-spectrum estimator, in particular to obtain reliable confidence intervals. This estimator is commonly used in the time and frequency community with its advantage to reject most of the measurement noise in order to better highlight the instabilities of the clocks. It is based on the use of signal covariances which makes it possible to keep only the common part of the signals. This study has a particular interest when the observations take so long that only few measurements are available as it is the case in radio-astronomy.

The first aspect of the work focused on adapting the algorithm defined in [86] based on a Kalman filter to detect time steps that affect time transfer links used in the calculation of UTC. We used the already defined 3-state clock model, thus modeling the phase, the frequency and the drift. Nevertheless we restricted the study only to the phase difference, with the possibility of being able to generalize the study thereafter to the frequency and drift if necessary. A jump is detected by the algorithm if the absolute value of the innovation, i.e. the difference between the measurement and a prediction of it, is greater than its standard deviation multiplied by a certain coefficient. This parameter has notably been optimized by carrying out numerous simulations of UTC. Given the large quantity of data accessible to the BIPM, tests were carried out on very different data sets from different types of clocks and time transfer methods. The parameters used in the algorithm require a detailed study of clock noise. A stability study using the Allan variance made it possible to analyze and extract the diffusion coefficients. Only the WPM and WFM were considered, and other types of noise were neglected. Considering that UTC is not computed in real time, we adapted and optimized the detection algorithm by applying the filter forwards and backwards in time; these filtered data are then combined after stopping both series at the date of the step. The outliers having already been eliminated, the detector works very well and an automatic procedure has been set up to analyze the data received each month at the BIPM.

The second aspect of this work concerns a Bayesian analysis on the cross-spectrum method. We chose as a relevant estimator only the real part of the cross-spectrum since the imaginary part contains only the measurement noise. Two cases arise, the first when a large number of measurements can be made and the second when only few measurements are available. In the first case, the statistics are simple since a Gaussian approximation can be realized. The main interest is the study of red noise at the lowest frequencies, which should occur in the TOAs of millisecond pulsars. We simulated this red noise by integrating white noise. Given Parseval's theorem, when performing the Fourier transform of our real signal, the variance should be the same for the real part and the imaginary part of the spectrum. However, it was observed that this was not true with the way chose to simulate the red noise. We showed that a spectral aliasing as well as a fake drift modifies the shape of the spectrum especially for the highest frequencies, which introduces a dissymmetry between the real and imaginary parts. We demonstrated that it is easy to remove the fake drift by removing the mean value of the white time series. In the event that we could perform several measurements in order to average them to remove the white noise, however our spectra must be uncorrelated. We have shown that a tuning of the oscillators breaks the memory of non-stationary processes which are in the phase or frequency noise. This process allows the analysis to converge to the phase or frequency PSD of the oscillator. An experimental confirmation is however necessary in order to confirm the simulations carried out. In the case where spectrum averaging is not possible, we have demonstrated that the PDF of the cross-spectrum estimator is a VΓ function in the case where there are two measuring instruments. This exact analytical solution was computed with Monte-Carlo simulations validating the PDF. If there are more than two devices, this distribution no longer corresponds to the exact PDF and there is no analytical solution to date. We proposed a numerical approach based on the Fourier transform of a characteristic function. Monte-Carlo simulations showed excellent agreement with the proposed distribution. A Bayesian analysis was then carried out in order to obtain a confidence interval on the signal level knowing the noise level of the measuring instruments. We chose a non-informative prior since we had no idea of the behavior of the parameter sought. Finally we compared this confidence interval with a commonly used estimator, the simple average of the spectra weighted by the noise of the devices. We found an upper limit of the signal level slightly in the advantage of the spectrum average, however this is biased and requires the noise to be removed. In addition, we noticed that the upper limit on the cross-spectrum could be much more restrictive in certain cases. The difference in the confidence intervals given by the two estimators is reduced when the number of devices is increased.

In conclusion, an automatic phase skip detection procedure in the time transfer link is operational at the BIPM. This algorithm nevertheless requires an improvement to differentiate phase jumps from outliers, especially when there are many of them. The exact PDF of the cross-spectrum is a VΓ distribution for two devices and a solution using the Fourier transform of the characteristic function product gives excellent results for more than two devices. Our approach provides access to the real PDF of the estimator, which so far in the literature has been approximated by Gaussians. It would be interesting to compare the cross-spectrum and the spectrum average estimators on an experiment with real data and then verify whether or not the millisecond pulsars could be used as time references.

Appendix

APPENDIX A

The cross-spectrum method

Measuring a device under test (DUT), the observed spectra contains the noise of the DUT called the *signal* and the background noise of the instruments. The two-channel measurement is modeled as the block diagram in Figure A.1 where $a(t)$ and $b(t)$ are the background noise of the two instruments and $c(t)$ the DUT noise. We consider $a(t)$, $b(t)$ and $c(t)$ statistically independent. The two instruments' outputs are

$$\begin{aligned} x(t) &= a(t) + c(t) \quad &\leftrightarrow \quad X &= A + C \\ y(t) &= b(t) + c(t) \quad &\leftrightarrow \quad Y &= B + C. \end{aligned} \tag{A.1}$$

where $\leftrightarrow$ denotes the Fourier transform and the frequency f is implicit. The Fourier transform can be rewritten as

$$\begin{aligned} X &= \Re[X] + \Im[X] = X' + iX'' \\ Y &= \Re[Y] + \Im[Y] \;= Y' + iY''. \end{aligned} \tag{A.2}$$

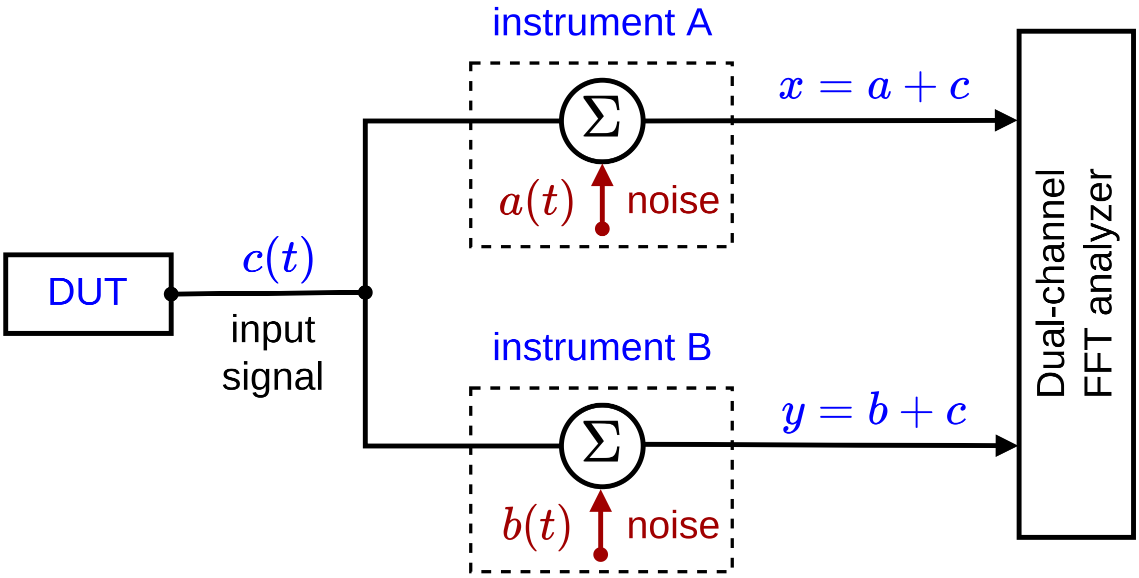

Figure A.1: Basics of the cross-spectrum method.

The one-sided PSD given a measurement X of an instrument can be calculated as

$$S_x = \frac{2}{T} X\tilde{X} = (\Re[X]^2 + \Im[X]^2) \qquad \text{for } f > 0, \tag{A.3}$$

where T is the acquisition time, $\tilde{\ }$ stands for the complex conjugate and the factor 2 is due to energy conservation after surpressing the negative frequencies. Consequently, the one-sided cross-PSD is defined by

$$S_{yx} = \frac{2}{T} Y\tilde{X} \qquad \text{for } f > 0. \tag{A.4}$$

The expectation value of Equation A.4 is given by

$$\begin{aligned}
\mathbb{E}[S_{yx}] &= \frac{2}{T}\mathbb{E}[Y\tilde{X}] \\
&= \frac{2}{T}\mathbb{E}[(B + C)(A + C)] \\
&= \frac{2}{T}\mathbb{E}[(B' + iB'' + C' + iC'')(A' - iA'' + C' - iC'')] \\
&= \frac{2}{T}\mathbb{E}[(B'A' + B''A'' + B'' + B'C' + B''C'' + C'A' + C''A'' + C'^2 + C''^2) \\
&\qquad +i(B''A' - B'A'' + B''C' - B'C'' + C''A' - C'A'')].
\end{aligned} \tag{A.5}$$

Looking at Equation A.5 and considering that A, B and C are zero-mean Laplace-Gauss random variable, we identify the following classes in Table A.1

terms	$\mathbb{E}$	comment
$B'A'$, $B''A''$, $B''A'$, $B'A''$	0	product of zero-mean Laplace-Gauss processes
$B'C'$, $B''C''$, $C'A'$, $C''A''$, $B''C'$, $B'C''$, $C''A'$, $C'A''$	0	product of zero-mean Laplace-Gauss processes
$C'^2 + C''^2$	$\mathbb{V}[C]$	sum of zero-mean square Laplace-Gauss processes.

Table A.1: Expected value of product of Laplace-Gauss processes contained in the cross-spectrum estimator.

Therefore $\Im[S_{yx}]$ contains only the background noise of the observation. According to [59], an unbiased estimator of the cross-spectrum can be defined by

$$S_{cs} = \frac{2}{T}\Re[Y\tilde{X}] \tag{A.6}$$

and can give sometimes negative values.

APPENDIX B

Variance of the sa and c-s estimators

B.1 Definitions

B.1.1 Measurements

Let us define n instruments' measurements X_1, X_2, … and X_n as

$$X_j = W'_j + iW''_j + R' + iR'' \tag{B.1}$$

where W'_j, W''_j are independent Gaussian centered random variables of variance $\sigma^2_W/2$, and R', R'' are independent Gaussian centered random variables of variance $\sigma^2_R/2$.

B.1.2 Estimates

The estimator $\widehat{S_{\text{cs}}}$ is defined by Equation 10.6 as

$$\begin{aligned}\widehat{S_{\text{cs}}} = \frac{1}{\binom{n}{2}} \sum_{j=1}^{n-1} \sum_{k=j+1}^{n} \Re[(W'_j + iW''_j + R' + iR'')\times \\ \times(W'_k - iW''_k + R' - iR'')].\end{aligned} \tag{B.2}$$

On the other hand, $\widehat{S_{\text{sa}}}$ is defined by Equation 10.6 as

$$\widehat{S_{\text{sa}}} = \left(\sum_{j}^{n} \frac{W_j' + nR'}{n} \right)^2 + \left(\sum_{j}^{n} \frac{W_j'' + nR''}{n} \right)^2 . \tag{B.3}$$

B.1.3 Statistics reminder

If A and B are 2 independent random Gaussian variables of zero expectation

$$\mathbb{V}[AB] = \mathbb{V}[A]\mathbb{V}[B] \tag{B.4}$$

according to Equation (a) from [171] where $\mathbb{V}[\cdot]$ stands for the variance of the quantity within the brackets. Moreover according to the Isserlis' theorem [172],

$$\begin{aligned} \mathbb{V}[A^2] &= \mathbb{E}[A^4] - \left\{\mathbb{E}[A^2]\right\}^2 = 3\left\{\mathbb{E}[A^2]\right\}^2 - \left\{\mathbb{E}[A^2]\right\}^2 \\ &= 2\mathbb{V}^2[A], \end{aligned} \tag{B.5}$$

where $\mathbb{E}[\cdot]$ stands for the mathematical expectation of the quantity within the brackets. It is also useful to consider the covariances. If A, B, C, and D are four Gaussian centered random variables,

$$\mathbb{E}[ABCD] = \mathbb{E}[AB] \cdot \mathbb{E}[CD] + \mathbb{E}[AC] \cdot \mathbb{E}[BD] + \mathbb{E}[AD] \cdot \mathbb{E}[BC]. \tag{B.6}$$

If A, B, C, and D are four **independent** Gaussian centered random variables, this can be derived to the following particular cases (Isserlis' theorem [172]):

- $\mathbb{E}[ABCD] = \mathbb{E}[AB] \cdot \mathbb{E}[CD] + \mathbb{E}[AC] \cdot \mathbb{E}[BD] + \mathbb{E}[AD] \cdot \mathbb{E}[BC] = 0$ since each mathematical expectation product $\mathbb{E}[XY]$ is null

- $\mathbb{E}[A^2BC] = \mathbb{E}[A^2] \cdot \mathbb{E}[BC] + 2\mathbb{E}[AB] \cdot \mathbb{E}[AC] = 0$ since the only mathematical expectation which is not null, $\mathbb{E}[A^2]$, is multiplied by $\mathbb{E}[CD] = 0$

- $\mathbb{E}[A^3B] = 3\mathbb{E}[A^2] \cdot \mathbb{E}[BC] = 0$ since $\mathbb{E}[BC] = 0$

- $\mathbb{E}[A^2B^2] = \mathbb{E}[A^2] \cdot \mathbb{E}[B^2] + 2\mathbb{E}^2[AB] = \mathbb{E}[A^2] \cdot \mathbb{E}[B^2] \neq 0.$

- $\text{Cov}[A^2B^2] = \mathbb{E}[A^2B^2] - \mathbb{E}[A^2] \cdot \mathbb{E}[B^2] = \mathbb{E}[A^2] \cdot \mathbb{E}[B^2] - \mathbb{E}[A^2] \cdot \mathbb{E}[B^2] = 0.$

B.2 Variance of the estimators

B.2.1 Variance of the cross-spectrum

From (B.2), we find

$$\begin{aligned}\widehat{S_{\text{cs}}} = \frac{1}{\binom{n}{2}} \Bigg[& \sum_{j=1}^{n-1} \sum_{k=j+1}^{n} (W_j W_k + W'_j W'_k) \times \\ & \times (n-1) \sum_{j=1}^{n} (W_j S + W'_j R') \times \\ & \times \binom{n}{2} (R^2 + R'^2) \Bigg] .\end{aligned} \tag{B.7}$$

Then,

$$\begin{aligned}\mathbb{V}[\widehat{S_{\text{cs}}}] = \frac{1}{\binom{n}{2}^2} \Bigg[& \sum_{j=1}^{n-1} \sum_{k=j+1}^{n} (\mathbb{V}[W_j W_k] + \mathbb{V}[W'_j W'_k]) \times \\ & \times (n-1)^2 \sum_{j=1}^{n} (\mathbb{V}[W_j R] + \mathbb{V}[W'_j R']) \times \\ & \times \binom{n}{2}^2 (\mathbb{V}[R^2] + \mathbb{V}[R'^2]) \Bigg] ,\end{aligned} \tag{B.8}$$

where all covariance terms are null thanks to Isserlis'theorem. From the properties (B.4) and (B.5), we find

$$\begin{aligned}\mathbb{V}[\widehat{S_{\text{cs}}}] = \frac{1}{\binom{n}{2}^2} \Bigg[& \sum_{j=1}^{n-1} \sum_{k=j+1}^{n} (\mathbb{V}[W_j]\mathbb{V}[W_k] + \mathbb{V}[W'_j]\mathbb{V}[W'_k]) \times \\ & \times (n-1)^2 \sum_{j=1}^{n} (\mathbb{V}[W_j]\mathbb{V}[R] + \mathbb{V}[W'_j]\mathbb{V}[R']) \times \\ & \times \binom{n}{2}^2 (2\mathbb{V}^2[R] + 2\mathbb{V}^2[R']) \Bigg] .\end{aligned} \tag{B.9}$$

Therefore,

$$\begin{aligned}\mathbb{V}[\widehat{S_{\text{cs}}}] &= \frac{1}{\binom{n}{2}^2} \left[2\binom{n}{2} \frac{\sigma_W^4}{4} + 2n(n-1)^2 \frac{\sigma_W^2 \sigma_R^2}{4} + 4\binom{n}{2}^2 \frac{\sigma_R^4}{4} \right] \\ &= \frac{1}{n(n-1)} \sigma_W^4 + \frac{2}{n} \sigma_W^2 \sigma_R^2 + \sigma_R^4 .\end{aligned} \tag{B.10}$$

B.2.2 Variance of spectrum average

From (B.3), we find

$$\begin{aligned}\widehat{S_{\text{sa}}} = \frac{1}{n^2}\Bigg[&\sum_{j=1}^{n}(W_j^2 + W_j'^2) + n^2(R^2 + R'^2) + \\ &+ 2\sum_{j=1}^{n-1}\sum_{k=j+1}^{n}(W_jW_k + W_j'W_k') + \\ &+ 2n\sum_{j=1}^{n}(W_jR + W_j'R')\Bigg].\end{aligned} \tag{B.11}$$

Then,

$$\begin{aligned}\mathbb{V}[\widehat{S_{\text{sa}}}] = \frac{1}{n^4}\Bigg[&\sum_{j=1}^{n}(\mathbb{V}[W_j^2] + \mathbb{V}[W_j'^2]) + n^4(\mathbb{V}[R^2] + \mathbb{V}[R'^2]) + \\ &+ 4\sum_{j=1}^{n-1}\sum_{k=j+1}^{n}(\mathbb{V}[W_jW_k] + \mathbb{V}[W_j'W_k']) + \\ &+ 4n^2\sum_{j=1}^{n}(\mathbb{V}[W_jR] + \mathbb{V}[W_j'R'])\Bigg],\end{aligned} \tag{B.12}$$

where all covariance terms are null thanks to Isserlis'theorem. From the properties (B.4) and (B.5), it comes

$$\begin{aligned}\mathbb{V}[\widehat{S_{\text{sa}}}] = \frac{1}{n^4}\Bigg[&\sum_{j=1}^{n}(2\mathbb{V}^2[W_j] + 2\mathbb{V}^2[W_j']) + n^4(2\mathbb{V}^2[R] + 2\mathbb{V}^2[R']) + \\ &+ 4\sum_{j=1}^{n-1}\sum_{k=j+1}^{n}(\mathbb{V}[W_j]\mathbb{V}[W_k] + \mathbb{V}[W_j']\mathbb{V}[W_k']) + \\ &+ 4n^2\sum_{j=1}^{n}(\mathbb{V}[W_j]\mathbb{V}[R] + \mathbb{V}[W_j']\mathbb{V}[R'])\Bigg].\end{aligned} \tag{B.13}$$

Therefore,

$$\begin{aligned}\mathbb{V}[\widehat{S_{\text{sa}}}] &= \frac{1}{n^4}\left[4n\frac{\sigma_W^4}{4} + 4n^4\frac{\sigma_R^4}{4} + 8\binom{n}{2}\frac{\sigma_W^4}{4} + 8n^3\frac{\sigma_W^2\sigma_R^2}{4}\right] \\ &= \frac{1}{n^2}\sigma_W^4 + \frac{2}{n}\sigma_W^2\sigma_R^2 + \sigma_R^4.\end{aligned} \tag{B.14}$$

B.3 Variance ratios

Let us compare the cross-spectrum and spectrum average estimates' variances for limit signal to noise ratio values.

If $\sigma_R^2 \ll \sigma_W^2$,

$$\mathbb{V}[\widehat{S_{\text{cs}}}] \approx \frac{1}{n(n-1)}\sigma_W^4 \qquad \text{and} \qquad \mathbb{V}[\widehat{S_{\text{sa}}}] \approx \frac{1}{n^2}\sigma_W^4. \tag{B.15}$$

Consequently,

$$\mathbb{V}[\widehat{S_{\text{cs}}}] \approx \frac{n}{n-1}\mathbb{V}[\widehat{S_{\text{sa}}}]. \tag{B.16}$$

If $\sigma_W^2 \ll \sigma_R^2$,

$$\mathbb{V}[\widehat{S_{\text{cs}}}] \approx \sigma_R^4 \qquad \text{and} \qquad \mathbb{V}[\widehat{S_{\text{sa}}}] \approx \sigma_R^4. \tag{B.17}$$

Consequently,

$$\mathbb{V}[\widehat{S_{\text{cs}}}] \approx \mathbb{V}[\widehat{S_{\text{sa}}}]. \tag{B.18}$$

APPENDIX C

Numerical results of the estimation of the parameters by fitting the cross-spectrum empirical PDF

For $\sigma_W = 1$:

σ_R	$\kappa \pm \Delta\kappa$	$\alpha \pm \Delta\alpha$	$\beta \pm \Delta\beta$
$1.00 \cdot 10^{-1}$	$4.95 \cdot 10^{-1} \pm 3.3 \cdot 10^{-4}$	$9.67 \cdot 10^{-3} \pm 2.4 \cdot 10^{-4}$	$9.90 \cdot 10^{-1} \pm 2.9 \cdot 10^{-4}$
$1.26 \cdot 10^{-1}$	$4.92 \cdot 10^{-1} \pm 2.5 \cdot 10^{-4}$	$1.56 \cdot 10^{-2} \pm 2.7 \cdot 10^{-4}$	$9.85 \cdot 10^{-1} \pm 2.3 \cdot 10^{-4}$
$1.58 \cdot 10^{-1}$	$4.88 \cdot 10^{-1} \pm 2.1 \cdot 10^{-4}$	$2.38 \cdot 10^{-2} \pm 4.3 \cdot 10^{-4}$	$9.76 \cdot 10^{-1} \pm 1.2 \cdot 10^{-4}$
$2.00 \cdot 10^{-1}$	$4.81 \cdot 10^{-1} \pm 6.1 \cdot 10^{-4}$	$3.68 \cdot 10^{-2} \pm 5.2 \cdot 10^{-4}$	$9.63 \cdot 10^{-1} \pm 4.9 \cdot 10^{-4}$
$2.51 \cdot 10^{-1}$	$4.70 \cdot 10^{-1} \pm 3.9 \cdot 10^{-4}$	$5.60 \cdot 10^{-2} \pm 2.5 \cdot 10^{-4}$	$9.44 \cdot 10^{-1} \pm 3.2 \cdot 10^{-4}$
$3.16 \cdot 10^{-1}$	$4.55 \cdot 10^{-1} \pm 4.5 \cdot 10^{-4}$	$8.32 \cdot 10^{-2} \pm 5.0 \cdot 10^{-4}$	$9.17 \cdot 10^{-1} \pm 4.3 \cdot 10^{-4}$
$3.98 \cdot 10^{-1}$	$4.32 \cdot 10^{-1} \pm 5.2 \cdot 10^{-4}$	$1.20 \cdot 10^{-1} \pm 2.1 \cdot 10^{-4}$	$8.80 \cdot 10^{-1} \pm 4.0 \cdot 10^{-4}$
$5.01 \cdot 10^{-1}$	$4.00 \cdot 10^{-1} \pm 3.6 \cdot 10^{-4}$	$1.67 \cdot 10^{-1} \pm 4.3 \cdot 10^{-4}$	$8.33 \cdot 10^{-1} \pm 4.4 \cdot 10^{-4}$
$6.31 \cdot 10^{-1}$	$3.58 \cdot 10^{-1} \pm 3.4 \cdot 10^{-4}$	$2.22 \cdot 10^{-1} \pm 5.5 \cdot 10^{-5}$	$7.78 \cdot 10^{-1} \pm 2.7 \cdot 10^{-4}$
$7.94 \cdot 10^{-1}$	$3.07 \cdot 10^{-1} \pm 3.9 \cdot 10^{-4}$	$2.79 \cdot 10^{-1} \pm 4.4 \cdot 10^{-4}$	$7.21 \cdot 10^{-1} \pm 4.9 \cdot 10^{-4}$
1.00	$2.50 \cdot 10^{-1} \pm 3.4 \cdot 10^{-4}$	$3.33 \cdot 10^{-1} \pm 3.0 \cdot 10^{-4}$	$6.67 \cdot 10^{-1} \pm 3.9 \cdot 10^{-4}$
1.26	$1.93 \cdot 10^{-1} \pm 1.6 \cdot 10^{-4}$	$3.80 \cdot 10^{-1} \pm 4.5 \cdot 10^{-4}$	$6.20 \cdot 10^{-1} \pm 4.4 \cdot 10^{-4}$
1.58	$1.42 \cdot 10^{-1} \pm 7.4 \cdot 10^{-5}$	$4.17 \cdot 10^{-1} \pm 2.1 \cdot 10^{-4}$	$5.83 \cdot 10^{-1} \pm 2.2 \cdot 10^{-4}$
2.00	$1.00 \cdot 10^{-1} \pm 7.1 \cdot 10^{-5}$	$4.45 \cdot 10^{-1} \pm 4.7 \cdot 10^{-4}$	$5.56 \cdot 10^{-1} \pm 4.7 \cdot 10^{-4}$
2.51	$6.84 \cdot 10^{-2} \pm 7.1 \cdot 10^{-5}$	$4.63 \cdot 10^{-1} \pm 8.1 \cdot 10^{-4}$	$5.37 \cdot 10^{-1} \pm 8.0 \cdot 10^{-4}$
3.16	$4.54 \cdot 10^{-2} \pm 2.0 \cdot 10^{-5}$	$4.76 \cdot 10^{-1} \pm 3.0 \cdot 10^{-4}$	$5.24 \cdot 10^{-1} \pm 3.1 \cdot 10^{-4}$
3.98	$2.97 \cdot 10^{-2} \pm 2.1 \cdot 10^{-5}$	$4.85 \cdot 10^{-1} \pm 9.2 \cdot 10^{-4}$	$5.16 \cdot 10^{-1} \pm 9.1 \cdot 10^{-4}$
5.01	$1.91 \cdot 10^{-2} \pm 2.5 \cdot 10^{-5}$	$4.90 \cdot 10^{-1} \pm 1.4 \cdot 10^{-3}$	$5.10 \cdot 10^{-1} \pm 1.4 \cdot 10^{-3}$
6.31	$1.22 \cdot 10^{-2} \pm 8.9 \cdot 10^{-6}$	$4.93 \cdot 10^{-1} \pm 7.5 \cdot 10^{-4}$	$5.06 \cdot 10^{-1} \pm 7.4 \cdot 10^{-4}$
7.94	$7.80 \cdot 10^{-3} \pm 6.8 \cdot 10^{-6}$	$4.95 \cdot 10^{-1} \pm 7.2 \cdot 10^{-4}$	$5.03 \cdot 10^{-1} \pm 7.1 \cdot 10^{-4}$
$1.00 \cdot 10^{+1}$	$4.95 \cdot 10^{-3} \pm 6.9 \cdot 10^{-6}$	$4.97 \cdot 10^{-1} \pm 1.8 \cdot 10^{-3}$	$5.02 \cdot 10^{-1} \pm 1.8 \cdot 10^{-3}$

For $\sigma_R = 1$:

σ_W	$\kappa \pm \Delta\kappa$	$\alpha \pm \Delta\alpha$	$\beta \pm \Delta\beta$
$1.00 \cdot 10^{-1}$	$4.97 \cdot 10^{-1} \pm 7.5 \cdot 10^{-4}$	$4.97 \cdot 10^{+1} \pm 1.7 \cdot 10^{-1}$	$5.02 \cdot 10^{+1} \pm 1.7 \cdot 10^{-1}$
$1.26 \cdot 10^{-1}$	$4.93 \cdot 10^{-1} \pm 5.1 \cdot 10^{-4}$	$3.13 \cdot 10^{+1} \pm 9.1 \cdot 10^{-2}$	$3.18 \cdot 10^{+1} \pm 9.1 \cdot 10^{-2}$
$1.58 \cdot 10^{-1}$	$4.88 \cdot 10^{-1} \pm 5.0 \cdot 10^{-4}$	$1.96 \cdot 10^{+1} \pm 6.7 \cdot 10^{-2}$	$2.01 \cdot 10^{+1} \pm 6.6 \cdot 10^{-2}$
$2.00 \cdot 10^{-1}$	$4.81 \cdot 10^{-1} \pm 1.0 \cdot 10^{-3}$	$1.23 \cdot 10^{+1} \pm 5.2 \cdot 10^{-2}$	$1.28 \cdot 10^{+1} \pm 5.2 \cdot 10^{-2}$
$2.51 \cdot 10^{-1}$	$4.71 \cdot 10^{-1} \pm 6.3 \cdot 10^{-4}$	$7.69 \pm 1.7 \cdot 10^{-2}$	$8.17 \pm 1.7 \cdot 10^{-2}$
$3.16 \cdot 10^{-1}$	$4.55 \cdot 10^{-1} \pm 1.5 \cdot 10^{-4}$	$4.76 \pm 8.3 \cdot 10^{-3}$	$5.24 \pm 8.0 \cdot 10^{-3}$
$3.98 \cdot 10^{-1}$	$4.32 \cdot 10^{-1} \pm 6.0 \cdot 10^{-4}$	$2.92 \pm 7.0 \cdot 10^{-3}$	$3.38 \pm 7.0 \cdot 10^{-3}$
$5.01 \cdot 10^{-1}$	$4.00 \cdot 10^{-1} \pm 6.5 \cdot 10^{-4}$	$1.77 \pm 3.6 \cdot 10^{-3}$	$2.21 \pm 3.6 \cdot 10^{-3}$
$6.31 \cdot 10^{-1}$	$3.58 \cdot 10^{-1} \pm 2.0 \cdot 10^{-4}$	$1.05 \pm 6.5 \cdot 10^{-4}$	$1.46 \pm 6.6 \cdot 10^{-4}$
$7.94 \cdot 10^{-1}$	$3.07 \cdot 10^{-1} \pm 2.0 \cdot 10^{-4}$	$6.03 \cdot 10^{-1} \pm 4.6 \cdot 10^{-4}$	$9.83 \cdot 10^{-1} \pm 5.2 \cdot 10^{-4}$
1.00	$2.50 \cdot 10^{-1} \pm 1.9 \cdot 10^{-4}$	$3.33 \cdot 10^{-1} \pm 2.3 \cdot 10^{-4}$	$6.67 \cdot 10^{-1} \pm 3.0 \cdot 10^{-4}$
1.26	$1.94 \cdot 10^{-1} \pm 1.7 \cdot 10^{-4}$	$1.76 \cdot 10^{-1} \pm 2.2 \cdot 10^{-4}$	$4.55 \cdot 10^{-1} \pm 2.6 \cdot 10^{-4}$
1.58	$1.42 \cdot 10^{-1} \pm 4.3 \cdot 10^{-5}$	$8.82 \cdot 10^{-2} \pm 5.3 \cdot 10^{-5}$	$3.10 \cdot 10^{-1} \pm 5.4 \cdot 10^{-5}$
2.00	$1.00 \cdot 10^{-1} \pm 5.4 \cdot 10^{-5}$	$4.20 \cdot 10^{-2} \pm 1.9 \cdot 10^{-5}$	$2.09 \cdot 10^{-1} \pm 6.2 \cdot 10^{-5}$
2.51	$6.84 \cdot 10^{-2} \pm 1.9 \cdot 10^{-5}$	$1.91 \cdot 10^{-2} \pm 2.1 \cdot 10^{-5}$	$1.39 \cdot 10^{-1} \pm 4.0 \cdot 10^{-5}$
3.16	$4.55 \cdot 10^{-2} \pm 2.6 \cdot 10^{-6}$	$8.34 \cdot 10^{-3} \pm 2.1 \cdot 10^{-5}$	$9.17 \cdot 10^{-2} \pm 1.2 \cdot 10^{-5}$
3.98	$2.97 \cdot 10^{-2} \pm 5.6 \cdot 10^{-6}$	$3.52 \cdot 10^{-3} \pm 2.1 \cdot 10^{-5}$	$5.96 \cdot 10^{-2} \pm 2.3 \cdot 10^{-5}$
5.01	$1.91 \cdot 10^{-2} \pm 3.0 \cdot 10^{-6}$	$1.48 \cdot 10^{-3} \pm 1.6 \cdot 10^{-5}$	$3.84 \cdot 10^{-2} \pm 1.2 \cdot 10^{-5}$
6.31	$1.23 \cdot 10^{-2} \pm 1.3 \cdot 10^{-6}$	$6.10 \cdot 10^{-4} \pm 3.3 \cdot 10^{-5}$	$2.45 \cdot 10^{-2} \pm 2.5 \cdot 10^{-5}$
7.94	$7.80 \cdot 10^{-3} \pm 2.8 \cdot 10^{-6}$	$2.14 \cdot 10^{-4} \pm 2.5 \cdot 10^{-5}$	$1.56 \cdot 10^{-2} \pm 3.0 \cdot 10^{-5}$
$1.00 \cdot 10^{+1}$	$4.95 \cdot 10^{-3} \pm 2.6 \cdot 10^{-6}$	$9.49 \cdot 10^{-5} \pm 3.3 \cdot 10^{-5}$	$9.89 \cdot 10^{-3} \pm 5.1 \cdot 10^{-5}$

APPENDIX D

Publications

List of publications in peer-reviewed journals:

- A. Baudiquez, E. Lantz, E. Rubiola, and F. Vernotte. Cross-Spectrum Measurement Statistics: Uncertainties and Detection Limit. IEEE Trans. Ultras. Ferroelec. Freq. Contr., 67(11):2461–2470, June 2020.
  DOI: 10.1109/TUFFC.2020.3005785
- A. Baudiquez, E. Lantz, E. Rubiola, and F. Vernotte. The Statistics of the Cross-Spectrum and the Spectrum Average: Generalization to Multiple Instruments. IEEE Trans. Ultras. Ferroelec. Freq. Contr., 69(8):2585–2594, June 2022.
  DOI: 10.1109/TUFFC.2022.3185528

IEEE TRANSACTIONS ON ULTRASONICS, FERROELECTRICS, AND FREQUENCY CONTROL, VOL. 67, NO. 11, NOVEMBER 2020 2461

Cross-Spectrum Measurement Statistics: Uncertainties and Detection Limit

Antoine Baudiquez, *Graduate Student Member, IEEE*, Éric Lantz,
Enrico Rubiola, *Member, IEEE*, and François Vernotte

***Abstract*—The cross-spectrum method consists in measuring a signal $c(t)$ simultaneously with two independent instruments. Each of these instruments contributes to the global noise by its intrinsic (white) noise, whereas the signal $c(t)$ that we want to characterize could be a (red) noise. We first define the real part of the cross spectrum as a relevant estimator. Then, we characterize the probability density function (pdf) of this estimator knowing the noise level (direct problem) as a Variance-gamma (VG) distribution. Next, we solve the "inverse problem" due to Bayes' theorem to obtain an upper limit of the noise level knowing the estimate. Checked by massive Monte Carlo simulations, VG proves to be perfectly reliable for any number of degrees of freedom (DOFs). Finally, we compare this method with another method using the Karhunen–Loève transform (KLT). We find an upper limit of the signal level slightly different as the one of VG since KLT better considers the available information.**

***Index Terms*—Bayesian statistics, confidence interval, cross spectrum, Karhunen–Loève transform (KLT), probability density function (pdf).**

See https://arxiv.org/pdf/2003.07118.pdf

Manuscript received March 16, 2020; accepted June 20, 2020. Date of publication June 29, 2020; date of current version October 26, 2020. This work was supported in part by the ANR Programmes d'Investissement d'Avenir (PIA) Oscillator IMP under Project 11-EQPX-0033 and in part by the Formation, Innovation, Recherche, Services et Transfert en Temps-Fréquence (FIRST-TF) under Project 10-LABX-0048. *(Corresponding author: Antoine Baudiquez.)*

Antoine Baudiquez is with FEMTO-ST, Department of Time and Frequency, UMR 6174, Université Bourgogne Franche-Comté, 25 030 Besançon, France (e-mail: antoine.baudiquez@femto-st.fr).

Éric Lantz is with FEMTO-ST, Département d'Optique P. M. Duffieux, UMR 6174 CNRS, Université Bourgogne Franche-Comté, 25 030 Besançon, France.

Enrico Rubiola is with FEMTO-ST, Department of Time and Frequency, UMR 6174, Université Bourgogne Franche-Comté, 25000 Besançon, France, and also with the Division of Quantum Metrology and Nanotechnology, Istituto Nazionale di Ricerca Metrologica (INRiM), 10135 Turin, Italy.

François Vernotte is with FEMTO-ST, Department of Time and Frequency, Observatory THETA, UMR 6174 CNRS, Université Bourgogne Franche-Comté, 25 030 Besançon, France.

Digital Object Identifier 10.1109/TUFFC.2020.3005785

Cross-Spectrum Measurement Statistics: uncertainties and detection limit

Antoine Baudiquez, Éric Lantz, Enrico Rubiola, François Vernotte

***Abstract*—The cross-spectrum method consists in measuring a signal $c(t)$ simultaneously with two independent instruments. Each of these instruments contributes to the global noise by its intrinsic (white) noise, whereas the signal $c(t)$ that we want to characterize could be a (red) noise.**

We first define the real part of the cross-spectrum as a relevant estimator. Then, we characterize the probability density function (PDF) of this estimator knowing the noise level (direct problem) as a Variance-Gamma (VG) distribution. Next, we solve the "inverse problem" thanks to Bayes' theorem to obtain an upper limit of the noise level knowing the estimate. Checked by massive Monte Carlo simulations, VG proves to be perfectly reliable for any number of degrees of freedom (dof).

Finally we compare this method with an other method using the Karhunen-Loève transform (KLT). We find an upper limit of the signal level slightly different as the one of VG since KLT better takes into account the available information.

***Index Terms*—Bayesian statistics, confidence interval, cross-spectrum, Karhunen-Loève transform, probability density function.**

I. INTRODUCTION

THE measurement of power spectra is a classical problem, ubiquitous in numerous branches of physics, as explained below. Power spectra are efficiently measured using Fourier transform methods with digitized data. Relevant bibliography is now found in classic books [1], [2], [3], [4].

We are interested in the measurement of weak statistical phenomena, which challenge the instruments and the mathematical tools, using the cross-spectrum method. This method consists of the simultaneous measurement of the signal with two separate and independent instruments [5]. The other approach, consisting on the observation of the spectral contrast in a chopped signal, broadly equivalent to the Dicke radiometer [6], is not considered here. Regarding the duration of the data record used to evaluate the Fast Fourier Transform (FFT), two asymptotic cases arise.

The first case is that of the measurement of fast phenomena, where a large number of records denoted m is possible in a reasonable observation time. At large m the central limit theorem rules and the background noise can be rejected by a factor approximately equal to $1/\sqrt{m}$, depending on the estimator. Numerous examples are found in the measurement of noise in semiconductors [7], phase noise in oscillators and components [8], [9], [10], [11], frequency fluctuations and relative intensity noise in lasers [12], [13], electromigration in thin films [14], etc. Restricting to one bin of the Fourier transform, the power spectral density integrated over a suitable frequency range is used in radiometry [15], [16], Johnson thermometry [17] and other applications.

The second case is that of slow phenomena, where the fluctuations are very long term or non ergodic. On one hand the background noise is still rejected as before but with a very low m which can actually be equal to one. On the other hand, the central limit theorem does not apply and the statistical uncertainties are not trivial. This case is of great interest in radio astronomy, where the observations are limited by the available resources and take a long time. As instance millisecond pulsars (MSP) can be used as very stable clocks at astronomical distances [18]. The radio pulses times of arrival (TOA) of MSP are affected by numerous physical process, one of them are gravitational-wave (GW) perturbations [19], [20]. Red noise originated from GW perturbations in the signal path common to the radio-telescopes can be detected [21], [22]. Like the analysis of the signals provided by the LIGO/VIRGO interferometers which use cross correlation methods [23], [24], the LEAP experiment (i.e. Large European Array for Pulsars) [25] could use such methods in order to access lower frequencies and observe imperceptible phenomena such as early phases well before the coalescence of black holes or GW of cosmological origin (for example cosmic strings, inflation, primordial black holes).

This article is intended to put an upper limit on the uncertainty of the cross-spectrum estimate. The method proposed here is totally general regardless the power law type of noise. Indeed, even if the pulsar signal would be constituted by white noise, the realisations of this white noise would be the same, for low frequency, at different observatories while the realisations of measurement white noise are independent. However this paper shows a particular interest to red noise. Gravitational-waves have not been yet discovered in the TOA of millisecond pulars. Thanks to the very long line of sight between the pulsars and us (several thousand light-years), we could access very low frequencies, inaccessible to LIGO/VIRGO, thus revealing much slower astrophysical phenomena. It is therefore important to develop statistical tools to improve measurement sensitivity to pulsar timing observations [26]. In this respect, we propose in Section II to state the cross-spectrum problem to define a proper

---

A. Baudiquez and E. Rubiola are with FEMTO-ST, Department of Time and Frequency, UMR 6174, Université Bourgogne Franche-Comté, France. Antoine's ORCID is 0000-0002-7007-5273

E. Lantz is with FEMTO-ST, Département d'Optique P.M. Duffieux, UMR 6174 CNRS, Université Bourgogne Franche-Comté, France.

E. Rubiola is also with the Division of Quantum Metrology and Nanotechnology, Istituto Nazionale di Ricerca Metrologica (INRiM), 10135 Turin, Italy. Enrico's ORCID is 0000-0002-5364-1835

F. Vernotte is with FEMTO-ST, Department of Time and Frequency, Observatory THETA, UMR 6174 CNRS, Université Bourgogne Franche-Comté, France. François's ORCID is 0000-0002-1645-5873

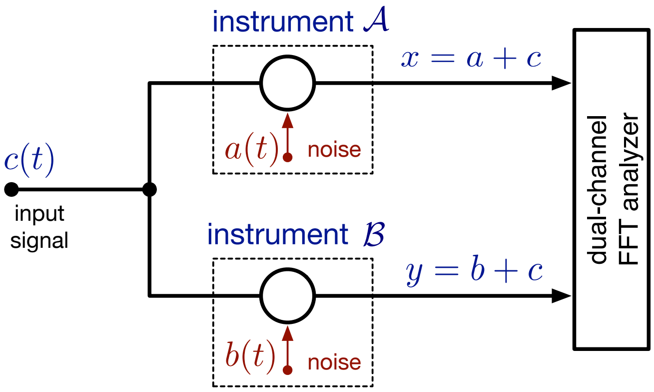

Fig. 1. Basics of the cross-spectrum method.

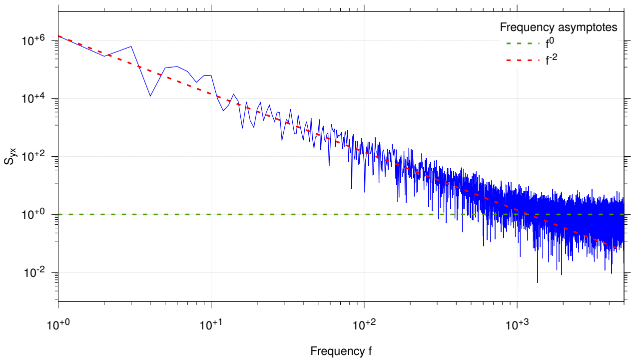

Fig. 2. This is a plot of a PSD estimate magnitude obtained via a discrete Fourier transform. The red and green dashed lines correspond to the power law frequency asymptotes related to the signal.

estimate. Based on the principle that the experiment is repeated m times, it is important to note that the estimation of the measurement uncertainty is A-Type as defined by the VIM [27]. Then in Section III we define the probability density function (i.e. "direct problem") of the cross-spectrum estimate which is used in Section IV to compute an upper limit by using a bayesian inference approach (i.e. "inverse problem"). The results obtained are compared to an another method using the Karhunen-Loève transform developed in [28] and the conclusions are presented in Section V.

II. STATEMENT OF THE PROBLEM

A. *Spectral Measurement*

This paper aims to measure the mathematical expectation of the amplitude for a frequency bin. This amplitude obviously depends on the frequency and this is what we are looking for as shown in Fig. 2. Let us remind at that the Fourier transform of a white noise is a white noise. Fourier transform, random signals have generally infinite energy so the real Fourier transform can not be generally defined. A description of a realistic white noise actually corresponds to a Markov process of the first order and the reader can report to [29] for discrete simulation of colored noise and stochastic processes. The random part of the amplitude of each frequency bin is then uncorrelated from each bin. Considering a red noise as a filtered white noise means that the red noise spectrum is the product of the white spectrum by a deterministic function and, therefore, the uncorrelation property of the random part of the red noise spectrum is perserved. Working directly in the frequency domain therefore changes absolutely nothing in terms of a random variable. Consequently it does not matter to know if the signals are stationary, uncorrelated or not since we are interested in the spectrum and in a bin of frequency in particular.

B. *Cross-spectrum Method*

Let us consider 3 statistically independent signals: $a(t)$, $b(t)$ and $c(t)$ as shown in Fig. 1. On one side the two first $a(t)$ and $b(t)$ are respectively the instrument noise of $\mathcal{A}$ and $\mathcal{B}$. On the other side $c(t)$ is an input signal which we want to characterize. This signal is stochastic and not necessarily stationary. In the case of pulsar measurement, this input signal is generally a red noise. The output of each channel is

$$\begin{aligned} x(t) &= a(t) + c(t) \\ y(t) &= b(t) + c(t). \end{aligned} \tag{1}$$

Processing experimental signals, we can assume that white noise is a continuous function of time, and that the Fourier Transform (FT) always exists if we look at a very short interval regarding the sampling period. The reader can refer to [30] for a more detailed model of realistic white noise. Applying the FT on each channel gives

$$\begin{aligned} X(f) &= A(f) + C(f) \\ Y(f) &= B(f) + C(f) \end{aligned} \tag{2}$$

where f is the frequency, $X(f)$, $Y(f)$, $A(f)$, $B(f)$ and $C(f)$ stand respectively for the Fourier Transform of $x(t)$, $y(t)$, $a(t)$, $b(t)$ and $c(t)$. Our interest is carried out on the power spectral density (PSD) rather than the spectrum. The cross-spectrum is defined as

$$S_{yx}(f) = \frac{1}{T}\mathbb{E}\left[Y(f)X^*(f)\right], \tag{3}$$

where the cross-spectrum is actually a cross-PSD and $\mathbb{E}[\cdot]$ stands for the mathematical expectation of the quantity within the brackets. The factor T is the measurement time which is necessary for because the power calculated in time domain and in frequency domain must be the same (Parseval theorem), and also for $S_{yx}(f)$ to have the dimension of power per unit of frequency. The * denotes the complex conjugate of the quantity placed before it. Eq. 3 is the two-sides PSD, which contains positive and negative frequencies. Experimentaly averaging over m spectra realizations leads to the following cross-PSD estimator

$$\langle S_{yx} \rangle_m = \frac{1}{T}\left\langle Y(f)X^*(f) \right\rangle_m. \tag{4}$$

C. *Cross Power Spectral Density*

Averaging on a large number of observations, the mathematics is made simple by the central limit theorem, by which all the probability density functions (PDF) become Gaussian.

More interesting for us is the case of a small number of realizations, each of which taking long observation time-up to several years in the case of the millisecond pulsars.

The random variables (rv) $a(t)$, $b(t)$ and $c(t)$ follow a centered normal distribution whatever the kind of noise. Even red noise (e.g. random walk) follows a normal distribution not on the time average but regarding its ensemble average over the probability space which means it is a non ergodic process. Moreover a stochastic process with zero-mean Gaussian distribution has a FT which is also a random process with centered Gaussian distribution.

The rv $A(f)$, $B(f)$ and $C(f)$ can then be decomposed into a real and imaginary part

$$\begin{aligned} A(f) &= A'(f) + iA''(f) \\ B(f) &= B'(f) + iB''(f) \\ C(f) &= C'(f) + iC''(f). \end{aligned} \tag{5}$$

The real and imaginary part are statistically independent rv with equal variance following a zero-mean Gaussian distribution. For an ensemble average, or a time sequence sufficiently long to ensure a good spectral resolution, the samples at different frequencies are independent of each other. Hence, all the results of this paper are given for a given frequency that we do not mention explicitely. Of course, there is a deterministic relation between the results and this frequency, except in the case of a signal constituted by white noise, which is not the most common assumption in the envisioned applications. Let us now expand Eq. 4,

$$\begin{aligned} \langle S_{yx}\rangle_m &= \frac{1}{T}\langle YX^*\rangle_m . \\ &= \frac{1}{T}\left[\langle A'B' + B'C' + C'A' + C'^2\rangle_m \right. \\ &+ \langle A''B'' + B''C'' + C''A'' + C''^2\rangle_m \\ &+ i\,\langle A'B'' + B''C' + C''A'\rangle_m \\ &\left. - i\,\langle A''B' + B'C'' + C'A''\rangle_m\right]. \end{aligned} \tag{6}$$

The terms in the imaginary part have a zero expectation, while the expectation in the real part is proportional to the PSD of the signal, i.e. what we are looking to characterize. As a consequence, the next sections focus solely on the real part $\Re\{S_{yx}\}$,

$$\langle \Re\{S_{yx}\}\rangle_m = \frac{1}{T}\left\langle (A^k + C^k)(B^k + C^k)\right\rangle_\nu \tag{7}$$

where $\nu = 2m$ the number of degree of freedom (dof). The superscript k means real or imaginary part because they are independent rv.

D. Statement of the Problem

1) Measurements, and Estimates: In the following, in order to simplify the notation, we will omit the superscript k. Thereby the real and imaginary part will be treated as 2 dof. Moreover to simplifiy the notations, we will omit the factor $\frac{1}{T}$ which does not affect the PDF. The **estimates** will be noted with a "*hat*" and we refer the cross-spectrum measurement for a given frequency to

$$\hat{Z} = (\hat{A} + \hat{C})(\hat{B} + \hat{C}) \tag{8}$$

where all $\hat{A}$, $\hat{B}$, $\hat{C}$ are rv which are independent, centered and normal. In the following, we will assume that $\hat{A}$, $\hat{B}$, $\hat{C}$ have only 1 dof, their real or their imaginary part, and that $\hat{Z}$ does not come from the average of different spectra. A generalization of this problem to 2 dof (real and imaginary parts) and then $2m$ dof (average of m spectra) will be given.

2) Direct and Inverse Problem: In order to assess the uncertainty over the estimator σ_C^2, called the *signal* level, we will have to distinguish to main issues:

- The **direct problem** consists in calculating the statistics of the cross-spectrum measurement $\hat{Z}$, knowing the model parameters σ_A^2, σ_B^2, σ_C^2.
- The **inverse problem**, conversely consists in calculating a confidence interval over the unknown model parameter σ_C^2, from the known parameters σ_A^2, σ_B^2 and the cross-spectrum measurement $\hat{Z}$.

III. DIRECT PROBLEM

In Sections III-A to III-E we will omit the "*hat*" for estimates since we deal with the mathematical models.

A. Vector Formalization of the Problem

We will reuse here the formalism we developed in [31], i.e. a vector space of normal laws. Since we have 3 normal rv, we are in a vector space of 3 dimensions that we will denote $\mathbb{LG}^3$ and which has the basis $(\vec{E}_A, \vec{E}_B, \vec{E}_C)$ defined as

$$\begin{cases} \vec{E}_A = \mathrm{LG}_A(0,1) \\ \vec{E}_B = \mathrm{LG}_B(0,1) \\ \vec{E}_C = \mathrm{LG}_C(0,1) \end{cases}$$

where $\mathrm{LG}(0,1)$ stands for a Laplace-Gauss (or normal) rv. with zero-mean (centered) and unity standard deviation ($\sigma = 1$). We assume that $\mathrm{LG}_A(0,1)$, $\mathrm{LG}_B(0,1)$, $\mathrm{LG}_C(0,1)$ are independent. We can define the scalar product between the basis vectors of $\mathbb{LG}^3$ in such a way:

$$\begin{cases} ||\vec{E}_A||^2 = \vec{E}_A \cdot \vec{E}_A = \mathrm{LG}_A \cdot \mathrm{LG}_A = \chi_A^2 \\ ||\vec{E}_B||^2 = \vec{E}_B \cdot \vec{E}_B = \mathrm{LG}_B \cdot \mathrm{LG}_B = \chi_B^2 \\ ||\vec{E}_C||^2 = \vec{E}_C \cdot \vec{E}_C = \mathrm{LG}_C \cdot \mathrm{LG}_C = \chi_C^2 \end{cases}$$

$$\begin{cases} \vec{E}_A \cdot \vec{E}_B = \mathrm{LG}_A \cdot \mathrm{LG}_B = \mathrm{V}\Gamma_{AB} \\ \vec{E}_B \cdot \vec{E}_C = \mathrm{LG}_B \cdot \mathrm{LG}_C = \mathrm{V}\Gamma_{BC} \\ \vec{E}_C \cdot \vec{E}_A = \mathrm{LG}_C \cdot \mathrm{LG}_A = \mathrm{V}\Gamma_{CA} \end{cases}$$

where $\chi^2_{A,B,C}$ are 3 independent χ^2 rv with 1 dof and $\mathrm{V}\Gamma_{AB,BC,CA}$ are 3 variance-Gamma (VΓ) rv [31], [32]. Any vector $\vec{U}$ may be written as

$$\vec{U} = \begin{pmatrix} u_A \\ u_B \\ u_C \end{pmatrix} = u_A\vec{E}_A + u_B\vec{E}_B + u_C\vec{E}_C$$

where u_A, u_B, u_C are 3 constant scalars since all the random part is carried by the basis vectors. The scalar product between 2 vectors $\vec{U}$ and $\vec{V}$ is then:

$$\begin{aligned}\vec{U}\cdot\vec{V} &= \left(u_A\vec{E}_A + u_B\vec{E}_B + u_C\vec{E}_C\right)\cdot \\ &\quad \left(v_A\vec{E}_A + v_B\vec{E}_B + v_C\vec{E}_C\right) \\ &= u_Av_A\vec{E}_A\cdot\vec{E}_A + u_Bv_B\vec{E}_B\cdot\vec{E}_B + u_Cv_C\vec{E}_C\cdot\vec{E}_C \\ &\quad +(u_Av_B + u_Bv_A)\vec{E}_A\cdot\vec{E}_B \\ &\quad +(u_Bv_c + u_Cv_B)\vec{E}_B\cdot\vec{E}_C \\ &\quad +(u_Cv_A + u_Av_C)\vec{E}_C\cdot\vec{E}_A.\end{aligned}$$

On the other hand, if we consider the mathematical expectation of these expressions, we obtain

$$\mathbb{E}\left[\vec{E}_P\cdot\vec{E}_Q\right] = \delta_{P,Q} \quad \text{with} \quad P,Q \in \{A,B,C\}$$

where $\delta_{P,Q}$ is the Kronecker delta. We see that we obtain the classical scalar product by using the mathematical expectation:

$$\mathbb{E}\left[\vec{U}\cdot\vec{V}\right] = u_Av_A + u_Bv_B + u_Cv_C.$$

Therefore, we will define that 2 vectors $\vec{U}$ and $\vec{V}$ are orthogonal if $\mathbb{E}\left[\vec{U}\cdot\vec{V}\right] = 0$.

B. From a normal Random Variable Product to a Chi-squared RV Difference

Following this formalism, Eq. (8) may be rewritten as

$$\begin{aligned}Z = \left(\vec{A}+\vec{C}\right)\cdot\left(\vec{B}+\vec{C}\right) &= \begin{pmatrix} a \\ 0 \\ c\end{pmatrix}\cdot\begin{pmatrix} 0 \\ b \\ c\end{pmatrix} \\ &= ab\mathrm{V}\Gamma_{AB} + ac\mathrm{V}\Gamma_{AC} + bc\mathrm{V}\Gamma_{BC} + c^2\chi_C^2\end{aligned} \tag{9}$$

where a, b, c are respectively the standard deviations of the rv A, B, C. As a consequence, $\mathbb{E}[Z] = c^2$. In the following, we will use the noise variances $\sigma_A^2 = a^2, \sigma_B^2 = b^2$ and the signal variance $\sigma_C^2 = c^2$.

As demonstrated in [33], a product of independent normal rv may be expressed as a difference of χ^2 rv. For this purpose, although we know that $(A + C)$ and $(B + C)$ are not independent, we introduce the rv $V_1 = (A + B)/2 + C$ and $V_2 = (A - B)/2$ in such a way that $A + C = V_1 + V_2$, $B + C = V_1 - V_2$ and therefore $(A+C)(B+C) = V_1^2 - V_2^2$. In this vectorial formalism:

$$\vec{V}_1 = \begin{pmatrix} a/2 \\ b/2 \\ c\end{pmatrix}, \quad \text{and} \quad \vec{V}_2 = \begin{pmatrix} a/2 \\ -b/2 \\ 0\end{pmatrix}.$$

Therefore, $(\vec{V}_1, \vec{V}_2)$ is the basis of the 2-dimensional subspace of $\mathbb{LG}^3$ in which lies our whole problem. Since the squared modulus of $\vec{V}_1, \vec{V}_2$ are:

$$\begin{cases} ||\vec{V}_1||^2 &= \dfrac{a^2}{4}\chi_A^2 + \dfrac{b^2}{4}\chi_B^2 + c^2\chi_C^2 \\ &\quad +\frac{ab}{2}\mathrm{V}\Gamma_{AB} + ac\mathrm{V}\Gamma_{AC} + bc\mathrm{V}\Gamma_{BC} \\ ||\vec{V}_2||^2 &= \dfrac{a^2}{4}\chi_A^2 + \dfrac{b^2}{4}\chi_B^2 - \dfrac{ab}{2}\mathrm{V}\Gamma_{AB},\end{cases}$$

their difference is consistent with Eq. (9) and then $Z = (\vec{A} + \vec{C})\cdot(\vec{B} + \vec{C}) = ||\vec{V}_1||^2 - ||\vec{V}_2||^2$. Moreover, we can calculate the mathematical expectations of these squared modulus:

$$\begin{aligned} v_1^2 = \mathbb{E}\left[||\vec{V}_1||^2\right] &= \frac{a^2+b^2}{4} + c^2 \\ v_2^2 = \mathbb{E}\left[||\vec{V}_2||^2\right] &= \frac{a^2+b^2}{4}.\end{aligned} \tag{10}$$

On the other hand, since

$$\mathbb{E}\left[\vec{V}_1\cdot\vec{V}_2\right] = \frac{a^2-b^2}{4} \tag{11}$$

the vector $\vec{V}_1$ and $\vec{V}_2$ are not orthogonal unless $a = b$, i.e. A and B have the same variance.

C. A Particular Case: A and B have the Same Variance

Let us define $\sigma_N^2 = \sigma_A^2 = \sigma_B^2 = n^2$, i.e. $n = a = b$. In this case

$$\mathbb{E}\left[\vec{V}_1\cdot\vec{V}_2\right] = \frac{n^2}{4} - \frac{n^2}{4} = 0,$$

$\vec{V}_1, \vec{V}_2$ are orthogonal which means that their squared modulus are 2 independent χ^2 rv:

$$||\vec{V}_1||^2 = v_1^2\chi_{v1}^2 \quad \text{and} \quad ||\vec{V}_2||^2 = v_2^2\chi_{v2}^2$$

Thanks to [31, Appendix A], we know that this χ^2 rv difference is a VΓ rv with a Probability Density Function (PDF), introduced by [34]:

$$p(x) = \frac{\gamma^{2\lambda}|x-\mu|^{\lambda-1/2}K_{\lambda-1/2}\left(\alpha|x-\mu|\right)}{\sqrt{\pi}\Gamma(\lambda)(2\alpha)^{\lambda-1/2}}e^{\beta(x-\mu)} \tag{12}$$

where $\gamma = \sqrt{\alpha^2-\beta^2}$, $\Gamma(\lambda)$ is the gamma function, $K_w(z)$ is a hyperbolic Bessel function of the second kind ($w \in \mathbb{R}$ and $z \in \mathbb{C}$) and with the following parameters:

$$\mu = 0, \quad \alpha = \frac{v_1^2+v_2^2}{4v_1^2v_2^2}, \quad \beta = \frac{v_1^2-v_2^2}{4v_1^2v_2^2}, \quad \lambda = \frac{1}{2} \tag{13}$$

where λ is the number of dof divided by 2. In this particular case, since $a^2 = b^2 = n^2$, v_1^2 and v_2^2 becomes

$$v_1^2 = \mathbb{E}\left[||\vec{V}_1||^2\right] = \frac{n^2}{2} + c^2 \quad \text{and} \quad v_2^2 = \mathbb{E}\left[||\vec{V}_2||^2\right] = \frac{n^2}{2},$$

and we obtain

$$\alpha = \frac{n^2+c^2}{n^2(2n^2+c^2)} \quad \text{and} \quad \beta = \frac{c^2}{n^2(2n^2+c^2)}$$

D. General Case

If $\sigma_A^2 \neq \sigma_B^2$, $\vec{V}_1$ and $\vec{V}_2$ are no longer orthogonal and therefore they are 2 correlated rv. We have then to search another set of basis vectors which are orthogonal. For this purpose, let us use the Gram-Schmidt process.

1) Gram-Schmidt Orthogonalization: Let us keep $\vec{V}_1$ unchanged. Let $\vec{V}_{2P}$ be the projection of $\vec{V}_2$ onto $\vec{V}_1$. Denoting θ the angle[1] between $\vec{V}_1$ and $\vec{V}_2$, it comes

$$\vec{V}_{2P} = v_2 \cos(\theta) \frac{\vec{V}_1}{v_1}.$$

with

$$\cos(\theta) = \frac{\mathbb{E}\left[\vec{V}_1 \cdot \vec{V}_2\right]}{v_1 v_2}$$

and then

$$\vec{V}_{2P} = \frac{\mathbb{E}\left[\vec{V}_1 \cdot \vec{V}_2\right]}{v_1^2} \vec{V}_1. \tag{14}$$

Therefore, we can build the vector $\vec{V}_{2N}$ which is the component of $\vec{V}_2$ orthogonal to $\vec{V}_1$:

$$\vec{V}_{2N} = \vec{V}_2 - \vec{V}_{2P} = \vec{V}_2 - \frac{\mathbb{E}\left[\vec{V}_1 \cdot \vec{V}_2\right]}{v_1^2} \vec{V}_1.$$

Using Eq. (10) and (11) yields

$$\begin{aligned}
\vec{V}_{2N} &= \begin{pmatrix} a/2 \\ -b/2 \\ 0 \end{pmatrix} - \frac{a^2 - b^2}{a^2 + b^2 + 4c^2} \begin{pmatrix} a/2 \\ b/2 \\ c \end{pmatrix} \\
&= \begin{pmatrix} \dfrac{a(b^2 + 2c^2)}{a^2 + b^2 + 4c^2} \\ -\dfrac{b(a^2 + 2c^2)}{a^2 + b^2 + 4c^2} \\ -\dfrac{c(a^2 - b^2)}{a^2 + b^2 + 4c^2} \end{pmatrix} = \begin{pmatrix} v_{2nA} \\ v_{2nB} \\ v_{2nC} \end{pmatrix}.
\end{aligned}$$

We have now to express the measurement vectors $\vec{A} + \vec{C}$ and $\vec{B} + \vec{C}$ as linear combinations of the new basis of orthogonal vectors $\vec{V}_1$ and $\vec{V}_{2N}$. In order to do this, we must project these 2 measurement vectors onto the 2 basis vectors in the same way that we have projected $\vec{V}_2$ onto $\vec{V}_1$ in Eq. (14):

$$\begin{cases} \vec{A} + \vec{C} &= k_{AC1} \vec{V}_1 + k_{AC2n} \vec{V}_{2N} \\ \vec{B} + \vec{C} &= k_{BC1} \vec{V}_1 + k_{BC2n} \vec{V}_{2N} \end{cases}$$

with

$$k_{AC1} = \frac{\mathbb{E}\left[\left(\vec{A} + \vec{C}\right) \cdot \vec{V}_1\right]}{\mathbb{E}\left[||\vec{V}_1||^2\right]} \quad k_{AC2n} = \frac{\mathbb{E}\left[\left(\vec{A} + \vec{C}\right) \cdot \vec{V}_{2N}\right]}{\mathbb{E}\left[||\vec{V}_{2N}||^2\right]}$$

$$k_{BC1} = \frac{\mathbb{E}\left[\left(\vec{B} + \vec{C}\right) \cdot \vec{V}_1\right]}{\mathbb{E}\left[||\vec{V}_1||^2\right]} \quad k_{BC2n} = \frac{\mathbb{E}\left[\left(\vec{B} + \vec{C}\right) \cdot \vec{V}_{2N}\right]}{\mathbb{E}\left[||\vec{V}_{2N}||^2\right]}.$$

Therefore, $Z = (\vec{A} + \vec{C}) \cdot (\vec{B} + \vec{C})$ may be written as

$$\begin{aligned}
Z &= k_{AC1} k_{BC1} ||\vec{V}_1||^2 + k_{AC2n} k_{BC2n} ||\vec{V}_{2N}||^2 \\
&\quad + \left(k_{AC1} k_{BC2n} + k_{AC2n} k_{BC1}\right) \vec{V}_1 \cdot \vec{V}_{2N} \\
&= k_{AC1} k_{BC1} \dot{\chi}^2 + k_{AC2n} k_{BC2n} \ddot{\chi}^2 \\
&\quad + \left(k_{AC1} k_{BC2n} + k_{AC2n} k_{BC1}\right) \mathrm{V}\Gamma
\end{aligned} \tag{15}$$

where $\dot{\chi}^2$ and $\ddot{\chi}^2$ are independent χ^2 rv corresponding respectively to the squared norm of $\vec{V}_1$ and $\vec{V}_{2N}$. Thus, this relationship involves the difference of 2 χ^2 rv (it can be proved that $k_{AC2n} k_{BC2n} < 0$), which is well known [31], [33], plus a $\mathrm{V}\Gamma$ rv, which makes the problem more complex. In order to simplify this problem, we should find a representation of Eq. (15) in which the cross term is identically null.

2) Normalization and Rotation of the Basis Vectors: Let $(\vec{V}_1', \vec{V}_2')$ be the normalized equivalent of the basis $(\vec{V}_1, \vec{V}_{2N})$:

$$\vec{V}_1' = \frac{\vec{V}_1}{\mathbb{E}\left[||\vec{V}_1||\right]} \quad \text{and} \quad \vec{V}_2' = \frac{\vec{V}_{2N}}{\mathbb{E}\left[||\vec{V}_{2N}||\right]}.$$

With this new basis, Eq. (15) may be rewritten as

$$\begin{aligned}
Z &= k_{AC1} k_{BC1} \mathbb{E}\left[||\vec{V}_1||\right]^2 ||\vec{V}_1'||^2 \\
&\quad + k_{AC2n} k_{BC2n} \mathbb{E}\left[||\vec{V}_{2N}||\right]^2 ||\vec{V}_2'||^2 \\
&\quad + k_{AC1} k_{BC2n} \mathbb{E}\left[||\vec{V}_1||\right] \mathbb{E}\left[||\vec{V}_{2N}||\right] \vec{V}_1' \cdot \vec{V}_2' \\
&\quad + k_{AC2n} k_{BC1} \mathbb{E}\left[||\vec{V}_1||\right] \mathbb{E}\left[||\vec{V}_{2N}||\right] \vec{V}_1' \cdot \vec{V}_2' \\
&= k_{11}' ||\vec{V}_1'||^2 - k_{22}' ||\vec{V}_2'||^2 + k_{12}' \vec{V}_1' \cdot \vec{V}_2'
\end{aligned} \tag{16}$$

with

$$\begin{cases} k_{11}' &= k_{AC1} k_{BC1} \mathbb{E}\left[||\vec{V}_1||\right]^2 \\ k_{22}' &= -k_{AC2n} k_{BC2n} \mathbb{E}\left[||\vec{V}_{2N}||\right]^2 \\ k_{12}' &= k_{AC1} k_{BC2n} \mathbb{E}\left[||\vec{V}_1||\right] \mathbb{E}\left[||\vec{V}_{2N}||\right] \\ & \quad + k_{AC2n} k_{BC1} \mathbb{E}\left[||\vec{V}_1||\right] \mathbb{E}\left[||\vec{V}_{2N}||\right]. \end{cases}$$

We can then consider Eq. (16) as the expression of a quadratic form Q which associate a scalar w_0 to any vector $\vec{W} = w_1 \vec{V}_1' + w_{2n} \vec{V}_2'$. Such a quadratic form may be described as

$$w_0 = \vec{w}^T [Q] \vec{w} \quad \text{with} \quad [Q] = \begin{pmatrix} k_{11}' & k_{12}'/2 \\ k_{12}'/2 & -k_{22}' \end{pmatrix}. \tag{17}$$

The simplification of our problem relies then in a rotation of the basis vectors in such a way that the quadratic form matrix $[Q]$ is diagonal. The eigenvalues of $[Q]$ are given by

$$\ell_1 = \frac{k_{11}' - k_{22}' - \sqrt{\Delta}}{2} \quad \text{and} \quad \ell_2 = \frac{k_{11}' - k_{22}' + \sqrt{\Delta}}{2}.$$

with $\Delta = (k_{11}' + k_{22}')^2 + k_{12}'^2$. Thanks to this rotation of the basis vectors, Eq. (15) and (16) become

$$Z = \ell_1 \dot{\chi}^2 + \ell_2 \ddot{\chi}^2.$$

As already stated in § III-C, Z is a $\mathrm{V}\Gamma$ rv with the following PDF parameters:

$$\mu = 0, \quad \alpha = \frac{\ell_1^2 + \ell_2^2}{4 \ell_1^2 \ell_2^2}, \quad \beta = \frac{\ell_1^2 - \ell_2^2}{4 \ell_1^2 \ell_2^2}, \quad \lambda = \frac{1}{2}. \tag{18}$$

---

[1] In the same way as the orthogonality between 2 vectors is defined by the null mathematical expectation of their scalar product, the angles as well as the other relationships between vectors must be taken into account as mathematical expectation since they are valid on average but not for only one particular realization of these vectors.

E. Generalization to Larger Degrees of Freedom

In the case of $2m$ dof, i.e. real part + imaginary part multiplied by m averaged uncorrelated spectra, the only change to apply concerns the parameter λ in Eq. (13) and (18) which becomes $\lambda = m$.
According to [35, Eq. 12 p.80] we have the following relation:

$$K_{n+\frac{1}{2}}(z) = \left(\frac{\pi}{2z}\right)^{\frac{1}{2}} e^{-z} \sum_{r=0}^{n} \frac{(n+r)!}{r!(n-r)!(2z)^r} \tag{19}$$

with $n \in \mathbb{N}$ and $z \in \mathbb{C}$. Moreover $m \in \mathbb{N}^*$ which leads to the relation $n = m - 1$. Therefore let us expand Eq. (12) using Eq. (19):

$$p(x) = \frac{\kappa(\alpha,\beta)^m \epsilon(x,\mu,\alpha,m)}{\Gamma(m)} e^{-\alpha|x-\mu|+\beta(x-\mu)} \tag{20}$$

with the following parameters:

$$\kappa(\alpha,\beta) = \frac{\alpha^2-\beta^2}{2\alpha} \quad \Gamma(m) = (m-1)!$$

$$\epsilon(x,\mu,\alpha,m) = \sum_{r=0}^{m-1} \frac{(m+r-1)!|x-\mu|^{m-r-1}}{r!(m-r-1)!(2\alpha)^r}$$

F. Validation of the Theoretical Probability Laws by Monte Carlo Simulations

1) Algorithm Description: According to § III-D2 the probability density of $\hat{Z}$, equal to the difference of two independent χ^2 rv, can now be calculated using the function $p(x)$ of the Eq. (20) by assigning the values to the parameters in Eq. (13) and (18). In order to perform this comparison we use two algorithms, one for Monte Carlo (MC) simulation and the other one for computing Eq. (20).

– MC simulation algorithm

The simulation algorithm follows these 6 steps

S1: Assignement of the 2 noise levels σ_A^2, σ_B^2, signal level σ_C^2 and the number of averaging spectra m.
S2: Drawing of $\hat{A}$, $\hat{B}$, $\hat{C}$, following a normal centered distribution with respectively σ_A, σ_B, σ_C as standard deviation.
S3: Computation of $\hat{Z} = (\hat{A}+\hat{C})(\hat{B}+\hat{C})$.
S4: Repetition $2m$ times of the steps S2 to S3 and sum all $\hat{Z}$ values.
S5: Repetition $N = 10^7$ times of the steps S2 to S4 of this sequence.
S6: Drawing the histogram of $\hat{Z}$.

In all simulations, we chose a number of dof $\nu = 2m$ in order to have a real and imaginary part in agreement with the experiment shown in Fig. (1).

– Modeling algorithm

The modeling algorithm follows also 6 steps:

S1: Assignement of the 2 noise levels σ_A^2, σ_B^2, signal level σ_C^2 and the number of averaging spectra m.
S2: **Independent basis**
- Computation of coefficients v_1^2, v_2^2 according to Eq. (10)
- if $\sigma_A^2 = \sigma_B^2$ go to step S5 else perform steps S3 and S4

S3: **Orthogonalization of the basis**
- Computation of coefficients k_{AC1}, k_{AC2n}, k_{BC1}, k_{BC2n} to determine the new basis according to Eq. (15)
- Normalization of the basis by determing coefficients k'_{11}, k'_{22}, k'_{12} according to Eq. (16)

S4: **Vector rotation**
- Diagonalization of the matrix Q according to Eq. (17)
- Computation of its roots l_1 and l_2

S5: Compute the coefficients α, β, and $\lambda = m$ according to Eq. (13) and (18).
S6: Plotting the probability density with Eq. (20).

2) When can the Instrument Noises be Assumed to be "About the Same"?: Although the problem is quite simple when the instrument noises σ_A^2 and σ_B^2 are the same (see § III-C), it becomes more complex when $\sigma_A^2 \neq \sigma_B^2$. The question is then how far can we assume that $\sigma_A^2 \approx \sigma_B^2$ and then use the particular case formalism of § III-C? In order to answer this question, we use Monte-Carlo simulations which were performed according to § III-F1.

Afterwards we perform a histogram of these realizations and compare it first with the PDF obtained from the model without rotation, i.e. by using the VΓ parameters of Eq. (13), and next with the PDF obtained from the model with rotation, i.e. by using the VΓ parameters of Eq. (18). Fig. 3 shows an example of such a comparison. In this case ($\sigma_A^2 = 2, \sigma_B^2 = 1/2, \sigma_C^2 = 0$), the PDF of the model with rotation is in perfect agreement with the histogram whereas there are large discrepancies with the PDF of the model without rotation. We have thus a first result: the model without rotation should not be used when the ratio $\sigma_A^2/\sigma_B^2 \geq 4$.

To improve the efficiency of the test, we compute the theoretical quantiles by using the model without rotation and then deduce from them the theoretical confidence intervals which are often used (68 %, 90 %, 95 % and 99 %). These quantiles and intervals are compared to the ones obtained from the simulation histogram. In one example of Table I, which corresponds to the case plotted in Fig. 3, the confidence intervals are strongly overestimated. For instance, the expected 68 % confidence interval is significantly too large since it encompasses an interval of 76 %. Similarly, the expected 90 % interval is actually a 94 % interval. This reinforces our decision of using the model with rotation for a noise variance ratio ≥ 4.

We use these 2 approaches, i.e. PDF curve as well as confidence intervals, for many different parameter sets (see Table I). In any case, the agreement between the model with rotation and the Monte-Carlo simulation histograms were perfect, since the residual deviations can be largely assumed to be due to the finite sample number of the simulation (less than 0.05 % of the CDF). However, this test is very interesting for the model without rotation since it allows us to answer to the question which is the title of this section: when can the

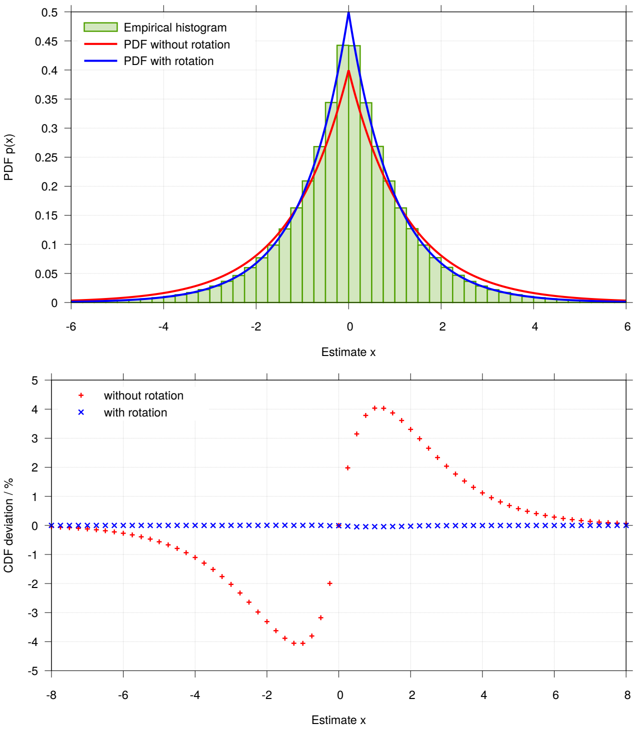

Fig. 3. Comparison of the empirical and theoretical PDF (above) with and without rotation of the basis vectors. The deviations between the empirical and the theoretical CDF are given in the bottom plot. The variances are: $\sigma_C^2 = 0, \sigma_A^2 = 2, \sigma_B^2 = 1/2$ and there are 2 dof.

TABLE I
COMPARISON OF THE EXPECTED QUANTILES AND INTERVALS

Expected probabilities (%)	**True probabilities (%)**					
	Degrees of freedom: 2				dof: 8	
	σ_C^2 =0				0	0.5
	σ_B^2 =2	1	2/3	1/2	1	1
Quantiles						
0.5	0.50	0.39	0.25	0.16	0.35	0.39
2.5	2.50	2.10	1.58	1.19	1.98	2.13
5.0	5.00	4.36	3.51	2.82	4.18	4.44
16.0	16.00	14.95	13.43	12.05	14.68	15.18
50.0	50.00	50.01	50.00	50.00	50.00	49.99
84.0	84.00	85.07	86.59	87.96	85.32	84.58
95.0	95.00	95.65	96.50	97.19	95.82	95.37
97.5	97.50	97.91	98.43	98.82	98.02	97.73
99.5	99.50	99.62	99.75	99.84	99.65	99.57
Intervals						
68.0	68.00	70.12	73.16	75.91	70.64	69.41
90.0	90.00	91.29	92.98	94.37	91.64	90.93
95.0	95.00	95.82	96.84	97.63	96.04	95.60
99.0	99.00	99.23	99.50	99.68	99.30	99.18

The expected quantiles (above) and intervals (below) are computed by using the parameters from Eq. (13) with empirical probabilities. For all realizations $\sigma_A^2 = 2$.

instrument noises be assumed to be "about the same"? Table I is very useful in this connection. In a first step, let us study the case where the number of dof is 2 and there is no signal since it is the case which is the most sensitive to the difference between the noise levels. We can see on this table that the model without rotation is perfect when the 2 noise levels are equal ($\sigma_B^2 = 2$), fair when the ratio of the noise levels is equal to 2 ($\sigma_B^2 = 1$), at the limit of acceptance when the ratio is 3 but not suitable for a ratio ≥ 4. The other columns of Table I, obtained with 8 dof and with $\sigma_C^2 = \sigma_A^2/4$, confirm that the model without rotation is acceptable when the ratio of the noise variances is equal to 2.

Then we recommend to use the vector rotation process if the ratio of the noise variance greater than 2.

IV. INVERSE PROBLEM

A. *Principle of the Method*

The bayesian statistician has to solve the inverse problem in order to define a confidence interval for the true variance σ_C^2, given a set of measurements and a priori information. Thereby the cross-spectrum measurement $\hat{Z}$ is now fixed as well as the instrument noise levels σ_A^2 and σ_B^2, whereas the signal true variance σ_C^2 appears as a random variable. According to the Bayes theorem the a posteriori density of an unknown true value θ given the measurements, here the cross-spectrum $\hat{Z}$, is

$$\begin{cases} p(\theta|\hat{Z}) \propto p(\hat{Z}|\theta) \cdot \pi(\theta) \\ \int_0^\infty p(\theta|\hat{Z}) d\theta = 1 \end{cases} \tag{21}$$

where $\pi(\theta)$ is the a priori density, named prior and $p(\hat{Z}|\theta)$ is the PDF which corresponds to Eq. (12) determined in the direct problem. It remains to determine the prior $\pi(\theta)$ (i.e. the PDF before any measurement) to compute the a posteriori density.

One of the main issue of Bayesian analysis concerns the choice of this prior. We have no a priori knowledge about the behavior of the parameter θ. A total ignorance of knowledge leads to a prior equal to θ^{-1} which means all order of magnitudes have the same probability. The choice of θ is subject to discussion and the reader should refer to [36, Appendix B].

The quantity that can be actually measured is the sum of the signal and the measurement noise. Hence the prior should be accordingly given as a function of this sum. In other words, it is not possible to have any information on a signal with a level much smaller than the measurement noise. Hence choosing a prior function of $\sigma_N^2 + \sigma_C^2$ ensures that the corresponding magnitude order of σ_C^2 do not dominate the a posteriori probability distribution. The measurement noise level decreases as m^{-1}, according to [5, Eq. 11], when averaging over different spectra realizations m. So it should depend to the number of dof $\nu = 2m$ (i.e. taking in account the real and imaginary part). From these considerations, we choose the following prior according to Fig. 4:

$$\pi(\theta) = \frac{1}{\theta} = \frac{1}{\sigma_N^2/\nu + \sigma_C^2}, \tag{22}$$

where $\sigma_N^2 = (\sigma_A^2 + \sigma_B^2)/2$ is the known, "not random" averaged noise level. Thus small level of σ_C^2 are distributed roughly uniformly on a linear scale and large values are distributed with equal probability for equal logarithmic intervals.

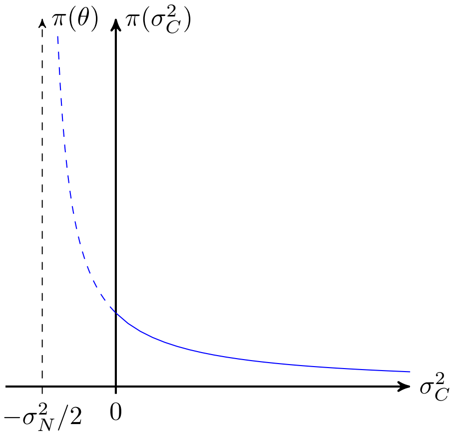

Fig. 4. Prior of the sum of the noise σ_N^2 and signal σ_C^2 levels for the case when there is no averaging spectra (i.e. $\nu = 2$).

B. *Check of the Posterior Probability Density Function*

According to Eq. (20), for 2 dof or $m = 1$ spectrum average and the particular case $\sigma_A^2 = \sigma_B^2 = \sigma_N^2$, we know that

$$p\left(\hat{Z}|\sigma_c^2\right) = \frac{e^{\hat{Z}/\sigma_N^2}}{2(\sigma_N^2 + \sigma_C^2)}.$$

Therefore, the posterior PDF of the cross-spectrum estimator is

$$\begin{cases} p\left(\sigma_C^2|\hat{Z}\right) \propto \dfrac{e^{\hat{Z}/\sigma_N^2}}{2(\sigma_N^2+\sigma_C^2)(\sigma_N^2+2\sigma_C^2)} & \text{if} \quad \hat{Z} \leq 0 \\ p\left(\sigma_C^2|\hat{Z}\right) \propto \dfrac{e^{-\hat{Z}/(\sigma_N^2+2\sigma_C^2)}}{2(\sigma_N^2+\sigma_C^2)(\sigma_N^2+2\sigma_C^2)} & \text{if} \quad \hat{Z} \geq 0. \end{cases} \tag{23}$$

We have checked this posterior PDF by using the inverse problem Monte-Carlo algorithm we already used in [31, § IV.B.1)] and [28, § IV.A.]. The principle is the following:

S1: Select a target estimate $\hat{Z} = Z_0$.

S2: Draw at random the signal level σ_C^2 according to

$$\sigma_C^2 = 10^{\left[\eta + u_{[0,1]}(e_{max}-\eta)\right]} - \frac{\sigma_N^2}{2}$$

where $\eta = \log_{10}(\sigma_N^2/2)$ and $u_{[0,1]}$ is a pseudo-random function which is uniform within $[0, 1]$. This draw ensures the parameter follows the prior of Eq. (22) up to $10^{e_{max}}$. We have chosen $e_{max} = 4$ which is in accordance with Fig. 4

S3: Draw at random (Gaussian) the noise and signal estimates $\hat{A}$, $\hat{B}$, $\hat{C}$ and compute the measurements $\hat{X}$, $\hat{Y}$ according to Eq. (8).

S4: Compute the estimate $\hat{Z}$.

S5: Compare the estimate $\hat{Z}$ with the target Z_0: if $\hat{Z} = Z_0 \pm p$, store the current σ_C^2 value as it is able to generate an estimate equal to the target; otherwise throw this σ_C^2 value. We have chosen $p = (Z_0 + \sigma_N^2/2)/50$ when $Z_0 > 0$ and $p = \sigma_N^2/100$ when $Z_0 \leq 0$.

S6: Go to step 2.

S7: Stop when a set of 10 000 σ_C^2 values is reached.

TABLE II
COMPARISON OF THE QUANTILES 95 % OBTAINED BY MONTE-CARLO SIMULATION AND BY THE POSTERIOR CDF

Target Z_0 (a.u.)	95 % bound		True prob. (%)
	Emp	Theo	
-1.00	14.04	13.65	94.90
0.00	15.11	13.65	94.53
0.10	14.52	14.27	94.91
0.20	14.98	14.90	94.96
0.32	15.87	15.66	94.94
0.50	17.37	16.90	94.87
1.00	20.40	20.14	94.93
2.00	27.61	28.65	95.18
3.16	38.19	39.08	95.08
5.00	57.15	56.55	94.91
10.00	109.66	104.82	94.78

The quantiles 95 % are computed for a noise level $\sigma_N^2 = 1$ a.u. The theoretical bounds (denoted "Theo") are obtained by numerical integration and then correspond to the true probabilities (denoted "True prob.").

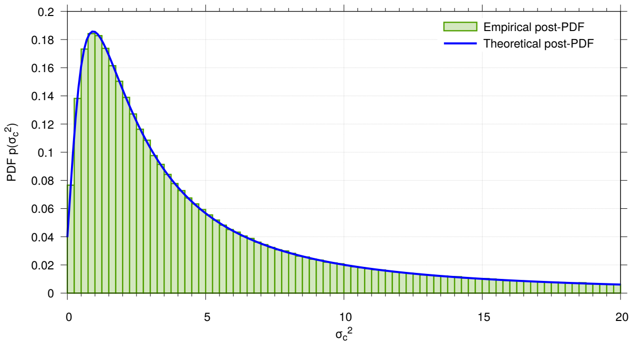

Fig. 5. Comparison of the empirical and theoretical posterior PDF for a noise level $\sigma_N^2 = 1$ a.u and a target estimate $Z_0 = 1$ a.u.

It must be noticed that such an algorithm is obviously not able to justify the choice of the prior since this prior is included in the algorithm. It will only ensure that no mistake has been done in the expression of the posterior PDF.

Fig. 5 shows the comparison of the posterior PDF computed according to Eq. (23) (blue curve) and the histogram obtained thanks to the inverse problem Monte-Carlo algorithm (green boxes) with a noise level $\sigma_N^2 = 1$ a.u and a target estimate $Z_0 = 1$ a.u. We can verify that the agreement is excellent.

Table II compares the 95% quantiles obtained by the inverse problem Monte-Carlo algorithm (denoted "Emp" for empirical) and by the integration of the posterior PDF (denoted "Theo" for theoretical), i.e. the posterior CDF, for different values of target and for a noise level $\sigma_N^2 = 1$. Here also the agreement is very good whether for the 95% bounds or for the true probabilities of the theoretical bounds. Moreover, the fluctuations of the empirical bounds prove that the slight differences between empirical and theoretical values are due to the fluctuations of the empirical bounds because of the limited number of realizations (10 000) of the inverse problem Monte-Carlo algorithm.

C. *KLT Method*

The KLT method stands for "Karhunen-Loève Tranform" and was developed in our previous paper [28]. In that paper, KLT has proved to be as efficient as well as rigorous method, making the most of the property of "sufficient statistics". However the difference with [28] is that we don't have the "*sufficient statistics*" property (see [37]). It means that KLT method will not give the same result as the cross-sprectrum method whereas it should have in the case of "*sufficient statistics*". First let us remind the theory. Then in a second time, we will explain what can bring the KLT method in addition to the cross-specrum one.

1) A Posteriori Distribution: The KLT method relies on the use of $\hat{X}$, and $\hat{Y}$ measurements according to Eq. (2), which are Gaussian rv instead of the product of $\widehat{AB}$, $\widehat{AC}$, $\widehat{BC}$ and $\widehat{C^2}$, which are linear combination of Bessel of the second kind functions and χ^2 random variables. The main advantage of this approach lays in the property of the Gaussian rv which remain Gaussian when they are linearly combined. However, these measurements are not independent. That is why we aim to determine two linear combinations of these rv that are independent one of each other. Hence we define the covariance matrix between $\hat{X}$ and $\hat{Y}$ given by

$$M = \begin{pmatrix} \sigma_A^2 + \sigma_C^2 & \sigma_C^2 \\ \sigma_C^2 & \sigma_B^2 + \sigma_C^2 \end{pmatrix}. \tag{24}$$

The KLT consists in using the rv corresponding to the diagonalization of this matrix. In order to simplify the equations we study solely the case where $\sigma_A^2 = \sigma_B^2 = \sigma_N^2$. The eigenvalues of M are

$$\begin{aligned} \lambda_1 &= \sigma_N^2 + 2\sigma_C^2 \\ \lambda_2 &= \sigma_N^2 \end{aligned} \tag{25}$$

with the following normalized eigenvectors,

$$V_1 = \tfrac{1}{\sqrt{2}} \begin{pmatrix} 1 \\ 1 \end{pmatrix} \qquad V_2 = \tfrac{1}{\sqrt{2}} \begin{pmatrix} 1 \\ -1 \end{pmatrix} \tag{26}$$

The likelihood function is then given by

$$p_{KLT}(\hat{Z}|\sigma_C^2) = \prod_{i=1}^{2} \frac{1}{\lambda_i^{\nu/2}} \exp\left(-\frac{\sum_{j=1}^{\nu} \hat{w}_{i,j}^2}{2\lambda_i} \right) \tag{27}$$

The numerator of the exponential argument is then the only term that depends on the actual measurements:

$$\hat{w}_{i,j}^2 = V_{i,1}^2 \hat{X}_j^2 + V_{i,2}^2 \hat{Y}_j^2 + 2V_{i,1}V_{i,2}\hat{Z}_j \tag{28}$$

where $||V_i||^2 = \sum_j V_{i,j}^2$. So the KLT method involve the spectral density $\hat{X}^2$, $\hat{Y}^2$ in addition to the cross-spectrum.

Keeping the same prior defined in Eq. (22) we have the following a posteriori density,

$$\begin{cases} p_{KLT}(\sigma_C^2|\hat{Z}) \propto \dfrac{1}{\sigma_N^2/2 + \sigma_C^2} \cdot p_{KLT}(\hat{Z}|\sigma_C^2) \\ \displaystyle\int_{\mathbb{R}} p_{KLT}(\sigma_C^2|\hat{Z}) d\sigma_C^2 = 1. \end{cases} \tag{29}$$

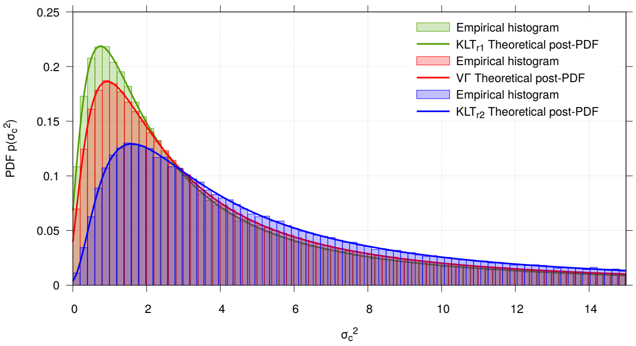

Fig. 6. Comparison of the empirical and theoretical posterior PDF for VΓ and KLT methods with a noise level $\sigma_N^2 = 1$ a.u and a target estimate $Z_0 = 5$ a.u. KLT$_{r1}$ and KLT$_{r2}$ are the same method but differ by their combination of spectral density $\hat{X}^2$ and $\hat{Y}^2$ which are fixed, see Table III, whereas they are rv for the VΓ method.

2) Validation of the Method by Monte Carlo Simulation: In order to validate the KLT method, we have compared its results to Monte Carlo simulations. The algorithm is as follows:

S1: Select a noise level $\sigma_N^2 = \sigma_A^2 = \sigma_B^2$, a target $\hat{Z} = Z_0$ and a combination $\hat{X} = X_0$, $\hat{Y} = Y_0 = Z_0/X_0$ for all the dof.

S2: Draw at random the signal level σ_C^2 according to

$$\sigma_C^2 = 10^{\left[\eta + u_{[0,1]}(e_{max} - \eta)\right]} - \frac{\sigma_N^2}{2}$$

where $\eta = \log_{10}(\sigma_N^2/2)$ and $u_{[0,1]}$ is a pseudo-random function which is uniform within $[0, 1]$. This draw ensures the parameter follows the prior of Eq. (22) up to $10^{e_{max}}$. We have chosen $e_{max} = 4$.

S3: Draw at random (Gaussian) the noise and signal estimates $\hat{A}$, $\hat{B}$, $\hat{C}$ and compute the measurements $\hat{X}$, $\hat{Y}$ according to Eq. (8).

S4: Compute the estimates $\hat{X}$ and $\hat{Y}$.

S5: Compare the estimates $\hat{X}$, $\hat{Y}$ with the targets X_0, Y_0 for all the dof: if $\hat{X} = X_0 \pm p$, $\hat{Y} = Y_0 \pm q$, store the current σ_C^2 value as it is able to generate an estimate equal to the target; otherwise throw this σ_C^2 value. We have chosen a precision p, q of tenths of respectively X_0 and Y_0.

S6: Go to step 2.

S7: Stop when a set of n σ_C^2 values is reached. The number of values n depending on the computation time.

3) Results and Discussion: Fig. 6 shows the comparison between the PDF of VΓ method developed in § III and the PDF of KLT method for two different realizations. The theoretical post-PDF fits very well the empirical histogram for each method. The "sufficient statistics" property being not valid, different combinations of the spectral density $\hat{X}$ and $\hat{Y}$ were tested and are given in Table III. Indeed KLT$_{r1}$ and KLT$_{r2}$ realizations do not give the same PDF unlike the VΓ method. KLT$_{r1}$ has then a peak which is higher than the VΓ method whereas KLT$_{r2}$ has a smaller one. This is explained by a more stringent confidence interval for KLT$_{r1}$ than VΓ, and a less stringent for KLT$_{r2}$ as refered in Table III. The 95 % quantiles

TABLE III
COMPARISON OF THE 95 % QUANTILES OBTAINED BY MONTE-CARLO SIMULATION (EMPIRICAL) AND BY THE POSTERIOR CDF

Method	Measurement				95 % bound	
	$\hat{X}'$	$\hat{X}''$	$\hat{Y}'$	$\hat{Y}''$	Emp	Theo
VΓ	rv	rv	rv	rv	56.4	56.6
KLT$_{r1}$	1.6	1.6	1.6	1.6	48.4	48.3
KLT$_{r2}$	4.0	0.6	2.5	1.0	82.3	80.8

The 95 % quantiles are computed for a noise level $\sigma_N^2 = 1$ and a target estimate $Z_0 = 5$ a.u.

obtained with MC simulations are in a good agreement with the theoretical ones, especially for KLT$_{r1}$ and VΓ methods. It is explained by the number of data which is not the same for all of these simulations. VΓ, KLT$_{r1}$ and KLT$_{r2}$ have respectively $1\,000\,000$; $500\,000$ and $245\,000$ data. VΓ MC simulations takes only 2 minutes whereas it needs respectively 54 hours and 35 days using 17 cores, for KLT$_{r1}$ and KLT$_{r2}$. KLT$_{r1}$ is chosen to have the spectral density combination which leads to the most stringent confidence interval. Whereas KLT$_{r2}$ is chosen to be more defavourable than the general case VΓ using only the knowledge of the cross-spectrum measurement.

The KLT method can then have a slightly more stringent confidence interval than the cross-spectrum method using VΓ for certain case. However it requires to have the knowledge of both spectral density of each channel. It then uses more information, the “sufficient statistics” property being not valid. So the KLT method is preferred when the spectral densities are known.

V. CONCLUSION

The method developed, VΓ, provides the Probability Density Function of the signal level studied when using the cross-spectrum method. It allows the determination of confidence intervals through numerical integration, where only the high bound has a physical meaning. It is especially relevant for one or several measurements of the cross-spectrum as the PDF will tend to a Gaussian distribution for many dof.

VΓ is a rigorous method since it is the exact density solution of the cross-spectrum real part statistics, with no approximation. We shall notice that the noise level of each measurement instruments has to be known. If these noise level are the same except at a factor of 4 and higher, we can assume that all the theoretical part of orthogonalizing and the rotation of the basis is not necessary. This method works whatever the number of measurement spectra and noise level.

However using KLT method to compute the confidence interval is a more rigorous method because it uses the knowledge of the spectral density in addition to the cross-spectrum. That is why we recommend to use the KLT method which turns out to be a slightly better estimator than VΓ.

VI. ACKNOWLEDGEMENT

This work was partially funded by the ANR Programmes d’Investissement d’Avenir (PIA) Oscillator IMP (Project 11-EQPX-0033) and FIRST-TF (Project 10-LABX-0048).

REFERENCES

[1] R. B. Blackman and J. W. Tuckey. *The Measurement of Power Spectra*. Dover, 1959.

[2] Gwilym M. Jenkins and Donald G. Watts. *Spectral Analysis and its Applications*. Holden Day, San Francisco, CA, 1968.

[3] O. E. Brigham. *The Fast Fourier Transform and its Applications*. Prentice-Hall, 1988.

[4] D. B. Percival and A. T. Walden. *Spectral Analysis for Physical Applications*. Cambridge, Cambridge, UK, 1993.

[5] E. Rubiola and F. Vernotte. The cross-spectrum experimental method. arXiv:1003.0113v1, March 2010.

[6] R. H. Dicke. The measurement of thermal radiation at microwave frequencies. *Rev. Sci. Instrum.*, 17(7):268–275, July 1946.

[7] M. Sampietro, L. Fasoli, and G. Ferrari. Spectrum analyzer with noise reduction by cross-correlation technique on two channels. *Rev. Sci. Instrum.*, 70(5):2520–2525, May 1999.

[8] A. Hati, C. W. Nelson, and D. A. Howe. Cross-spectrum measurement of thermal-noise limited oscillators. *Rev. Sci. Instrum.*, 87:034708, March 2016.

[9] Y. Gruson, V. Giordano, U. L. Rohde, A. K. Poddar, and E. Rubiola. Cross-spectrum pm noise measurement, thermal energy, and metamaterial filters. *IEEE Trans. Ultras. Ferroelec. Freq. Contr.*, 64(3):634–642, March 2017.

[10] A. C. Cárdenas-Olaya, E. Rubiola, Friedt J.-M., P.-Y. Bourgeois, M. Ortolano, S. Micalizio, and C. E. Calosso. Noise characterization of analog to digital converters for amplitude and phase noise measurements. *Rev. Sci. Instrum.*, 88:065108 1–9, June 2017.

[11] G. Feldhaus and A. Roth. A 1 MHz to 50 GHz direct down-conversion phase noise analyzer with cross-correlation. In *Proc. Europ. Freq. Time Forum*, York, UK, April 4-7 2016.

[12] T. M. Fortier, C. W. Nelson, A. Hati, F. Quinlan, J. Taylor, H. Jiang, C. W. Chou, T. Rosenband, A. Lemke, N. Ludlow, D. Howe, C. W. Oates, and S. A. Diddams. Sub-femtosecond absolute timing jitter with a 10 ghz hybrid photonic-microwave oscillator. *Appl. Phys. Lett.*, 100:231111 1–3, June 7 2012.

[13] E. Rubiola. The measurement of am noise of oscillators. arXiv:physics/0512082, December 2005.

[14] A. H. Verbruggen, H. Stoll, K. Heeck, and R. H. Koch. A novel technique for measuring resistance fluctuations independently of background noise. *Appl. Phys. A*, 48:233–236, March 1989.

[15] C. M. Allred. A precision noise spectral density comparator. *J. Res. NBS*, 66C:323–330, October-December 1962.

[16] J. A. Nanzer and R. L. Rogers. Applying millimeter-wave correlation radiometry to the detection of self-luminous objects at close range. *IEEE Trans. Microw. Theory Tech.*, 56(9):2054–2061, September 2008.

[17] D. R. White, R. Galleano, A. Actis, H. Brixy, M. De Groot, J. Dubbeldam, A. L. Reesink, F. Edler, H. Sakurai, R. L. Shepard, and Gallop J. C. The status of Johnson noise thermometry. *Metrologia*, 33(4):325–335, August 1996.

[18] J. P. W. Verbiest, M. Bailes, W. A. Coles, G. B. Hobbs, W. Van Straten, D. J. Champion, F. A. Jenet, R. N. Manchester, N. D. R. Bhat, J. M. Sarkissian, et al. Timing stability of millisecond pulsars and prospects for gravitational-wave detection. *Month. Not. Roy. Astronom. Soc.*, 400(2):951–968, 2009.

[19] S. Detweiler. Pulsar timing measurements and the search for gravitational waves. *Am. Astronom. Soc.*, 234:1100–1104, December 1979.

[20] R. W. Hellings and G. S. Downs. Upper limits on the isotopic gravitational radiation background frompulsar timing analysis. *Am. Astronom. Soc.*, 265:39–42, February 1983.

[21] S. R. Taylor, M. Vallisneri, J. A. Ellis, C. M. F. Mingarelli, T. J. W. Lazio, and R. van Haasteren. Are we there yet? time to detection of nanohertz gravitational waves based on pulsar-timing array limits. *Astrophys. J. Lett.*, 819(1):6, 2016.

[22] D. Perrodin and A. Sesana. *Radio Pulsars: Testing Gravity and Detecting Gravitational Waves*, volume 457 of *Astrophysics and Space Science Library*. Springer, Cham, 2018.

[23] S. Drasco and E. E. Flanagan. Detection methods for non-gaussian gravitational wave stochastic backgrounds. *Phys. Rev. D*, 67(8):082003, 2003.

[24] N. J. Cornish and J. D. Romano. Towards a unified treatment of gravitational-wave data analysis. *Phys. Rev. D*, 87(12):122003, 2013.

[25] C. G. Bassa, G. H. Janssen, R. Karuppusamy, M. Kramer, K. J. Lee, K. Liu, J. McKee, D. Perrodin, M. Purver, S. Sanidas, R. Smits, and B. W. Stappers. Leap: the large european array for pulsars. *Month. Not. Roy. Astronom. Soc.*, 456(2):2196–2209, December 2015.

[26] S. Chen, F. Vernotte, and E. Rubiola. Applying clock comparison methods to pulsar timing observations. *MNRAS*, 2020.

[27] International vocabulary of basic and general terms in metrology (VIM). International Organization for Standardization (ISO), 2004.

[28] E. Lantz, C. E. Calosso, E. Rubiola, V. Giordano, C. Fluhr, B. Dubois, and F. Vernotte. KLTS: A rigorous method to compute the confidence intervals for the three-cornered hat and for Groslambert covariance. *IEEE Trans. Ultras. Ferroelec. Freq. Contr.*, 66(12):1942–1949, December 2019.

[29] N. J. Kasdin. Discrete simulation of colored noise and stochastic processes and 1/f power law noise generation. *Proceedings of the IEEE*, 83(5):802–827, May 1995.

[30] F. Vernotte, G. Zalamansky, and E. Lantz. Time stability characterization and spectral aliasing part i: a time-domain approach. *Metrologia*, 35:723–730, 1998.

[31] F. Vernotte and E. Lantz. Three-cornered hat and Groslambert covariance: A first attempt to assess the uncertainty domains. *IEEE Trans. Ultras. Ferroelec. Freq. Contr.*, 66(3):643–653, March 2019.

[32] M. Haas and C. Pigorsch. *Financial Economics, Fat-Tailed Distributions*, pages 3404–3435. Springer New York, New York, NY, 2009.

[33] B. Sorin and P. Thionet. Lois de probabilités de bessel. *Rev. Stat. App.*, 16(4):65–72, 1968.

[34] D. Madan and E. Seneta. The variance gamma (v.g.) model for share market returns. *J. Business*, 63(4):511–524, 1990.

[35] G. N. Watson. *A Treatise on the Theory of Bessel Functions*. Cambridge University Press, 1922.

[36] M. P. McHugh, G. Zalamansky, F. Vernotte, and E. Lantz. Pulsar timing and the upper limits on a gravitational wave background : a Bayesian approach. *Phys. Rev. D*, 54(10):5993–6000, November 1996.

[37] G. Saporta. *Probabilités, analyse des données et statistique*. Technip, 1990.

IEEE TRANSACTIONS ON ULTRASONICS, FERROELECTRICS, AND FREQUENCY CONTROL, VOL. 69, NO. 8, AUGUST 2022 2585

The Statistics of the Cross-Spectrum and the Spectrum Average: Generalization to Multiple Instruments

Antoine Baudiquez, *Graduate Student Member, IEEE*, Éric Lantz,
Enrico Rubiola, *Member, IEEE*, and François Vernotte

***Abstract*—This article addresses the measurement of the power spectrum of red noise processes at the lowest frequencies, where the minimum acquisition time is so long that it is impossible to average on a sequence of data record. Therefore, averaging is possible only on simultaneous observation of multiple instruments. This is the case of radio astronomy, which we take as the paradigm, but examples may be found in other fields such as climatology and geodesy. We compare the Bayesian confidence interval of the red noise parameter using two estimators, the spectrum average and the cross-spectrum. While the spectrum average is widely used, the cross-spectrum using multiple instruments is rather uncommon. With two instruments, the cross-spectrum estimator leads to the Variance–Gamma distribution. A generalization to *q* devices based on the Fourier transform of characteristic functions is provided, with the example of the observation of millisecond pulsars with five radio telescopes (RTs). The simulations show that the spectrum average is by a small amount more efficient than the cross-spectrum, chiefly when the background exceeds the signal. However, some notable differences between their upper limit indicate that it should be wiser to compute both estimators.**

***Index Terms*—Bayesian statistics, characteristic function, confidence interval, cross-spectrum, Karhunen-Loève transform (KLT), Monte Carlo simulation, probability density function, QR decomposition, spectrum average.**

[redacted]

See https://arxiv.org/pdf/2202.13969.pdf

Manuscript received 14 March 2022; accepted 20 June 2022. Date of publication 22 June 2022; date of current version 29 July 2022. This work was supported in part by the Agence Nationale de la Recherche (ANR) Programs d'Investissement d'Avenir (PIA) Oscillateur Instability Measurement Platform (IMP) under Project 11-EQPX-0033 and in part by FIRST-TF under Project 10-LABX-0048. *(Corresponding author: Antoine Baudiquez.)*

Antoine Baudiquez is with the Department of Time and Frequency, FEMTO-ST, UMR 6174, Université Bourgogne Franche-Comté, 25030 Besançon, France (e-mail: antoine.baudiquez@femto-st.fr).

Éric Lantz is with the Département d'Optique P.M. Duffieux, FEMTO-ST, UMR 6174 CNRS, Université Bourgogne Franche-Comté, 25030 Besançon, France.

Enrico Rubiola is with the Department of Time and Frequency, FEMTO-ST, UMR 6174 CNRS, Université Bourgogne Franche-Comté, 25030 Besançon, France, and also with the Physics Metrology Division, Istituto Nazionale di Ricerca Metrologica (INRiM), 10135 Turin, Italy.

François Vernotte is with the Department of Time and Frequency, FEMTO-ST, Observatory THETA, UMR 6174 CNRS, Université Bourgogne Franche-Comté, 25030 Besançon, France.

Digital Object Identifier 10.1109/TUFFC.2022.3185528

The Statistics of the Cross-Spectrum and the Spectrum Average: Generalization to Multiple Instruments

Antoine Baudiquez, Éric Lantz, Enrico Rubiola, François Vernotte

***Abstract*—This article addresses the measurement of the power spectrum of red noise processes at the lowest frequencies, where the minimum acquisition time is so long that it is impossible to average on a sequence of data record. Therefore, averaging is possible only on simultaneous observation of multiple instruments. This is the case of radio astronomy, which we take as the paradigm, but examples may be found in other fields such as climatology and geodesy.**

We compare the Bayesian confidence interval of the red noise parameter using two estimators, the spectrum average and the cross-spectrum. While the spectrum average is widely used, the cross-spectrum using multiple instruments is rather uncommon. With two instruments, the cross-spectrum estimator leads to the Variance-Gamma distribution. A generalization to q devices based on the Fourier transform of characteristic functions is provided, with the example of the observation of millisecond pulsars with 5 radio telescopes. The simulations show that the spectrum average is by a small amount more efficient than the cross-spectrum, chiefly when the background exceeds the signal. However some notable differences between their upper limit indicate that it should be wiser to compute both estimators.

***Index Terms*—Bayesian statistics, Monte Carlo simulation, confidence interval, cross-spectrum, spectrum average, Karhunen-Loève transform, QR decomposition, characteristic function, probability density function.**

I. INTRODUCTION

The term red noise refers to a variety of processes sharing the property that the power spectral density (PSD) grows at low frequency as $1/f^2$ (Brownian noise) or $1/f^\alpha$, with $\alpha > 2$. We are interested in the estimation of the PSD of such random signals out of the background noise of the instrument in the specific case of very slow phenomena, which take too long acquisition time for the average on a sequence of data sets to be viable. Therefore, averaging out the background is possible only by exploiting simultaneous measurements of the same signal taken with multiple instruments, under the obvious hypothesis that they are independent. The frequency stability of the millisecond pulsars is the example we have in mind. Such rapidly rotating neutron stars, emitting highly stable periodic pulses out of the magnetic poles, rival the best atomic clocks [1]–[4]. Among other fields, slow phenomena are found in climatology [5] and geodesy, the latter nowadays measured with Very Large Baseline Interferometry [6]. The measurement of noise and phase noise with fully digital instruments is another appealing application because increasing the number of channels is reasonably simple. The phase noise of oscillators can be measured with the multi-channel tracking DDS [7]. An improved 16-channel version of the Tracking DDS is now a semi-commercial instrument (we have recently purchased two beta-test samples), albeit there is still no official announcement. In Si, Ge and GaAs semiconductors, low $1/f$ noise is a quality indicator related to the effective number of defects [8].

With the purposes stated in mind, we compare the efficiency of the spectrum average (s.a) and with the cross-spectrum (c-s) measuring the signal with q instruments simultaneously. The s.a estimator is the average of the q observed spectra S_i, weighted with the background noise $\sigma^2_{N,i}$ of the i-th instrument. The c-s method is the average of the all combinatorial choices of the cross-spectrum $S_{j,i}$, $i \neq j$. The s.a is the classical estimator used in these cases [9], while the c-s is rather uncommon. Data are analyzed with the Bayesian statistics, also known as the inverse problem, which consists of estimating the most probable value of the signal (the slowest spectral components) from the experimental outcomes and their statistical properties. We take the 95% upper limit as the efficiency criterion. Accordingly, the most efficient estimator is the one that provides the most stringent upper limit on the variance of the signal with the same data set.

Our previous article [10] shows that the Variance-Gamma ($V\Gamma$) distribution is the exact solution for the probability density function (PDF) of the cross-spectrum in the case of two instruments. We generalize the result to the case of the cross spectrum of q instruments, each with its own background noise $\sigma^2_{N_i}$, assessing the confidence interval on the signal level σ^2_R. Of course, the PDF is no longer a $V\Gamma$, and can only be calculated numerically. The case of equally noisy instruments is simpler, and at first sight similar to that of $q = 2$, but it has no analytical solution.

We run a simulation with up to five instruments, inspired to the LEAP experiment [11]. Such experiment gathers the five largest European radio telescopes (RTs) in order to increase the sensitivity of high-precision pulsar timing. Interestingly, Pulsar Timing Arrays seem a promising option to explore the low-frequency gravity waves crossing our Galaxy [12], [13].

A. Baudiquez and E. Rubiola are with FEMTO-ST, Department of Time and Frequency, UMR 6174, Université Bourgogne Franche-Comté, France. Antoine's ORCID is 0000-0002-7007-5273

E. Lantz is with FEMTO-ST, Département d'Optique P.M. Duffieux, UMR 6174 CNRS, Université Bourgogne Franche-Comté, France.

E. Rubiola is also with the Division of Quantum Metrology and Nanotechnology, Istituto Nazionale di Ricerca Metrologica (INRiM), 10135 Turin, Italy. Enrico's ORCID is 0000-0002-5364-1835

F. Vernotte is with FEMTO-ST, Department of Time and Frequency, Observatory THETA, UMR 6174 CNRS, Université Bourgogne Franche-Comté, France. François's ORCID is 0000-0002-1645-5873

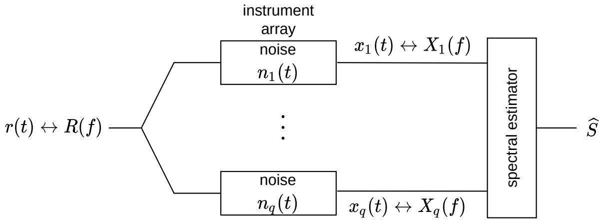

Fig. 1: Array of q instruments measuring the signal $r(t)$. Each instrument adds a white noise to the output $x(t)$ whose Fourier transform is $X(f)$. Then the estimate $\widehat{S}$ is computed.

The c-s estimator commonly used in the frequency metrology has recently been used in [14] to show the detection limit of correlated red noise. Hence defining a confidence interval on this estimator and comparing it with the commonly used s.a will give hints on which estimator has to be privileged to improve the sensitivity.

This article is intended to compare the s.a and the c-s estimators generalized to multiple instruments measuring a random signal, e.g. a red noise. In this respect, we define both estimators of the power spectral density and describe their statistical properties in Section II. Then in Section III we gives their probability density function. Sections IV and V compare the confidence interval of the red noise respectively between the s.a and the Karhunen-Loève transform (KLT), and between the s.a and the c-s. Conclusions are presented in Sec. VI.

II. TWO ESTIMATORS OF THE PSD

A. Spectral Measurement

Let us consider a **red** noise $r(t)$ which is measured by q independent instruments as shown in Fig. 1. We assume that each instrument adds a white noise $n_i(t)$ to the measurement and that all these white noises are uncorrelated. In the following, we call the red noise the "signal" and the white noise from the measurement instrument is referred as the "measurement noise". The output of each channel is then

$$x_i = r + n_i \leftrightarrow X_i = R + N_i \tag{1}$$

where the subscript i corresponds to the i-th instrument, $\leftrightarrow$ stands for the Fourier transform and inverse Fourier transform pair, lower case is time domain, upper case is frequency domain, and the variables t and f are implied. Let us remind that the Fourier transform of a white noise is a white noise, at least for sampled signals. Indeed even if continuous pure white noise have an infinite power, the Fourier transform for discrete simulation can be defined. A realistic white noise corresponds to a Markov process of the first order, more details about colored noise are given in [15].

On the other hand, a red noise can be described as a filtered white noise. Its spectrum is then the product of a white spectrum by a deterministic function; so the random part of a red noise is uncorrelated for each frequency bin. Consequently in term of random variable, working in the frequency domain gives a precious advantage because the Fourier components (frequency bins) are statistically independent unlike the time data.

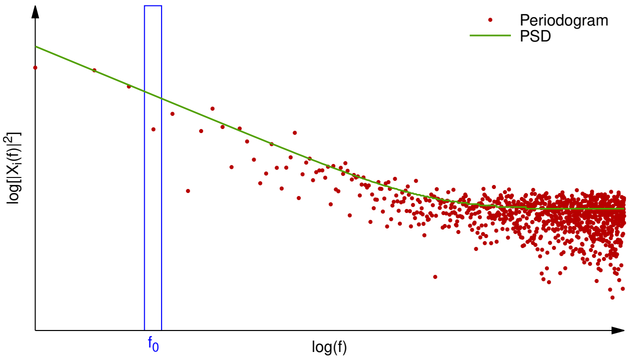

Fig. 2: Periodogram of x (white noise plus red noise). The PSD is the expectation of the periodogram.

In the following we focus solely on **one frequency bin**, thanks to energy equipartition it follows,

$$\begin{aligned} \mathbb{V}\left[N_i\right] &= 2\mathbb{V}\left[\Re\left[N_i\right]\right] = 2\mathbb{V}\left[\Im\left[N_i\right]\right] = \sigma_{N,i}^2 \\ \mathbb{V}\left[R\right] &= 2\mathbb{V}\left[\Re\left[R\right]\right] = 2\mathbb{V}\left[\Im\left[R\right]\right] = \sigma_R^2 \end{aligned} \tag{2}$$

where $\mathbb{V}[\cdot]$, $\Re[\cdot]$, $\Im[\cdot]$ respectively denote the variance, the real and imaginary part of the quantity within the brackets.

B. Periodogram and Power Spectral Density

First, let us recall some basics of frequency analysis. Using a data record of duration T sampled at a suitable frequency, the periodogram is

$$P_x(f) = \frac{2}{T}|X(f)|^2, \qquad f > 0 \tag{3}$$

where the factor "2" is needed for energy conservation after deleting the negative frequencies. The expectation of the periodogram is the Power Spectral Density (PSD),

$$S_x(f) = \mathbb{E}\left[\frac{2}{T}|X(f)|^2\right], \qquad f > 0. \tag{4}$$

Figure 2 shows the periodogram and the PSD. We estimate the PSD as the average periodogram, with the ultimate goal of expecting the red noise parameters of r out of the measurement noise n. Of course r is the same for all instruments, while the n_i are specific to the i-th instrument and its environnement.

The total duration of the experiment is the major problem, as the lowest frequency of interest sets T. In turn, a long T goes with a small number p of averages because the total duration of the experiment is pT. In this paper we focus on the slowest red noise phenomena, up to years, for which we have to set $p = 1$. In other words, the phenomena of interest are so slow that we cannot average on multiple acquisitions.

C. Estimators

We are now focusing on one bin of the periodogram of a single simultaneous measurement with q instruments, e.g. f_0 as represented on Fig. 2. Let us emphasize on the term periodogram which designates a unique realization of the red noise since all instruments observe this red noise realization at the same time. Nevertheless, taking into account the uncorrelated white noises coming from the instruments, we have to deal with the PSD S. One bin of S represents the power in a given bandwidth, i.e. the 2-nd central moment, or variance. Hereinafter, we work on a generic bin, thus $S(f)$ at that frequency is replaced with σ^2.

Because the N_i are all different, it is appropriate to use a weighted average, where the weights α_i are to be found for the optimum detection of R. We denote the **estimates** with a "*hat*", then

$$\widehat{\mu} = \frac{\sum_i^q \alpha_i X_i}{\sum_i^q \alpha_i}, \tag{5}$$

where q is the number of instruments. The variance of the estimate $\widehat{\mu}$ is

$$\mathbb{V}\left[\widehat{\mu}\right] = \frac{\sum_i^q \alpha_i^2 \left(\sigma_{N,i}^2 + \sigma_R^2\right)}{\left[\sum_i^q \alpha_i\right]^2}. \tag{6}$$

An optimal choice is obtained by solving,

$$\frac{\partial \mathbb{V}\left[\widehat{\mu}\right]}{\partial \alpha_i} = 0 \tag{7}$$

which leads to the solution,

$$\alpha_i = \frac{1}{\sigma_{N,i}^2}. \tag{8}$$

Therefore the inverse-variance weighted average, described in [16] with applications examples, has the least variance among all weighted averages. Then Eq. (6) becomes

$$\sigma_\mu^2 = \mathbb{V}\left[\widehat{\mu}\right] = \left(\sum_i^q \frac{1}{\sigma_{N,i}^2}\right)^{-1}. \tag{9}$$

Let us define now the two **estimators** of interest: the spectrum average weighted by the noise variance $\sigma_{N,i}^2$ and the cross-spectrum,

$$\begin{aligned} \widehat{S_{\text{sa}}} &= \left\{\Re\left[\sigma_\mu^2 \sum_i^q \frac{X_i}{\sigma_{N,i}^2}\right]\right\}^2 + \left\{\Im\left[\sigma_\mu^2 \sum_i^q \frac{X_i}{\sigma_{N,i}^2}\right]\right\}^2 \\ \widehat{S_{\text{cs}}} &= \langle \Re\left[X_i \cdot \tilde{X}_j\right] \rangle_m \qquad \text{with} \quad i \neq j. \end{aligned} \tag{10}$$

Moreover σ_μ^2 corresponds to the noise weight normalization factor defined in Eq. (9). Finally $\langle\cdot\rangle$ stands for the m average over the different combinations of instruments with $m = \binom{q}{2}$ and $\tilde{\cdot}$ stands for the complex conjugate of the quantity which is below. For better readability, we have omitted in Eq. (10) a factor $2/T$, where T is the measurement time (acquisition of the data record for one FFT), necessary for $S(f)$ to have the dimension of a PSD, and the factor fix the total power after deleting the negative frequencies. In addition, only the random part has a direct influence on the probability density function. Denoting $\mathbb{E}[\cdot]$ the mathematical expectation of the quantity within the brackets,

$$\begin{cases} \mathbb{E}\left[\widehat{S_{\text{sa}}}\right] &= \sigma_R^2 + \sigma_\mu^2 \\ \mathbb{E}\left[\widehat{S_{\text{cs}}}\right] &= \sigma_R^2 \end{cases} \tag{11}$$

which means that the spectrum average estimator is **biased**. Usually one removes the bias to have the s.a estimate average over realizations which tends towards the sought signal level σ_R^2. This gives a clear advantage to the c-s estimator. However, we will see that the computation of the confidence interval over the signal level σ_R^2 requires an estimation of this bias σ_μ^2 whatever the chosen estimator, s.a or c-s. Therefore we want to estimate the PSD and we assume it follows a $1/f^\alpha$ power law, then we only have to estimate a level and exponent of the first frequency bins.

We now compare the estimator defined in Eq. (10) by determining their variance. We can demonstrate provided that $\forall i,\ \sigma_{N,i}^2 = \sigma_N^2$ (see Annexe A),

$$\mathbb{V}\left[\widehat{S_{\text{cs}}}\right] \approx \begin{cases} \mathbb{V}\left[\widehat{S_{\text{sa}}}\right] & \text{if } \sigma_R^2 \gg \sigma_N^2 \\ \frac{q}{q-1}\mathbb{V}\left[\widehat{S_{\text{sa}}}\right] & \text{if } \sigma_R^2 \ll \sigma_N^2. \end{cases} \tag{12}$$

This is confirmed by Fig. 3 which exhibits the variance of the estimates of both estimators applied to a signal composed of a mixture of uncorrelated white noise of level 1 arbitrary unit (a.u.) and a common f^{-4} noise of level 4096 a.u. for 2 instruments. Therefore the variance decreases in f^{-8} and Fig. 3 compares these variances to the square of the PSD. At $f = 4$ a.u., the signal PSD is 16 times higher than the white level and therefore its square is 256 times higher. In this case, the variances of both estimators coincide. On the other hand, for frequencies higher than 16 a.u., the signal PSD is less than 16 times lower than the white level (256 for their squares) and the variance of the c-s estimates is 2 times higher than the variance of the s.a estimates. This seems to indicate a better efficiency of the s.a estimator. Indeed the spectrum average estimator is a sufficient estimator which means of minimal variance.

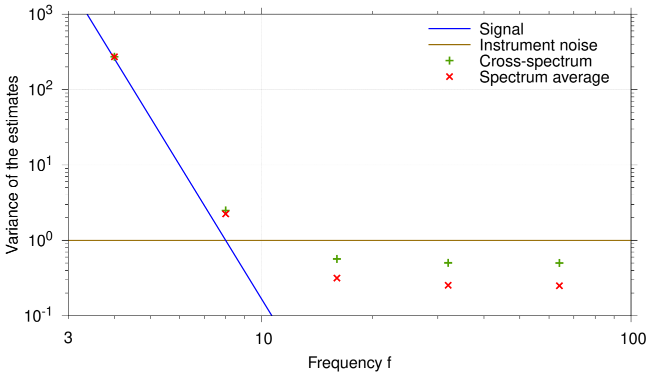

Fig. 3: Variance of the estimate with the signal variance which is of the form $(\sigma_R^2/f^\alpha)^2$, where $\sigma_R^2 = 4096$ a.u. is the signal level and $\alpha = 4$ the red noise exponent. The noise model is a white noise of level $\sigma_N^2 = 1$ a.u. with 2 instruments.

However what about the PDF of the estimates knowing the parameter σ_R^2 for a given frequency?

III. PROBABILITY DENSITY FUNCTION

A. Spectrum Average Method

The spectrum average estimator leads to the following χ^2 distribution with 2 degrees of freedom resulting from the real and imaginary part of the spectrum,

$$p(\widehat{S_{\mathrm{sa}}}|\sigma_R^2) = \frac{e^{-\frac{\widehat{S_{\mathrm{sa}}}}{2\sigma^2}}}{2\sigma^2} \tag{13}$$

where,

$$\sigma^2 = \tfrac{1}{2}\left(\sigma_\mu^2 + \sigma_R^2\right). \tag{14}$$

where σ_μ^2 is the weighted noise level according to Eq. (9) and σ_R^2 the signal level of interest.

B. Karhunen-Loève Transform

The KLT method, denoting to the Karhunen-Loève transform, has been developed in [17]. It uses the statistics of the data themselves instead of the statistics of the estimates. This method has the advantage to combine linearly independent Gaussian estimates. Furthermore it also forms a sufficient statistics like the s.a method. It is based on determining the covariance matrix M associated to the real or imaginary part of the measurement X_i obtained by the q instruments,

$$\begin{cases} M_{ii} = \dfrac{1}{2}\left(\sigma_{N,i}^2 + \sigma_R^2\right) \\ M_{ij} = \dfrac{1}{2}\sigma_R^2 \qquad \text{with} \quad i \neq j \end{cases} \tag{15}$$

where the extra factors $1/2$ come from Eq. (2). This covariance matrix has to be diagonalized and we denote the eigenvalues λ_i. Their associated normalized eigenvectors are V_i and the PDF is then given by

$$p(\widehat{S_{\mathrm{KLT}}}|\sigma_R^2) = \prod_{i=1}^{q} \frac{1}{(2\pi\lambda_i)^{\nu/2}}\, \mathrm{e}^{\left(-\frac{\sum_{j=1}^{\nu} w_{ij}^2}{2\lambda_i}\right)} \tag{16}$$

where j highlights the real and imaginary part obtained through the Fourier transform therefore $\nu = 2$. Let us remind that X corresponds to the matrix containing the set of Fourier transform of the measurements at the output of each instrument. The numerator of the exponential argument is then

$$w = X \cdot V \tag{17}$$

where V are the eigenvectors obtained from the diagonalized covariance matrix.

C. Cross-spectrum

The cross-spectrum estimator leads to the variance-gamma (VΓ) distribution for 2 instruments as described in Section III in [10] but for more than 2 instruments it is no longer the case. Having no exact solution known nowadays, we propose a solution based on the characteristic function. Expanding the model from the case of 2 instruments, we define a basis such as in [10],

$$\mathcal{B} = \begin{pmatrix} \sigma_{N,1}/2 & \sigma_{N,1}/2 & \dots & \dots & \sigma_{N,1}/2 \\ \sigma_{N,2}/2 & -\sigma_{N,2}/2 & 0 & \dots & 0 \\ 0 & 0 & -\sigma_{N,3}/2 & \dots & 0 \\ \vdots & \vdots & \vdots & \ddots & -\sigma_{N,q}/2 \\ \sigma_R & 0 & 0 & \dots & 0 \end{pmatrix}. \tag{18}$$

We apply the DGEQRF LAPACK subroutine on $\mathcal{B}$. The outputs enable the computation of the product of elementary reflectors which is a matrix $\mathcal{Q}(q+1, q+1)$. Then we define $\mathcal{W}$ the matrix where each column contains the standard deviation of the spectrum according to Eq. (1) as

$$\mathcal{W} = \frac{1}{\sqrt{2}} \begin{pmatrix} \sigma_{N,1} & 0 & \dots & \dots & 0 \\ 0 & \sigma_{N,2} & 0 & \dots & 0 \\ 0 & 0 & \sigma_{N,3} & \dots & 0 \\ \vdots & \vdots & \vdots & \ddots & \sigma_{N,q} \\ \sigma_R & \sigma_R & \sigma_R & \dots & \sigma_R \end{pmatrix}. \tag{19}$$

All the measurement noises are independent, as assumed, whereas the signal is common. Then the columns of $\mathcal{W}$ are projected onto the orthogonal basis $\mathcal{Q}$ and each pair of cross-spectra according to Eq. (10) is determined. Finally we compute the eigenvalues λ_j of the resulting components by using the DSYEV LAPACK subroutine. This leads to a linear combination of χ^2 distribution as follows,

$$\widehat{S_{\mathrm{cs}}} = \sum_{j}^{q} \lambda_j \chi_k^2 \tag{20}$$

where k is the number of degrees of freedom corresponding to each eigenvalue, e.g. equal to 2 for the real and imaginary part without degeneration. In the special case of 2 instruments we obtain the subtraction of two χ^2 random variables with the same number of degrees of freedom. The characteristic function of the χ_k^2 distribution is defined as

$$\phi_j(t) = (1 - 2i\lambda_j t)^{-k/2} \tag{21}$$

where i is the imaginary unit and we apply a variable change of $-t$ for the negative eigenvalues. The χ^2 distributions according to Eq. (20) being independent, the characteristic function of the c-s becomes

$$\phi(t) = \prod_{j}^{q} \phi_j(t). \tag{22}$$

It leads to the moment generating function of the VΓ distribution for 2 instruments but it is no longer the case for more instruments. When all the instruments have the same level of intrinsic noise σ_{n}^2, the diagonalization of the matrix $\mathcal{W}$

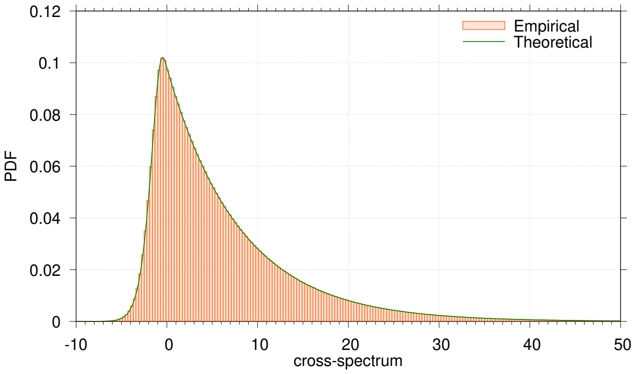

Fig. 4: Comparison of the empirical (red boxes) and theoretical (green line) PDF of the c-s for 5 instruments where the variances are $\sigma_R^2 = 6$ a.u. and $\sigma_N^2 = 10$ a.u.

defined by Eq. (19) leads to two eigenvalues. One is unique and the second one has a degeneration of $q-1$ with q the number of instruments. Consequently, it leads to the difference of two χ^2 random variables with different degrees of freedom. However even if it looks like the case with 2 instruments, the difference in the degrees of freedom of the χ^2 distributions has no analytical solution. Therefore the probability density function of the c-s for any noise level is defined as

$$p(\widehat{S_{\mathrm{cs}}}|\sigma_R^2) = \frac{1}{2\pi}\int_{\mathbb{R}} \mathrm{e}^{-it\widehat{S_{\mathrm{cs}}}}\,\phi(t)dt. \tag{23}$$

We perform the integration of the real part of the function by using the Simpson method only on the positive reals because the real part of this function is even whereas the imaginary part is odd. Figure 4 shows that the theoretical probability density function fits very well the histogram obtained by 10^7 Monte Carlo simulations for 5 instruments. The variance of each white noise is the same $\sigma_N^2 = 10$ a.u. whereas the signal level is $\sigma_R^2 = 6$ a.u.

D. Bayesian inference

1) A posteriori distribution: We seek to determine a confidence interval on σ_R^2, but Eq. (13), (16) and (23) define the PDF of a set of measurement X given the sought parameter σ_R^2. So we have to solve the inverse problem which means to determine the PDF of σ_R^2 given a set of measurement X called the *posterior* distribution. The Bayes theorem leads to the following relation,

$$\begin{cases} p(\sigma_R^2|X) \propto p(X|\sigma_R^2)\cdot\pi(\sigma_R^2) \\ \int_0^\infty p(\sigma_R^2|X)d\sigma_R^2 = 1 \end{cases} \tag{24}$$

where $\pi(\sigma_R^2)$ is the prior, i.e. the PDF before any measurement. One of the main issue of Bayesian analysis concerns the choice of this prior.

2) Choice of the prior: In order to be as general as possible, we will assume a total ignorance of the signal level. In such a case, it is generally considered that any order of magnitude has the same probability which suggests a constant prior in a logarithmic scale, i.e $\pi\left(\sigma_R^2\right) = 1/\sigma_R^2$. However, our perfect knowledge of the measurement noise level induces an implicit scale factor. In other words, since we did not remove the "bias" σ_μ^2 in Eq. (11), the s.a estimator is shifted by σ_μ^2. In a very similar case [18], we decided that the true parameter should be the sum of both levels $\theta = \sigma_\mu^2 + \sigma_R^2$. Moreover according to Eq. (9) higher noise will have lower weight and in our case, since the mathematical expectation of the s.a estimator is $\sigma_\mu^2 + \sigma_R^2$, it comes naturally that the true parameter should be:

$$\theta = \sigma_\mu^2 + \sigma_R^2. \tag{25}$$

From these considerations, we will choose $\pi(\theta) = 1/\theta = \frac{1}{\sigma_\mu^2+\sigma_R^2}$ and then, our prior for the s.a estimator will be

$$\pi(\sigma_R^2) \propto \frac{1}{\sigma_\mu^2 + \sigma_R^2}. \tag{26}$$

In order to be fair in the trial of c-s against s.a, the same prior will be used for both estimators.
In the following we will compare the different methods, starting with the spectrum average and KLT in Sec. IV.

IV. SPECTRUM AVERAGE AND KLT COMPARISON

A. A particular case: all the instruments have the same variance

Let us define $\forall i, \sigma_{N,i}^2 = \sigma_N^2$, i.e. all the q instruments have the same noise level. At a first step we determine the s.a PDF, in this case according to Eq. (9) and (2), the variance defined by Eq. (14) leads to the following expression,

$$\sigma^2 = \frac{1}{2}\left(\frac{\sigma_N^2}{q} + \sigma_R^2\right). \tag{27}$$

From Eq. (10), the estimate $\widehat{S_{\mathrm{sa}}}$ now becomes

$$\begin{aligned}\widehat{S_{\mathrm{sa}}} &= \left\{\Re\left[\sigma_\mu^2\sum_i^q \frac{X_i}{\sigma_{N,i}^2}\right]\right\}^2 + \left\{\Im\left[\sigma_\mu^2\sum_i^q \frac{X_i}{\sigma_{N,i}^2}\right]\right\}^2 \\ &= \frac{1}{q^2}\left(\left\{\Re\left[\sum_i^q X_i\right]\right\}^2 + \left\{\Im\left[\sum_i^q X_i\right]\right\}^2\right)\end{aligned} \tag{28}$$

According to Eq. (13), the s.a PDF is given by

$$p(\widehat{S_{\mathrm{sa}}}|\sigma_R^2) = \frac{e^{-\frac{\frac{1}{q^2}\left\{\Re[\sum_i^q X_i]^2 + \Im[\sum_i^q X_i]^2\right\}}{\frac{\sigma_N^2}{q}+\sigma_R^2}}}{\frac{\sigma_N^2}{q} + \sigma_R^2}. \tag{29}$$

In a second step let us define the KLT PDF. The eigenvalues of the covariance matrix resulting from Eq. (15) are given by

$$\begin{aligned}\lambda_1 &= \tfrac{1}{2}\left(\sigma_N^2 + q\sigma_R^2\right) \\ \lambda_i &= \tfrac{1}{2}\sigma_N^2 \qquad \text{with} \quad i \in \{2, ..., q\}\end{aligned} \tag{30}$$

The first and highest eigenvalue being the only one to depend of σ_R^2, we solely define its associated eigenvector

$$V_1 = \frac{J_{q,1}}{\sqrt{q}} \tag{31}$$

where $J_{q,1}$ is the all-ones column vector. Then the numerator in the exponential in Eq. (16) is

$$\begin{aligned} \sum_j^{\nu} \hat{w}_{1,j}^2 &= \sum_j^{\nu} \left[X_j \cdot V_1\right]^2 \\ &= \tfrac{1}{q} \sum_j^{\nu} \left[X_j \cdot J_{q,1}\right]^2 \\ &= \tfrac{1}{q} \sum_j^{\nu} \left[\sum_i^q X_{ij}\right]^2 \\ &= \tfrac{1}{q} \left\{ \Re\left[\sum_i^q X_i\right]^2 + \Im\left[\sum_i^q X_i\right]^2 \right\}. \end{aligned} \tag{32}$$

The KLT PDF defined by Eq. (16) is given by

$$p(\widehat{S_{\mathrm{KLT}}}|\sigma_R^2) = C \frac{e^{-\frac{\frac{1}{q}\left\{\Re[\sum_i^q X_i]^2 + \Im[\sum_i^q X_i]^2\right\}}{\sigma_N^2 + q\sigma_R^2}}}{\pi\left(\sigma_N^2 + q\sigma_R^2\right)} \tag{33}$$

where C is the Gaussian remaining product with a variance depending only on the measurement noise level. However what we want to characterize is not the estimates but the parameter σ_R^2. According to Eq. (24), the PDF of the true parameter σ_R^2 is proportional to the prior $\pi(\sigma_R^2)$ multiplied respectively by Eq. (29) and (33) for the s.a and KLT estimates. The Bayes theorem leads then to

$$p(\sigma_R^2|\widehat{S_{\mathrm{sa}}}) \propto \pi(\sigma_R^2) \frac{e^{-\frac{\frac{1}{q}\left\{\Re[\sum_i^q X_i]^2 + \Im[\sum_i^q X_i]^2\right\}}{\sigma_N^2 + q\sigma_R^2}}}{\sigma_N^2 + q\sigma_R^2} \tag{34}$$

and

$$p(\sigma_R^2|\widehat{S_{\mathrm{KLT}}}) \propto \pi(\sigma_R^2) \frac{e^{-\frac{\frac{1}{q}\left\{\Re[\sum_i^q X_i]^2 + \Im[\sum_i^q X_i]^2\right\}}{\sigma_N^2 + q\sigma_R^2}}}{\sigma_N^2 + q\sigma_R^2}. \tag{35}$$

Multiplying respectively Eq. (34) and (35) by a factor $1/q$ and π does not change the PDF since it is normalized. It is exactly the same for Eq. (35) where C does not depend on σ_R^2 and vanish through the normalization. Therefore both expressions are exactly the same. It should also be noted that the noise level σ_N^2 is necessary in both cases and the bias does not influence the sought parameter density whereas it does regarding the estimates. This implies a very interesting consequence: both PDF for the s.a and KLT leads to the exact **same** confidence interval for the same noise level.

B. General case

In this part any number of instruments and different noise level for each of them can be considered. In Section IV-A, we showed analytically that both methods lead to the same PDF of the signal level knowing the estimates in the event that all noise levels are the same. However when each noise level is different Eq. (30) giving the relation between the eigenvalues and the signal becomes much more complicated without degeneration. In this case, let us consider a number of instruments solely up to 5, refering as instance to the number of radio telescopes (RTs) part of the LEAP project. Then we make several empirical comparisons by computing the upper limit at 95% for the spectrum average and KLT methods. It should be noticed that the 5% lower bound has no interest since we are more particularly interested in the case where the signal is weaker than the noise level. This bound then greatly depends on the prior and is very close to zero.

TABLE I: Upper limit average of the parameter σ_R^2 taking into account 2 to 5 RTs. These data were obtained from a set of 1 000 simulated spectra. The signal and noise level used for the computation are $\sigma_R^2 = 1$ and $\sigma_{N,i}^2 = i$ where i is the index of the RT.

	Spectrum average / KLT		95% upper limit		
RTs number	Mean	Median	Std	Min	Max
2	17.44	12.88	3.10	6.30	115.32
3	16.32	11.78	2.39	5.16	91.78
4	15.66	11.10	2.95	4.54	108.82
5	14.84	10.67	2.28	4.14	86.99

Table I gives the average over 1 000 realizations of the 95% upper bound for 2 to 5 RTs. The signal and noise levels are respectively $\sigma_R^2 = 1$ a.u. and $\sigma_{N,i}^2 = i$ a.u. where i is the i-th RT. Then the 2-nd and 3-rd RT are respectively 2 and 3 times more noisy than the first one and so forth.

First, these comparisons show as expected that the 95% bounds obtained by both estimators as in Sec. IV-A for the same noise variance, are exactly the same.

Second, the mean and median of the 95% upper limit of the s.a and KLT estimates obtained over 1 000 realizations are decreasing as the number of RTs increases. Therefore adding a new instrument to the array, as long as we have a perfect knowledge of its noise level, necessarily contributes to lowering the upper limit and then improve the parameter estimation. The maximum value is not really significant since the tail of the distribution is very long and thin.

Finally, it should be noticed that both methods require the noise level knowledge for the expression of the probability density function. The spectrum average method being the fastest way to compute the confidence interval is then to be privileged. Therefore we will only compare the spectrum average method with the cross-spectrum in the next section.

V. 95% UPPER LIMIT: SPECTRUM AVERAGE VS CROSS-SPECTRUM

We have set the direct problem, i.e. the statistics of the s.a or c-s knowing the signal level and noise level (which is assumed to be known), respectively in Sections III-A and III-C. Now we tackle the inverse problem from the direct problem, i.e. the statistics of the signal level knowing the s.a or c-s estimate. The Bayes theorem enables us to establish this link as described in section III-D. The posterior distribution of the s.a and c-s are given by

$$p(\sigma_R^2|\widehat{S_{\mathrm{sa}}}) \propto \frac{1}{(\sigma_\mu^2+\sigma_R^2)^2}\, \mathrm{e}^{\frac{-\widehat{S_{\mathrm{sa}}}}{\sigma_\mu^2+\sigma_R^2}} \tag{36}$$

and

$$p(\sigma_R^2|\widehat{S_{\mathrm{cs}}}) \propto \frac{1}{2\pi(\sigma_\mu^2+\sigma_R^2)} \int_{\mathbb{R}} \mathrm{e}^{-it\widehat{S_{\mathrm{cs}}}}\, \phi(t)dt \tag{37}$$

where σ_μ^2 is the noise variance weighting according to Eq. (9). Let us describe our simulation algorithm in order to assess the

95% upper limit.

First simulation (S_1 to S_3): simulate a set of real data from q instruments, assuming the red noise level is known (as well as, of course, the measurement noise levels).

S_1: Assign the number of RTs, the noise variance of each one and the sought **true** signal level.

S_2: Generate a set of spectral measurement according to Eq. (1)

S_3: Compute the s.a and c-s estimates, as stated in Eq. (10), which are now fixed as parameters.

Second simulation: we no longer modify the data (these are acquired measurement results) and we look for a confidence interval on the red noise, assuming the level of the measurement noise is known.

S_4: Define any basis and perform an orthogonalization and normalization of it by using the DGEQRF subroutine from LAPACK

S_5: Establish, from Eq. (19), one $\mathcal{W}$ matrix for each signal level **varying** from 0 to an upper limit for which Eq. (36) and (37) are close enough to zero according to the required precision.

S_6: Peform S_7 to S_{11} for each σ_R^2 value.

S_7: Project the $\mathcal{W}$ matrix onto the orthogonal basis.

S_8: Compute the c-s denoted $\mathcal{Z}$ from the result of S_6.

S_9: Determine the eigenvalues of $\mathcal{Z}$ by using the DSYEV subroutine from LAPACK which has now the form of Eq. (20).

S_{10}: Define the product of each characteristic function defined by Eq. (21).

S_{11}: Compute the posterior distribution respectively of the s.a and c-s estimates according to Eq. (36) and (37). For the c-s, we perform a numerical integration of one signal value by using the Simpson method.

S_{12}: Normalize the s.a and c-s posterior PDF.

S_{13}: Determine the cumulative distribution function (cdf) by integrating the s.a and c-s posterior PDF and find the 95% upper limit corresponding onto the cdf value associated to the signal level.

The loops for the different values of the signal are computed in parallel in order to save computing time. Let us give an example of such a process. We set the number of RTs to 5 and the variances of the signal and noise are respectively $\sigma_R^2 = 6$ a.u., $\sigma_{\mathrm{n}}^2 = 10$ a.u. Then we produce 2 sets of random measurement with these parameters, shown in Table II. The first measurement set gives respectively $\widehat{S_{\mathrm{sa},1}} = 14.886$ a.u. and $\widehat{S_{\mathrm{cs},1}} = 13.226$ a.u. for the s.a and c-s estimates whereas the second one gives $\widehat{S_{\mathrm{sa},2}} = 20.730$ a.u. and $\widehat{S_{\mathrm{cs},2}} = 18.564$ a.u. It leads for the first set to the 95% upper limit on the signal σ_R^2 following value, 125.8 for the s.a and 127.3 for the c-s. Furthermore the second set gives us 167.1 for the s.a and 164.8 for the c-s. These results show that either the c-s or the s.a can be the most efficient even with the same parameters, then it only depends on the measurement set. However, the difference between the 95% upper limit for both methods is relatively low.

TABLE II: Measurement set for the outputs of each RT (5 in total) where $\sigma_R^2 = 6$ a.u. and $\sigma_N^2 = 10$ a.u.

	measurement set 1		measurement set 2	
	Real part	Imaginary part	Real part	Imaginary part
X_1	-3.8947	-1.7994	-0.1494	8.9456
X_2	-5.0950	-3.9125	-0.5275	4.4659
X_3	-2.5133	-5.5431	0.2176	5.7742
X_4	0.6433	-1.9566	1.6044	3.2146
X_5	-0.2294	-2.5738	-0.5284	0.3563

Let us now compare the s.a and c-s 95% upper limit over 100 simulations as shown in Table III for the sought signal level set to 6 a.u. and a noise level equal to 10 a.u. for each RT. The 95% upper limit is given respectively for, from the top of the Table to the bottom, the spectrum average, the cross-spectrum and the ratio of the 95% bound of s.a over c-s. The mean and median are decreasing when the number of RTs is increasing. However for 4 RTs the results are much more lower but it is just an artefact of "luck". Indeed the maximum value is 1.4 times lower than for 5 RTs and the standard deviation (std) is also very much more lower. The sample size can have a significant effect on the values obtained but is necessary to have a good precision with a reasonable computation time. However, the minimum value of the 95% bound obtained for both methods permits to override this randomness. Indeed when the cross-spectrum estimate is negative or the spectrum average estimate tends towards zero it leads to the smallest 95% bound. Whereas the maximum 95% bound obtainable for a reasonable amount of simulations can "wriggle" a lot as the tail of the posterior PDF is very long especially with higher noise level than signal level which is of interest. The minimum value of the upper bound decreases as the number of RTs increases. It seems that the s.a method gives the most stringent confidence interval.

Figure 5 shows the histogram of the 95% limit with 5 RTs for 10 000 realizations, $\sigma_R^2 = 6$ a.u. and $\sigma_N^2 = 10$ a.u. Both histograms exhibit a similar distribution which extend up to high values. However the first bin corresponding to the lowest 95% bound shows a high number of realizations for the c-s method. This can be explained by a negative estimate for the cross-spectrum which may corresponds to a spectrum average estimate having a not so small value and so a higher 95% bound. Figure 6 shows the comparison of the 95% upper limit for the s.a and c-s methods for a window of hundred data among the same set of realizations. The 6 620-th realization framed by a blue rectangle highlights the fact that the c-s can sometimes be much more stringent than the s.a method. However in most of the other realizations we notice that the 95% limit is almost the same.

Figure 7 depict the 95% upper bound median among 1 000 simulations with 5 RTs, for the s.a over c-s ratio depending on the signal-to-noise level ratio (with $\sigma_N^2 = 1$ a.u.). When $\sigma_R^2 \ll \sigma_N^2$ then the s.a seems to be the most stringent most of the time. However when the signal level becomes higher than the noise level, both the s.a and the c-s methods give in median the same 95% limit.

Considering all these observations it is wiser to compute both estimators and use the most restrictive one. Even if most of the time both estimators give a very close upper bound, sometimes

TABLE III: 95% upper limit statistics for the s.a (top), c-s (middle) and the ratio of the s.a by the c-s over 100 simulations where $\sigma_R^2 = 6$ a.u. and $\sigma_N^2 = 10$ a.u. Each rows respectively from the left to the right corresponds to the number of RTs, the mean, median, standard deviation, minimun and maximum value of the 95% upper bound.

RTs number	Spectrum average 95% upper limit				
	Mean	Median	Std	Min	Max
2	112.99	79.45	32.93	48.50	440.60
3	98.41	72.60	35.66	31.70	453.20
4	78.00	51.50	18.30	23.80	260.10
5	90.11	67.95	28.47	19.00	373.40

RTs number	Cross-spectrum 95% upper limit				
	Mean	Median	Std	Min	Max
2	116.49	83.00	27.38	67.90	388.90
3	99.74	79.65	34.54	41.00	443.40
4	76.37	54.10	18.03	28.50	255.80
5	91.87	65.35	28.98	22.20	380.20

RTs number	s.a/c-s 95% upper limit				
	Mean	Median	Std	Min	Max
2	0.97	0.90	0.12	0.71	2.21
3	0.98	0.94	8.13×10^{-2}	0.74	1.79
4	1.02	0.98	4.86×10^{-2}	0.74	1.50
5	0.97	0.96	3.73×10^{-2}	0.78	1.34

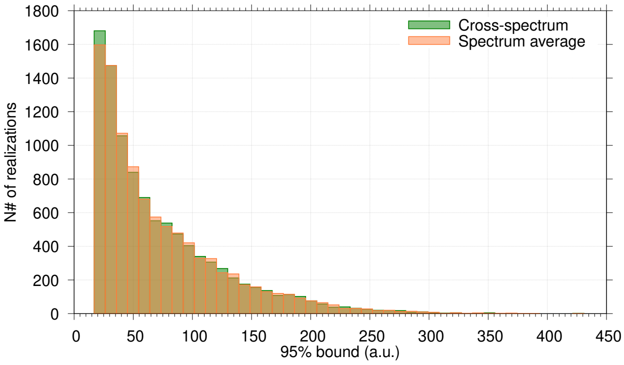

Fig. 5: Histogram comparison of 95% upper bound between the c-s and s.a for 10 000 realizations. The parameters are set for 5 RTs, $\sigma_R^2 = 6$ a.u. and $\sigma_N^2 = 10$ a.u.

the gap is clearly significant.

VI. Conclusion

First, we demonstrated that the spectrum average variance is $q/(q-1)$ lower than the cross-spectrum variance for $q \geq 2$.

Second, in order to assess the confidence interval of the signal level we defined its probability density function knowing the s.a and c-s estimates but also the noise of each instruments (radio telescopes). In addition a method directly using the statistics of the measurement (KLT) has also been compared. It turns out that the KLT and the s.a methods lead to the exact same PDF of the signal level σ_R^2 knowing the estimates, so the precision is the same. Furthermore whereas the cross-spectrum has a well-defined analytic probability density function for 2 instruments called VΓ, there is no equivalent for more than 2 instruments. We proposed then a generalized method based on a numerical integration of the characteristic function product. This method works very well according to the Monte Carlo simulations.

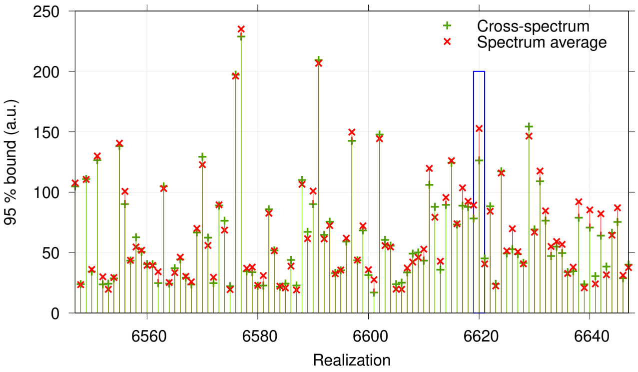

Fig. 6: Set of 100 realizations for 5 RTs of 95% bounds for cross-spectrum (green +) and spectrum average (red ×) where $\sigma_R^2 = 6$ a.u. and $\sigma_N^2 = 10$ a.u.

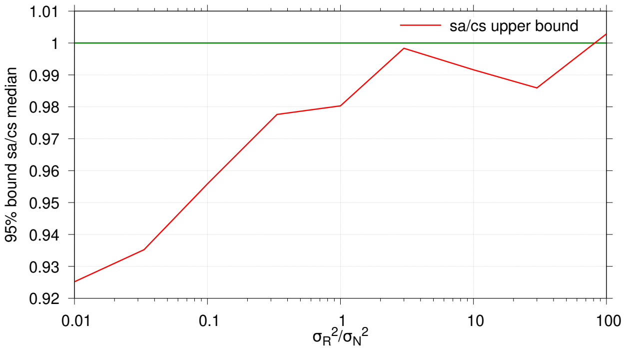

Fig. 7: Evolution of the 95% upper bound median of the s.a over c-s ratio obtained for 1 000 realizations depending on the signal-to-noise level ratio. The parameters are set for 5 RTs and $\sigma_N^2 = 1$ a.u. The red curve corresponds to the sa/cs upper bound and the green curve indicates when both s.a and c-s have the same upper bound in median.

Finally the efficiency of both estimators, the spectrum average versus the cross-spectrum, is highlighted through the comparison of the 95% Bayesian upper limit. We found a slight advantage for the spectrum average estimator when the noise level is higher than the signal level. However we showed that sometimes the c-s gives the most stringent confidence interval but above all a little more often than the s.a for the lowest upper limit. Nevertheless it is the s.a method which gives us the minimum 95% limit reachable. To conclude it is wiser to compute both estimates and use the most stringent.

Acknowledgement

This work was partially funded by the ANR Programmes d'Investissement d'Avenir (PIA) Oscillateur IMP (Project 11-EQPX-0033) and FIRST-TF (Project 10-LABX-0048).

REFERENCES

[1] L. A. Rawley, J. H. Taylor, M. M. Davis, and D. W. Allan. Millisecond pulsar psr 1937+21: A highly stable clock. *Science*, 238(4828):761–765, 1987.

[2] J. H. Taylor. Millisecond pulsars: nature's most stable clocks. *Proceedings of the IEEE*, 79(7):1054–1062, 1991.

[3] J. G. Hartnett and A. N. Luiten. Colloquium: Comparison of astrophysical and terrestrial frequency standards. *Rev. Mod. Phys.*, 83:1–9, Jan 2011.

[4] R. N. Manchester. Millisecond pulsars, their evolution and applications. *Journal of Astrophysics and Astronomy*, 38:1–18, 2017.

[5] J. E. Hansen and M. Sato. Paleoclimate implications for human-made climate change. In A. Berger, F. Mesinger, and D. Sijacki, editors, *Climate Change*, pages 21–47, Vienna, 2012. Springer Vienna.

[6] A. Nothnagel. Elements of geodetic and astrometric very long baseline interferometry, Nov 2021. https://www.vlbi.at/data/publications/2021_Nothnagel_Elements_of_VLBI_20211102.pdf.

[7] Massimo Caligaris, Giovanni Antonio Costanzo, and Claudio Eligio Calosso. 6/12-channel synchronous digital phasemeter for ultrastable signal characterization and use. In *Proc. Europ. Freq. Time Forum*, pages 681–683, Denver, CO, USA, April 12–16, 2015.

[8] Vilius Palenskis and Kestutis Maknys. Nature of low-frequency noise in homogeneous semiconductors. *Scientific Reports*, 5(1), December 2015.

[9] M. E. Tiuri. Radio-telescope receivers. In *Radio Astronomy*, chapter 7 of J. D. Kraus. New York: McGraw Hill, 1966.

[10] A. Baudiquez, E. Lantz, E. Rubiola, and F. Vernotte. Cross-spectrum measurement statistics: Uncertainties and detection limit. *IEEE Trans. Ultras. Ferroelec. Freq. Contr.*, 67(11):2461–2470, June 2020.

[11] C. G. Bassa, G. H. Janssen, R. Karuppusamy, M. Kramer, K. J. Lee, K. Liu, J. McKee, D. Perrodin, M. Purver, S. Sanidas, R. Smits, and B. W. Stappers. Leap: the large european array for pulsars. *Month. Not. Roy. Astronom. Soc.*, 456(2):2196–2209, December 2015.

[12] J. P. W. Verbiest, S. Osłowski, and S. Burke-Spolaor. Pulsar timing array experiments. *Handbook of Gravitational Wave Astronomy*, pages 1–42, 2021.

[13] B. Goncharov, R. M. Shannon, D. J. Reardon, G. Hobbs, A. Zic, M. Bailes, M. Curyło, S. Dai, M. Kerr, M. E. Lower, and et al. On the evidence for a common-spectrum process in the search for the nanohertz gravitational-wave background with the parkes pulsar timing array. *The Astrophysical Journal Letters*, 917(2):L19, Aug 2021.

[14] Siyuan Chen, François Vernotte, and Enrico Rubiola. Applying clock comparison methods to pulsar timing observations. *Month. Not. Roy. Astronom. Soc.*, 503(3):4496–4507, 03 2021.

[15] N. J. Kasdin. Discrete simulation of colored noise and stochastic processes and 1/f power law noise generation. *Proceedings of the IEEE*, 83(5):802–827, May 1995.

[16] J. Hartung, G. Knapp, and B. K. Sinha. *Statistical Meta-Analysis with Applications*. Wiley, 2008.

[17] E. Lantz, C. E. Calosso, E. Rubiola, V. Giordano, C. Fluhr, B. Dubois, and F. Vernotte. KLTS: A rigorous method to compute the confidence intervals for the three-cornered hat and for Groslambert covariance. *IEEE Trans. Ultras. Ferroelec. Freq. Contr.*, 66(12):1942–1949, December 2019.

[18] M. P. McHugh, G. Zalamansky, F. Vernotte, and E. Lantz. Pulsar timing and the upper limits on a gravitational wave background : a Bayesian approach. *Phys. Rev. D*, 54(10):5993–6000, November 1996.

[19] H. A. R. Barnett. The variance of the product of two independent variables and its application to an investigation based on sample data. *Journal of the Institute of Actuaries*, 81(2):190–190, 1955.

[20] L. Isserlis. On a Formula for the Product-Moment Coefficient of any Order of a Normal Frequency Distribution in any Number of Variables. *Biometrika*, 12(1/2):134–139, November 1918.

APPENDIX

Glossary of symbols

q	Number of instruments
$r(t)$	Common signal measured by q RTs (red noise)
$R(f)$	Fourier transform of $r(t)$
S_r(f)	Power spectral density of $r(t)$
$n_i(t)$	Intrinsic white noise of the i-th RT
$N_i(f)$	Fourier transform of $n_i(t)$
$S_{n,i}$(f)	Power spectral density of $n_i(t)$
$x_i(t)$	$x_i(t) = r(t) + n_i(t)$, received at the output of the i-th RT
$X_i(f)$	Fourier transform of x_i(t)
$S_{x,i}$(f)	Power spectral density of $x_i(t)$
$\widehat{\ }$ estimate as in $\widehat{S}$. Here we consider three estimators,	
$\widehat{S_{\text{sa}}}$	Spectrum average
$\widehat{S_{\text{KLT}}}$	Karhunen-Loève transform
$\widehat{S_{\text{cs}}}$	Cross-spectrum
σ_R^2	Variance of R in a bandwidth, i.e. the power in one bin of $S(f)$. It takes three different flavors: s.a, KLT or c-s
$\sigma_{N,i}^2$	Same as above, with the noise of the i-th RT
σ_μ^2	Noise weight factor, inverse of the sum of the inverse of $\sigma_{N,i}^2$

Variance of the estimators $\widehat{S_{\text{sa}}}$ and $\widehat{S_{\text{cs}}}$

1) Measurements: Let us define q instruments measurements X_1, X_2, … and X_q as

$$X_j = N_j + iN'_j + R + iR' \tag{38}$$

where N_j, N'_j are independent Gaussian centered random variables of variance $\sigma_N^2/2$ and R, R' are independent Gaussian centered random variables of variance $\sigma_R^2/2$.

2) Estimators: The estimator $\widehat{S_{\text{cs}}}$ is defined by Eq. (10) as

$$\begin{aligned}\widehat{S_{\text{cs}}} = \frac{1}{\binom{q}{2}} \sum_{j=1}^{q-1} \sum_{k=j+1}^{q} \Re[(N_j + iN'_j + R + iR')\times \\ \times(N_k - iN'_k + R - iR')].\end{aligned} \tag{39}$$

On the other hand, $\widehat{S_{\text{sa}}}$ is defined by Eq. (10) as

$$\widehat{S_{\text{sa}}} = \left(\sum_j^q \frac{N_j + qR}{q}\right)^2 + \left(\sum_j^q \frac{N'_j + qR'}{q}\right)^2. \tag{40}$$

3) Statistics reminder: If A and B are 2 independent random variables of zero expectation

$$\mathbb{V}[AB] = \mathbb{V}[A]\mathbb{V}[B] \tag{41}$$

according to Eq. (a) from [19] where $\mathbb{V}[\cdot]$ stands for the variance of the quantity within the brackets. Moreover according to the Isserlis' theorem [20],

$$\begin{aligned}\mathbb{V}[A^2] &= \mathbb{E}[A^4] - \left\{\mathbb{E}[A^2]\right\}^2 = 3\left\{\mathbb{E}[A^2]\right\}^2 - \left\{\mathbb{E}[A^2]\right\}^2 \\ &= 2\mathbb{V}^2[A]\end{aligned} \tag{42}$$

where $\mathbb{E}[\cdot]$ stands for the mathematical expectation of the quantity within the brackets. It is also useful to consider the covariances. If A, B, C, D are 4 Gaussian centered random variable

$$\mathbb{E}[ABCD] = \mathbb{E}[AB]\cdot\mathbb{E}[CD] + \mathbb{E}[AC]\cdot\mathbb{E}[BD] + \mathbb{E}[AD]\cdot\mathbb{E}[BC]. \tag{43}$$

If A, B, C, D are 4 **independent** Gaussian centered random variables, this can be derived to the following particular cases (Isserlis' theorem [20]):

- $\mathbb{E}[ABCD] = \mathbb{E}[AB]\cdot\mathbb{E}[CD] + \mathbb{E}[AC]\cdot\mathbb{E}[BD] + \mathbb{E}[AD]\cdot\mathbb{E}[BC] = 0$ since each mathematical expectation product $\mathbb{E}[XY]$ is null
- $\mathbb{E}[A^2BC] = \mathbb{E}[A^2]\cdot\mathbb{E}[BC] + 2\mathbb{E}[AB]\cdot\mathbb{E}[AC] = 0$ since the only mathematical expectation which is not null, $\mathbb{E}[A^2]$, is multiplied by $\mathbb{E}[CD] = 0$
- $\mathbb{E}[A^3B] = 3\mathbb{E}[A^2]\cdot\mathbb{E}[BC] = 0$ since $\mathbb{E}[BC] = 0$
- $$\begin{aligned}\mathbb{E}[A^2B^2] &= \mathbb{E}[A^2]\cdot\mathbb{E}[B^2] + 2\mathbb{E}^2[AB]\\ &= \mathbb{E}[A^2]\cdot\mathbb{E}[B^2] \neq 0.\end{aligned}$$
- $$\begin{aligned}\mathrm{Cov}[A^2B^2] &= \mathbb{E}[A^2B^2] - \mathbb{E}[A^2]\cdot\mathbb{E}[B^2]\\ &= \mathbb{E}[A^2]\cdot\mathbb{E}[B^2] - \mathbb{E}[A^2]\cdot\mathbb{E}[B^2] = 0.\end{aligned}$$

4) Variance of $\widehat{S_{\mathrm{cs}}}$: From (39), it comes

$$\begin{aligned}\widehat{S_{\mathrm{cs}}} = \frac{1}{\binom{q}{2}} \Bigg[&\sum_{j=1}^{q-1}\sum_{k=j+1}^{q} (N_jN_k + N'_jN'_k)\times\\ &\times(q-1)\sum_{j=1}^{q}(N_jR + N'_jR')\times\\ &\times\binom{n}{2}(R^2 + R'^2)\Bigg].\end{aligned} \tag{44}$$

Then,

$$\begin{aligned}\mathbb{V}[\widehat{S_{\mathrm{cs}}}] = \frac{1}{\binom{q}{2}^2} \Bigg[&\sum_{j=1}^{q-1}\sum_{k=j+1}^{q} (\mathbb{V}[N_jN_k] + \mathbb{V}[N'_jN'_k])\times\\ &\times(q-1)^2\sum_{j=1}^{q}(\mathbb{V}[N_jR] + \mathbb{V}[N'_jR'])\times\\ &\times\binom{q}{2}^2(\mathbb{V}[R^2] + \mathbb{V}[R'^2])\Bigg].\end{aligned} \tag{45}$$

where all covariance terms are null thanks to Isserlis'theorem. From the properties (41) and (42), it comes

$$\begin{aligned}\mathbb{V}[\widehat{S_{\mathrm{cs}}}] = \frac{1}{\binom{q}{2}^2} \Bigg[&\sum_{j=1}^{q-1}\sum_{k=j+1}^{q} (\mathbb{V}[N_j]\mathbb{V}[N_k] + \mathbb{V}[N'_j]\mathbb{V}[N'_k])\times\\ &\times(q-1)^2\sum_{j=1}^{q}(\mathbb{V}[N_j]\mathbb{V}[R] + \mathbb{V}[N'_j]\mathbb{V}[R'])\times\\ &\times\binom{q}{2}^2(2\mathbb{V}^2[R] + 2\mathbb{V}^2[R'])\Bigg].\end{aligned} \tag{46}$$

According to the binomial formula,

$$\binom{q}{2} = \frac{q!}{2!(q-2)!} = \frac{q(q-1)}{2}. \tag{47}$$

Therefore,

$$\begin{aligned}\mathbb{V}[\widehat{S_{\mathrm{cs}}}] &= \frac{1}{\binom{q}{2}^2}\left[2\binom{q}{2}\frac{\sigma_N^4}{4} + 2q(q-1)^2\frac{\sigma_N^2\sigma_R^2}{4} + 4\binom{q}{2}^2\frac{\sigma_R^4}{4}\right]\\ &= \frac{1}{q(q-1)}\sigma_N^4 + \frac{2}{q}\sigma_N^2\sigma_R^2 + \sigma_R^4.\end{aligned} \tag{48}$$

5) Variance of $\widehat{S_{\mathrm{sa}}}$: From (40), it comes

$$\begin{aligned}\widehat{S_{\mathrm{sa}}} = \frac{1}{q^2}\Bigg[&\sum_{j=1}^{q}(N_j^2 + N_j'^2) + q^2(R^2 + R'^2) +\\ &+ 2\sum_{j=1}^{q-1}\sum_{k=j+1}^{q}(N_jN_k + N'_jN'_k) +\\ &+ 2q\sum_{j=1}^{q}(N_jR + N'_jR')\Bigg]\end{aligned} \tag{49}$$

Then,

$$\begin{aligned}\mathbb{V}[\widehat{S_{\mathrm{sa}}}] = \frac{1}{q^4}\Bigg[&\sum_{j=1}^{q}(\mathbb{V}[N_j^2] + \mathbb{V}[N_j'^2]) + q^4(\mathbb{V}[R^2] + \mathbb{V}[R'^2]) +\\ &+ 4\sum_{j=1}^{q-1}\sum_{k=j+1}^{q}(\mathbb{V}[N_jN_k] + \mathbb{V}[N'_jN'_k]) +\\ &+ 4q^2\sum_{j=1}^{q}(\mathbb{V}[N_jR] + \mathbb{V}[N'_jR'])\Bigg]\end{aligned} \tag{50}$$

where all covariance terms are null thanks to Isserlis'theorem. From the properties (41) and (42), it comes

$$\begin{aligned}\mathbb{V}[\widehat{S_{\mathrm{sa}}}] = \frac{1}{q^4}\Bigg[&\sum_{j=1}^{q}(2\mathbb{V}^2[N_j] + 2\mathbb{V}^2[N'_j]) + q^4(2\mathbb{V}^2[R] + 2\mathbb{V}^2[R']) +\\ &+ 4\sum_{j=1}^{q-1}\sum_{k=j+1}^{q}(\mathbb{V}[N_j]\mathbb{V}[N_k] + \mathbb{V}[N'_j]\mathbb{V}[N'_k]) +\\ &+ 4q^2\sum_{j=1}^{q}(\mathbb{V}[N_j]\mathbb{V}[R] + \mathbb{V}[N'_j]\mathbb{V}[R'])\Bigg]\end{aligned} \tag{51}$$

Therefore,

$$\begin{aligned}\mathbb{V}[\widehat{S_{\mathrm{sa}}}] &= \frac{1}{q^4}\left[4q\frac{\sigma_N^4}{4} + 4q^4\frac{\sigma_R^4}{4} + 8\binom{q}{2}\frac{\sigma_N^4}{4} + 8q^3\frac{\sigma_N^2\sigma_R^2}{4}\right]\\ &= \frac{1}{q^2}\sigma_N^4 + \frac{2}{q}\sigma_N^2\sigma_R^2 + \sigma_R^4.\end{aligned} \tag{52}$$

6) Variance ratios: Let us compare the cross-spectrum and spectrum average estimates variances for limit signal to noise ratio values.
If $\sigma_R^2 \ll \sigma_N^2$,

$$\mathbb{V}[\widehat{S_{\mathrm{cs}}}] \approx \frac{1}{q(q-1)}\sigma_N^4 \qquad \text{and} \qquad \mathbb{V}[\widehat{S_{\mathrm{sa}}}] \approx \frac{1}{q^2}\sigma_N^4. \tag{53}$$

Consequently,

$$\mathbb{V}[\widehat{S_{\mathrm{cs}}}] \approx \frac{q}{q-1}\mathbb{V}[\widehat{S_{\mathrm{sa}}}]. \tag{54}$$

If $\sigma_N^2 \ll \sigma_R^2$,

$$\mathbb{V}[\widehat{S_{\mathrm{cs}}}] \approx \sigma_R^4 \qquad \text{and} \qquad \mathbb{V}[\widehat{S_{\mathrm{sa}}}] \approx \sigma_R^4. \tag{55}$$

Consequently,

$$\mathbb{V}[\widehat{S_{\mathrm{cs}}}] \approx \mathbb{V}[\widehat{S_{\mathrm{sa}}}]. \tag{56}$$

List of Figures

List of Tables

References

[1] Michael A Lombardi. Fundamentals of time and frequency. The Mechatronics Handbook, 2, 2006. (Cited on pages 5, 6, and 9.)

[2] Judah Levine. Introduction to time and frequency metrology. Review of scientific instruments, 70(6):2567–2596, 1999. (Cited on page 5.)

[3] Elisa Felicitas Arias. The metrology of time. Philosophical Transactions of the Royal Society A: Mathematical, Physical and Engineering Sciences, 363(1834):2289–2305, 2005. (Cited on page 5.)

[4] François Vernotte and Laurent Poupard. La (re)fondation des observatoires astronomiques sous la IIIe République. Histoire contextuelle et perspectives actuelles, chapter L'observatoire de Besançon et la mesure du temps. Presses Universitaires de Bordeaux, 2011. (Cited on pages 6, 7, and 8.)

[5] G. M. Clemence. On the system of astronomical constants. Astronomical Journal, 53:169, 1948. (Cited on page 8.)

[6] Louis Essen and Jack VL Parry. An atomic standard of frequency and time interval: a caesium resonator. Nature, 176(4476):280–282, 1955. (Cited on page 8.)

[7] J Terrien. News from the international bureau of weights and measures. Metrologia, 4(1):41, 1968. (Cited on pages 8 and 21.)

[8] BIPM. Comptes Rendus de la 13e CGPM (1967/68). `shorturl.at/NPUY6`, 1969. (Cited on pages 8 and 21.)

[9] William Markowitz, R Glenn Hall, L Essen, and JVL Parry. Frequency of cesium in terms of ephemeris time. Physical Review Letters, 1(3):105, 1958. (Cited on page 8.)

[10] Michael A Lombardi, Thomas P Heavner, and Steven R Jefferts. NIST primary frequency standards and the realization of the SI second. NCSLI Measure, 2(4):74–89, 2007. (Cited on page 10.)

[11] BIPM. Circular T. available from (`www.bipm.org`). (Cited on pages 10, 21, 23, and 47.)

[12] BIPM. Primary and Secondary Frequency Standards participating to TAI. `https://webtai.bipm.org/database/show_psfs.html`. (Cited on page 11.)

[13] J Robert Oppenheimer and George M Volkoff. On massive neutron cores. Physical Review, 55(4):374, 1939. (Cited on page 13.)

[14] JM Lattimer and M Prakash. Neutron star structure and the equation of state. The Astrophysical Journal, 550(1):426, 2001. (Cited on page 13.)

[15] Duncan Ross Lorimer and Michael Kramer. Handbook of pulsar astronomy. Cambridge Univ. Press, 2012. (Cited on page 13.)

[16] Alice K Harding. Pulsar emission physics: The first fifty years. In Proceedings of the International Astronomical Union, volume 13, pages 52–57. Cambridge University Press, 2017. (Cited on page 13.)

[17] DB Melrose and MZ Rafat. Pulsar radio emission mechanism: Why no consensus? In Journal of Physics: Conference Series, volume 932, page 012011. IOP Publishing, 2017. (Cited on page 13.)

[18] D. C. Backer, Shrinivas R Kulkarni, Carl Heiles, M.M. Davis, and W.M. Goss. A millisecond pulsar. Nature, 300(5893):615–618, 1982. (Cited on page 13.)

[19] David W Allan and Lin Ping-Ping. Estimating Combined Errors Due to Propagation and Ephemeris and Their Effect on Time and Frequency Transfer. In 41st Annual Symposium on Frequency Control, pages 144–148. IEEE, 1987. (Cited on page 13.)

[20] David W Allan, Marc A. Weiss, and Trudi K. Peppler. In search of the best clock. IEEE Transactions on Instrumentation and Measurement, 38(2):624–630, 1989. (Cited on page 13.)

[21] S. Hama, M. Imae, H. Kiuchi, H. Takaba, and F. Takahashi. Observation Plan of High-stable Pulsars in CRL. In Proc. PTTI, volume 21, pages 289–294, 1989. (Cited on page 13.)

[22] AW Hotan, M Bailes, and SM Ord. High-precision baseband timing of 15 millisecond pulsars. Monthly Notices of the Royal Astronomical Society, 369(3):1502–1520, 2006. (Cited on page 13.)

[23] B. A. Jacoby. Recycled Pulsars. PhD thesis, Cal-Tech, Pasadena, California, 2005. (Cited on page 13.)

[24] Demetrios Nicholas Matsakis, Joseph Hooton Taylor, and T Marshall Eubanks. A statistic for describing pulsar and clock stabilities. Astronomy and Astrophysics, 326:924–928, 1997. (Cited on page 13.)

[25] J. H. Taylor. Millisecond pulsars: nature's most stable clocks. Proceedings of the IEEE, 79(7):1054–1062, 1991. (Cited on pages 13 and 60.)

[26] RN Manchester. Observational properties of pulsars. Science, 304(5670):542–546, 2004. (Cited on page 13.)

[27] Gérard Petit and Patrizia Tavella. Pulsars and time scales. Astronomy and Astrophysics, 308:290–298, 1996. (Cited on page 13.)

[28] L. A. Rawley, J. H. Taylor, M. M. Davis, and D. W. Allan. Millisecond Pulsar PSR 1937+21: A Highly Stable Clock. Science, 238(4828):761–765, 1987. (Cited on pages 13 and 60.)

[29] J. Roy and B. C. Venkatasubramani, T. L. Joshi. Evaluation of frequency standard using inter-comparison techniques and pulsar data. In Proceedings of the XXVIIIth URSI General Assembly, 2005. (Cited on page 13.)

[30] J. P. W. Verbiest, M. Bailes, W. A. Coles, G. B. Hobbs, W. Van Straten, D. J. Champion, F. A. Jenet, R. N. Manchester, N. D. R. Bhat, J. M. Sarkissian, et al. Timing stability of millisecond pulsars and prospects for gravitational-wave detection. Month. Not. Roy. Astronom. Soc., 400(2):951–968, 2009. (Cited on pages 13 and 60.)

[31] Chong-xia Zhong and Ting-gao Yang. Wavelet analysis algorithm for synthetic pulsar time. Chinese Astronomy and Astrophysics, 31(4):443–454, 2007. (Cited on page 13.)

[32] Anjum S Mukadam, Souza Oliveira Kepler, Don Earl Winget, R Edward Nather, Mukremin Kilic, Fergal Mullally, Ted von Hippel, Scot J Kleinman, Atsuko Nitta, Joyce Ann Guzik, et al. Constraining the evolution of ZZ Ceti. The Astrophysical Journal, 594(2):961, 2003. (Cited on page 13.)

[33] Souza Oliveira Kepler, Jose Eduardo da Silveira Costa, Bárbara Garcia Castanheira, Donald Earl Winget, Fergal Mullally, R Edward Nather, Mukremin Kilic, Ted von Hippel, Anjum S Mukadam, and Denis J Sullivan. Measuring the evolution of the most stable optical clock G 117-B15A. The Astrophysical Journal, 634(2):1311, 2005. (Cited on page 13.)

[34] Demetrios N Matsakis and Roger S Foster. Application of Millisecond Pulsar Timing to the Long-Term Stability of Clock Ensembles. In Amazing Light, pages 445–462. Springer, 1996. (Cited on page 13.)

[35] J. G. Hartnett and A. N. Luiten. Colloquium: Comparison of astrophysical and terrestrial frequency standards. Rev. Mod. Phys., 83:1–9, Jan 2011. (Cited on pages 14 and 60.)

[36] BJ Bloom, TL Nicholson, JR Williams, SL Campbell, M Bishof, X Zhang, W Zhang, SL Bromley, and J Ye. An optical lattice clock with accuracy and stability at the 10^{-18} level. Nature, 506(7486):71–75, 2014. (Cited on page 14.)

[37] Gérard Petit and Ismaël Cognard. How can millisecond pulsars transfer the accuracy of atomic time? In 2011 XXXth URSI General Assembly and Scientific Symposium, pages 1–4, 2011. (Cited on page 14.)

[38] Albert Einstein. Die feldgleichungen der gravitation. Sitzung der physikalische-mathematischen Klasse, 25:844–847, 1915. (Cited on page 14.)

[39] Stephen W Hawking and Werner Israel. Three hundred years of gravitation. Cambridge University Press, 1989. (Cited on page 14.)

[40] David T Wilkinson. Anisotropy of the cosmic blackbody radiation. Science, 232(4757):1517–1522, 1986. (Cited on page 14.)

[41] S. Detweiler. Pulsar timing measurements and the search for gravitational waves. Am. Astronom. Soc., 234:1100–1104, December 1979. (Cited on pages 15 and 60.)

[42] Christopher J. Moore, Robert H. Cole, and Christopher P.L. Berry. Gravitational-wave sensitivity curves. Classical and Quantum Gravity, 32(1), 2014. (Cited on page 15.)

[43] A. Hewish, S. J. Bell, J. D. H. Pilkington, P. F. Scott, and R. A. Collins. Observation of a rapidly pulsating radio source. Nature, 217:709–713, 1968. (Cited on page 15.)

[44] Joseph Weber. Evidence for discovery of gravitational radiation. Physical Review Letters, 22(24):1320, 1969. (Cited on page 15.)

[45] Barry C Barish and Rainer Weiss. LIGO and the detection of gravitational waves. Physics Today, 52:44–50, 1999. (Cited on page 16.)

[46] G. Desvignes, R. N. Caballero, L. Lentati, J. P. W. Verbiest, D. J. Champion, B. W. Stappers, G. H. Janssen, P. Lazarus, S. Osłowski, S. Babak, C. G. Bassa, P. Brem, M. Burgay, I. Cognard, J. R. Gair, E. Graikou, L. Guillemot, J. W. T. Hessels, A. Jessner, C. Jordan, R. Karuppusamy, M. Kramer, A. Lassus, K. Lazaridis, K. J. Lee, K. Liu, A. G. Lyne, J. McKee, C. M. F. Mingarelli, D. Perrodin, A. Petiteau,

A. Possenti, M. B. Purver, P. A. Rosado, S. Sanidas, A. Sesana, G. Shaifullah, R. Smits, S. R. Taylor, G. Theureau, C. Tiburzi, R. van Haasteren, and A. Vecchio. High-precision timing of 42 millisecond pulsars with the European Pulsar Timing Array. Monthly Notices of the Royal Astronomical Society, 458(3):3341–3380, 03 2016. (Cited on page 16.)

[47] B B P Perera, M E DeCesar, P B Demorest, M Kerr, L Lentati, D J Nice, S Osłowski, S M Ransom, M J Keith, Z Arzoumanian, M Bailes, P T Baker, C G Bassa, N D R Bhat, A Brazier, M Burgay, S Burke-Spolaor, R N Caballero, D J Champion, S Chatterjee, S Chen, I Cognard, J M Cordes, K Crowter, S Dai, G Desvignes, T Dolch, R D Ferdman, E C Ferrara, E Fonseca, J M Goldstein, E Graikou, L Guillemot, J S Hazboun, G Hobbs, H Hu, K Islo, G H Janssen, R Karuppusamy, M Kramer, M T Lam, K J Lee, K Liu, J Luo, A G Lyne, R N Manchester, J W McKee, M A McLaughlin, C M F Mingarelli, A P Parthasarathy, T T Pennucci, D Perrodin, A Possenti, D J Reardon, C J Russell, S A Sanidas, A Sesana, G Shaifullah, R M Shannon, X Siemens, J Simon, R Spiewak, I H Stairs, B W Stappers, J K Swiggum, S R Taylor, G Theureau, C Tiburzi, M Vallisneri, A Vecchio, J B Wang, S B Zhang, L Zhang, W W Zhu, and X J Zhu. The International Pulsar Timing Array: second data release. Monthly Notices of the Royal Astronomical Society, 490(4):4666–4687, 10 2019. (Cited on page 16.)

[48] Md F. Alam, Zaven Arzoumanian, Paul T. Baker, Harsha Blumer, Keith E. Bohler, Adam Brazier, Paul R. Brook, Sarah Burke-Spolaor, Keeisi Caballero, Richard S. Camuccio, Rachel L. Chamberlain, Shami Chatterjee, James M. Cordes, Neil J. Cornish, Fronefield Crawford, H. Thankful Cromartie, Megan E. DeCesar, Paul B. Demorest, Timothy Dolch, Justin A. Ellis, Robert D. Ferdman, Elizabeth C. Ferrara, William Fiore, Emmanuel Fonseca, Yhamil Garcia, Nathan Garver-Daniels, Peter A. Gentile, Deborah C. Good, Jordan A. Gusdorff, Daniel Halmrast, Jeffrey S. Hazboun, Kristina Islo, Ross J. Jennings, Cody Jessup, Megan L. Jones, Andrew R. Kaiser, David L. Kaplan, Luke Zoltan Kelley, Joey Shapiro Key, Michael T. Lam, T. Joseph W. Lazio, Duncan R. Lorimer, Jing Luo, Ryan S. Lynch, Dustin R. Madison, Kaleb Maraccini, Maura A. McLaughlin, Chiara M. F. Mingarelli, Cherry Ng, Benjamin M. X. Nguyen, David J. Nice, Timothy T. Pennucci, Nihan S. Pol, Joshua Ramette, Scott M. Ransom, Paul S. Ray, Brent J. Shapiro-Albert, Xavier Siemens, Joseph Simon, Renée Spiewak, Ingrid H. Stairs, Daniel R. Stinebring, Kevin Stovall, Joseph K. Swiggum, Stephen R. Taylor, Michael Tripepi, Michele Vallisneri, Sarah J. Vigeland, Caitlin A. Witt, and Weiwei Zhu and. The NANOGrav 12.5 yr Data Set: Observations and Narrowband Timing of 47 Mil-

lisecond Pulsars. The Astrophysical Journal Supplement Series, 252(1):4, dec 2020. (Cited on page 16.)

[49] Matthew Kerr, Daniel J Reardon, George Hobbs, Ryan M Shannon, Richard N Manchester, Shi Dai, Christopher J Russell, Songbo Zhang, Willem Van Straten, Stefan Osłowski, et al. The parkes pulsar timing array project: second data release. Publications of the Astronomical Society of Australia, 37, 2020. (Cited on page 16.)

[50] Karsten Danzmann. LISA mission overview. Advances in Space Research, 25(6):1129–1136, 2000. (Cited on page 16.)

[51] Benjamin P Abbott, Richard Abbott, TD Abbott, MR Abernathy, Fausto Acernese, Kendall Ackley, Carl Adams, Thomas Adams, Paolo Addesso, RX Adhikari, et al. Observation of gravitational waves from a binary black hole merger. Physical review letters, 116(6):061102, 2016. (Cited on page 16.)

[52] S. R. Taylor, M. Vallisneri, J. A. Ellis, C. M. F. Mingarelli, T. J. W. Lazio, and R. van Haasteren. Are we there yet? Time to detection of nanohertz gravitational waves based on pulsar-timing array limits. Astrophys. J. Lett., 819(1):6, 2016. (Cited on pages 16 and 60.)

[53] D. Perrodin and A. Sesana. Radio Pulsars: Testing Gravity and Detecting Gravitational Waves, volume 457 of Astrophysics and Space Science Library, chapter 3, pages 95–148. Springer, Cham, 2018. (Cited on pages 16 and 60.)

[54] C. G. Bassa, G. H. Janssen, R. Karuppusamy, M. Kramer, K. J. Lee, K. Liu, J. McKee, D. Perrodin, M. Purver, S. Sanidas, R. Smits, and B. W. Stappers. LEAP: the Large European Array for Pulsars. Month. Not. Roy. Astronom. Soc., 456(2):2196–2209, December 2015. (Cited on pages 16, 60, and 61.)

[55] James A. Barnes, Andrew R. Chi, Leonard S. Cutler, Daniel J. Healey, David B. Leeson, Thomas E. McGunigal, James A. Mullen, Warren L. Smith, Richard L. Sydnor, Robert F. C. Vessot, and Gernot M. R. Winkler. Characterization of Frequency Stability. IEEE Transactions on Instrumentation and Measurement, IM-20(2):105–120, 1971. (Cited on page 16.)

[56] James E Gray and David W Allan. A method for estimating the frequency stability of an individual oscillator. In 28th Annual Symposium on Frequency Control, pages 243–246. IEEE, 1974. (Cited on page 16.)

[57] Jacques Rutman. Characterization of phase and frequency instabilities in precision frequency sources: Fifteen years of progress. In Proc. IEEE, volume 66, pages 1048–1075. IEEE, 1978. (Cited on pages 16 and 31.)

[58] D.W. Allan and J.A. Barnes. A modified Allan variance with increased oscillator characterization ability. In Proc 35th Ann Freq Control Symposium, pages 470–474, 1981. (Cited on page 16.)

[59] E. Rubiola and F. Vernotte. The cross-spectrum experimental method. arXiv:1003.0113v1, March 2010. (Cited on pages 16, 59, 79, 116, and 154.)

[60] J Terrien. News from the international bureau of weights and measures. Metrologia, 7(1):43–47, 1971. (Cited on page 21.)

[61] ITU. ITU-R Recommendations Reports, TF series and recommendation ITU-R TF, 2008. (Cited on page 21.)

[62] G. Panfilo and F. Arias. The Coordinated Universal Time (UTC). Metrologia, 56(4), 2019. (Cited on pages 21 and 23.)

[63] BIPM. UTCr. `https://www.bipm.org/en/time-ftp/utcr`. (Cited on page 21.)

[64] BIPM. The International System of Units. `shorturl.at/bCIPZ`, 2019. (Cited on page 22.)

[65] Arias, E Felicitas and Panfilo, Gianna and Petit, Gérard. Timescales at the bipm. Metrologia, 48(4):S145, 2011. (Cited on pages 22 and 23.)

[66] Michael A Lombardi et al. Selecting a Primary Frequency Standard for a Calibration Laboratory. Cal Lab, pages 33–39, 2008. (Cited on page 23.)

[67] Gianna Panfilo and E. Felicitas Arias. Algorithms for International Atomic Time. IEEE Trans. Ultras. Ferroelec. Freq. Contr., 57(1):140–150, 2010. (Cited on page 23.)

[68] G. Petit, F. Arias, and G. Panfilo. International atomic time: Status and future challenges. Comptes Rendus Physique, 16(5):480–488, 2015. The measurement of time / La mesure du temps. (Cited on page 23.)

[69] Panfilo, Gianna and Arias, E. Felicitas. Studies and possible improvements on the eal algorithm. IEEE Trans. Ultras. Ferroelec. Freq. Contr., 57(1):154–160, 2010. (Cited on page 23.)

[70] Gianna Panfilo, Aurelie Harmegnies, and Laurent Tisserand. A new prediction algorithm for the generation of International Atomic Time. Metrologia, 49(1):49, 2011. (Cited on page 23.)

[71] B. Guinot and C. Thomas. Establishment of international atomic time, Annu. Rep. BIPM Time Sect. 1. available from (`www.bipm.org`), 1988. (Cited on page 23.)

[72] G. Panfilo, A. Harmegnies, and L. Tisserand. A new weighting procedure for UTC. Metrologia, 51(3):285–292, may 2014. (Cited on page 23.)

[73] BIPM. Geographical map of laboratories contributing to TAI. `https://webtai.bipm.org/database/maps.html`. (Cited on page 24.)

[74] P Defraigne, G Petit, and C Bruyninx. Use of geodetic receivers for TAI. In Proceedings of the 33th Annual Precise Time and Time Interval Systems and Applications Meeting, pages 341–348, 2001. (Cited on pages 25 and 26.)

[75] David W Allan and Marc Abbott Weiss. Accurate time and frequency transfer during common-view of a GPS satellite. In 34th Annual Symposium on Frequency Control, pages 334–346. IEEE, 1980. (Cited on pages 25 and 26.)

[76] G Petit and Z Jiang. GPS All in View time transfer for TAI computation. Metrologia, 45(1):35, 2007. (Cited on page 26.)

[77] Miho Fujieda, Michito Imae, and Yasuhisa Shibuya. Effects of ionospheric correction on GPS time transfer throughout Asia. Metrologia, 41(3):145, 2004. (Cited on page 26.)

[78] Pascale Defraigne and G Petit. Time transfer to TAI using geodetic receivers. Metrologia, 40(4):184, 2003. (Cited on page 26.)

[79] Jan Kouba and Pierre Héroux. Precise point positioning using IGS orbit and clock products. GPS solutions, 5(2):12–28, 2001. (Cited on page 26.)

[80] Gérard Petit and Zhiheng Jiang. Precise point positioning for TAI computation. In 2007 IEEE International Frequency Control Symposium Joint with the 21st European Frequency and Time Forum, pages 395–398. IEEE, 2007. (Cited on page 26.)

[81] D Wayne Hanson. Fundamentals of two-way time transfers by satellite. In Proceedings of the 43rd Annual Symposium on Frequency Control, pages 174–178. IEEE, 1989. (Cited on page 27.)

[82] Dieter Kirchner. Two-way time transfer via communication satellites. Proceedings of the IEEE, 79(7):983–990, 1991. (Cited on page 27.)

[83] Franco Cordara, Luca Lorini, V Pettiti, P Tavella, D Piester, J Becker, T Polewka, G De Jong, O Koudelka, H Ressler, et al. Calibration of the IEN-PTB TWSTFT link with a portable reference station. In Proceedings of the 18th European Frequency and Time Forum, 2004, 2004. (Cited on page 28.)

[84] W Lewandowski, F Cordara, Luca Lorini, V Pettiti, A Bauch, D Piester, and O Koudelka. A simultaneous calibration of the IEN/PTB time link by GPS CV and TWSTFT portable equipment. In Proceedings of the 18th European Frequency and Time Forum, 2004, 2004. (Cited on page 28.)

[85] W Lewandowski, D Matsakis, G Panfilo, and Patrizia Tavella. The evaluation of uncertainties in [UTC- UTC (k)]. Metrologia, 43(3):278, 2006. (Cited on page 29.)

[86] L. Galleani and P. Tavella. Detection of atomic clock frequency jumps with the Kalman filter. IEEE Trans. Ultras. Ferroelec. Freq. Contr., 59(3):504–509, March 2012. (Cited on pages 30, 43, 47, and 147.)

[87] Cristina Zucca and Patricia Tavella. The clock model and its relationship with the Allan and related variances. IEEE Trans. Ultras. Ferroelec. Freq. Contr., 52(2):289–296, 2005. (Cited on pages 31 and 36.)

[88] Patrizia Tavella. Statistical and mathematical tools for atomic clocks. Metrologia, 45(6):S183, 2008. (Cited on pages 31, 32, and 33.)

[89] G Panfilo and Patrizia Tavella. Atomic clock prediction based on stochastic differential equations. Metrologia, 45(6):S108, 2008. (Cited on page 31.)

[90] Samuel Karlin. A first course in stochastic processes. Academic press, 1975. (Cited on page 31.)

[91] Maurice Bertram Priestley. Spectral analysis and time series: Univariate series, volume 1. Academic press, 1981. (Cited on page 31.)

[92] Franck Beichelt and L. Paul Fatti. Stochastic Processes and Their Applications. CRC Press, 2002. (Cited on page 31.)

[93] Richard H Jones and Peter V Tryon. Continuous time series models for unequally spaced data applied to modeling atomic clocks. SIAM Journal on Scientific and Statistical Computing, 8(1):71–81, 1987. (Cited on pages 31 and 36.)

[94] James W Chaffee. Relating the Allan variance to the diffusion coefficients of a linear stochastic differential equation model for precision oscillators. IEEE Trans. Ultras. Ferroelec. Freq. Contr., 34:655–658, 1987. (Cited on pages 31, 36, and 39.)

[95] L Galleani, L Sacerdote, Patrizia Tavella, and Cristina Zucca. A mathematical model for the atomic clock error. Metrologia, 40(3):S257, 2003. (Cited on pages 31, 33, and 36.)

[96] L Arnold. Stochastic differential equations: Theory and applications. Wiley, 1974. (Cited on pages 31 and 37.)

[97] Peter E Kloeden and Eckhard Platen. Stochastic differential equations. In Numerical solution of stochastic differential equations, chapter 4, pages 103–160. Springer, 1992. (Cited on pages 31 and 37.)

[98] David W Allan. Time and frequency(time-domain) characterization, estimation, and prediction of precision clocks and oscillators. IEEE Trans. Ultras. Ferroelec. Freq. Contr., 34(6):647–654, 1987. (Cited on page 31.)

[99] William C Lindsey and Chak Ming Chie. Theory of oscillator instability based upon structure functions. In Proc. IEEE, volume 64, pages 1652–1666. IEEE, 1976. (Cited on page 31.)

[100] F Vernotte and E Lantz. Time stability: An improvement of the multi-variance method for the oscillator noise analysis. In Proc. 6th Eur. Freq. Time Forum, pages 343–347, 1992. (Cited on page 31.)

[101] Todd Walter. A multi-variance analysis in the time domain. In Proc. 24th Annu. Precise Time and Time Interval and Applications Meeting, pages 413–426, 1992. (Cited on page 31.)

[102] Steven T Hutsell. Relating the Hadamard variance to MCS Kalman filter clock estimation. In Proc. 27th Annu. Precise Time and Time Interval and Applications Meeting, pages 291–302, 1995. (Cited on pages 31, 36, and 39.)

[103] Peter Kartaschoff. Frequency and time. Monographs in Physical Measurement, 1978. (Cited on page 32.)

[104] David W Allan. Statistics of atomic frequency standards. Proceedings of the IEEE, 54(2):221–230, 1966. (Cited on pages 33 and 35.)

[105] F. Vernotte, C. Plantard, A. Kinali, and F. Meyer. SigmaTheta Software. `https://sourcesup.renater.fr/www/sigmatheta/`. (Cited on page 34.)

[106] E.A. Gerber and A. Ballato. Precision Frequency Control: Oscillators and standards. Academic Press, 1985. (Cited on page 36.)

[107] Charles A Greenhall. Forming stable timescales from the Jones–Tryon Kalman filter. Metrologia, 40(3):S335, 2003. (Cited on page 36.)

[108] Kenneth R Brown. The theory of the GPS composite clock. In Proc. Inst. Navig. - Global Posit. Syst. Institute of Navigation, 1991. (Cited on page 36.)

[109] André J Van Dierendonck and JB McGraw. Relationship between Allan variances and Kalman filter parameters. In Proc. 16th Annu. Precise Time and Time Interval and Applications Meeting, pages 273–293, 1984. (Cited on page 36.)

[110] Robert G. Brown and Patrick Y. C. Hwang. Introduction to random signals and applied Kalman filtering. New York, Wiley, 1992. (Cited on page 36.)

[111] Rudolph Emil Kalman. A new approach to linear filtering and prediction problems. J. Basic Eng., 1960. (Cited on page 41.)

[112] F. Parisi and G. Panfilo. A new approach to UTC calculation by means of the Kalman filter. Metrologia, 53(5):1185–1192, 2016. (Cited on page 41.)

[113] Mohinder S Grewal, Lawrence R Weill, and Angus P Andrews. Global positioning systems, inertial navigation, and integration. John Wiley & Sons, 2007. (Cited on page 41.)

[114] Richard H Jones and Peter V Tryon. Estimating time from atomic clocks. Journal of research of the National Bureau of Standards, 88(1):17, 1983. (Cited on page 41.)

[115] R. B. Blackman and J. W. Tuckey. The Measurement of Power Spectra. Dover, 1959. (Cited on page 59.)

[116] Gwilym M. Jenkins and Donald G. Watts. Spectral Analysis and its Applications. Holden Day, San Francisco, CA, 1968. (Cited on page 59.)

[117] O. E. Brigham. The Fast Fourier Transform and its Applications. Prentice-Hall, 1988. (Cited on page 59.)

[118] D. B. Percival and A. T. Walden. Spectral Analysis for Physical Applications. Cambridge, Cambridge, UK, 1993. (Cited on page 59.)

[119] R. H. Dicke. The measurement of thermal radiation at microwave frequencies. Rev. Sci. Instrum., 17(7):268–275, July 1946. (Cited on page 59.)

[120] M. Sampietro, L. Fasoli, and G. Ferrari. Spectrum Analyzer with Noise Reduction by Cross-Correlation Technique on Two Channels. Rev. Sci. Instrum., 70(5):2520–2525, May 1999. (Cited on page 59.)

[121] A. Hati, C. W. Nelson, and D. A. Howe. Cross-spectrum measurement of thermal-noise limited oscillators. Rev. Sci. Instrum., 87:034708, March 2016. (Cited on page 60.)

[122] Y. Gruson, V. Giordano, U. L. Rohde, A. K. Poddar, and E. Rubiola. Cross-Spectrum PM Noise Measurement, Thermal Energy, and Metamaterial Filters. IEEE Trans. Ultras. Ferroelec. Freq. Contr., 64(3):634–642, March 2017. (Cited on page 60.)

[123] A. C. Cárdenas-Olaya, E. Rubiola, Friedt J.-M., P.-Y. Bourgeois, M. Ortolano, S. Micalizio, and C. E. Calosso. Noise characterization of analog to digital converters for amplitude and phase noise measurements. Rev. Sci. Instrum., 88:065108 1–9, June 2017. (Cited on page 60.)

[124] G. Feldhaus and A. Roth. A 1 MHz to 50 GHz Direct Down-Conversion Phase Noise Analyzer with Cross-Correlation. In Proc. Europ. Freq. Time Forum, York, UK, April 4-7 2016. (Cited on page 60.)

[125] T. M. Fortier, C. W. Nelson, A. Hati, F. Quinlan, J. Taylor, H. Jiang, C. W. Chou, T. Rosenband, A. Lemke, N. Ludlow, D. Howe, C. W. Oates, and S. A. Diddams. Sub-femtosecond absolute timing jitter with a 10 GHz hybrid photonic-microwave oscillator. Appl. Phys. Lett., 100:231111 1–3, June 7 2012. (Cited on page 60.)

[126] E. Rubiola. The measurement of AM noise of oscillators. arXiv:physics/0512082, December 2005. (Cited on page 60.)

[127] A. H. Verbruggen, H. Stoll, K. Heeck, and R. H. Koch. A Novel Technique for Measuring Resistance Fluctuations Independently of Background Noise. Appl. Phys. A, 48:233–236, March 1989. (Cited on page 60.)

[128] C. M. Allred. A Precision Noise Spectral Density Comparator. J. Res. NBS, 66C:323–330, October-December 1962. (Cited on page 60.)

[129] J. A. Nanzer and R. L. Rogers. Applying Millimeter-Wave Correlation Radiometry to the Detection of Self-Luminous Objects at Close Range. IEEE Trans. Microw. Theory Tech., 56(9):2054–2061, September 2008. (Cited on page 60.)

[130] D. R. White, R. Galleano, A. Actis, H. Brixy, M. De Groot, J. Dubbeldam, A. L. Reesink, F. Edler, H. Sakurai, R. L. Shepard, and Gallop J. C. The status of Johnson noise thermometry. Metrologia, 33(4):325–335, August 1996. (Cited on page 60.)

[131] R. W. Hellings and G. S. Downs. Upper limits on the isotopic gravitational radiation background frompulsar timing analysis. Am. Astronom. Soc., 265:39–42, February 1983. (Cited on page 60.)

[132] S. Drasco and E. E. Flanagan. Detection methods for non-Gaussian gravitational wave stochastic backgrounds. Phys. Rev. D, 67(8):082003, 2003. (Cited on page 60.)

[133] N. J. Cornish and J. D. Romano. Towards a unified treatment of gravitational-wave data analysis. Phys. Rev. D, 87(12):122003, 2013. (Cited on page 60.)

[134] R. N. Manchester. Millisecond Pulsars, their Evolution and Applications. Journal of Astrophysics and Astronomy, 38:1–18, 2017. (Cited on page 60.)

[135] J. E. Hansen and M. Sato. Paleoclimate Implications for Human-Made Climate Change. In A. Berger, F. Mesinger, and D. Sijacki, editors, Climate Change, pages 21–47, Vienna, 2012. Springer Vienna. (Cited on page 60.)

[136] A. Nothnagel. Elements of Geodetic and Astrometric Very Long Baseline Interferometry, Nov 2021. `https://www.vlbi.at/data/publications/2021_Nothnagel_Elements_of_VLBI_20211102.pdf`. (Cited on page 60.)

[137] Massimo Caligaris, Giovanni Antonio Costanzo, and Claudio Eligio Calosso. 6/12-Channel Synchronous Digital Phasemeter for Ultrastable Signal Characterization and Use. In EFTF, pages 681–683, Denver, CO, USA, apr 2015. (Cited on page 60.)

[138] Vilius Palenskis and Kestutis Maknys. Nature of low-frequency noise in homogeneous semiconductors. SREP, 5(1), dec 2015. (Cited on page 61.)

[139] M. E. Tiuri. Radio-Telescope Receivers. In Radio Astronomy, chapter 7 of J. D. Kraus. New York: McGraw Hill, 1966. (Cited on page 61.)

[140] J. P. W. Verbiest, S. Osłowski, and S. Burke-Spolaor. Pulsar Timing Array Experiments, pages 1–42. Springer Singapore, Singapore, 2020. (Cited on page 61.)

[141] B. Goncharov, R. M. Shannon, D. J. Reardon, G. Hobbs, A. Zic, M. Bailes, M. Curyło, S. Dai, M. Kerr, M. E. Lower, and et al. On the Evidence for a Common-spectrum Process in the Search for the Nanohertz Gravitational-wave Background with the Parkes Pulsar Timing Array. The Astrophysical Journal Letters, 917(2):L19, Aug 2021. (Cited on page 61.)

[142] Siyuan Chen, François Vernotte, and Enrico Rubiola. Applying clock comparison methods to pulsar timing observations. Month. Not. Roy. Astronom. Soc., 503(3):4496–4507, 03 2021. (Cited on page 61.)

[143] International Vocabulary of Basic and General Terms in Metrology (VIM). International Organization for Standardization (ISO), 2004. (Cited on page 62.)

[144] N. J. Kasdin. Discrete simulation of colored noise and stochastic processes and 1/f power law noise generation. Proceedings of the IEEE, 83(5):802–827, May 1995. (Cited on pages 63 and 82.)

[145] F. Vernotte. Métrologie Temps-Fréquence, volume Mesures et tests électroniques of Mesures - Analyse, chapter Stabilité temporelle et fréquentielle des oscillateurs : modèles, pages R680/1–R680/10. Techniques de l'Ingénieur, Paris, 2006. (Cited on page 68.)

[146] F. Vernotte. Application of the moment condition to noise simulation and to stability analysis. IEEE Trans. Ultras. Ferroelec. Freq. Contr., 49(4):508–513, April 2002. (Cited on page 69.)

[147] H. Shima and T. Nakayama. Higher Mathematics for Physics and Engineering. Springer, Berlin, 2010. (Cited on pages 72 and 75.)

[148] F. Stenger. Handbook of Sinc Numerical Methods. CRC Press, Boca Raton, 2011. (Cited on page 75.)

[149] J. A. Fessler. On Transformations of Random Vectors. Technical Report 314, Dept. of Electrical Engineering and Computer Science, Univ. of Michigan, 1998. https://web.archive.org/web/20131218214647if_/http://andywilliamson.org/_/wp-content/uploads/2010/04/White-Noise.pdf. (Cited on page 79.)

[150] A. Baudiquez, E. Lantz, E. Rubiola, and F. Vernotte. Cross-Spectrum Measurement Statistics: Uncertainties and Detection Limit. IEEE Trans. Ultras. Ferroelec. Freq. Contr., 67(11):2461–2470, June 2020. (Cited on pages 91 and 132.)

[151] B. Sorin and P. Thionet. Lois de probabilités de Bessel. Rev. Stat. App., 16(4):65–72, 1968. (Cited on pages 96, 106, and 109.)

[152] F. Vernotte and E. Lantz. Three-Cornered Hat and Groslambert Covariance: A first attempt to assess the uncertainty domains. IEEE Trans. Ultras. Ferroelec. Freq. Contr., 66(3):643–653, March 2019. (Cited on pages 96, 104, 105, 107, 109, and 117.)

[153] D. Jankov Maširević and T. K. Pogány. On series representations for modified Bessel function of second kind of integer order. Integral Transforms and Special Functions, 30(3):181–189, March 2019. (Cited on page 97.)

[154] R.A. Meyers. Complex Systems in Finance and Econometrics. Complex Systems in Finance and Econometrics. Springer, 2010. (Cited on page 97.)

[155] M. Haas and C. Pigorsch. Financial Economics, Fat-Tailed Distributions, pages 3404–3435. Springer New York, New York, NY, 2009. (Cited on page 105.)

[156] D. Madan and E. Seneta. The Variance Gamma (V.G.) Model for Share Market Returns. J. Business, 63(4):511–524, 1990. (Cited on page 107.)

[157] G. N. Watson. A Treatise on the Theory of Bessel Functions. Cambridge University Press, 1922. (Cited on page 111.)

[158] T. Bayes. An Essay towards solving a Problem in the Doctrine of Chances. Phyl. Transact. Royal Soc. London, 53:370–418, 1763. (Cited on page 116.)

[159] D. V. Lindley. Fiducial Distributions and Bayes' Theorem. Journal of the Royal Statistical Society, 20(1):102–107, 1958. (Cited on page 116.)

[160] J. Bernardo and A. Smith. Bayesian Theory. Wiley Series in Probability and Statistics. Wiley & Sons, 1994. (Cited on page 116.)

[161] M. P. McHugh, G. Zalamansky, F. Vernotte, and E. Lantz. Pulsar timing and the upper limits on a gravitational wave background : a Bayesian approach. Phys. Rev. D, 54(10):5993–6000, November 1996. (Cited on pages 116 and 135.)

[162] Robert E Kass and Larry Wasserman. The selection of prior distributions by formal rules. Journal of the American statistical Association, 91(435):1343–1370, 1996. (Cited on page 116.)

[163] Zaven Arzoumanian, PT Baker, Adam Brazier, Sarah Burke-Spolaor, SJ Chamberlin, Shami Chatterjee, Brian Christy, James M Cordes, Neil J Cornish, Fronefield

Crawford, et al. The NANOGrav 11 year data set: pulsar-timing constraints on the stochastic gravitational-wave background. The Astrophysical Journal, 859(1):47, 2018. (Cited on page 116.)

[164] Jeffrey S Hazboun, Joseph Simon, Xavier Siemens, and Joseph D Romano. Model dependence of Bayesian gravitational-wave background statistics for pulsar timing arrays. The Astrophysical Journal Letters, 905(1):L6, 2020. (Cited on page 116.)

[165] A Philip Dawid, Mervyn Stone, and James V Zidek. Marginalization paradoxes in Bayesian and structural inference. Journal of the Royal Statistical Society: Series B (Methodological), 35(2):189–213, 1973. (Cited on page 116.)

[166] Ronald Christensen, Wesley Johnson, Adam Branscum, and Timothy E Hanson. Bayesian ideas and data analysis: an introduction for scientists and statisticians. CRC press, 2010. (Cited on page 116.)

[167] E. Lantz, C. E. Calosso, E. Rubiola, V. Giordano, C. Fluhr, B. Dubois, and F. Vernotte. KLTS: A Rigorous Method to Compute the Confidence Intervals for the Three-Cornered Hat and for Groslambert Covariance. IEEE Trans. Ultras. Ferroelec. Freq. Contr., 66(12):1942–1949, December 2019. (Cited on pages 117, 119, and 132.)

[168] G. Saporta. Probabilités, analyse des données et statistique. Technip, 1990. (Cited on page 119.)

[169] A. Baudiquez, E. Lantz, E. Rubiola, and F. Vernotte. The Statistics of the Cross-Spectrum and the Spectrum Average: Generalization to Multiple Instruments. IEEE Trans. Ultras. Ferroelec. Freq. Contr., 69(8):2585–2594, June 2022. (Cited on page 129.)

[170] J. Hartung, G. Knapp, and B. K. Sinha. Statistical Meta-Analysis with Applications. Wiley, 2008. (Cited on page 130.)

[171] H. A. R. Barnett. The variance of the product of two independent variables and its application to an investigation based on sample data. Journal of the Institute of Actuaries, 81(2):190–190, 1955. (Cited on page 156.)

[172] L. Isserlis. On a Formula for the Product-Moment Coefficient of any Order of a Normal Frequency Distribution in any Number of Variables. Biometrika, 12(1/2):134–139, nov 1918. (Cited on page 156.)

Title: Metrology and statistics: From clocks to millisecond pulsars

Keywords: atomic clocks, bayesian statistics, confidence interval, cross-spectrum, metrology, phase jump, probability density function, spectrum average, time-frequency analysis, time stability

Time is the physical quantity that is measured with the greatest precision, far ahead of all the others. Recent advances in atomic clocks have made it possible to achieve relative stabilities of the order of a few 10^{-18}, thus corresponding to an uncertainty of about one second in the age of the Universe. However, it is not because these uncertainties become ridiculously small that they should be neglected, quite the contrary. The aim of this work is to contribute to improving the determination of these uncertainties. It is divided in two parts and concerns the fine characterization and improvement of a set of estimation methods.

In the present work we first describe a procedure to determine the jumps which can affect the time links used in the Coordinated Universal Time (UTC), calculated by the BIPM. This tool, based on a Kalman filter, should correctly determine the date of the steps and their magnitude, mainly for time steps, and give a warning to the BIPM Time Department about this unexpected problem. This warning will help to understand the nature of the steps which, in some cases, can affect the behavior of UTC. A critical example is the receiver calibration causing a step in time links and potentially impacting UTC behavior. To ensure the long-term stability of UTC, it is crucial to verify the data and identify problems.

The second part of the work mainly concerns a detailed analysis of frequency instabilities in terms of Bayesian statistics. In particular we want to obtain reliable confidence intervals around the measurements of the power spectrum of red noise processes at the lowest frequencies, e.g. the observation of millisecond pulsars in radio astronomy. Thus it is only possible to average on simultaneous observation of multiple instruments. We compare 95% upper limit of the red noise parameter using the spectrum average and cross-spectrum. Checked by massive Monte Carlo simulations, the cross-spectrum estimator leads to the variance-Gamma distribution with two instruments and a generalization to n instruments based on the Fourier transform of characteristic functions is provided.

Titre : Métrologie et statistiques : de l'horlogerie aux pulsars millisecondes

Mots clés : analyse temps-fréquence, densité de probabilité, horloges atomiques, intervalle de confiance, métrologie, moyenne du spectre, saut de phase, spectre croisé, stabilité temporelle, statistiques bayésiennes

Le temps est la grandeur physique qui se mesure avec la plus grande précision, loin devant toutes les autres. Les progrès récents des horloges atomiques ont permis d'atteindre des stabilités relatives de l'ordre de quelques 10^{-18}, correspondant ainsi à une incertitude d'environ une seconde sur l'âge de l'Univers. Cependant, ce n'est pas parce que ces incertitudes deviennent dérisoires qu'il faut les négliger, bien au contraire. Le but de ce travail est de contribuer à améliorer la détermination de ces incertitudes. Il est divisé en deux parties et porte sur la caractérisation fine et l'amélioration d'un ensemble de méthodes d'estimation.

Dans ce travail, nous décrivons d'abord une procédure pour déterminer les sauts qui peuvent affecter les liens de transfert de temps utilisés dans le calcul de l'échelle du Temps Universel Coordonnée (UTC), calculé par le BIPM. Cet outil, basé sur un filtre de Kalman, devrait déterminer correctement la date des sauts et leur grandeur, principalement pour les sauts de temps, et avertir le service du temps du BIPM de ce problème inattendu. Cet avertissement aidera à comprendre la nature des étapes qui, dans certains cas, peuvent affecter le comportement d'UTC. Un exemple critique est l'étalonnage du récepteur qui provoque un saut dans les transfert de temps et qui a potentiellement un impact sur le comportement d'UTC. Pour assurer la stabilité à long terme d'UTC, il est crucial de vérifier les données et d'identifier les problèmes.

La deuxième partie du travail concerne principalement une analyse détaillée en termes de statistiques bayésiennes des instabilités de fréquence. En particulier, nous voulons obtenir des intervalles de confiance fiables autour des mesures du spectre de puissance des processus de bruit rouge aux fréquences les plus basses, par ex. l'observation des pulsars millisecondes en radioastronomie. Ainsi, il n'est possible de faire la moyenne que sur l'observation simultanée de plusieurs instruments. Nous comparons la limite supérieure à 95% sur le paramètre de bruit rouge en utilisant la moyenne du spectre et le spectre croisé. Vérifié par des simulations massives de Monte Carlo, l'estimateur à spectre croisé conduit à la distribution variance-Gamma avec deux instruments et une généralisation à n instruments basée sur la transformée de Fourier des fonctions caractéristiques est fournie.

Université Bourgogne Franche-Comté
32, avenue de l'Observatoire
25000 Besançon